

AD625556

AFTAC Project VT/4053

ARRAY RESEARCH

by

Milo M. Backus, Project Scientist
FL 7-5411 Ext. 319

CLEARINGHOUSE FOR FEDERAL SCIENTIFIC AND TECHNICAL INFORMATION	
Hardcopy	Microfilm
\$5.00	1.25/153 <i>as</i>
ARCHIVE COPY	
<i>code 1</i>	

Robert Roden
Sam Rodgers

John Burg
John Hoffman

Aaron Booker
Frank Binder

TEXAS INSTRUMENTS INCORPORATED
P. O. Box 5621
Dallas, Texas 75222

Contract No. AF 33(657)-12747
Date of Contract: 13 November 1963
Contract Expiration Date: 31 December 1965

SEMIANNUAL TECHNICAL REPORT NO. 3
Covering the Period
15 November 1964 to 15 May 1965

Prepared for
AIR FORCE TECHNICAL APPLICATIONS CENTER
Washington, D.C.

ARPA Order No. 104-60
Project Code No. 8100

DISTRIBUTION OF THIS
DOCUMENT IS UNLIMITED.

**BEST
AVAILABLE COPY**

ARRAY RESEARCH
SEMIANNUAL TECHNICAL REPORT NO. 3

AFTAC Project VT/4053
Contract AF 33(657)-12747

Principal authors of this report are:

Section I	Robert Roden
Section II	Robert Roden John Hoffman
Section III	Aaron Booker
Section IV	Frank Binder
Section V	Sam Rodgers
Section VI	John Burg

Prepared for
AIR FORCE TECHNICAL APPLICATIONS CENTER
Washington, D.C.
3 June 1965

BLANK PAGE

TABLE OF CONTENTS

Section	Title	Page
	SUMMARY	
	A. VERTICAL ARRAYS FOR TELESEISMIC SIGNAL EXTRACTION	
	B. DECONVOLUTION AND AUTOCORRELATION STUDY	
	C. PROBABILISTIC PROCESSING	
	D. STUDY OF PARTIAL ARRAYS AT CPO	
	E. INITIAL PROCESSING AND ANALYSIS OF THE LONG TFO NOISE SAMPLE	
I	VERTICAL ARRAYS FOR TELESEISMIC SIGNAL EXTRACTION	I-1
	A. SUMMARY	I-1
	B. ANALYSIS OF UBO VERTICAL ARRAY DATA	I-1
	C. COLLECTION OF VERTICAL ARRAY DATA AT GRAPEVINE	I-41
II	DECONVOLUTION AND AUTOCORRELATION STUDY	II-1
	A. DESCRIPTION OF DATA	II-1
	B. AVERAGE AUTOCORRELATIONS FROM ENSEMBLE I	II-10
	C. INDIVIDUAL-EVENT DECONVOLUTION OF ENSEMBLES II AND III	II-13/14
III	PROBABILISTIC PROCESSING	III-1
	A. INTRODUCTION	III-1
	B. CALCULATION OF THE TEST STATISTIC	III-2
	C. PROGRESS AND FUTURE GOALS	III-11/12
IV	STUDY OF PARTIAL ARRAYS AT CPO	IV-1
	A. INTRODUCTION	IV-1
	B. MULTICHANNEL FILTER SYSTEMS DESIGN	IV-1
	C. EVALUATION OF THE MULTICHANNEL FILTER SYSTEMS	IV-2
	D. MCF SYSTEM'S RESPONSES TO INFINITE-VELOCITY SIGNAL	IV-5
	E. NOISE SUPPRESSION AND SIGNAL-TO-NOISE IMPROVEMENT	IV-16
	F. K-SPACE RESPONSE OF SYSTEMS	IV-24

TABLE OF CONTENTS (CONTD)

Section	Title	Page
V	INITIAL PROCESSING AND ANALYSIS OF THE LONG TFO NOISE SAMPLE	V-1
	A. RECORDING AND PRELIMINARY PROCESSING AND ANALYSIS	V-1
	B. CALIBRATION ANALYSIS OF THE LARGE CROSS ARRAY	V-5
VI	FURTHER ANALYSIS OF TFO AMBIENT NOISE	VI-1
	A. SUMMARY	VI-1
	B. PROCESSING OF THE AUTO-AND CROSS-CORRELATION FUNCTIONS	VI-1
	C. ANALYSIS OF THE CORRELATION DISPLAYS	VI-8
	D. PREPARATION OF THE HORIZONTAL-VERTICAL COHERENCE DATA	VI-20
	E. ANALYSIS OF THE HORIZONTAL-VERTICAL COHERENCES AND POWER SPECTRA	VI-20
VII	REFERENCES	VII-1

SUMMARY

A. VERTICAL ARRAYS FOR TELESEISMIC SIGNAL EXTRACTION

Deep-well seismic data recorded at UBO in September-October 1964 are used to estimate the capabilities of three 3-element vertical arrays and one hypothetical 6-element vertical array. It is shown that two deeply buried receivers can be employed to estimate accurately the signal observed by a surface instrument. It is estimated that the maximum signal-to-noise ratio improvement obtainable from a single vertical array at UBO is approximately 6 to 8 db but that a vertical array should be able to provide greater improvement at a high-noise site. It appears that the percentage of ambient noise due to P-waves is a dominant factor contributing to the performance limit.

The vertical array data from UBO consisted of simultaneous recordings from three seismometers, one held at a depth of 200 ft and the other two placed at all possible depth pairs of five deeper depth positions. Correlations from these recordings were combined to estimate the correlation matrix for a hypothetical 6-seismometer vertical array. This built-up correlation matrix was not positive definite, i. e., was not, in fact, a possible correlation matrix. All attempts at generating a 6-channel multichannel filter system failed, both in the time domain and frequency domain. The correlation functions are in good visual agreement with theoretical correlation functions and indicate considerable mantle P-wave noise at UBO. However, to insure the necessary mathematical interrelations between the auto- and crosscorrelations for MCF design for an array of seismometers a simultaneous recording from the full array seems to be a practical necessity.

B. DECONVOLUTION AND AUTOCORRELATION STUDY

The application of deconvolution and autocorrelation techniques to three ensembles of earthquake records from the multichannel processor at CPO is being studied. Statistics of discrepancies between observed and USC&GS reported origin times, magnitudes and depths of focus are examined.

Ensemble and subensemble average autocorrelations are presented for Ensemble I (73 Kurile Islands events). Very little difference can be observed among the subensembles or between unweighted and normalized averages. It is hypothesized that certain features in the autocorrelations are due to reflections from the Conrad and Mohorovicic discontinuities under CPO.

Ensembles II and III (60 and 119 events of worldwide distribution are described and the results of individual-event deconvolution presented. Although signal waveforms are contracted somewhat, there is no obvious improvement in detectability of later phases. The nature of the ambient noise recorded at CPO is discussed briefly.

C. PROBABILISTIC PROCESSING

A description of the mathematical operations and computer programs required to perform probabilistic processing is given in Section III. In particular, an efficient iterative formula for inverting a multichannel correlation matrix is derived, a technique for generating a synthetic multichannel time series with a given correlation matrix is discussed and a recursive procedure for solving the generalized eigenvalue problem for single-channel correlation matrices is presented. The status of these programs and future goals are discussed.

D. STUDY OF PARTIAL ARRAYS AT CPO

Four multichannel filter systems for CPO were designed using the full array and three partial arrays. These systems were synthesized using measured noise correlations and an infinite velocity signal model. The MCF systems were evaluated on the computer to compare the ability of the partial arrays to suppress noise while preserving high-velocity signals.

Results show that the partial arrays are almost as effective as the full array near 1 cps. Below approximately 0.7 cps, seismometer gain inequalities appear to be affecting the output of the systems. At higher frequencies, the K-space aliasing of some of the partial arrays prevents effective noise suppression.

To help evaluate the effects of seismometer gain inequalities, MCF systems will be designed using a signal model incorporating statistical gain fluctuation. This will be the subject of a separate report.

E. INITIAL PROCESSING AND ANALYSIS OF THE LONG TFO NOISE SAMPLE

Section V contains information concerning the recording and preliminary processing and analysis of a 20-min ambient seismic noise sample from the ring array, the large cross array and a 3-component seismometer at Tonto Forest Seismological Observatory. Also presented is an analysis of calibration data for the large cross array recorded on the same day as the long noise sample.

F. FURTHER ANALYSIS OF TFO AMBIENT NOISE

Section VI presents the complete set of auto- and crosscorrelation functions from the 21 seismometers in the large cross array at TFO as found from the long noise sample discussed in Section V. Also presented is the complete set of 10 coherences between the two horizontal seismometers and three vertical seismometers. The analysis of this data shows that the 4 to 6 sec energy is coming from $N60^{\circ}E$ with a velocity of about 3.4 km/sec. The other energy below 1.2 cps is mantle P-wave noise, which is definitely nonisotropic. Above 1.2 cps, the energy is random, seismometer to seismometer, except for some highly coherent lines in the spectra. The horizontal seismometer in line with the 4 to 6 sec energy shows a high coherence with the vertical seismometers in that frequency range, but the transverse seismometer has very small coherence with all other seismometers. This is further proof that this energy is Rayleigh motion. The presence of Love wave energy on the transverse seismometer can be inferred from its lack of coherence with the other seismometers.

BLANK PAGE

SECTION I

VERTICAL ARRAYS FOR TELESEISMIC SIGNAL EXTRACTION

A. SUMMARY

Deep-well seismic data recorded at UBO in September-October 1964 are used to estimate the capabilities of three 3-element vertical arrays and one hypothetical 6-element vertical array. It is shown that two deeply buried receivers can be employed to estimate accurately the signal observed by a surface instrument. It is estimated that the maximum signal-to-noise ratio improvement obtainable from a single vertical array at UBO is approximately 6 to 8 db but that a vertical array should be able to provide greater improvement at a high-noise site. It appears that the percentage of ambient noise due to P-waves is a dominant factor contributing to the performance limit.

The vertical array data from UBO consisted of simultaneous recordings from three seismometers, one held at a depth of 200 ft and the other two placed at all possible depth pairs of five deeper depth positions. Correlations from these recordings were combined to estimate the correlation matrix for a hypothetical 6-seismometer vertical array. This built-up correlation matrix was not positive definite, i.e., was not, in fact, a possible correlation matrix. All attempts at generating a 6-channel multi-channel filter system failed, both in the time domain and frequency domain. The correlation functions are in good visual agreement with theoretical correlation functions and indicate considerable mantle P-wave noise at UBO. However, to insure the necessary mathematical interrelations between the auto- and crosscorrelations for MCF design for an array of seismometers, a simultaneous recording from the full array seems to be a practical necessity.

During March 1965, a program of deep-well recording was conducted at Grapevine, Texas. This report presents a description of the data.

B. ANALYSIS OF UBO VERTICAL ARRAY DATA

1. Description of Data

As described in a previous report¹, a program of digital recording of seismic data was conducted at Uinta Basin Observatory (UBO) during the period 9 September through 13 October 1964. The analysis reported in this section uses data obtained from three instruments designated

SH-1, DH-1 and DH-2. SH-1 remained at a depth of 200 ft (0.06 km) throughout the recording period, while DH-1 and DH-2 were moved about in order to permit simultaneous recording at each of the possible pairs of the following five depths: 900 ft (0.27 km), 2900 ft (0.88 km), 4900 ft (1.49 km), 6900 ft (2.10 km), 8900 ft (2.71 km).

Data edited from the field records consisted of 50 records of seismic noise (five from each pair of depths of DH-1 and DH-2) and 16 records of teleseismic signal (two when possible from each depth pair). Each record consisted of 2 min of data recorded digitally with 24-msec sampling interval. High-cut filtering was applied so the data could be resampled at 72 msec, and gain factors were applied to equalize instrument response at 1.0 cps. The records are listed in Tables I-1 and I-2.

2. Preliminary Investigation of Data

Four noise samples and three signals from two sets of recording depths were selected in order to investigate certain properties of signal and noise as observed in the UBO deep well. Playbacks of the original records are reproduced in Figure I-1. No visible alteration of the records was produced by the filtering and resampling operation.

Power spectra computed for the selected events are illustrated in Figures I-2 and I-3. Absolute power levels may be determined by means of the smooth curve which corresponds to a power density of $1 \text{ m}\mu^2/\text{cps}$. The average system noise level over the range 0 to 4.0 cps was found to be -43 db relative to $1 \text{ m}\mu^2/\text{cps}$ at 1.0 cps.

A significant difference was found in the spectra of the signals studied. However, only relatively small differences in depth-dependence can be observed. Some depth-dependence differences would be expected to result from differences in angle of emergence of the signals. The peaks and troughs in the spectra for buried seismometers generally are located where the theory predicts. When smoothing is applied, the noise spectrum at 200 ft is found to be relatively constant. Apparent variations in the frequency and depth-dependence of the noise probably are not significant, so it is impossible to draw conclusions as to whether important changes may have occurred in the modal structure of the noise. Nonstationarity of the signal and noise is the most probable explanation for the failure of attempts to evaluate a 6-element vertical array using the UBO data. Refer to subsection B-4 for further details.

For each of the selected events, a short deconvolution filter was designed to whiten the spectrum of the 200-ft trace. This filter was applied to each of the three traces, and coherence functions were

Table I-1
CATALOG OF UBO DEEP-WELL NOISE SAMPLES
(Dates and GCT Start Times)

DH-1 Depth (ft)	DH-2 Depth (ft)	Noise Sample 1	Noise Sample 2	Noise Sample 3	Noise Sample 4	Noise Sample 5
8900	900	9/13 21:17:20	9/14 22:10:10	9/15 12:48:50	9/15 14:01:50	9/15 14:30:00
8900	2900	9/17 12:07:50	9/17 13:10:40	9/17 13:52:10	9/17 21:14:20	9/17 21:54:20
8900	4900	9/20 19:08:30	9/21 20:00:10	9/21 13:28:10	9/21 15:57:10	9/21 17:17:10
6900	900	9/27 18:55:20	9/27 20:47:10	9/28 14:56:20	9/28 15:41:20	9/28 16:42:30
6900	2900	9/29 22:16:20	9/29 22:54:20	9/30 22:07:00	9/30 22:45:26	9/30 23:01:10
6900	4900	10/1 19:17:16	10/2 20:28:50	10/2 22:47:20	10/2 23:34:10	10/2 23:52:50
4900	2900	10/4 15:34:10	10/4 16:05:10	10/4 18:43:10	10/5 02:08:10	10/5 02:36:30
4900	900	10/6 18:32:50	10/6 18:57:50	10/6 19:10:00	10/6 20:28:30	10/6 20:34:10
2900	900	10/8 19:16:10	10/9 00:09:10	10/9 00:23:50	10/9 14:27:10	10/9 15:00:10
8900	6900	10/12 18:58:10	10/12 19:39:10	10/13 02:14:10	10/13 03:53:10	10/13 04:09:10

Table I-2

CATALOG OF UBO DEEP-WELL TELESEISM RECORDS

Ser. No.	DH-1 Depth (ft)	DH-2 Depth (ft)	Date	Arrival Time	Location	M ₆	Δ (degrees)
1	8900	900	9/15	12:56:25	Samoa	5.3	81
3	8900	2900	9/17	13:35:54	Unidentified	Teleseism	
5	8900	4900	9/21	13:37:07	Peru-Brazil	4.6	58
6	8900	4900	9/21	16:40:23	Kurile Is.	4.8	75
8	6900	900	9/28	16:38:05	Honshu	5.0	82
9	6900	2900	9/30	19:26:18	Honshu	4.8	82
10	6900	2900	9/30	20:33:51	Kodiak Is.	5.1	32
11	6900	4900	10/2	20:51:24	Peru	4.6	55
13	4900	2900	10/5	03:37:38	Hokkaido	4.7	74
14	4900	2900	10/5	03:46:45	Hokkaido	5.0	74
15	4900	900	10/6	18:34:40	Jan Maven	4.8	57
16	4900	900	10/6	19:25:30	N Hebrides	5.4	94
17	2900	900	10/8	17:01:14	Foxe Is.	4.5	40
18	2900	900	10/9	00:26:02	Easter Is.	4.5	75
19	8900	6900	10/13	02:31:51	Kurile Is.	5.2	71
20	8900	6900	10/13	03:25:45	Tonga Is.	4.7	81

UBO VERTICAL ARRAY ORIGINAL DATA

24 MS SAMPLE RATE

0 - 20.83 CPS

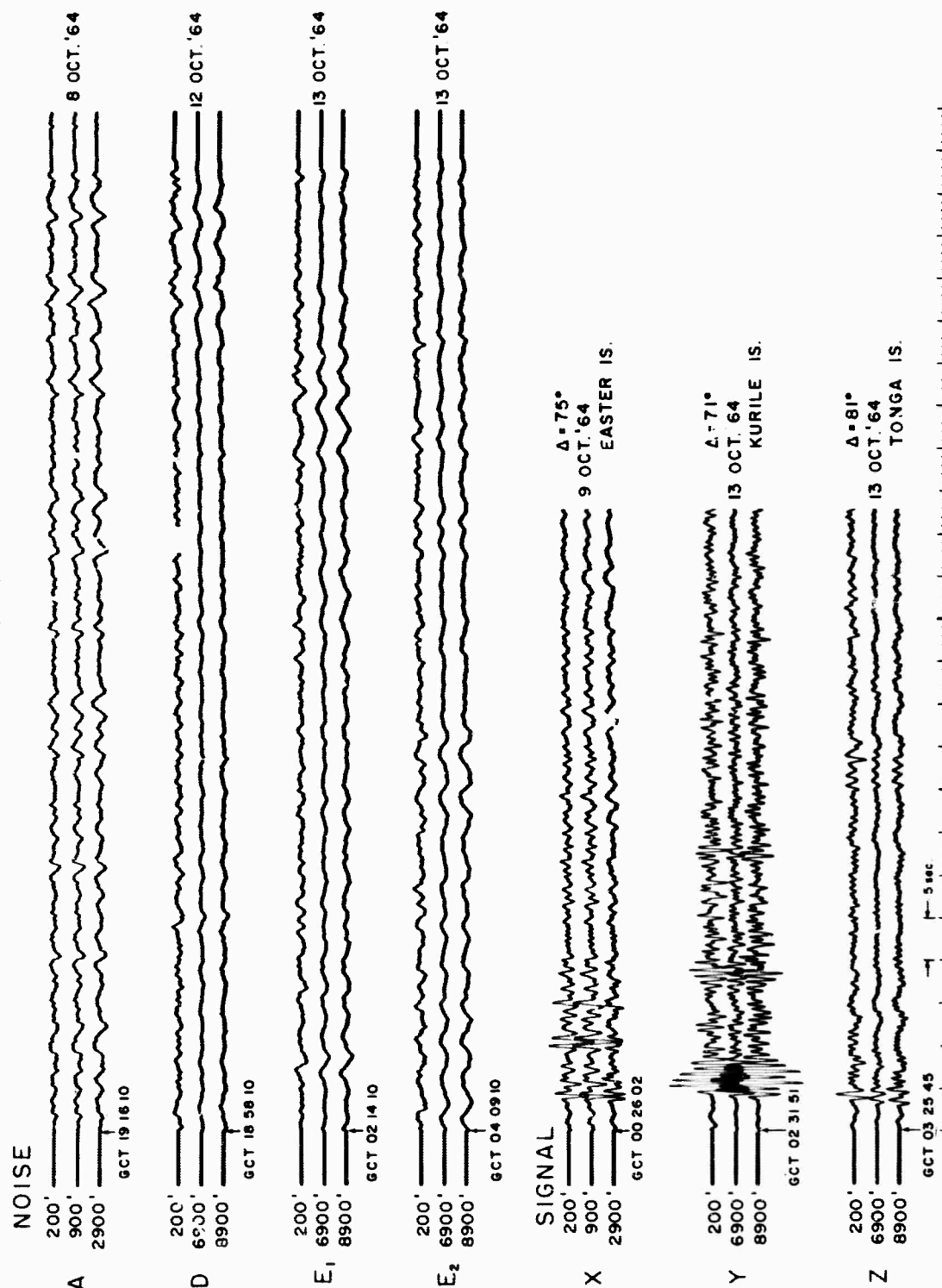


Figure I-1. Ambient Noise Samples and Teleseisms Recorded in the UBO Deep Well

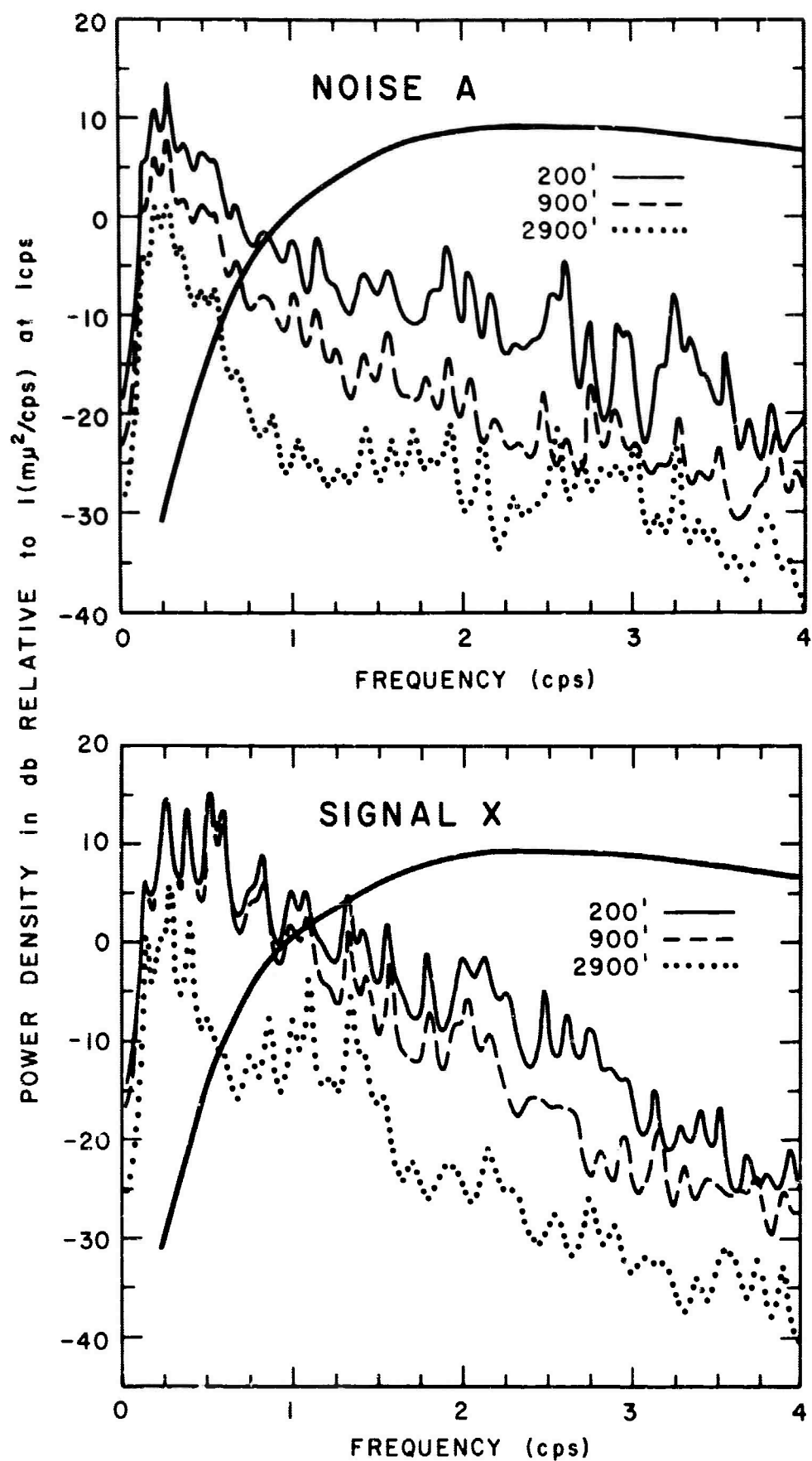


Figure I-2. Signal and Noise Power Spectra Computed from Data Recorded at Depths of 200, 900 and 2900 Ft. The smooth curve corresponds to 1 mμ²/cps

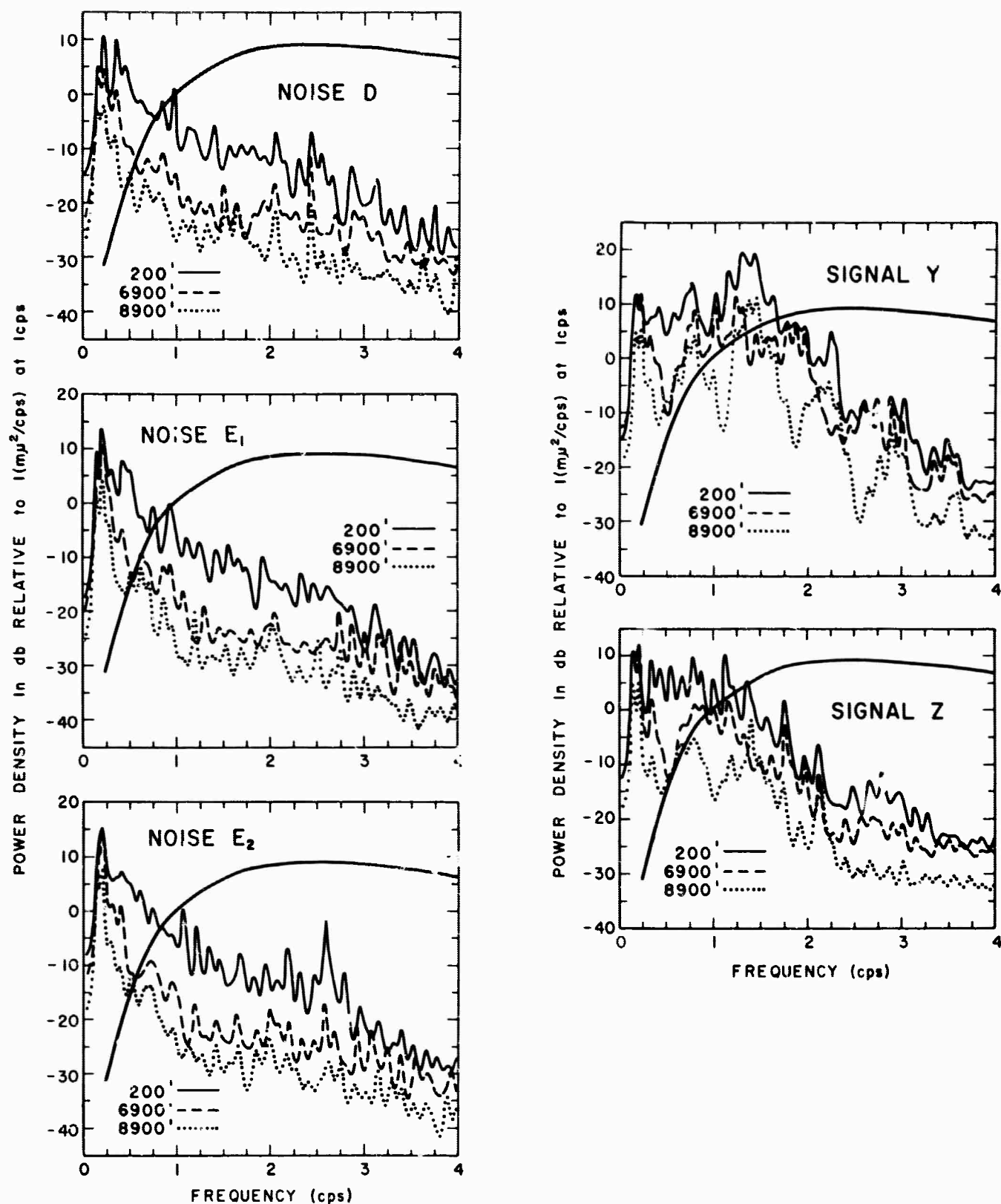


Figure I-3. Signal and Noise Power Spectra Computed from Data Recorded at Depths of 200, 6900 and 8900 Ft. The smooth curve corresponds to 1 mμ²/cps

computed from the whitened data. These results are presented in Figures I-4 and I-5.

The coherence of the noise is observed to be dependent upon receiver separation. When the separation is small (200-ft and 900-ft depths), the noise is highly coherent at all frequencies to 2.0 cps. As the separation increases, the frequency range over which the noise is significantly predictable contracts. In the case of the largest receiver spacing, there is no significant coherence above 0.5 cps except for a few peaks which do not exhibit time-stationarity. The persistent trough at 0.5 cps in the noise coherence functions for 6900 and 8900 ft is in close agreement with the theoretical predictions¹ for vertically traveling P-waves and with the trough observed in the experimental signal coherences. This result suggests that mantle P-waves form a major component of the ambient noise at that frequency. The low coherence at higher frequencies could result from a multiplicity of modes of propagation.

The signals are observed to be highly coherent over the frequency range in which there is appreciable signal power. This range is seen to be different for different signals. Notches in the coherence functions occur at each frequency corresponding to a signal null at either of the two receiver depths. These troughs are found to be in good agreement with the theoretical predictions.

3. Investigations of 3-Element Arrays

Experimental estimates of the performance of 3-element vertical arrays were obtained for the following recording configurations:

- 200, 2900 and 4900 ft
- 200, 6900 and 8900 ft
- 200, 4900 and 8900 ft

In each case, the five noise samples and two teleseisms were used to determine the (signal + noise) statistics as shown in Figures I-6 through I-8. The second teleseism of the set was used to describe the signal statistics for the right side of the filter design equation. After filtering and resampling at 144 msec, optimum multichannel filters to enhance signal at the 200-ft seismometer were designed in the time domain using both the Wiener least-mean-square-error formulation and the prediction-error approach. Filter lengths were 25 points (3.5 sec).

Evaluations of the filters were obtained by applying each multichannel filter to noise sample 1 and teleseism 2 of the corresponding data set. Power spectra were computed for the filter output and trace 1

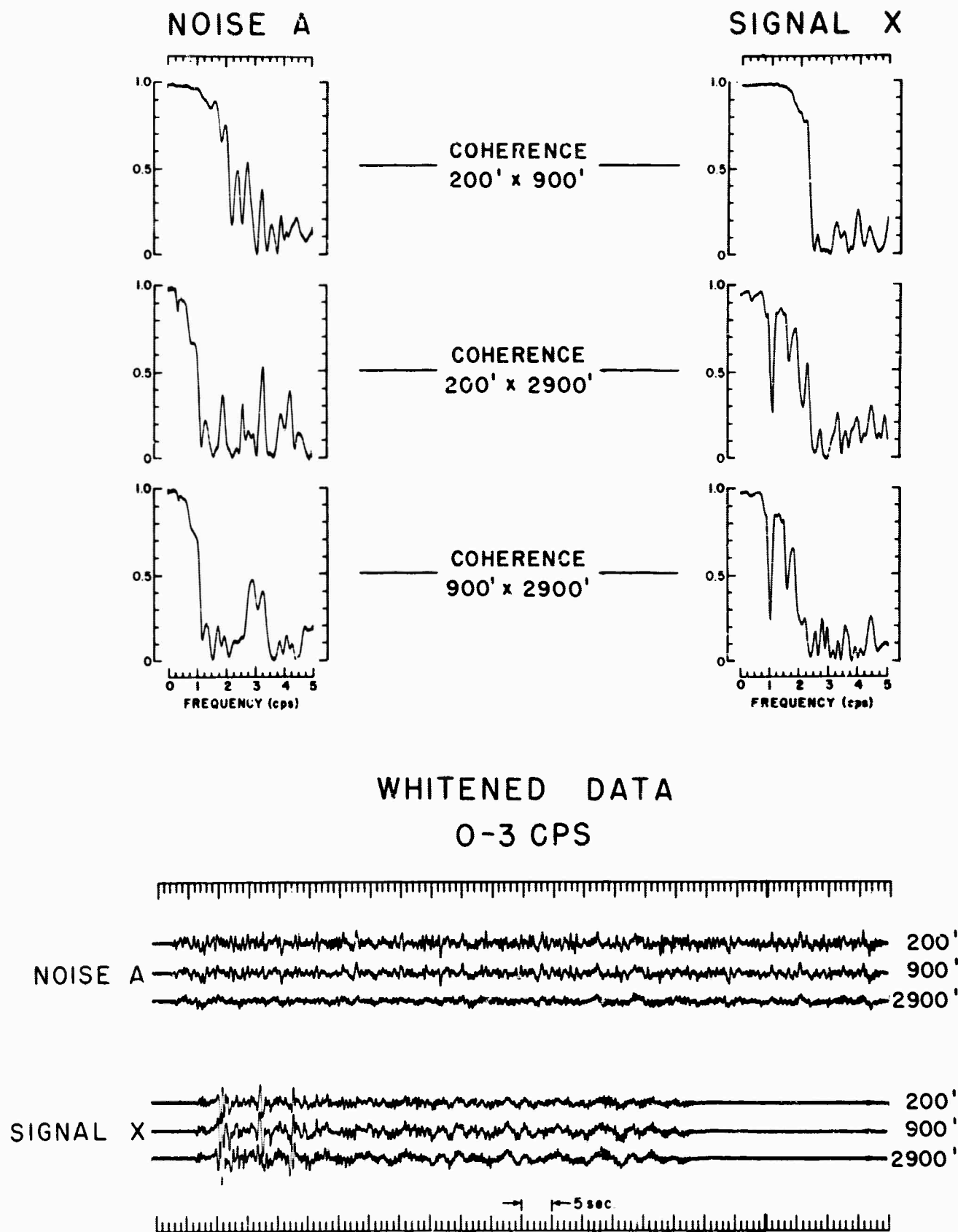
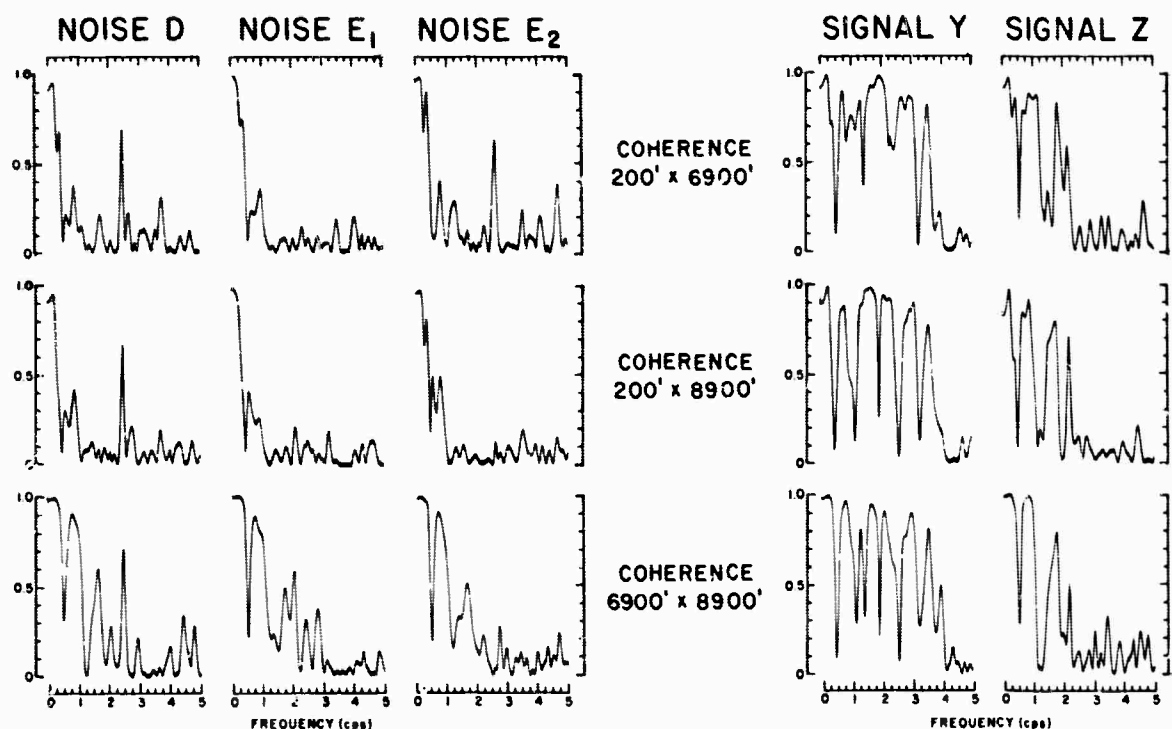


Figure I-4. Coherence Functions Computed from Data Recorded at Depths of 200, 900 and 2900 Ft



WHITENED DATA 0-3 CPS

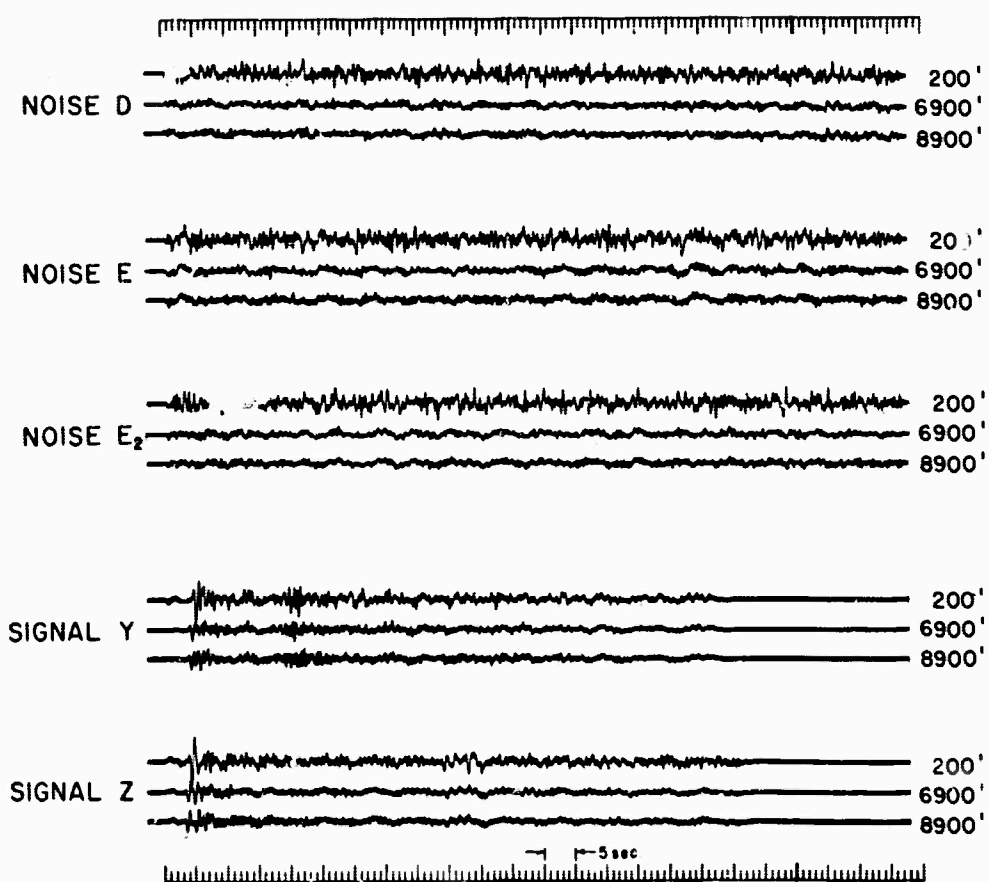


Figure I-5. Coherence Functions Computed From Data Recorded at Depths of 200, 6900 and 8900 Ft

Timing Lines = 0.72 Sec

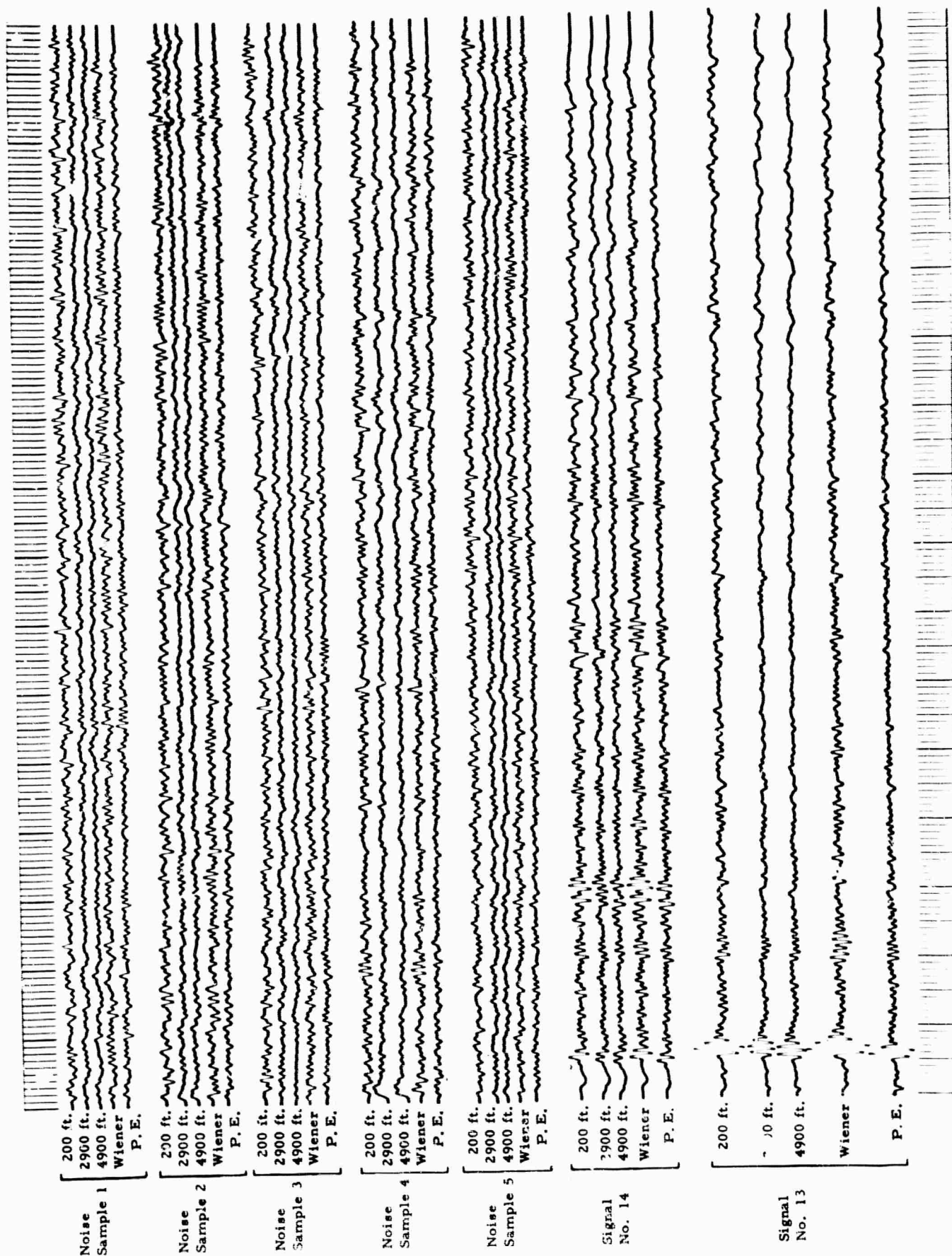


Figure I-6. 3-Channel UBO Data from 200, 2900 and 4900 Ft

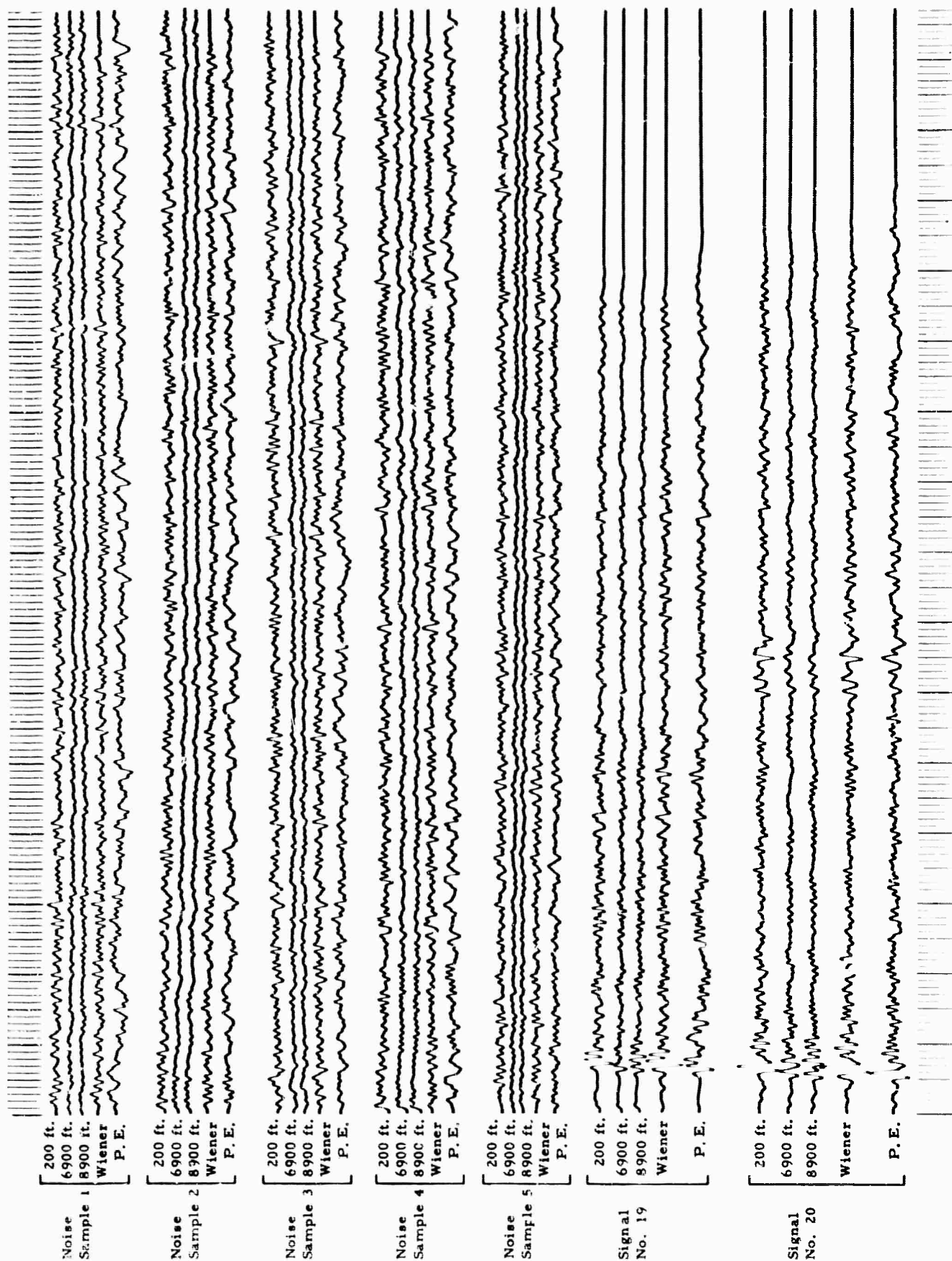


Figure I-7. 3-Channel UBO Data from 200, 6900 and 8900 Ft

Timing Lines = 0.72 Sec

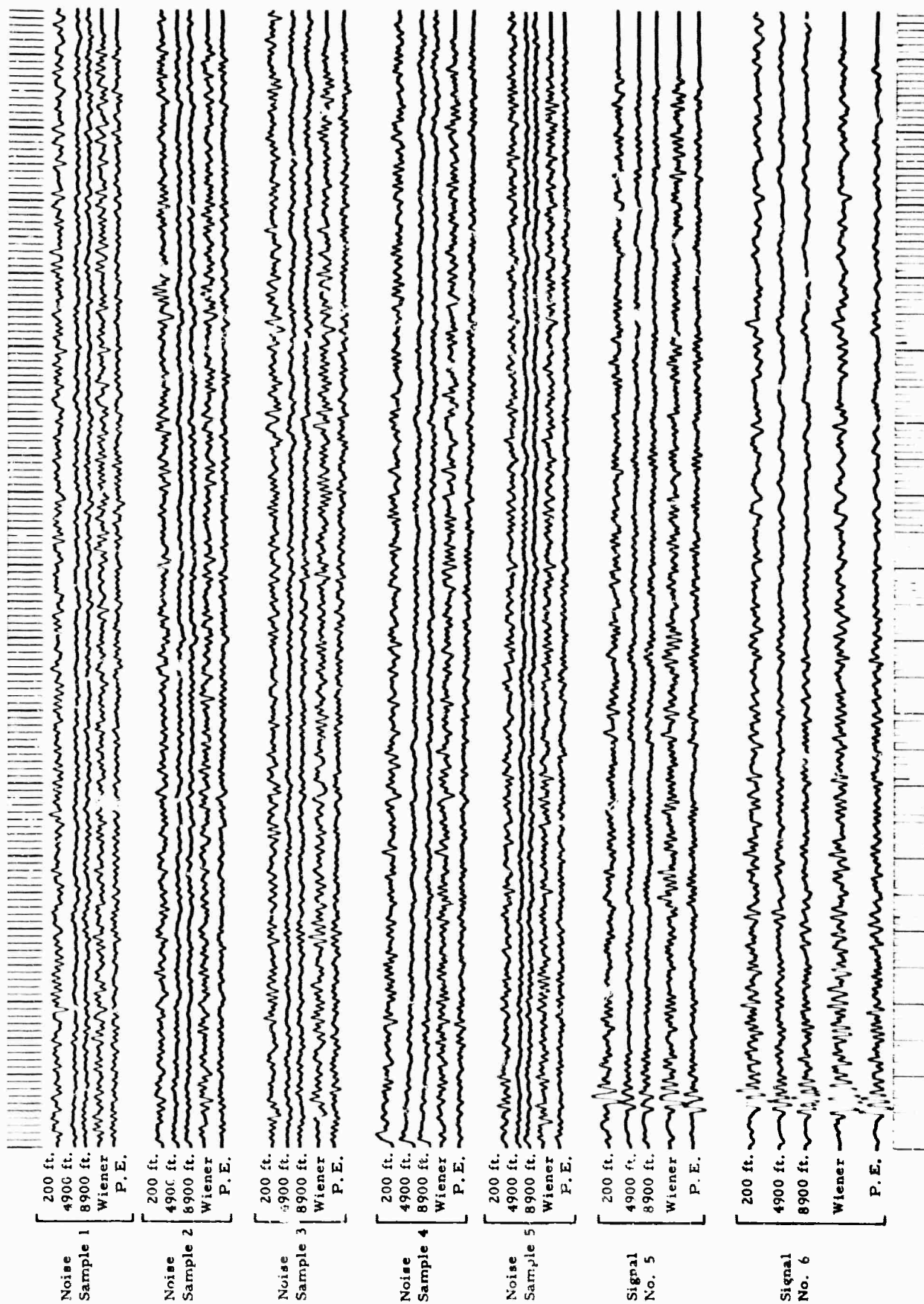


Figure I-8. 3-Channel UPO Data from 200, 4900 and 8900 Ft

(200-ft depth) input. Signal-to-noise ratio improvement estimates computed in this way are shown in Figures I-9 through I-11.

These results are difficult to interpret in detail. They suggest that, in the frequency range below 3.0 cps, a 3-element vertical array should be capable of providing an average improvement in signal-to-noise ratio of approximately 4 to 5 db relative to a single seismometer at 200-ft depth. Since the noise power at 200-ft depth appears to be lower by 1 to 2 db than the noise observed within 10 ft of the surface, this result implies an improvement of about 6 db relative to a single near-surface instrument. However, this estimate is probably low because of the method used in designing and evaluating the filters. For the filter design, signal statistics were computed from entire signal records rather than from only the portions where signal-to-noise ratio was high. Therefore, the signal statistics were contaminated by noise, and the optimum filters were required to pass not only signal but also ambient noise, to a lesser degree. In the evaluation stage, entire signal records again were used to compute input and output power spectra of signal. Thus, response functions computed for signal were actually some kind of average of the signal and noise responses. Both of these effects tend to reduce the estimate of optimum improvement. It is possible that more meaningful results could be obtained by employing a theoretical signal model, although this approach has its pitfalls in that artificial signal-to-noise improvements can occur because of seismometer gain inequality.^{2, 3}

The Wiener filters are designed for wideband signal preservation, whereas the prediction error filters are used to enhance the first cycle or two of the signal. Signal-to-noise ratio improvements for the two types of filters are similar; however, the prediction error filters are designed without regard to distortion of the signal.

A deghosting routine⁴ was applied to the 6900-ft and 8900-ft records to separate the upward- and downward-traveling parts of the teleseismic signals. Figure I-12 illustrates results of applying this method to the five noise samples and two teleseisms recorded at those depths. When the correct time-shifts are applied, a remarkable similarity is found among the estimated upward- and downward-traveling signals and the signals observed at 200 ft (Figure I-7). Similarities in the noise records could be evidence of P-wave noise.

The results show that a pair of deeply-buried instruments can be used effectively to estimate the signal which should be observed at the surface. In this case, the signal-to-noise improvement relative to the shallow instrument is limited, but the improvement would probably be much better in high-noise areas, such as Grapevine, where the attenuation of noise with depth is more severe.

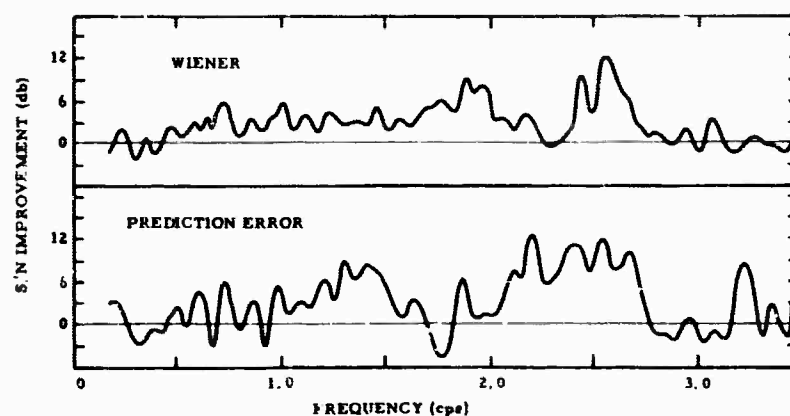


Figure I-9. Estimated Performance of the Optimum 25-Point Filters for an Array Occupying Depths of 200, 2900 and 4900 Ft

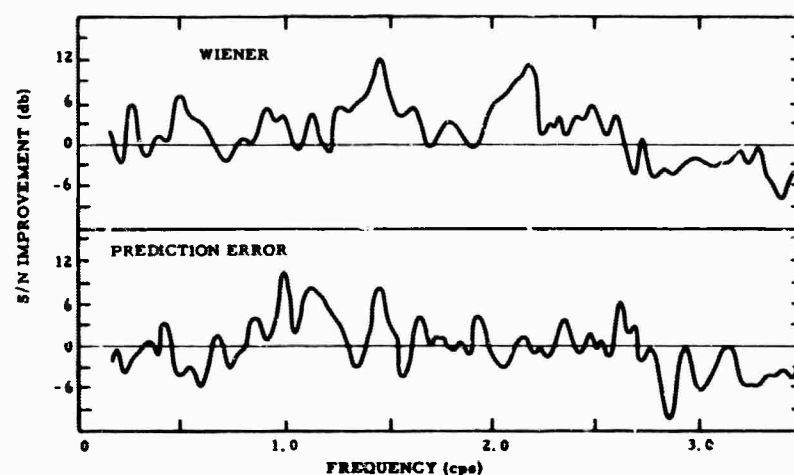


Figure I-10. Estimated Performance of the Optimum 25-Point Filters for an Array Occupying Depths of 200, 6900 and 8900 Ft

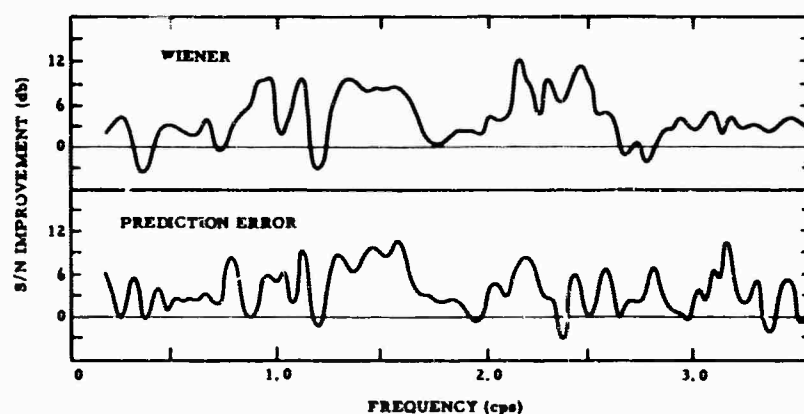


Figure I-11. Estimated Performance of the Optimum 25-Point Filters for an Array Occupying Depths of 200, 4900 and 8900 Ft

Timing Lines = 0.72 Sec

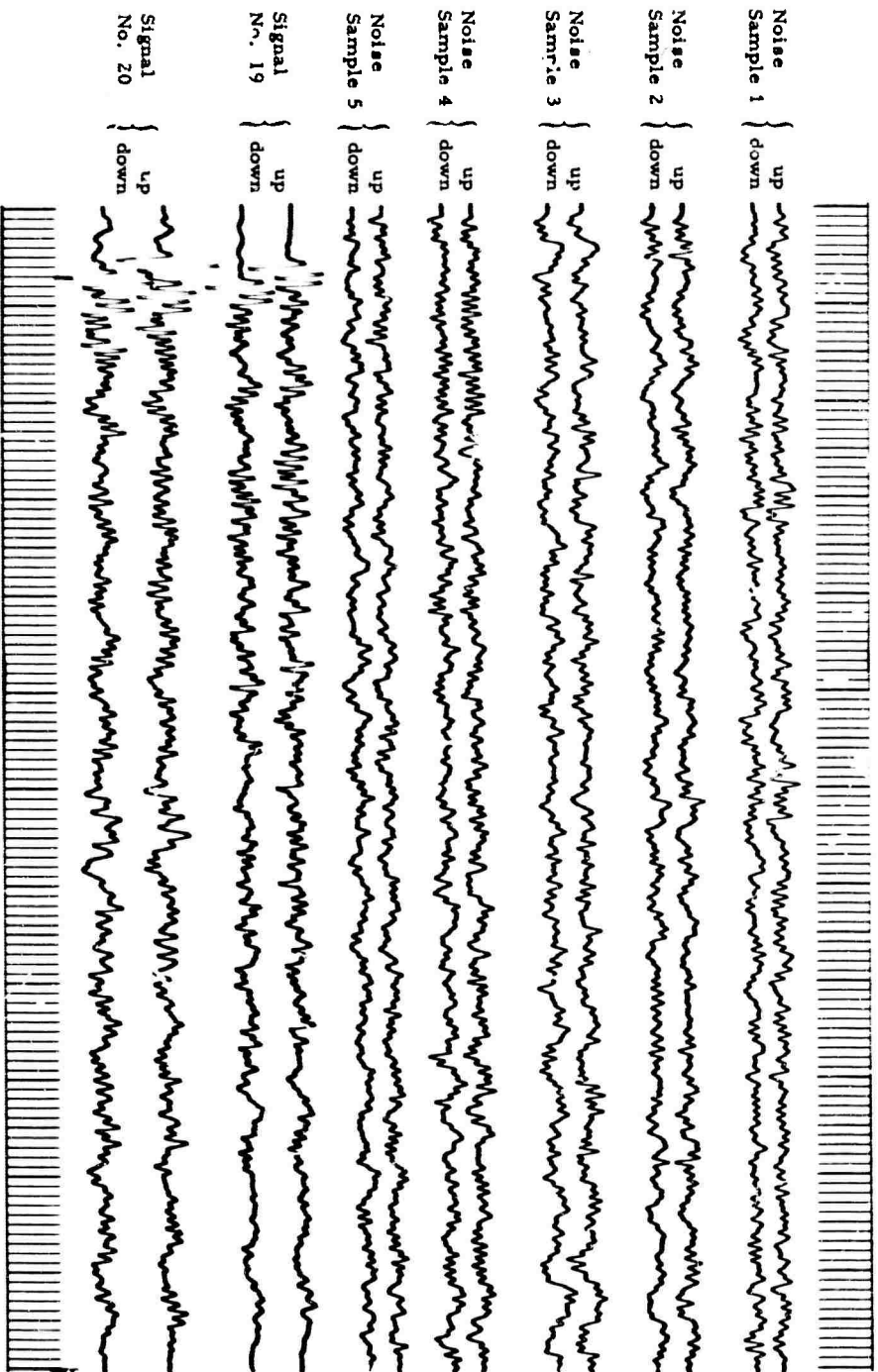


Figure I-12. Estimates of Upward- and Downward-Travelling Waves
Computed from 6900 and 8900 Ft Recordings

4. Investigations of a 6-Element Array

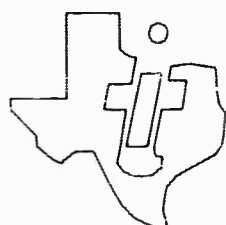
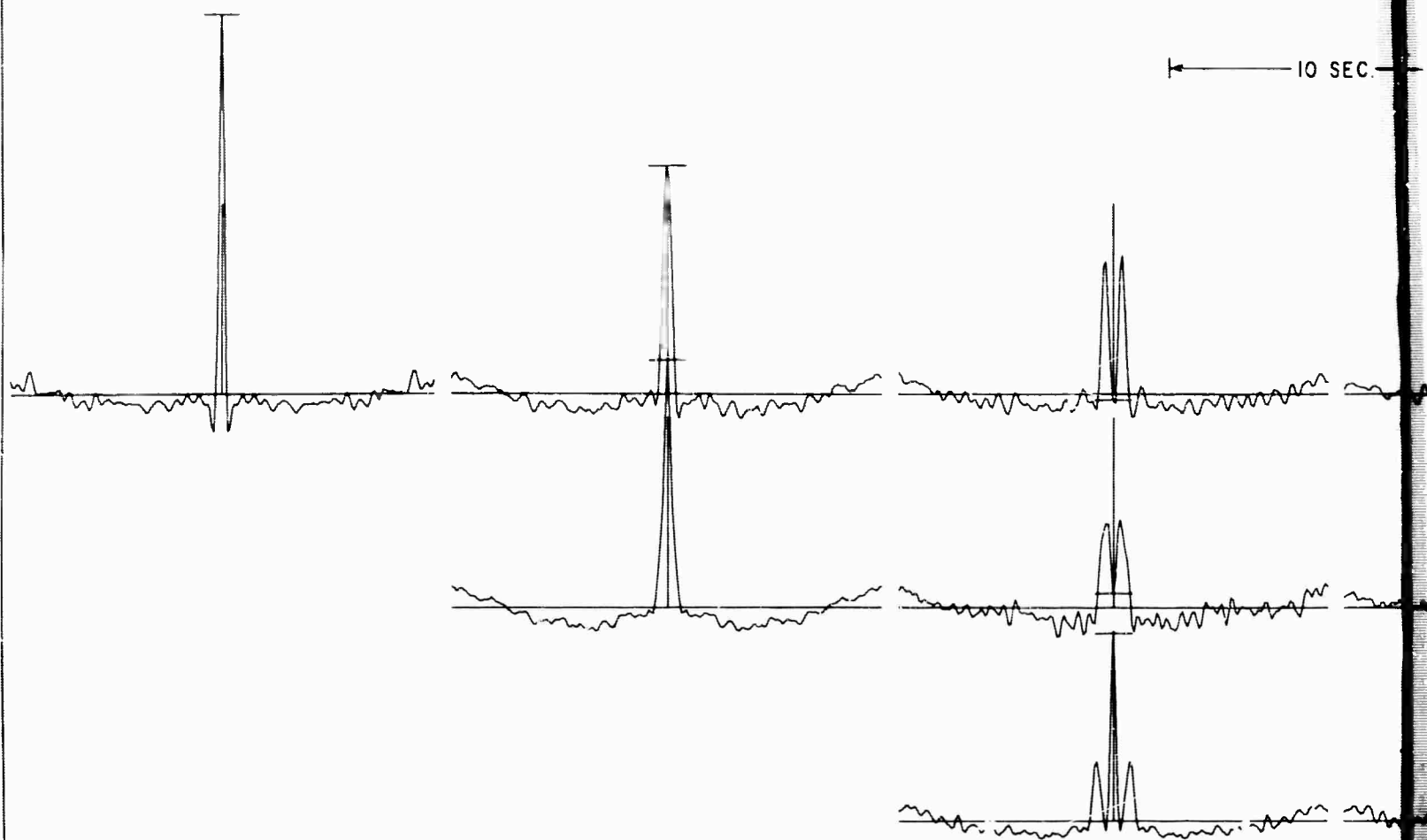
An attempt has been made to evaluate a 6-element vertical array by means of the data recorded at UBO. The recordings listed in Tables I-1 and I-2 were sufficient to provide estimates of all the required auto- and crosscorrelations of signal and noise.

Because of poor quality, it was necessary to discard three noise samples (recorded on 13 October). One teleseism record (SN 18) had to be discarded because of a computing error which would have been expensive to rectify. For each record, a 55-point deconvolution filter was designed to whiten and normalize the spectrum of the 200-ft trace. This filter then was applied to the three traces. The purpose of this step was to "equalize" noise or signal samples obtained at different times. Phase responses of the deconvolution filters were not determined since they have no effect on the subsequent results. After deconvolution, the set of three autocorrelations and three crosscorrelations was computed for each record.

Six-channel correlation matrices were constructed by equating each of the constituent correlation functions to the average of all the available estimates. The number of estimates varied from 50 (1 x 1 noise correlation) to 1 (2 x 3, 2 x 5, 2 x 6, 3 x 6, and 4 x 5 signal correlations) where the channels are numbered in an order of increasing seismometer depth. The resulting 6-channel correlation sets are illustrated in Figures I-13 and I-14. The curve in the m^{th} and n^{th} column is the correlation function $\varphi_{mn}(\tau)$. Horizontal bars indicate the zero-lag values $\varphi(0)$. Only half of the matrix is plotted since the remaining crosscorrelations are simply the time-reverse of those shown.

For comparison, theoretical correlation sets are shown in Figures I-15 through I-18. These correlation functions were obtained from the UBO P-wave and surface-wave models¹ by inverse transformation of the auto- and crosspower spectra after a scaling operation which whitened the spectrum of the near-surface instrument. Agreement is excellent between the experimental and theoretical signal correlations even though the experimental curves are contaminated by noise. Visual interpretation of the noise correlations is difficult since the noise undoubtedly consists of several modes with different spectra. However, there is a strong suggestion that mantle P-wave noise is an important constituent of the noise field. This is especially evident in the case of the 1 x 5 and 1 x 6 experimental noise correlations where spacing of the peaks agrees with the experimental signal and theoretical P-wave correlations but not with any of the theoretical surface-wave correlations. It is planned to use a multivariate regression operation to attempt to separate the observed noise model into its constituent modes.

10 SEC.



UBD VERTICAL ARRAY AVERAGE CORRELATIONS - EXPERIMENTAL SIGNAL

SCALE FACTOR = $10^{.602}$

A

10 SEC.

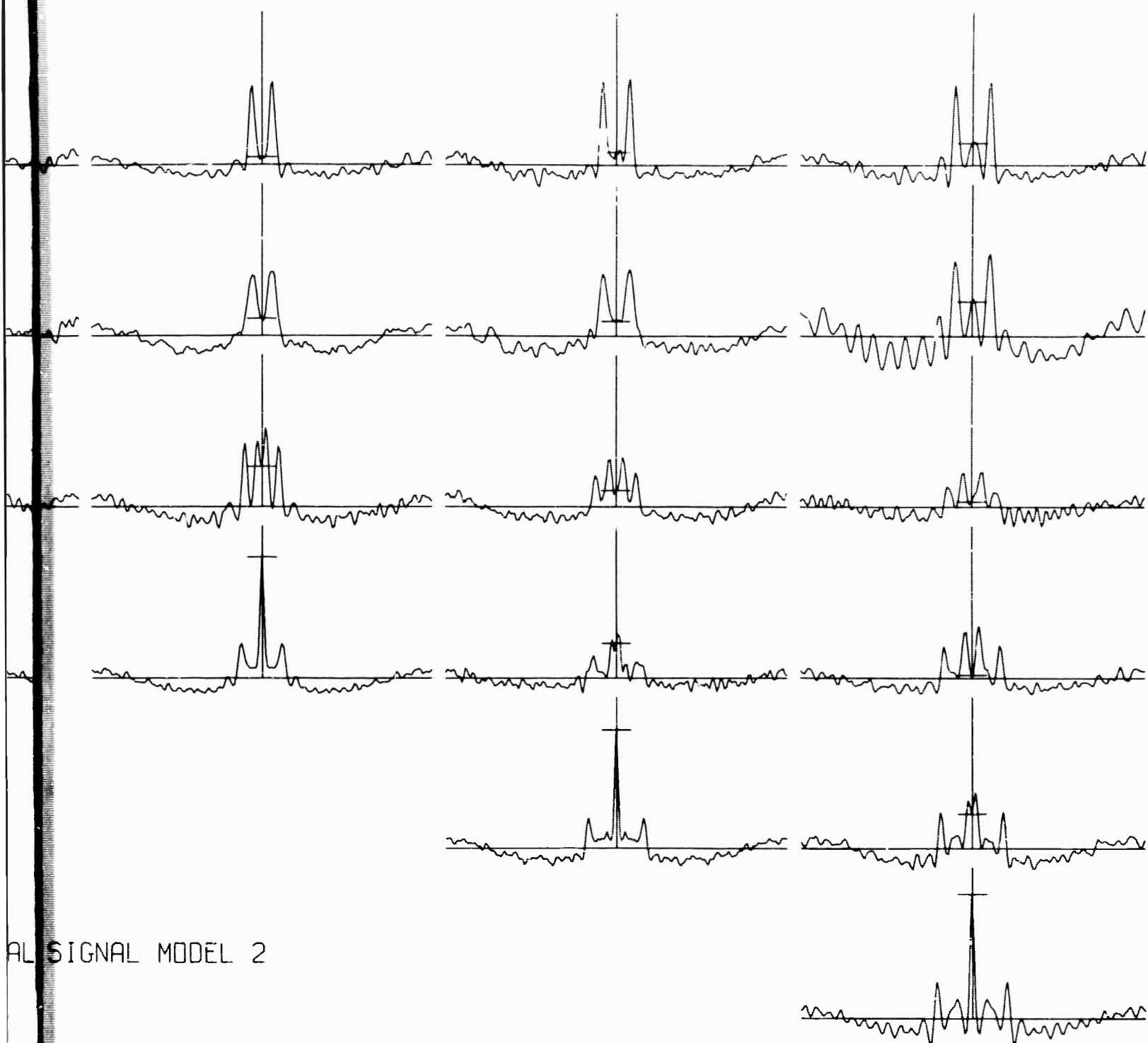
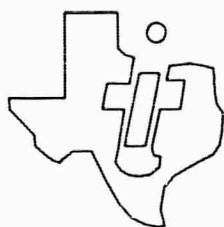
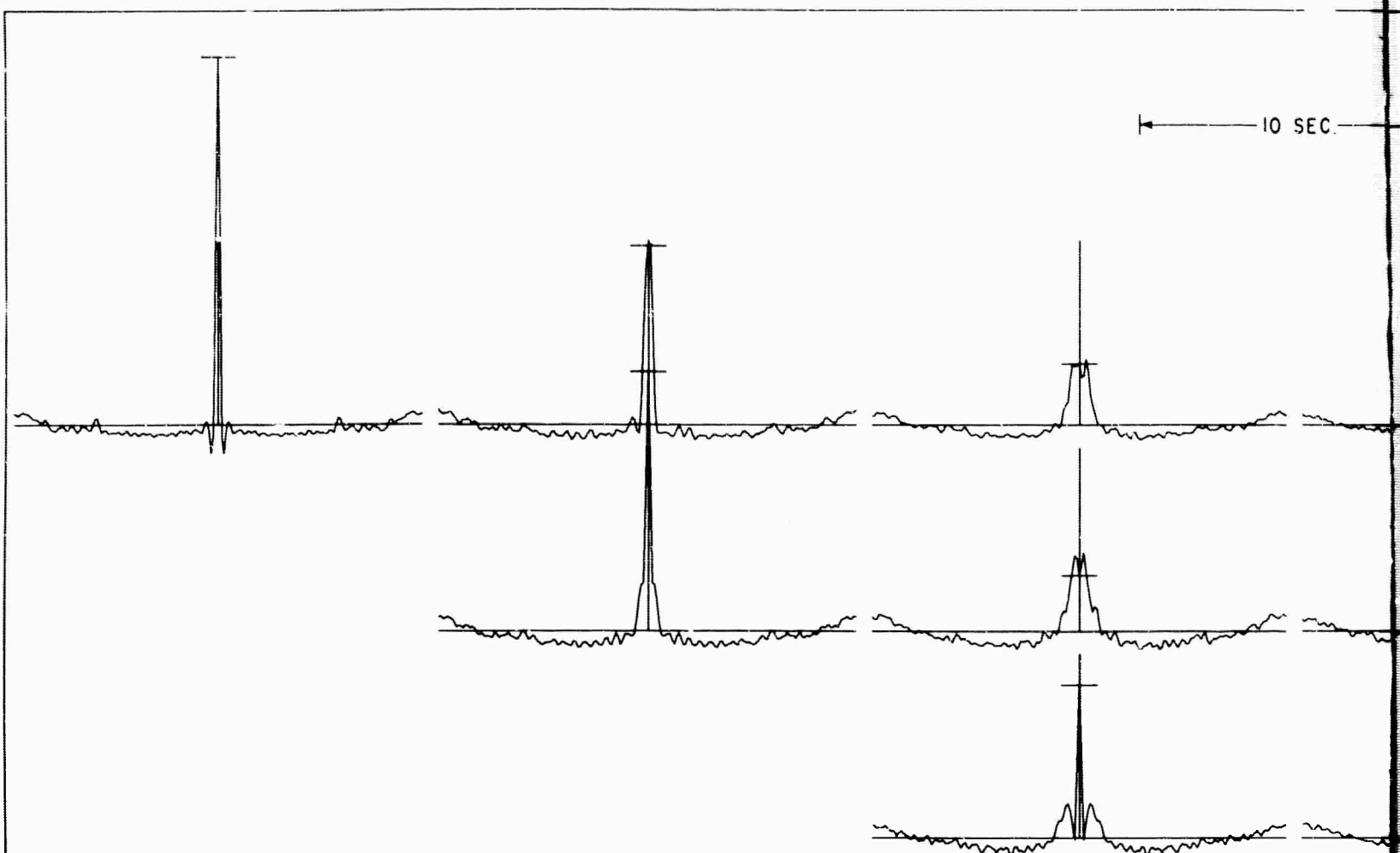


Figure I-13. Matrix of Experimental Signal Correlations
for 6-Element UBO Vertical Array

B



UBD VERTICAL ARRAY AVERAGE CORRELATIONS - EXPERIMENTAL NOISE

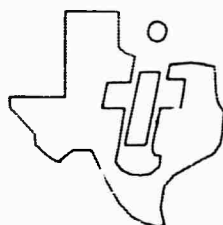
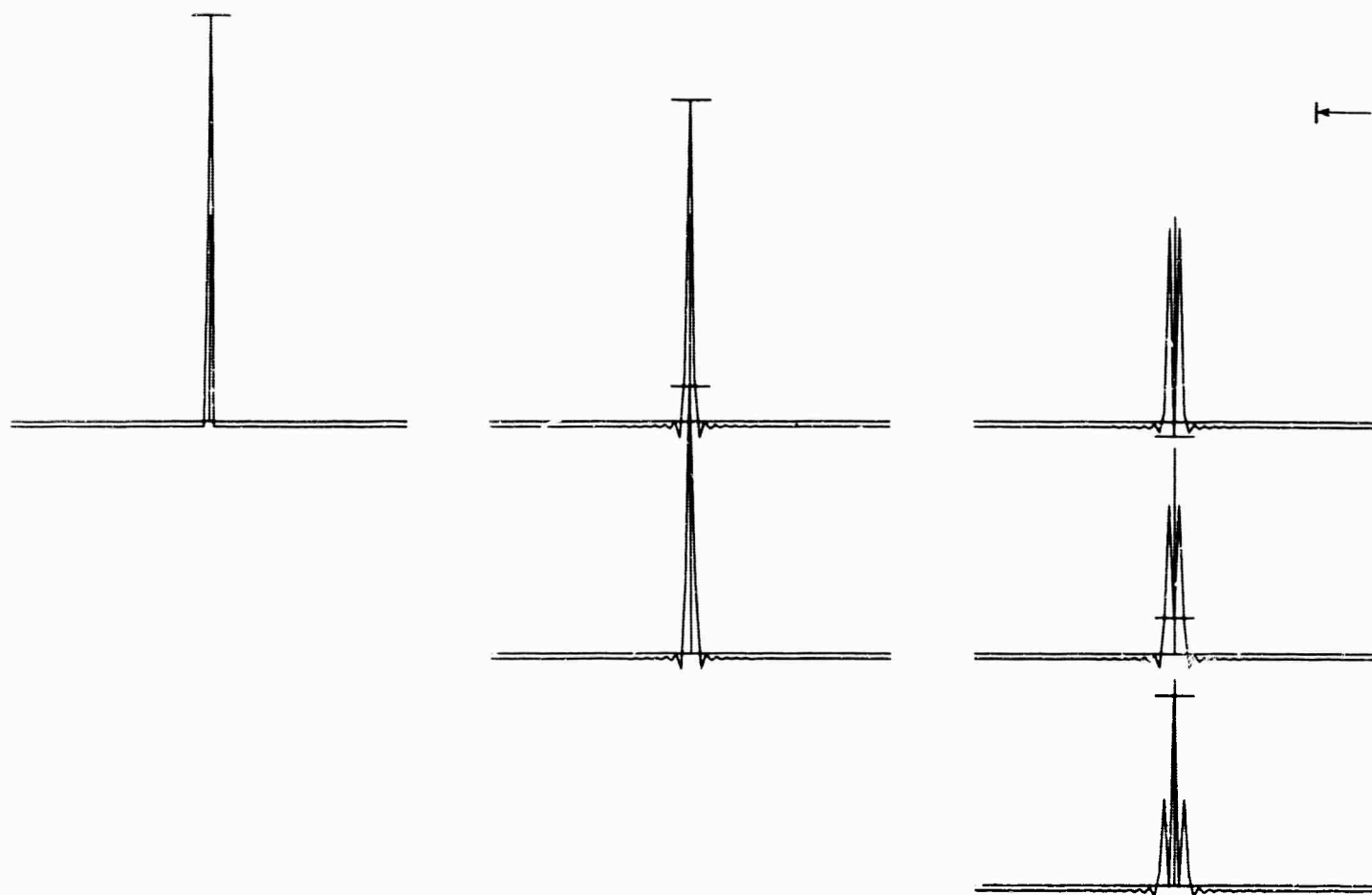
SCALE FACTOR = 10^{-602}

A



Figure I-14. Matrix of Experimental Noise Correlations
for 6-Element UBO Vertical Array

B

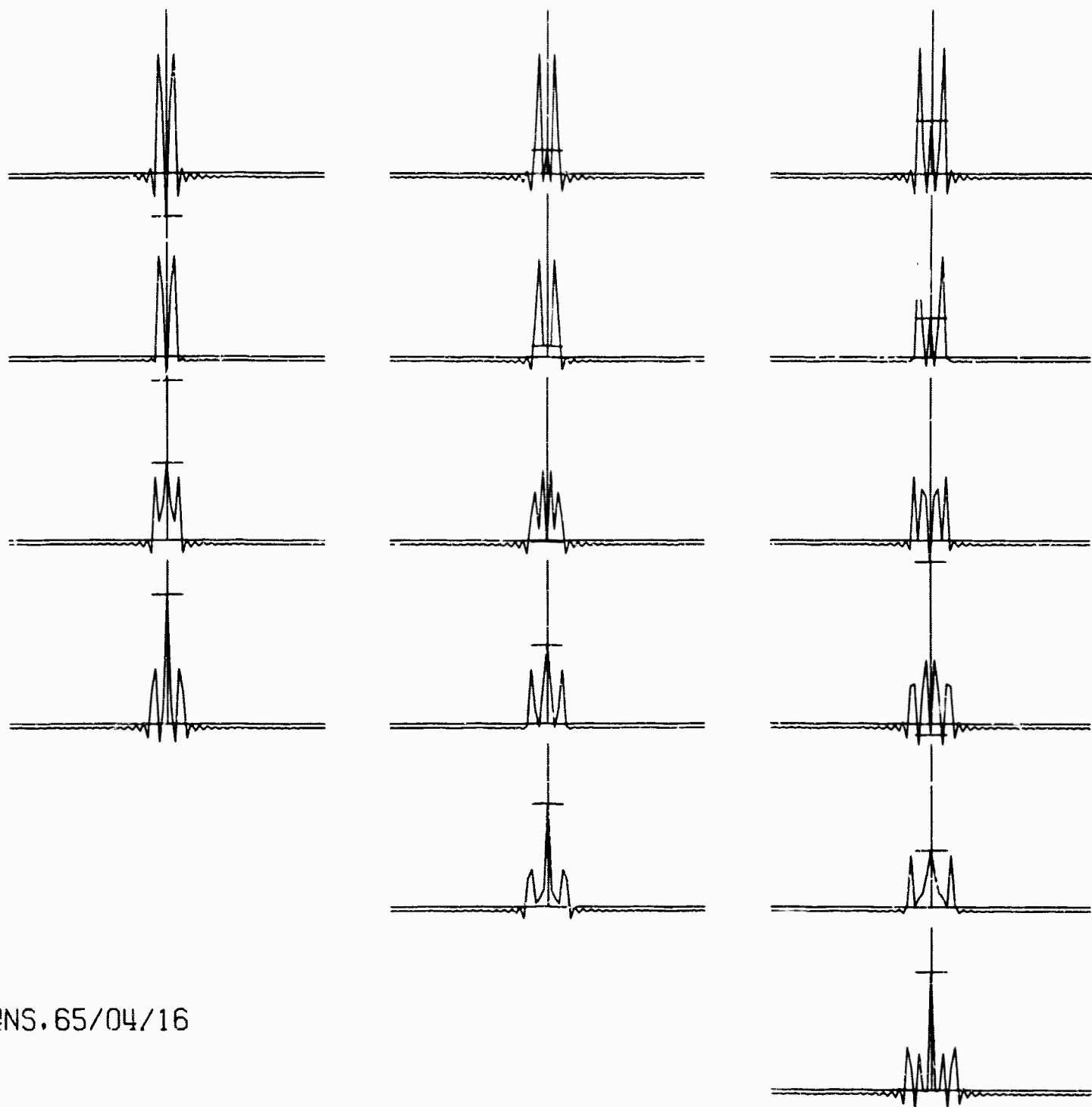


UBO VERTICAL ARRAY THEORETICAL 10-SECOND SIGNAL CORRELATIONS.

SCALE FACTOR = 10^{301}

A

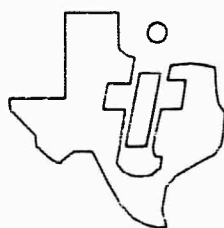
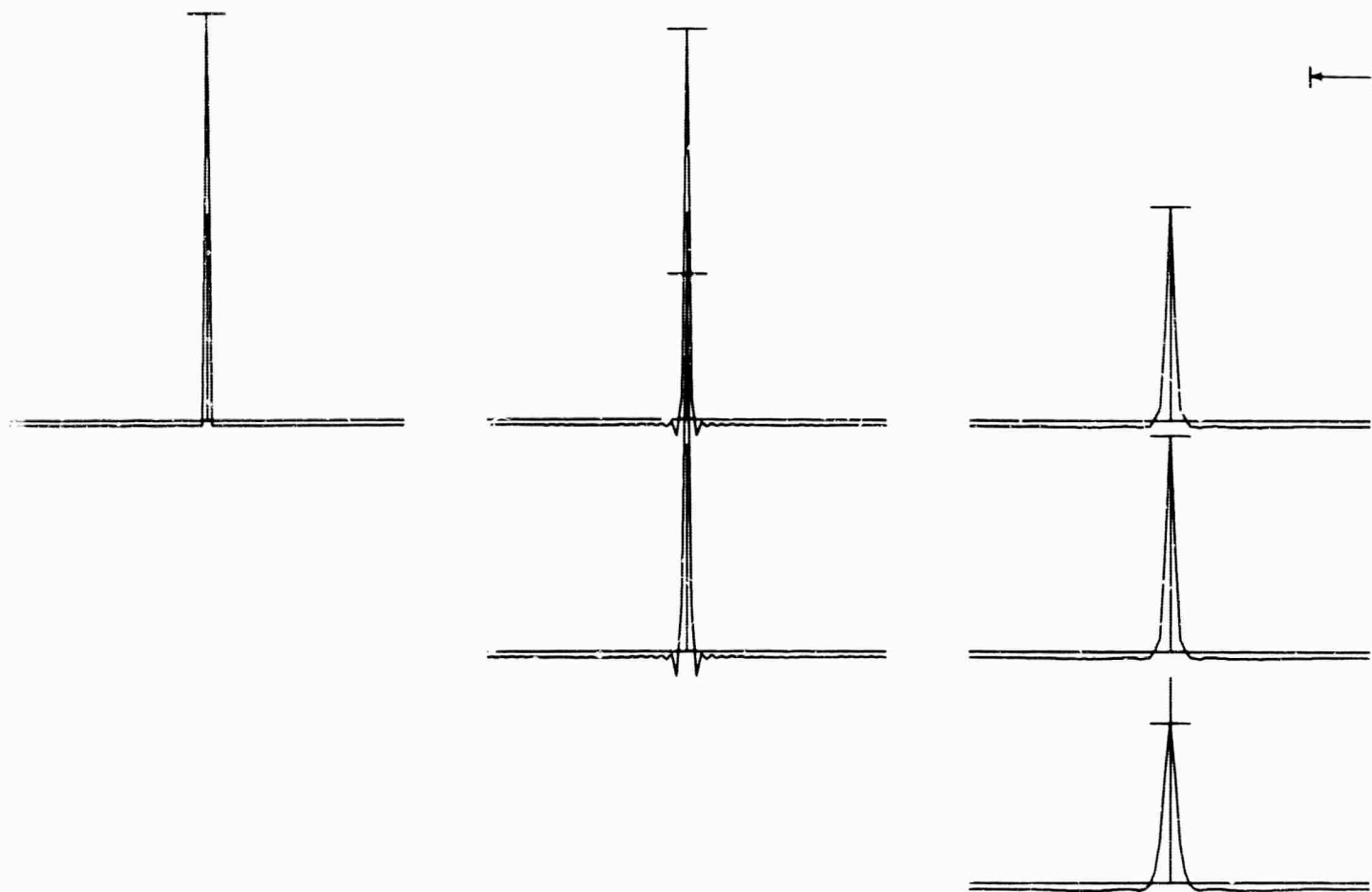
10 SEC.



NS. RELATIONS. 65/04/16

Figure I-15. Matrix of Theoretical Signal Correlations for
6-Element UBO Vertical Array

B



UBJ VERTICAL ARRAY. THEORETICAL CORRELATIONS FOR RAYLEIGH MODE

SCALE FACTOR = $10^{.301}$

A

SEC. 10 SEC.

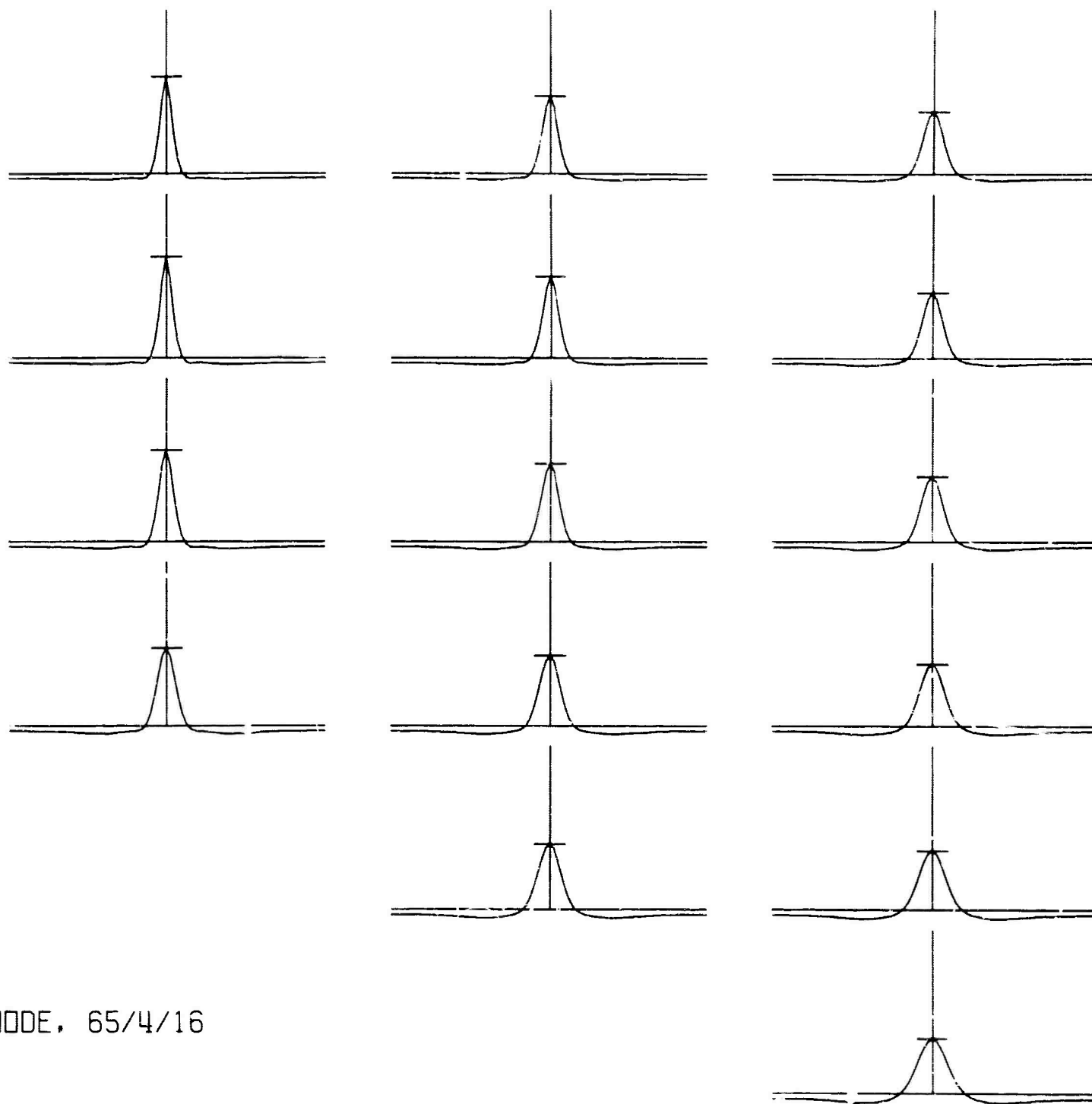
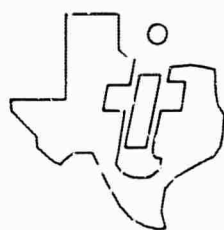
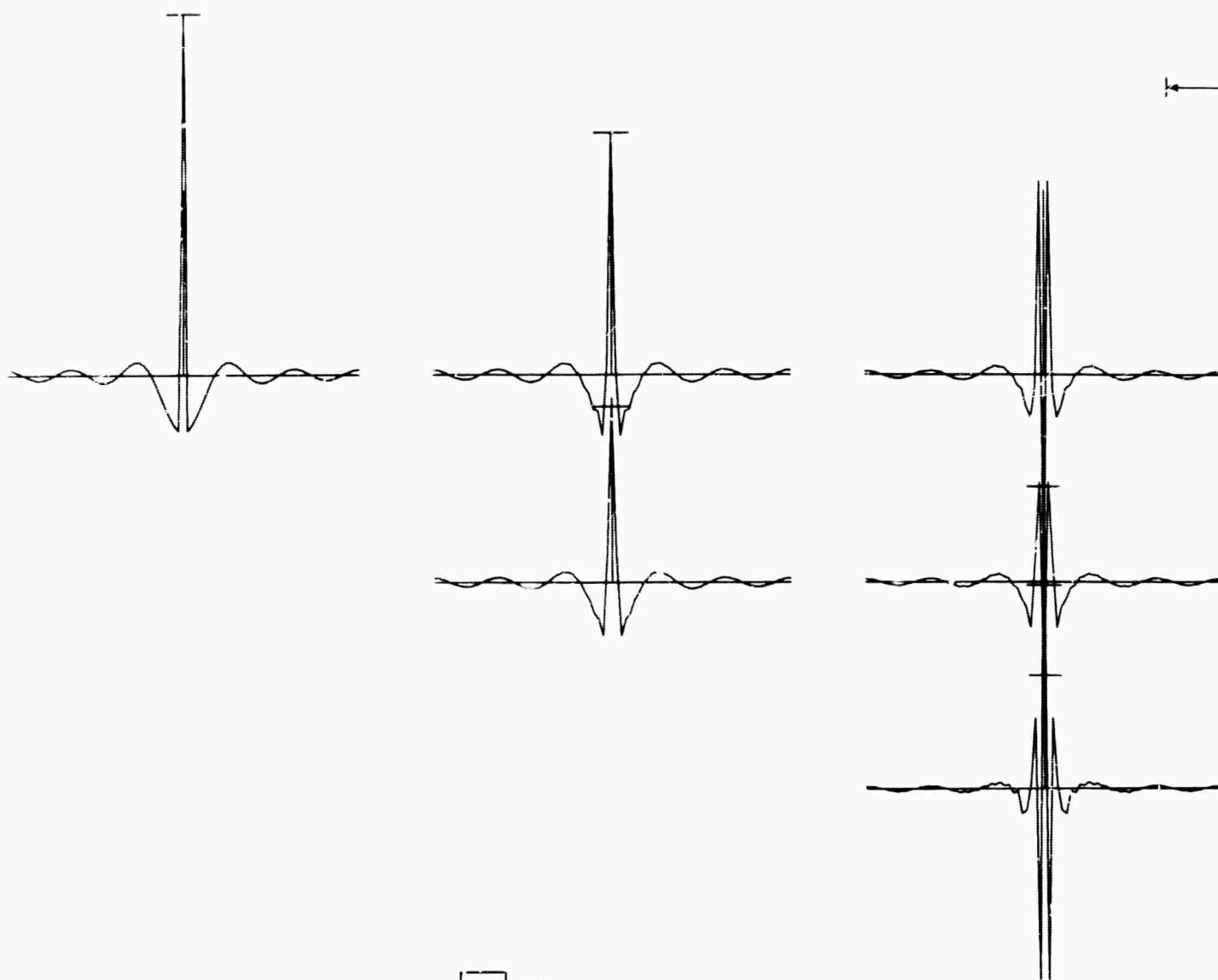


Figure I-16. Matrix of Theoretical Rayleigh-Mode Correlations for 6-Element UBO Vertical Array

B

10 SEC

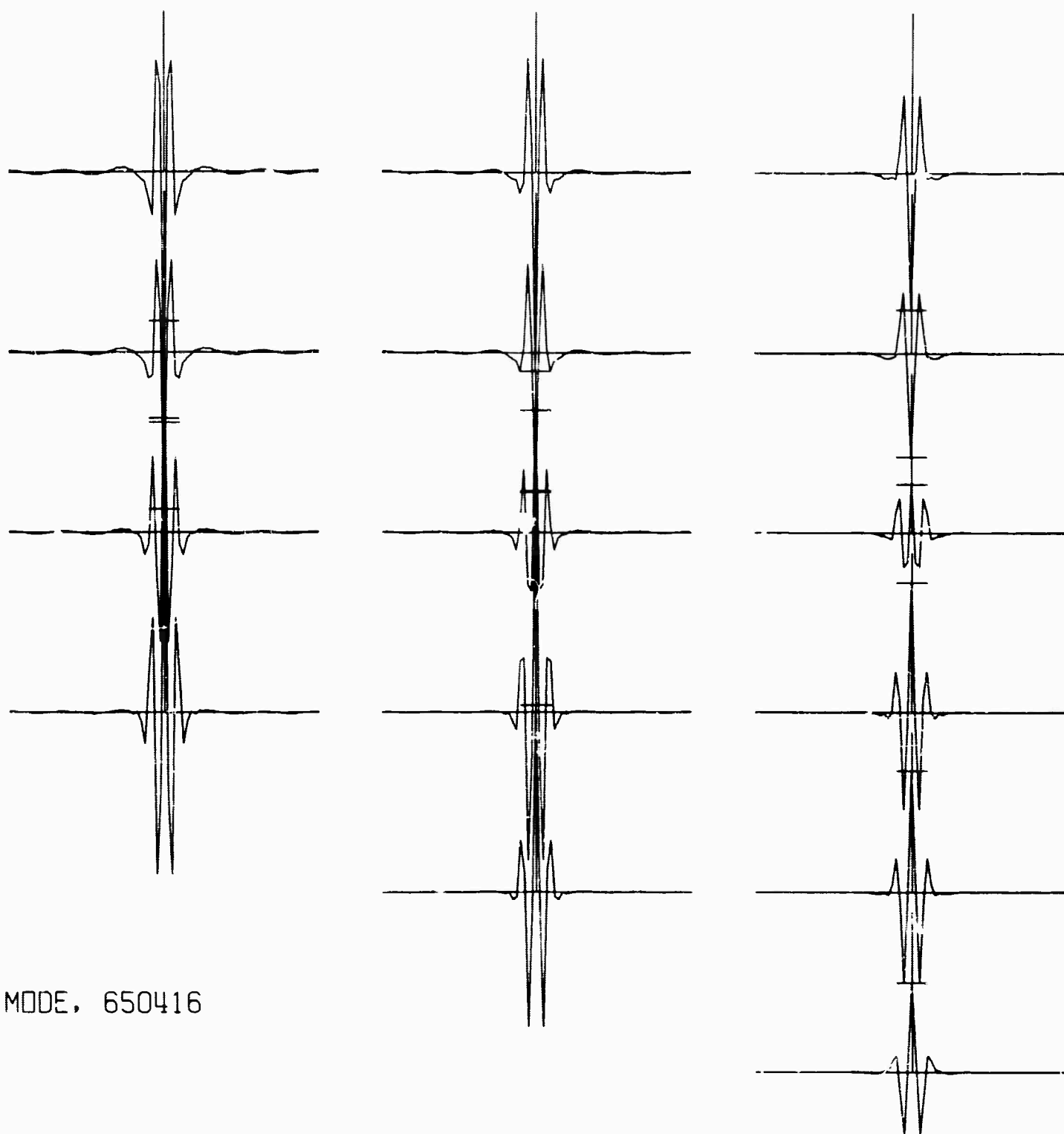


U60 VERTICAL ARRAY, THEORETICAL CORRELATIONS FOR 1ST SHEAR MODE

SCALE FACTOR = 10^{357}

A

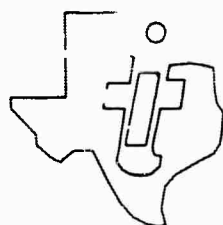
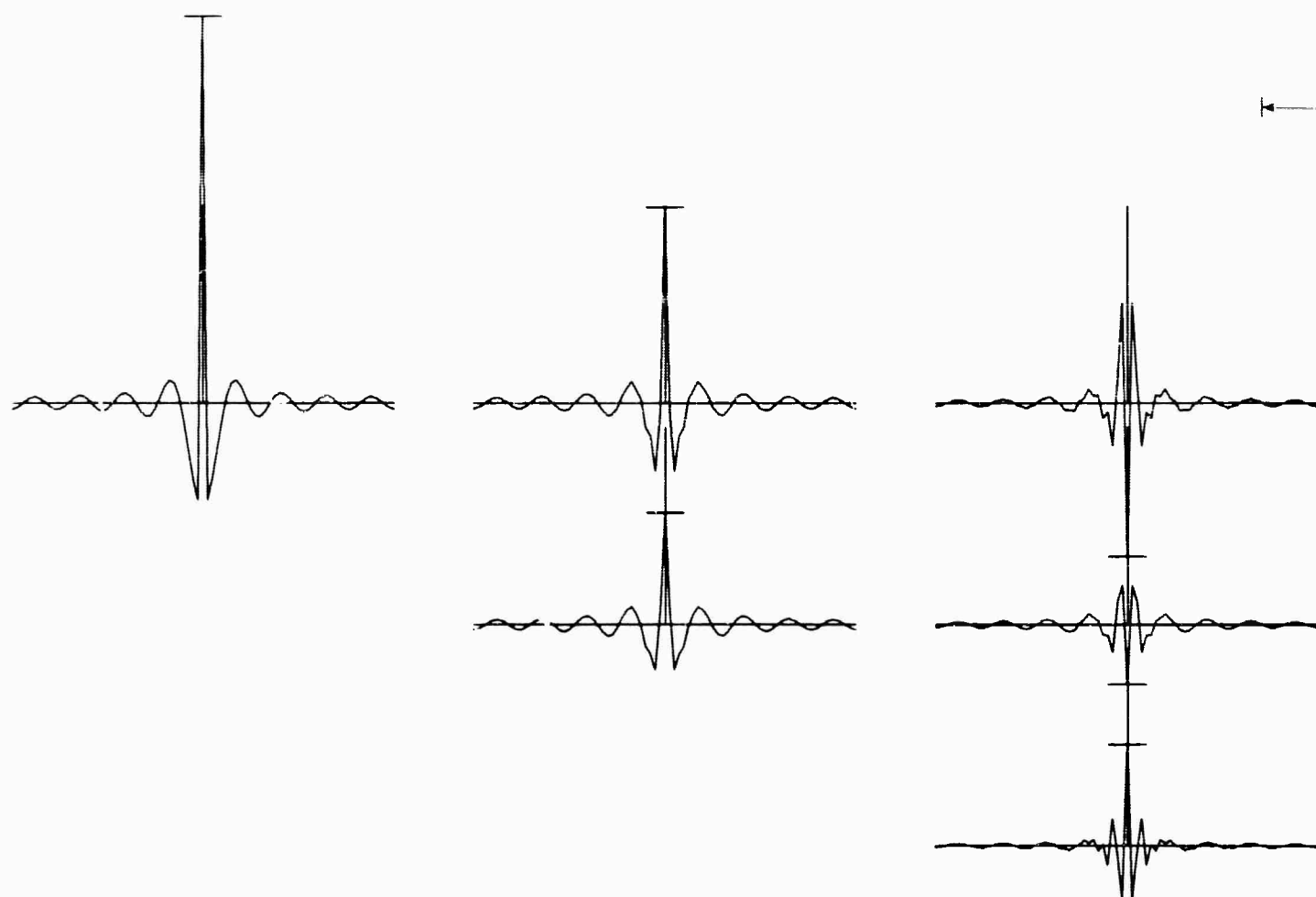
10 SFC →



D HEAR MODE, 650416

Figure I-17. Matrix of Theoretical First-Shear-Mode Correlations for 6-Element UBO Vertical Array

B

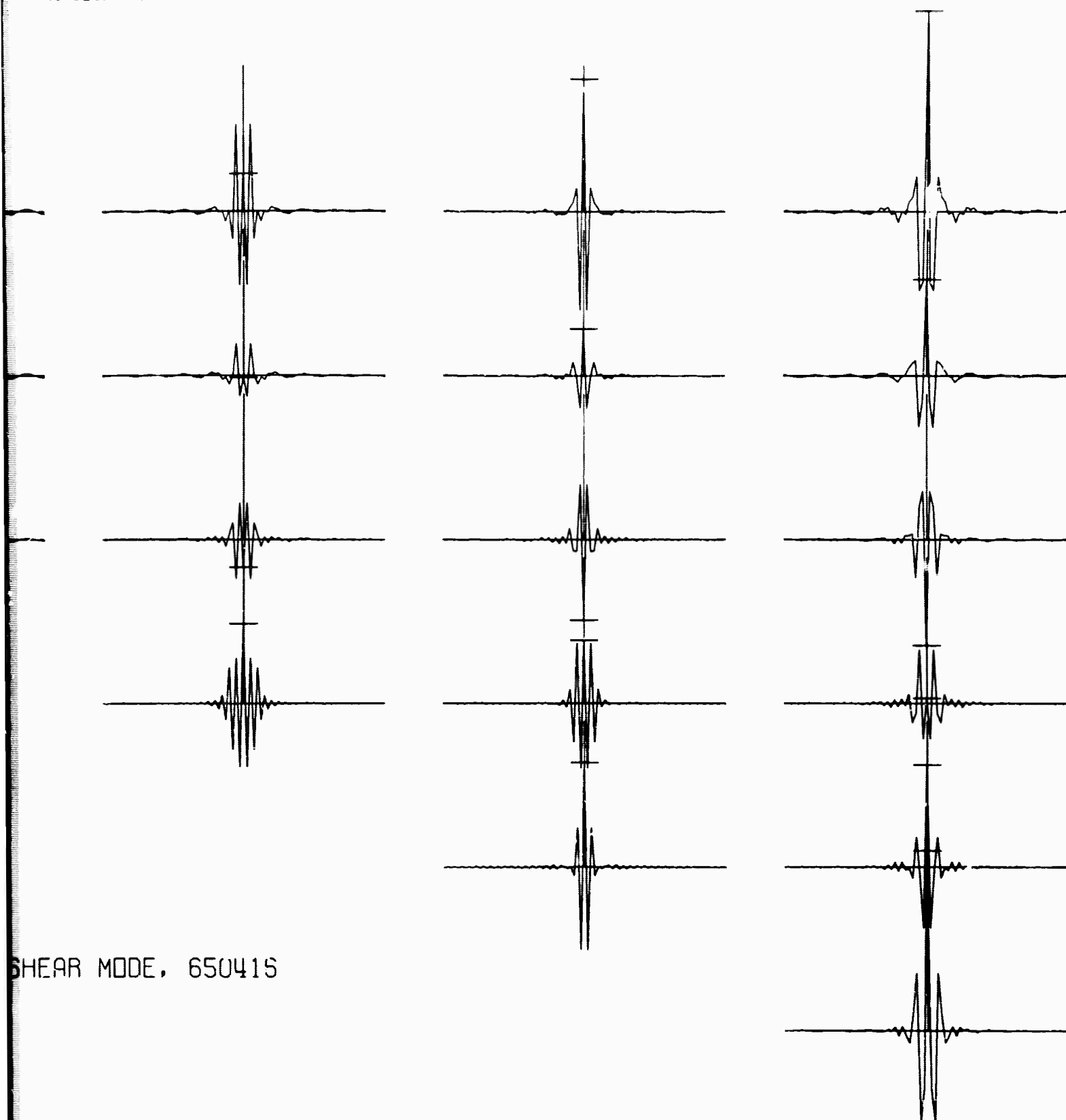


UBD VERTICAL ARRAY, THEORETICAL CORRELATIONS FOR 2ND SHEAR M

SCALE FACTOR = 10^{-397}

A

10 SEC.



SHEAR MODE, 650415

Figure I-18. Matrix of Theoretical Second-Shear Mode Correlations for 6-Element UBO Vertical Array

B

I-29/I-30

BLANK PAGE

The average signal and noise power at each depth is given by the corresponding zero-lag value of the autocorrelation. These values are plotted in Figure I-19. Relative to 200-ft depth, the average signal-to-noise ratio improvement which may be gained by deep burial is found to be only about 1 db.

There was an attempt to design a 6-channel signal enhancement filter in the time domain using the Wiener-Levinson formulation, but it was unsuccessful since the input correlations failed to meet the necessary conditions imposed by that method. This result was not entirely unexpected since there is only a small likelihood that data combined in the manner described above will produce a valid correlation matrix.

Because the requirements are less stringent in the frequency domain, it was decided to investigate the frequency-domain stability of the experimental model. The correlation functions were Fourier-transformed to produce auto- and crosspower spectra. Figures I-20 and I-21 illustrate the autopower spectra obtained for signal and noise when a hanning lag window was applied. Frequency-domain filters were designed for 3 models: transform of correlations with no smoothing, transform with first-order hanning, and transform with fourth-order hanning. Even in the frequency domain, the data were not of sufficiently high quality to prevent instabilities. Figure I-22 shows the results obtained, ignoring frequencies where the predicted output power or signal-to-noise improvement was negative.

Since the predicted improvements (where they could be obtained) were less than those estimated for 3-element arrays (Figures I-9, I-10, I-11), it is concluded that none of the results presented in Figure I-22 can safely be considered meaningful. The attempt to combine data of differing quality and from different times has resulted in a model which is not physically possible, containing elements with unrealistic properties such as coherences greater than unity. The data, although they do not meet the requirements for input to multichannel filter evaluation programs, should be sufficiently good to permit application of some interpretive techniques to derive information about the generation and propagation of ambient noise at UBO.

5. Comparison of Theoretical and Experimental Results

The design of a theoretical signal and noise model for UBO has been described.¹ Theoretical performance estimates for various array configurations were presented in another report.⁵ Signal enhancement capabilities predicted for vertical arrays from the theoretical model were considerably greater than those suggested by the experimental results. The

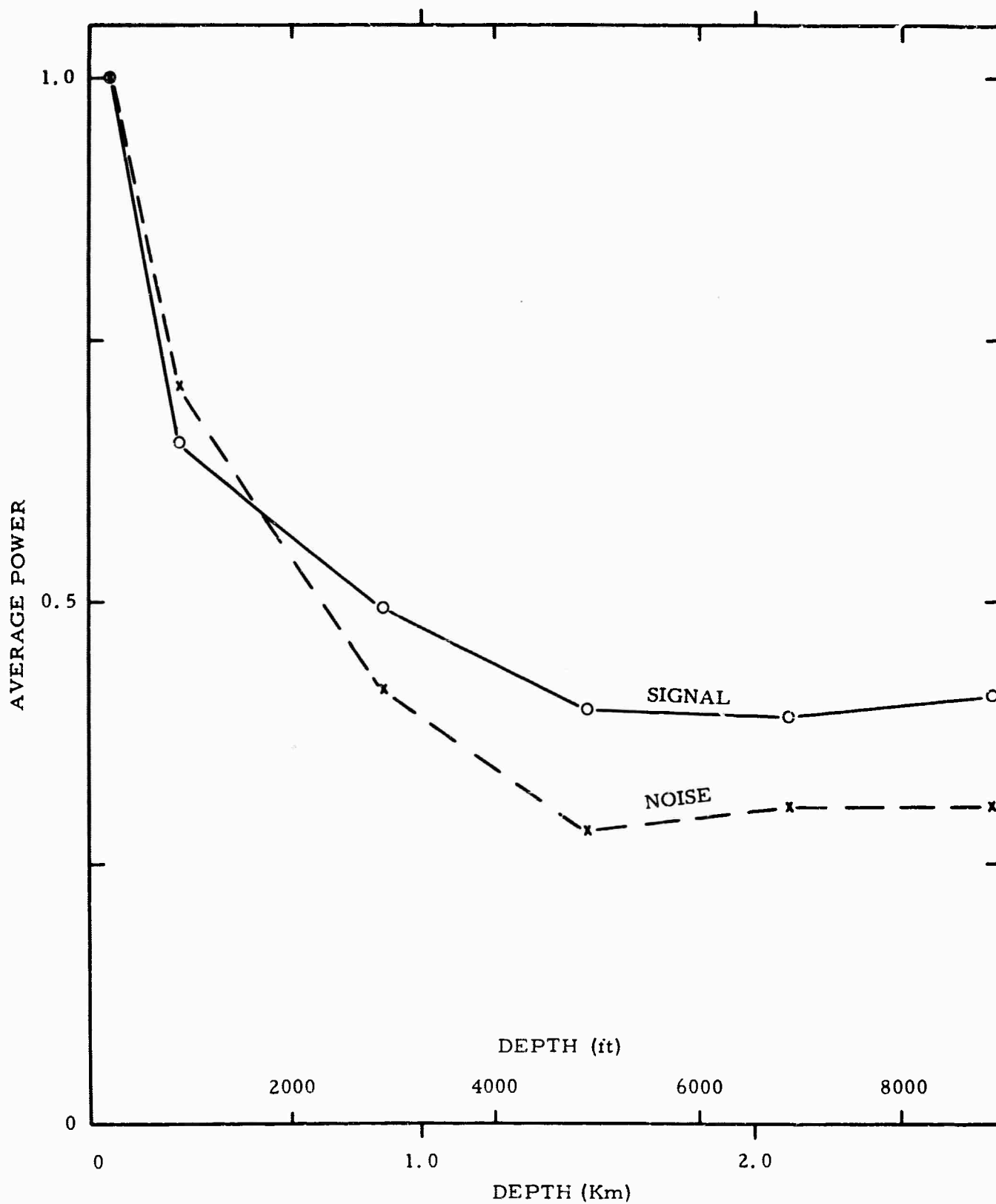


Figure I-19. Average Power of Signal and Noise as Functions of Depth

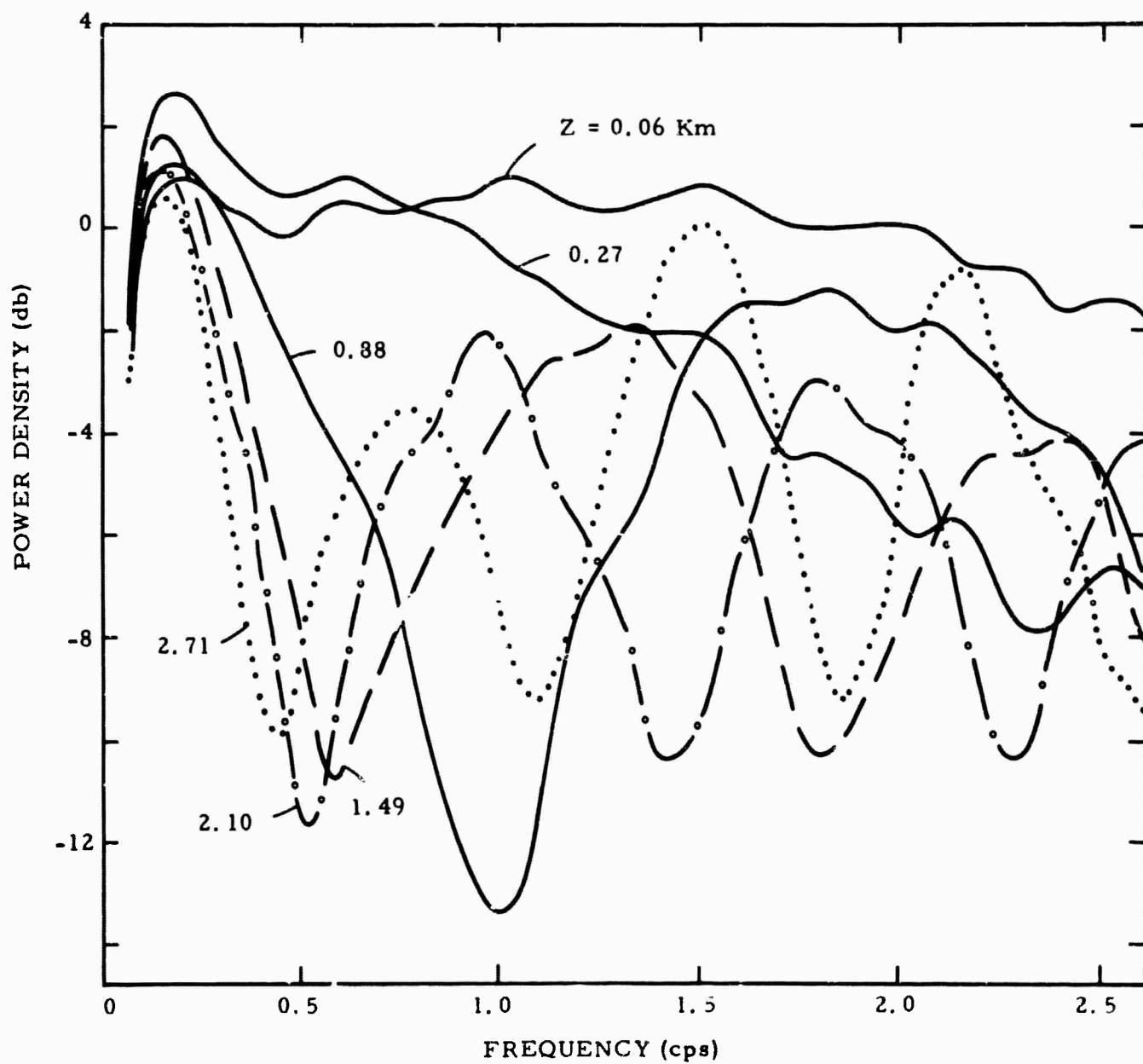


Figure I-20. Average Signal Power Spectra Computed from Experimental UBO Vertical Array Data

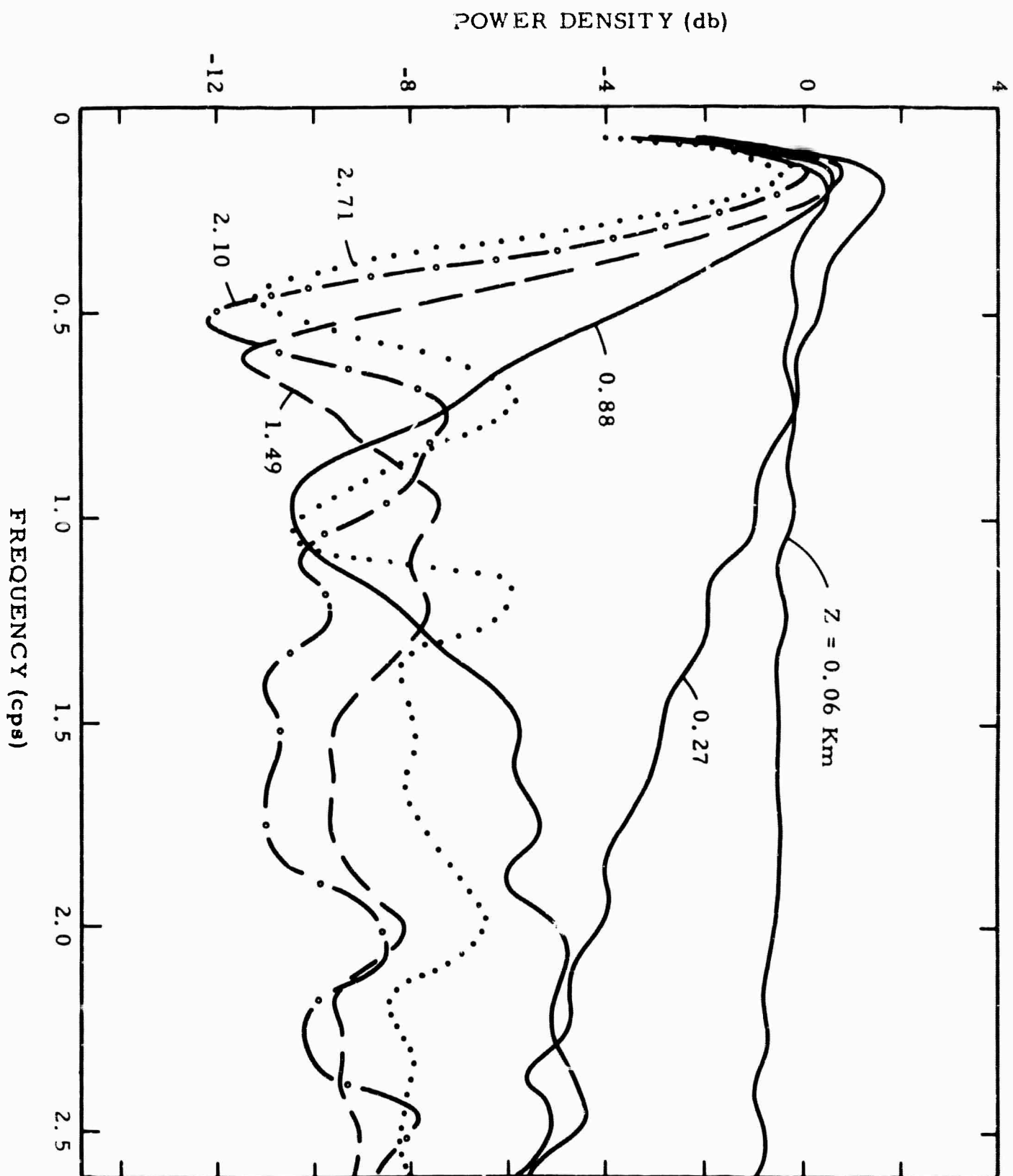


Figure I-21. Average Noise Power Spectra Computed from Experimental UBO Vertical Array Data

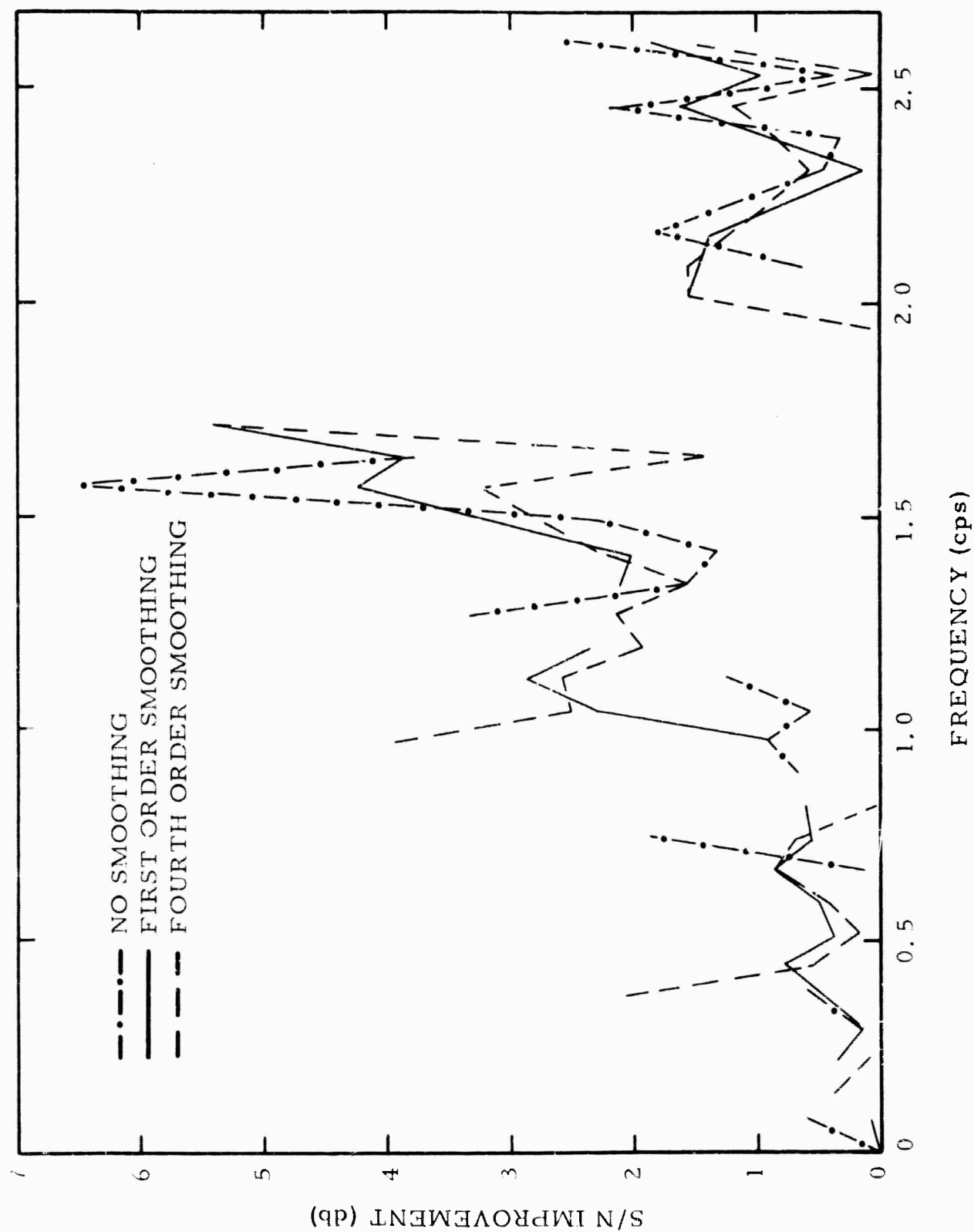


Figure I-22. Predicted Signal-To-Noise Ratio Improvement for
6-Channel Frequency-Domain Filters Operating
on UBO Experimental Model

most probable reason for this disagreement is that the theoretical noise model is not an accurate representation of the ambient noise field at UBO.

The theoretical model was derived from the assumption of uniform, isotropic, perfectly elastic sedimentary layers overlying a uniform, isotropic, perfectly elastic half-space. It was found then that over 90 percent of the noise energy observed at the surface should be propagating in the fundamental Rayleigh mode. However, if inelastic attenuation and scattering mechanisms are considered, it is found that the noise power becomes redistributed among the modes. The data recorded at UBO support the contention that Rayleigh mode noise is not the only significant constituent of the ambient noise.

Computations have been made in order to investigate the effect of redistribution of energy. This signal and noise power spectra previously assumed for a near-surface seismometer are reproduced in Figure I-23. White incoherent noise was included with assumed power levels of -13.9 db (relative to the maximum signal power density) at the surface and -33.9 db at depths of 200 ft or more (UBO Model 20). Two vertical arrays were investigated, array B being identical to the 6-element experimental array studied in this report and array A being the same except that the 200-ft instrument was replaced by a surface instrument. The noise model has been modified by applying to the Rayleigh mode an attenuation factor which was an exponential function of frequency. The modified spectrum is shown by the broken line in Figure I-23. In Figure I-24, the predicted signal-to-noise ratio improvements are presented. The solid curves show the improvement of vertical array A relative to a single surface seismometer, while the broken curves show the improvement of array B relative to a seismometer at 200-ft depth. The outputs of the two arrays are very similar. The differences between the A and B curves represent improvements in single seismometer performance which, it is assumed, may be obtained by shallow burial.

It is clear from Figure I-24 that a redistribution of energy which reduces the importance of the Rayleigh mode is likely to reduce the effectiveness of a vertical array. This is probably because the higher modes resemble P-waves much more closely than does the Rayleigh mode (as seen by a vertical array). Since velocity filtering with a horizontal array should not be affected much by a redistribution of energy, it follows that the predicted advantage of horizontal arrays over vertical arrays should be increased when the noise model is made more realistic.

Another probable source of disagreement between experimental and theoretical results is the presence of P-wave noise in the field data. Figures I-25 and I-26 are contoured plots of wavenumber spectra

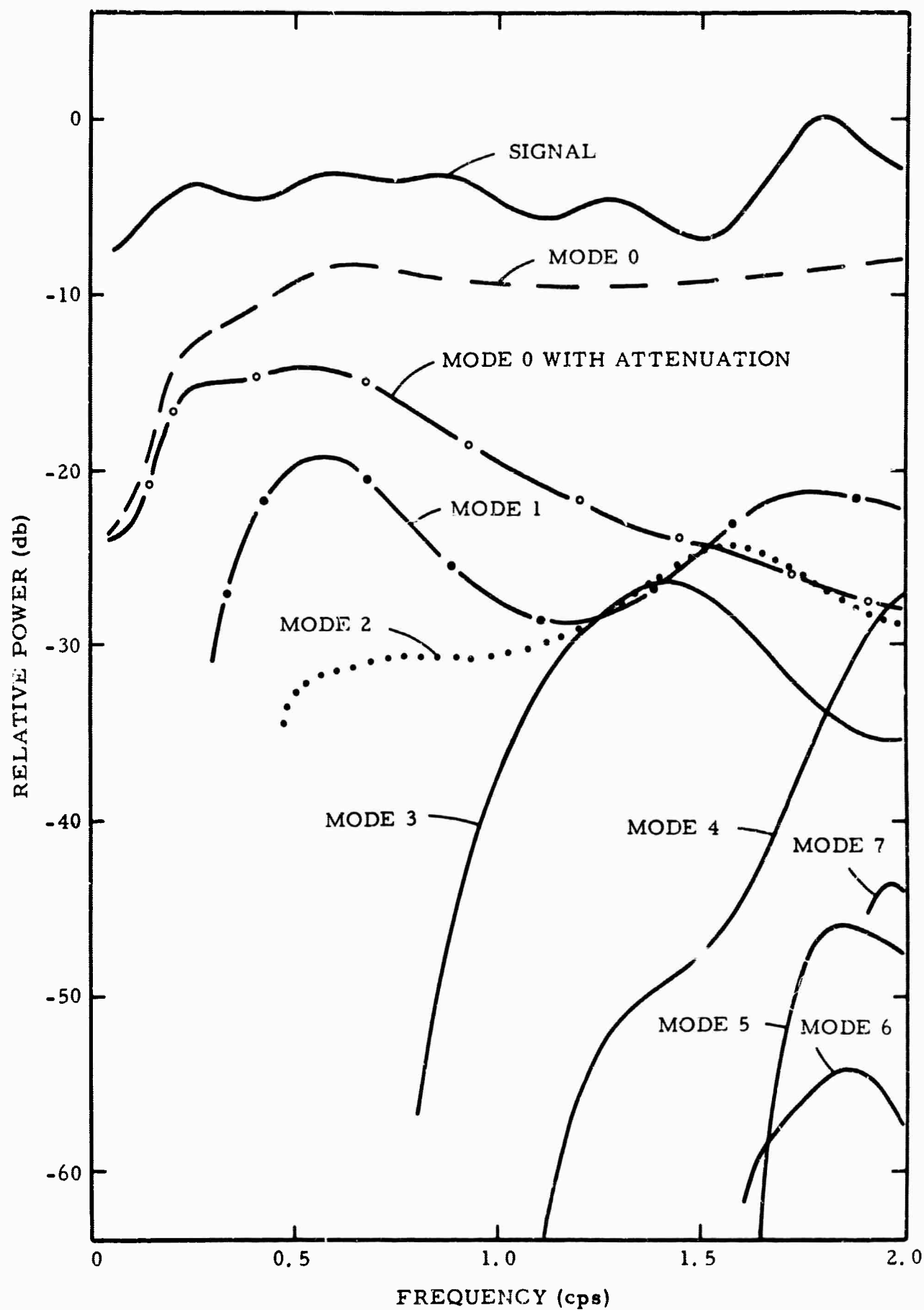


Figure I-23. Assumed Input Power Spectra of Signal and Noise at a Surface Seismometer, Expressed in db Relative to the Maximum Signal Power

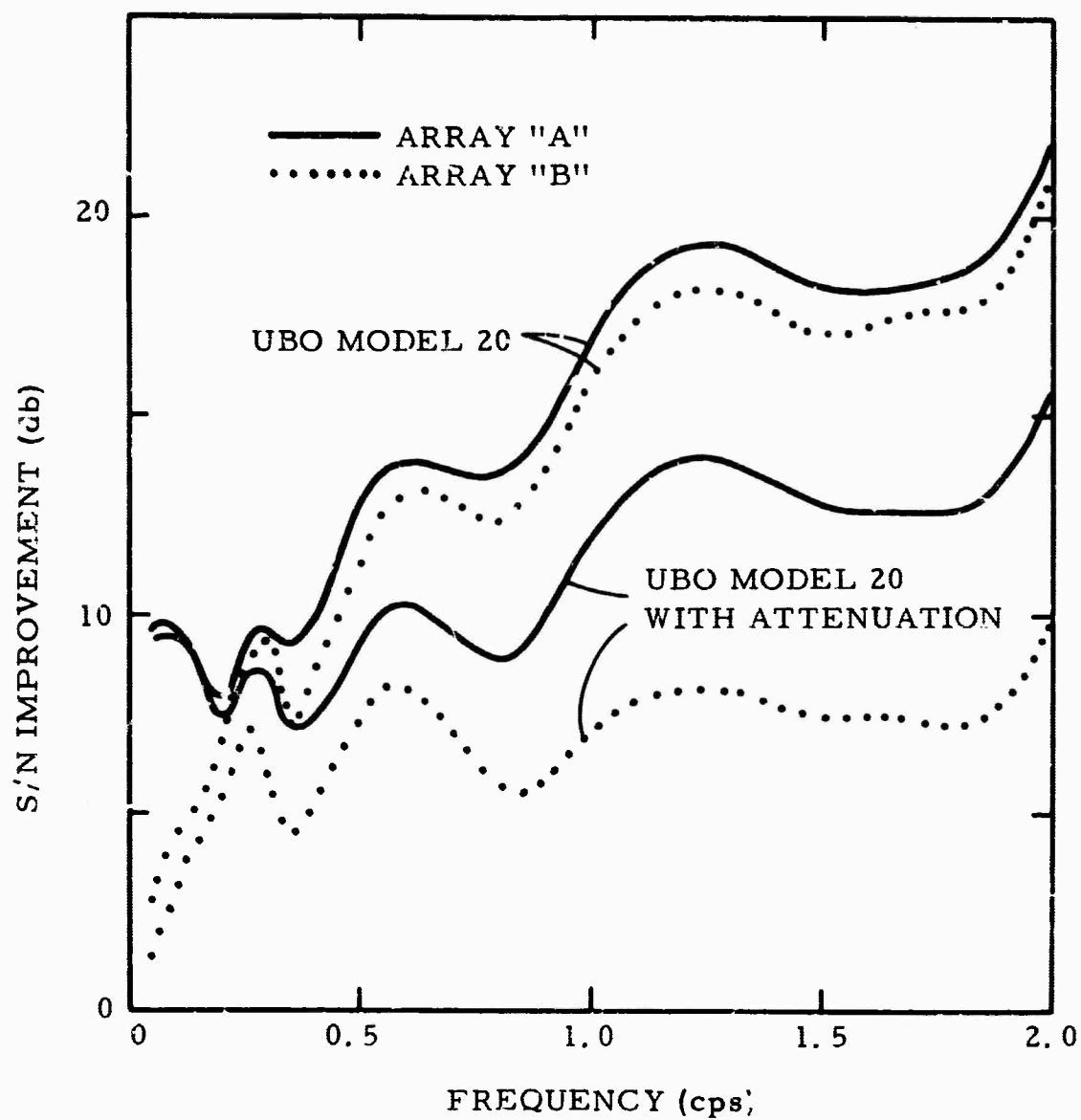


Figure I-24. Effect on Vertical Array Performance of Attenuation of Rayleigh Mode

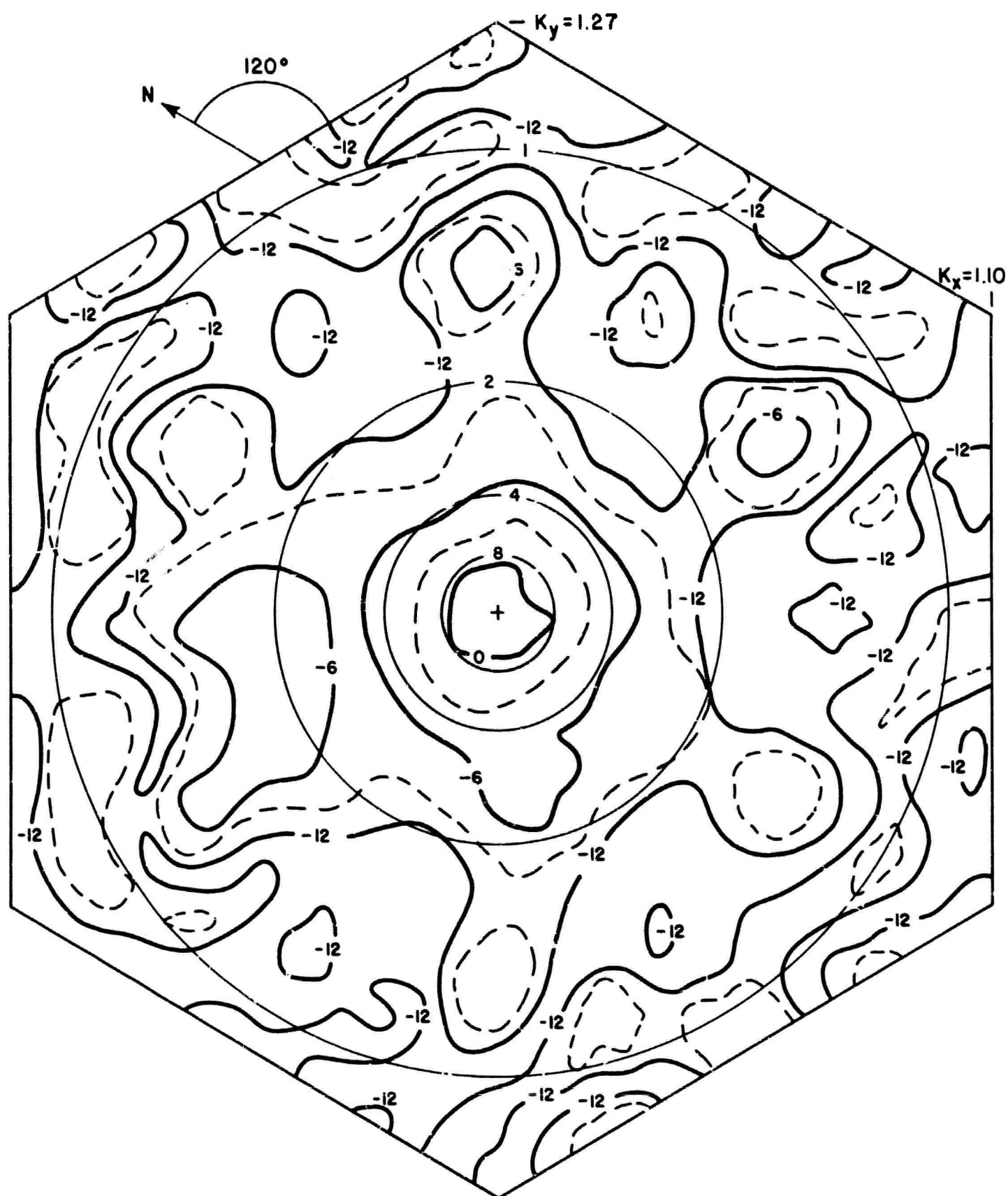


Figure I-25. UBO 2-Dimensional Wavenumber Spectrum for
1 Cps (3 Db Contours)

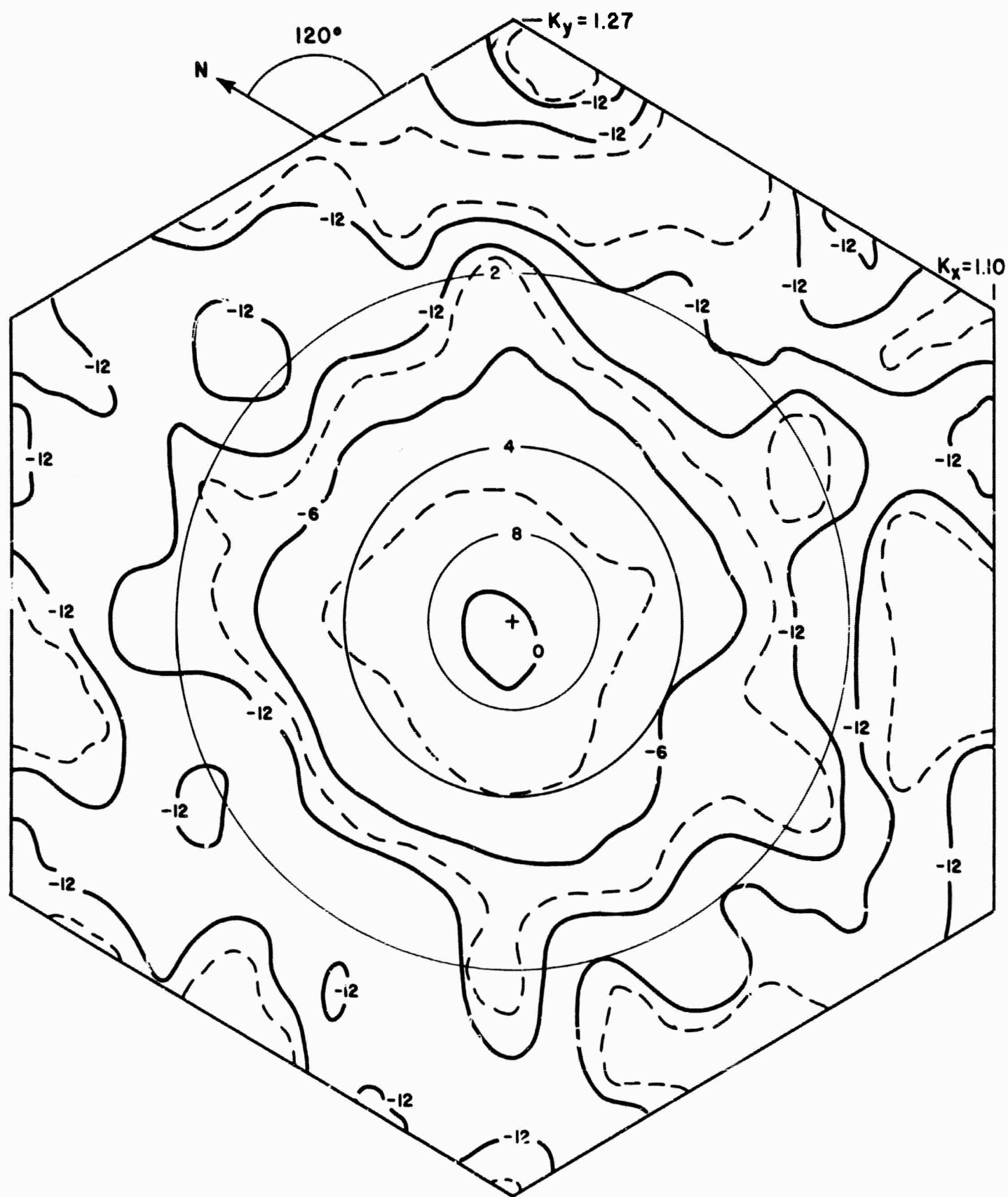


Figure I-26. UBO 2-Dimensional Wavenumber Spectrum for
1.5 Cps (3 Db Contours)

computed from data recorded 12 October 1964 with the 10-element UBO surface array. Visual examination of these spectra indicates that approximately 15 to 20 percent of the ambient noise at 1 cps and 1.5 cps was associated with propagation velocities greater than 6 km/sec. The symmetry of this part of the spectra suggests that the high-velocity noise is more likely to be due to mantle P-waves than to atmospheric effects. This amount of P-wave noise implies an improvement limit of 7 to 8 db, even if the surface-wave noise and incoherent noise could be rejected perfectly.

It is planned to attempt to separate the experimentally observed noise into its component parts and use these results to modify the theoretical model. The performance estimates for horizontal and vertical arrays then may be recomputed for a more realistic model.

C. COLLECTION OF VERTICAL ARRAY DATA AT GRAPEVINE

Digital seismic data were recorded intermittently during the period 3 March to 16 March 1965 at the Trigg research well near Grapevine, Texas. Instruments which were employed included deep-well seismometers at depths of 4500 ft (1.37 km), 5500 ft (1.68 km), 6500 ft (1.98 km), 7500 ft (2.28 km), 8500 ft (2.59 km), and 9500 ft (2.89 km), and a 3-component system at the surface. The digitization and recording equipment was the same as that used at UBO for vertical array recording¹ with high- and low-gain channels recorded for each instrument.

Data edited off the field tapes for computer analysis consist of 60 two-minute noise samples, 16 local events (such as quarry blasts) and 12 events tentatively designated as near-regional events (300 series) or teleseisms (400 series). These are listed in Tables I-3 through I-5.

It is planned to use the Grapevine recordings for vertical array evaluations such as were attempted with the UBO data. The Grapevine data should be more suitable for this purpose since the entire array was in operation throughout the recording period, and it will not be necessary to rely upon time-stationarity to construct an array of more than three elements.

Table I-3

CATALOG OF 2-MIN SAMPLES FROM GRAPEVINE

Date	Code No.	Start Time (GCT)	Date	Code No.	Start Time (GCT)
3/4	500	15:27:20	3/6	536	22:27:10
	501	15:39:10		537	22:29:10
	502	15:47:30	3/8	540	02:58:10
	503	15:49:30		541	03:00:10
3/5	504	15:51:30		542	03:02:10
	505	15:56:10		543	03:13:10
	506	16:03:50		544	03:15:10
	507	16:05:50		545	03:17:10
	510	16:17:30		546	11:45:20
	511	21:38:10		547	11:47:20
	512	21:00:10		550	11:49:20
	513	21:02:10		551	12:07:10
	514	21:11:10		552	12:09:10
3/6	515	19:55:20	3/13	553	00:26:10
	516	19:56:20		554	00:33:10
	517	19:59:20		555	00:56:50
	520	20:15:40		556	05:54:50
	521	20:17:40		557	06:02:10
	522	20:34:10		560	06:25:10
	523	20:36:10		561	06:27:10
	524	20:49:50		562	06:42:10
	525	20:51:50		563	07:09:10
	526	20:53:50		564	07:29:20
3/10	527	21:01:30		565	10:25:10
	530	10:21:10		566	11:25:10
	531	10:23:10		567	14:04:10
	532	10:37:20		570	14:28:10
	533	14:30:40	3/16	571	15:54:10
	534	22:17:50		572	16:46:20
	535	22:25:10		573	16:56:50

Table I-4

CATALOG OF LOCAL EVENTS RECORDED AT GRAPEVINE

Date	Code No.	Start Time (GCT)	Date	Code No.	Start Time (GCT)
3/5	201	20:51:40	3/4	210	16:33:20
3/6	202	20:19:40		211	17:03:10
3/13	203	13:49:10		212	17:07:30
	204	14:41:50		214	17:45:00
3/16	205	17:09:10	3/5	215	16:55:50
	206	17:12:10		216	17:01:40
	207	17:19:10		217	17:07:10
				220	17:10:00
				221	17:30:30

Table I-5

CATALOG OF GRAPEVINE RECORDINGS TENTATIVELY DESIGNATED
TELESEISMS AND NEAR-REGIONAL EVENTS

Date	Code No.	Arrival Time (GCT)	Source Information (where available)		
			Location	Magnitude	Δ (degrees)
3/5	400	21:36:23			
3/6	401	20:43:42	Philippines	5.8	116
	300-305	21:10:20	SE Missouri	5.3	6
3/8	306	03:08:10			
	403	12:12:23	Alaska	4.5	44
3/10	402	10:26:25			
3/13	404	01:33:58	Chile	4.4	65
	405, 406	07:42:13	Alaska	5.5	50
	410	14:06:57	Fiji	5.7	93
	411	14:32:36	Rat Is.	4.6	61
3/16	307	16:35:00			
	412	16:59:04	E of Honshu	5.6	89

BLANK PAGE

SECTION II

DECONVOLUTION AND AUTOCORRELATION STUDY

The application of deconvolution and autocorrelation techniques to three ensembles of earthquake records from the multichannel processor at CPO is being studied. Statistics of discrepancies between observed and USC&GS reported origin times, magnitudes and depths of focus are examined.

Ensemble and subensemble average autocorrelations are presented for Ensemble I (73 Kurile Islands events). Very little difference can be observed among the subensembles or between unweighted and normalized averages. It is hypothesized that certain features in the autocorrelations are due to reflections from the Conrad and Mohorovicic discontinuities under CPO.

Ensembles II and III (60 and 119 events of worldwide distribution) are described and the results of individual-event deconvolution presented. Although signal waveforms are contracted somewhat, there is no obvious improvement in detectability of later phases. The nature of the ambient noise recorded at CPO is discussed briefly.

A. DESCRIPTION OF DATA

1. Introduction

Three distinct groups (ensembles) of earthquakes recorded at the Cumberland Plateau Seismological Observatory (CPO) are being studied by use of deconvolution, autocorrelation and depth-of-focus estimation. Analog FM tape recordings of the output of the CPO array processor were converted to digital format for computer analysis. Ensemble I, consisting of a suite of 73 events from the Kurile Islands, was described in detail in an earlier report.⁶ Ensemble II consists of all non-Kurile Islands USC&GS reported events between 25 September 1963 and 18 October 1963. Ensemble III consists of randomly selected events reported by the USC&GS between 20 February 1963 and 14 May 1963.

Figures II-1 and II-2 (CPO polar projection maps) show the random geographic distribution of the 86 Ensemble II events. Figures II-3 and II-4 are similar presentations for the 174 Ensemble III events.

The multichannel filter operating at CPO when Ensemble III was recorded was IP-8.⁷ Ensembles I and II were recorded while processor MIP-4 was in use.⁸

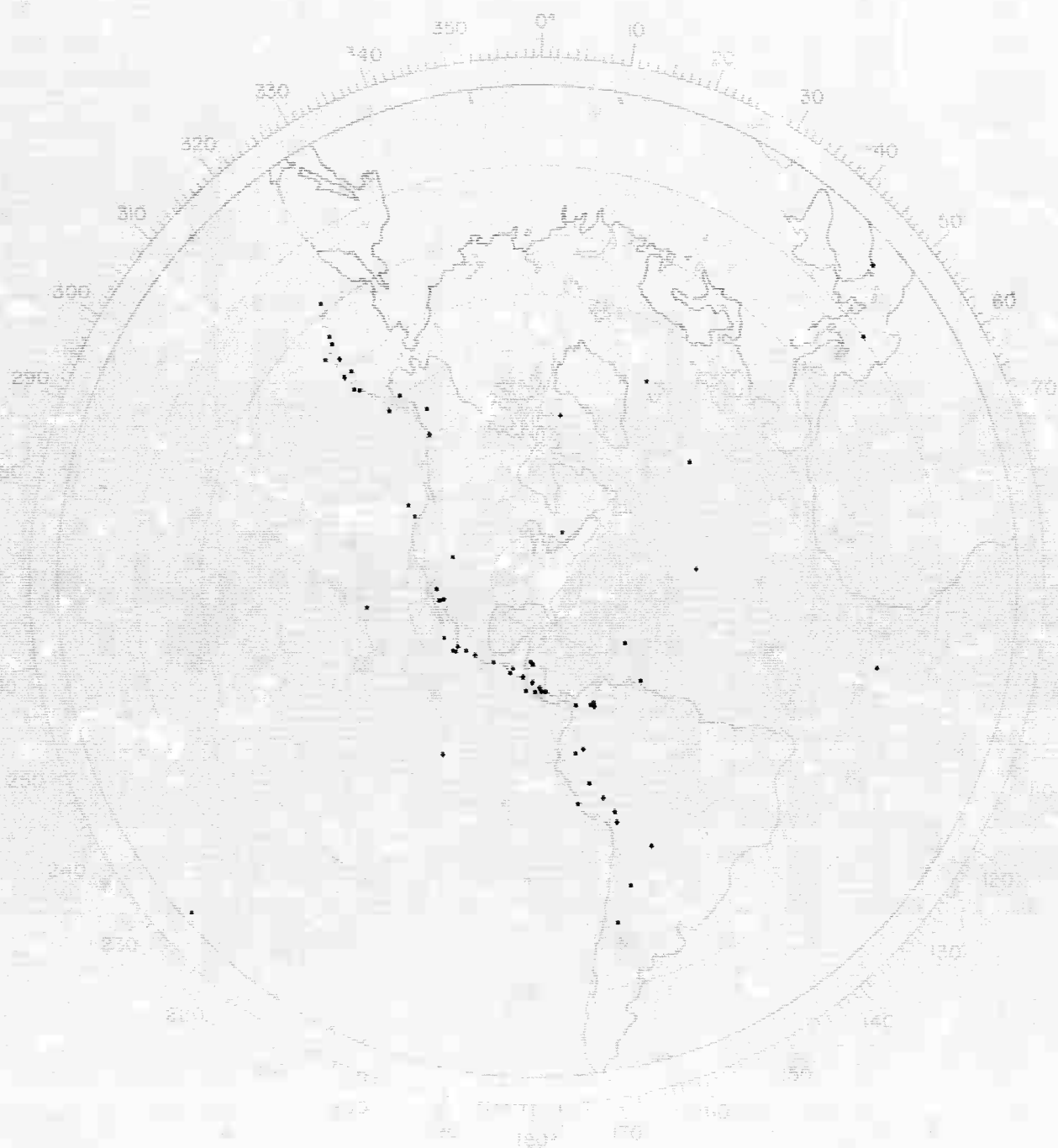


Figure II-1. Geographic Distribution of Ensemble II Events Within 90°



Figure II-2. Geographic Distribution of Ensemble II Events Beyond 90°

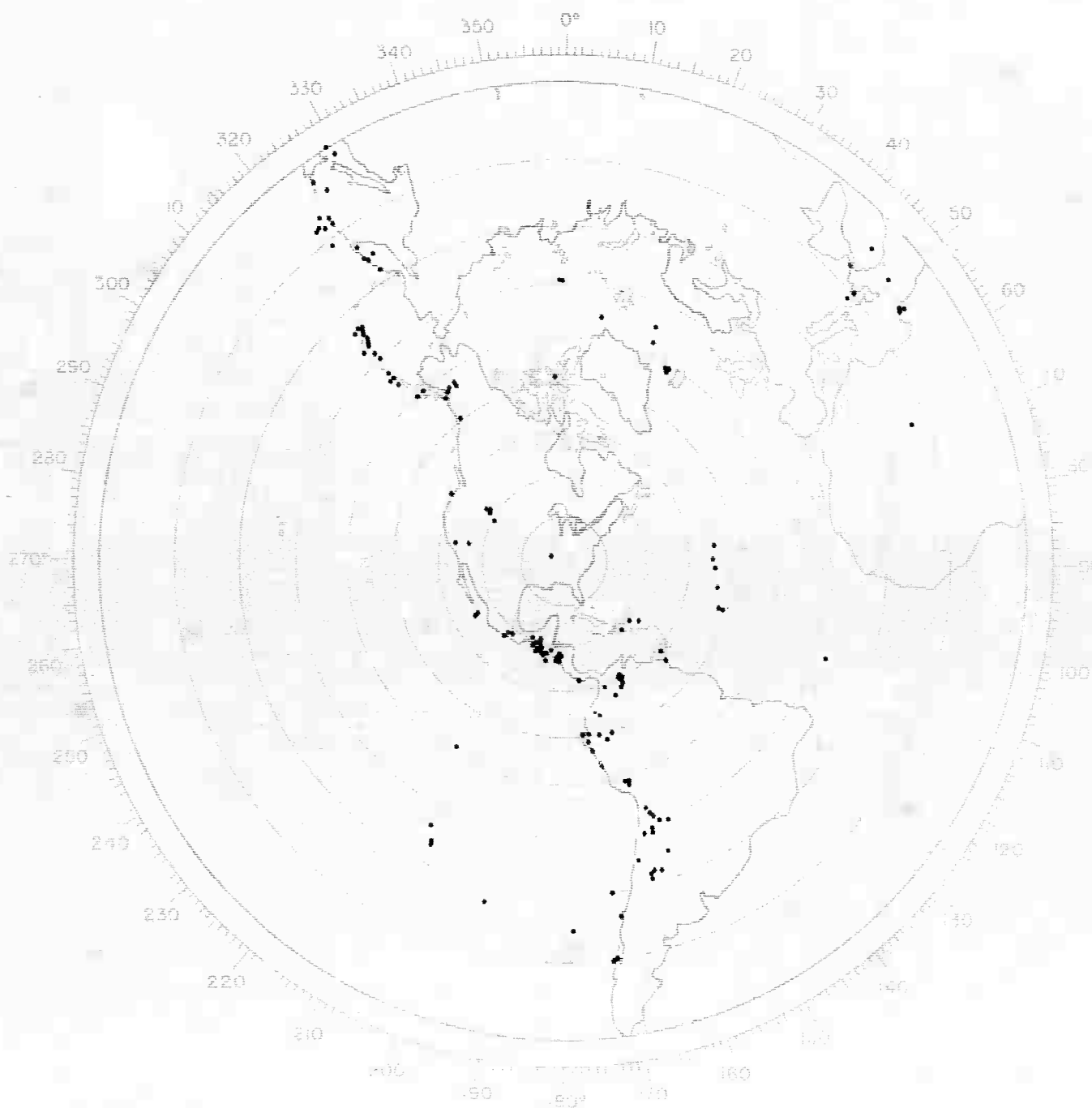


Figure II-3. Geographic Distribution of Ensemble III Events Within 90°

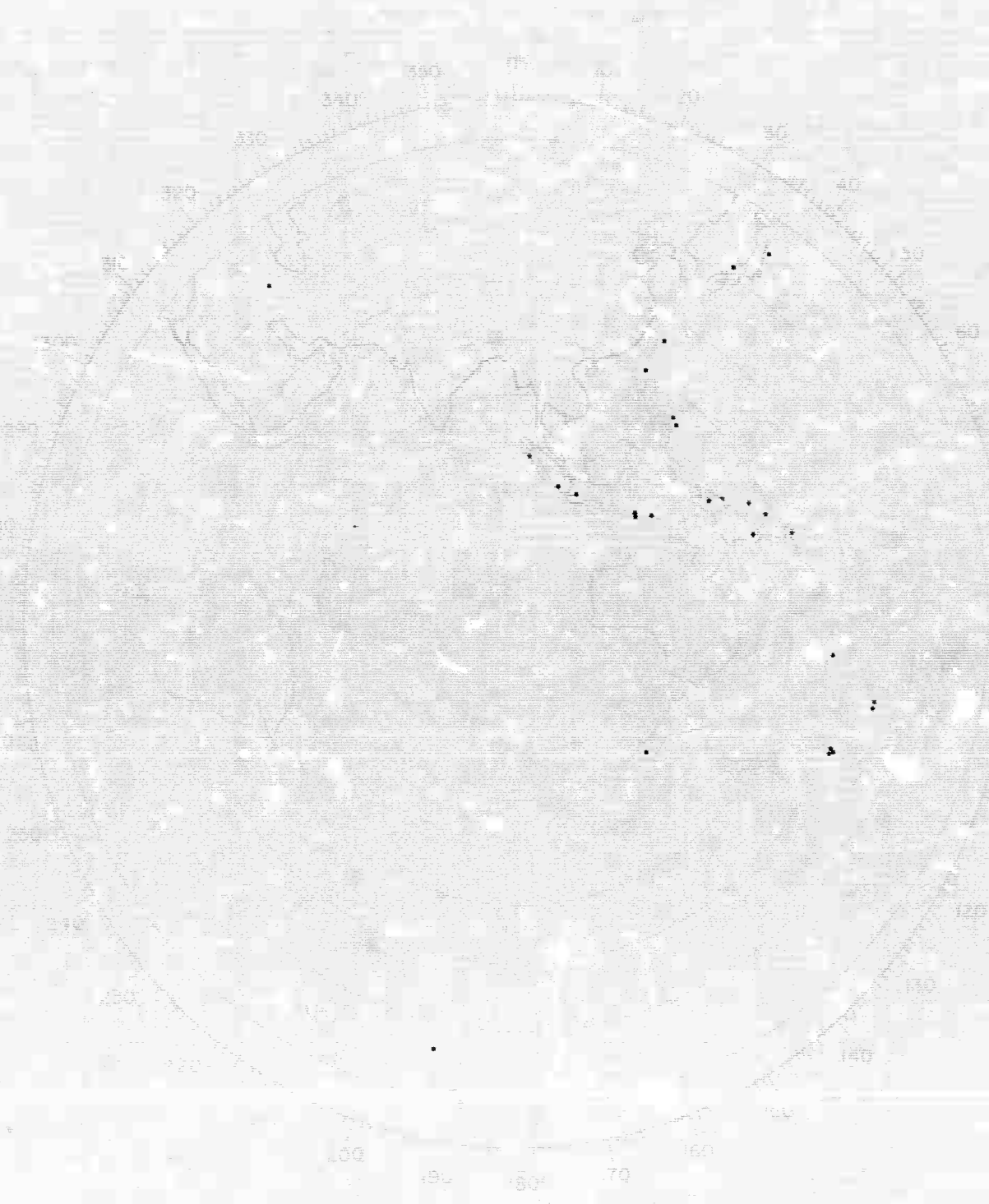


Figure II-4. Geographic Distribution of Ensemble III Events Beyond 90°

2. Arrival Times

Observed P arrival times for Ensemble II averaged 0.1 ± 1.9 sec later than those predicted from Jeffreys-Bullen (J-B) travel-time tables and USC&GS reported epicenters and origin times. Ensemble III observed P's averaged 0.1 ± 1.7 sec ahead of prediction. Figure II-5 is a normalized distribution plot of observed-minus-predicted arrival times for all three ensembles.

For some distant events, PKP was the first arrival. In Ensemble II, observed PKP averaged 1.3 ± 1.9 sec later than predicted, while observed PKP in Ensemble III was 0.3 ± 2.6 sec later than predicted.

The curve for Ensemble I in Figure II-5 shows a bias of about $+0.4$ sec, whereas Ensembles II and III show a much more even distribution of arrival-time anomalies. This bias could be due to some properties of the travel path common to all events from the Kurile Islands.

These results differ from those obtained in another study⁹ where average time residuals for CPO were determined to be 0.02 ± 1.00 sec for 270 Kurile Islands events and -0.26 ± 0.98 sec for 609 events with worldwide distribution.

3. Magnitudes

Magnitudes computed from trace measurements using prescribed USC&GS techniques for Ensemble II averaged 0.3 ± 0.04 less than reported by USC&GS. Those computed for Ensemble III were 0.1 ± 0.5 less than reported. Figure II-6 is a normalized distribution plot of observed-minus-published magnitude for all three ensembles. The curves for Ensembles I and II show more of a trend toward negative differences than Ensemble III. One reason for this difference is that a narrow-band filter was applied to Ensembles I and II. This filter had the effect of lowering the trace amplitude and, hence, the observed magnitude.

4. Depth

Observed depths of foci were calculated from pP-P arrival-time differences. Figure II-7 is a normalized distribution plot of observed depths minus published depths for the three ensembles. As seen from the figure, 100 percent of the events for which pP was observed in Ensemble I lay within the ± 25 km accuracy professed by the USC&GS. Ensemble II pP depths showed 91 percent agreement with the published depths ± 25 km while, in Ensemble III, 88 percent of the depths determined from pP lay within ± 25 km of published estimates.

Figure II-8 is a histogram of pP observance over the magnitude and epicentral distance ranges encountered in each of the ensembles.

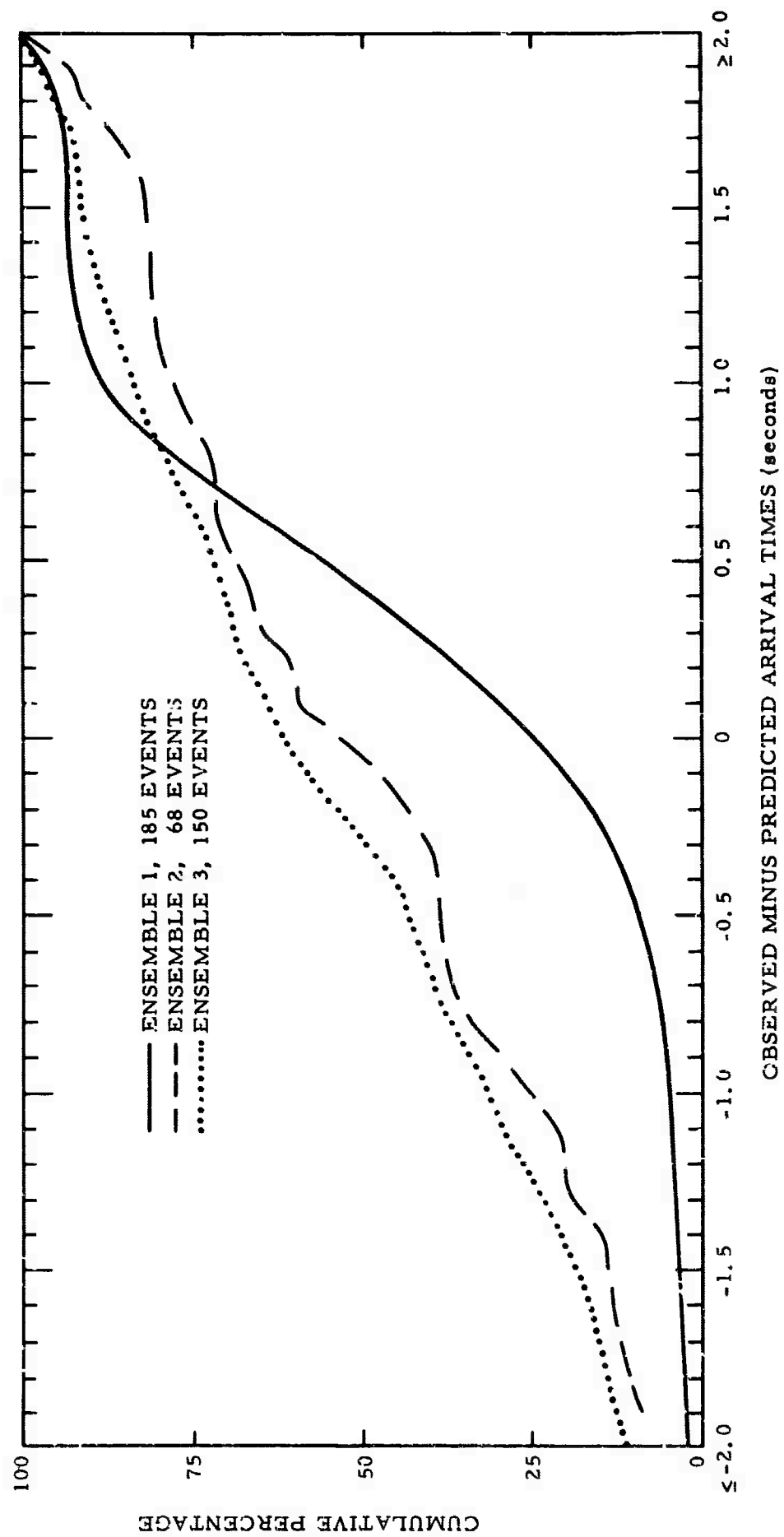


Figure II-5. Cumulative Distribution of Difference Between Observed and Predicted Arrival Times

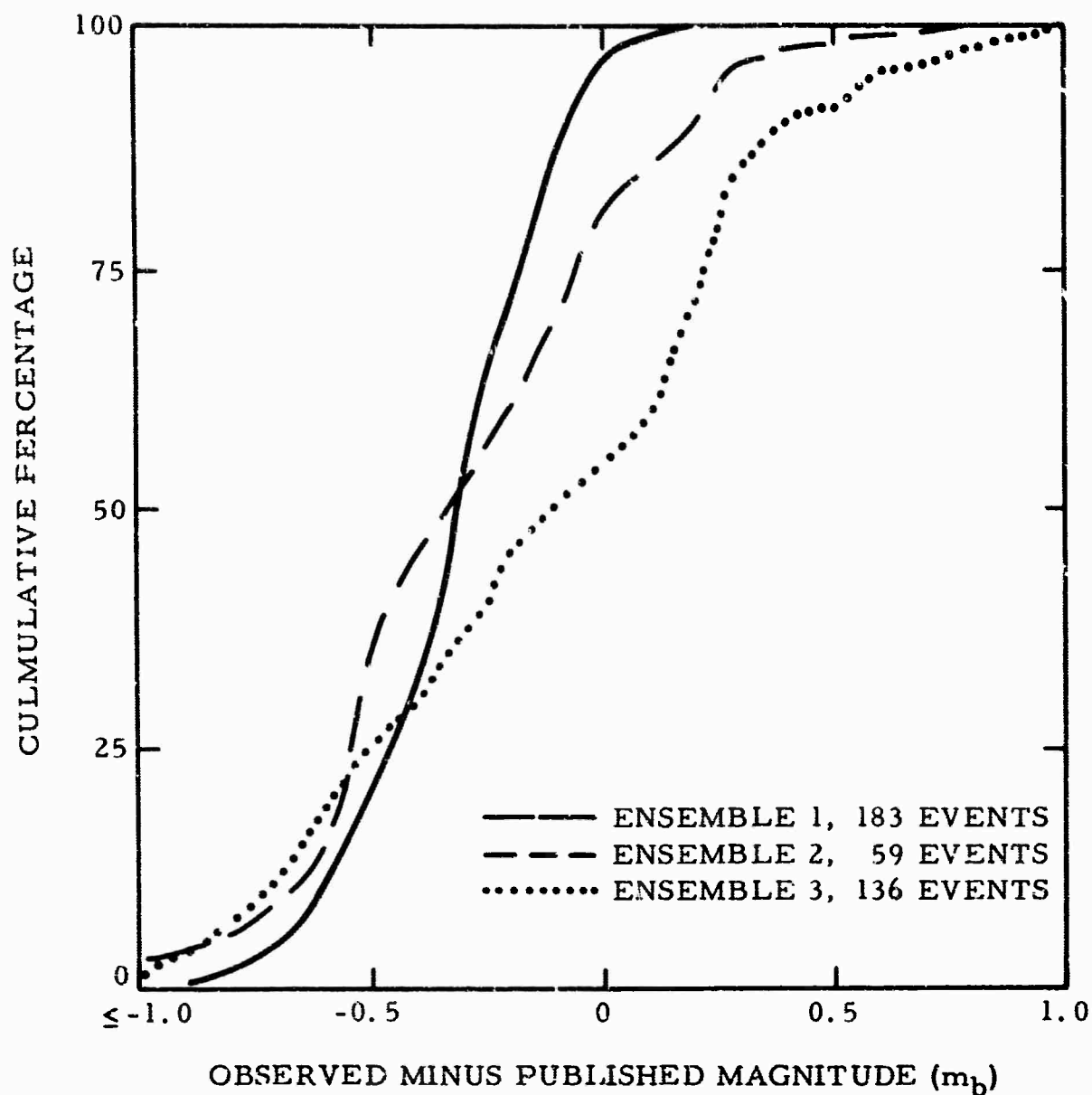


Figure II-6. Cumulative Distribution of Differences Between Computed and Published Magnitudes

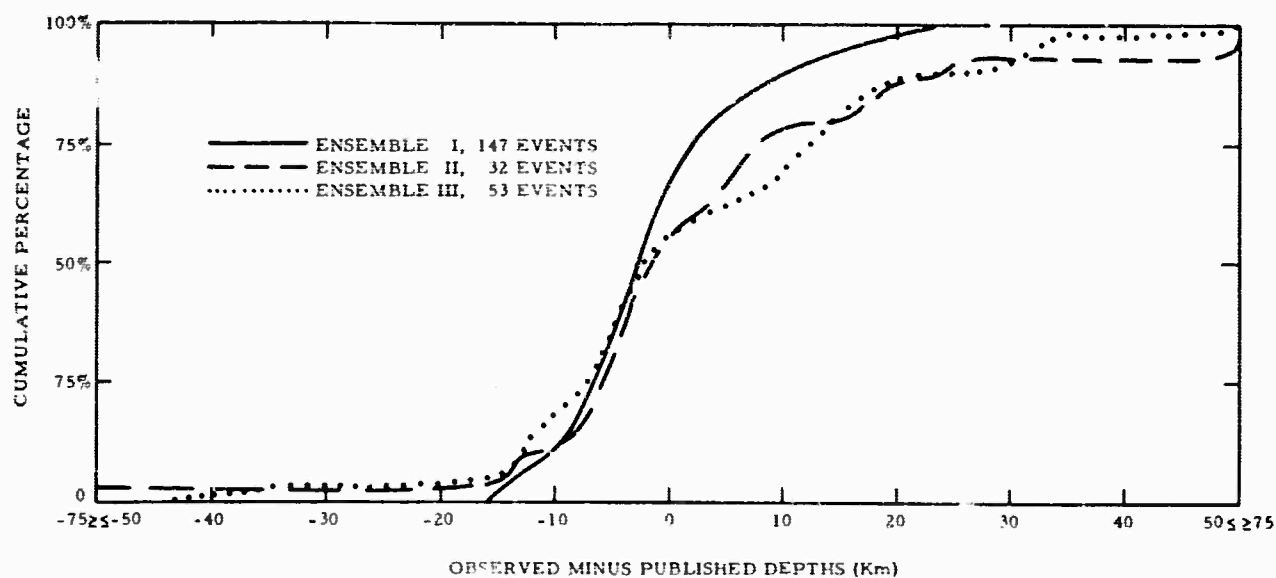


Figure II-7. Cumulative Distribution of Differences Between Depths of Foci Computed from pP Arrival Time and Estimated by USC&GS

ENSEMBLE I

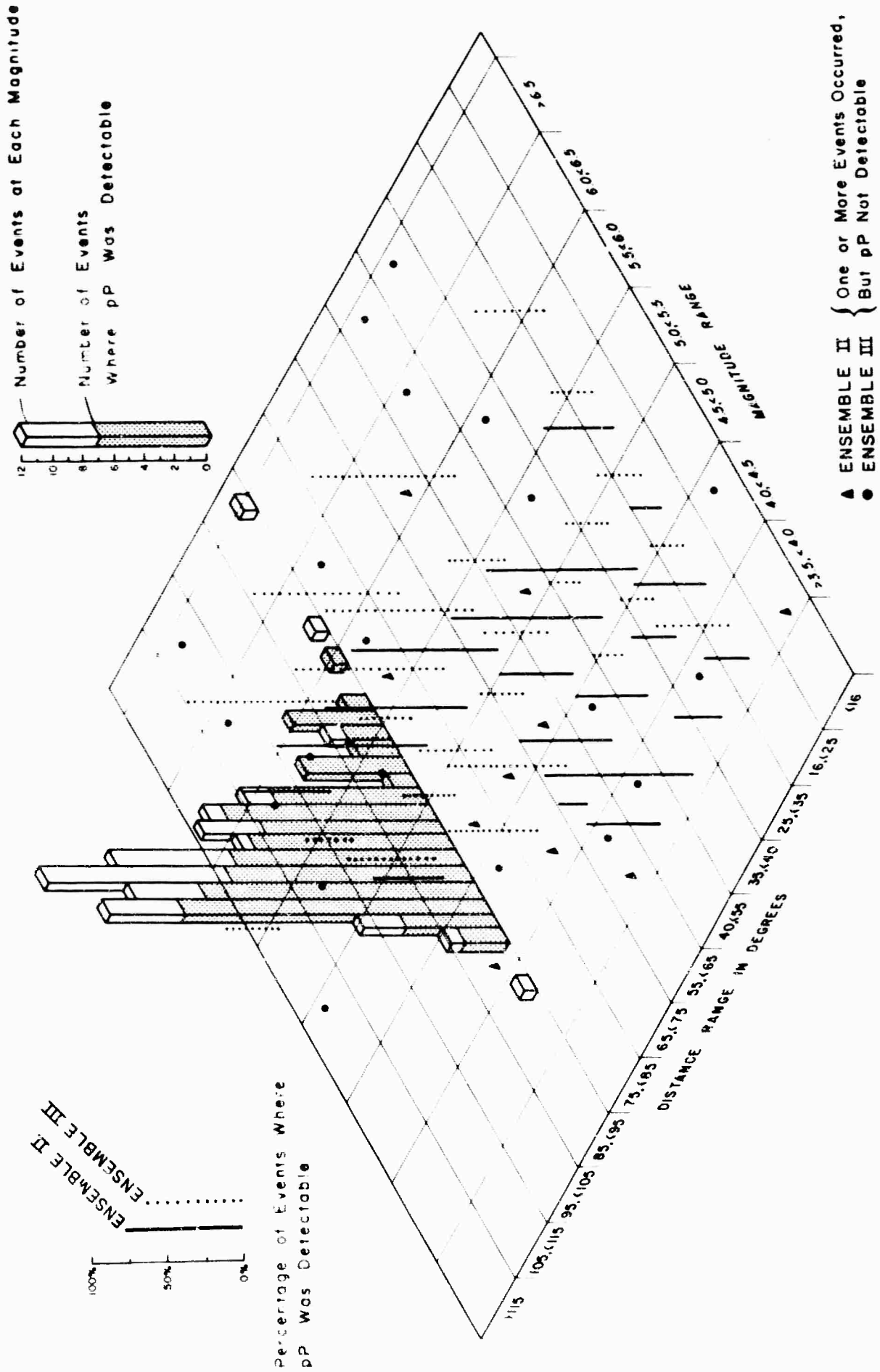


Figure II-8. Histogram of Detectability of pP Events Associated with Teleseisms Recorded at CPO

It is worthy of note that all of Ensemble I (the Kurile Islands data) would necessarily occur about 85° . There is some evidence from this figure that intermediate magnitudes, in particular 5.0 to 6.0 magnitude, yield the highest percentage of pP. The pP phases from large events often are masked by the P wave train and pP phases from small events often are hidden by noise. The optimum magnitude for pP observance is generally less in the case of near events than more distant ones because the P wave train from near events is more elongated.

B. AVERAGE AUTOCORRELATIONS FROM ENSEMBLE I

In an earlier report,¹ use of deconvolution filters designed from ensemble-average statistics was described. Results were found to differ only slightly from those obtained when each record was deconvolved using a filter based only upon its own statistics. In that study, the ensemble-average statistics were determined by computing an unweighted mean of the autocorrelations of the 73 events. It was suggested that a method should be investigated in which the events are normalized to the same mean-square value before averaging.

There are advantages and disadvantages to both approaches. If an unweighted mean of the autocorrelations is used, only the large events will have any significant influence on the results. If the autocorrelations are weighted to normalize their zero-lag values, added importance will be given to small events which generally have small signal-to-noise ratios. Thus, the output from the normalized set may be expected to be contaminated by noise to a greater degree than that from the unnormalized set.

Unnormalized and normalized average autocorrelations computed for six subgroups chosen from Ensemble I and for the complete ensemble are illustrated in Figures II-9 and II-10. Autocorrelations were computed to lags of 24.8 sec using 45-sec records starting just prior to the P onset. The groups represented in Figures II-9 and II-10 are as follows:

- (1) 31 events with observable pP and a uniform distribution of P-pP intervals
- (2) 15 events with large amplitudes
- (3) 26 events with medium amplitudes
- (4) 30 events with small amplitudes
- (5) 30 events with clear later phases
- (6) 42 events with "ringy" autocorrelations (this phenomenon is apparently an effect of source mechanism since it does not appear consistently)
- (7) All 73 events of Ensemble I

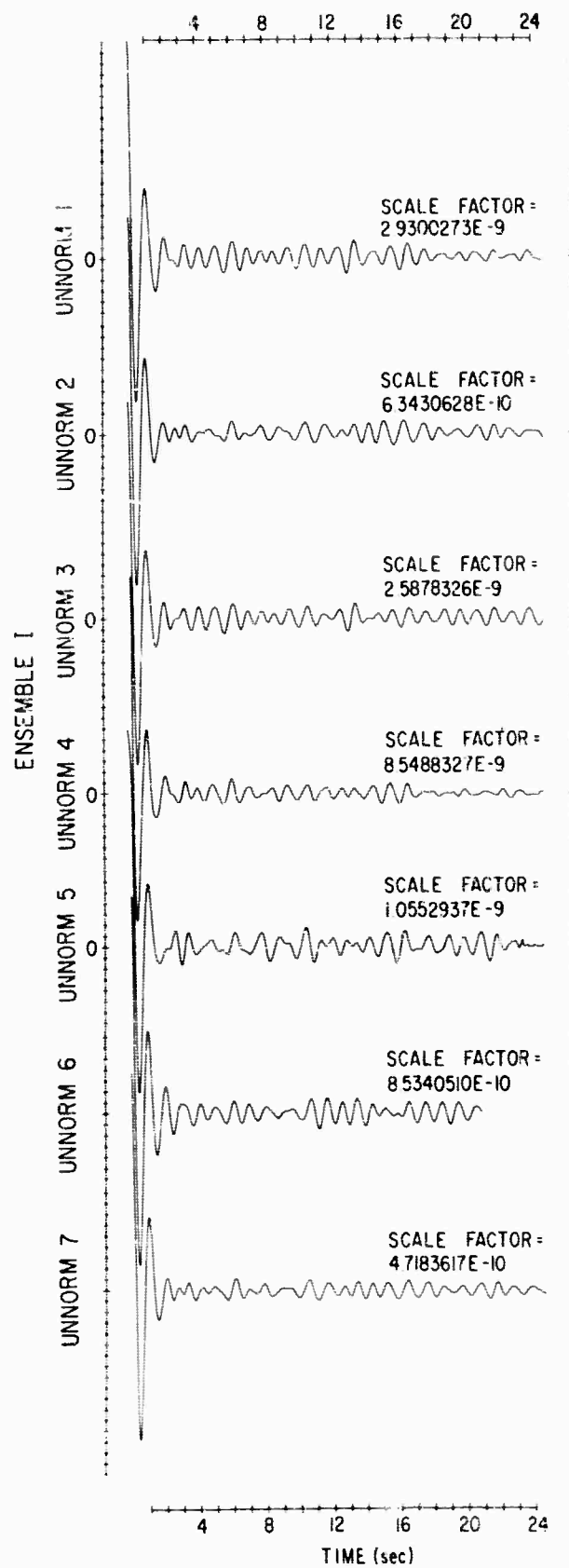


Figure II-9. Unnormalized Average Autocorrelations of Subgroups of Events from Ensemble I

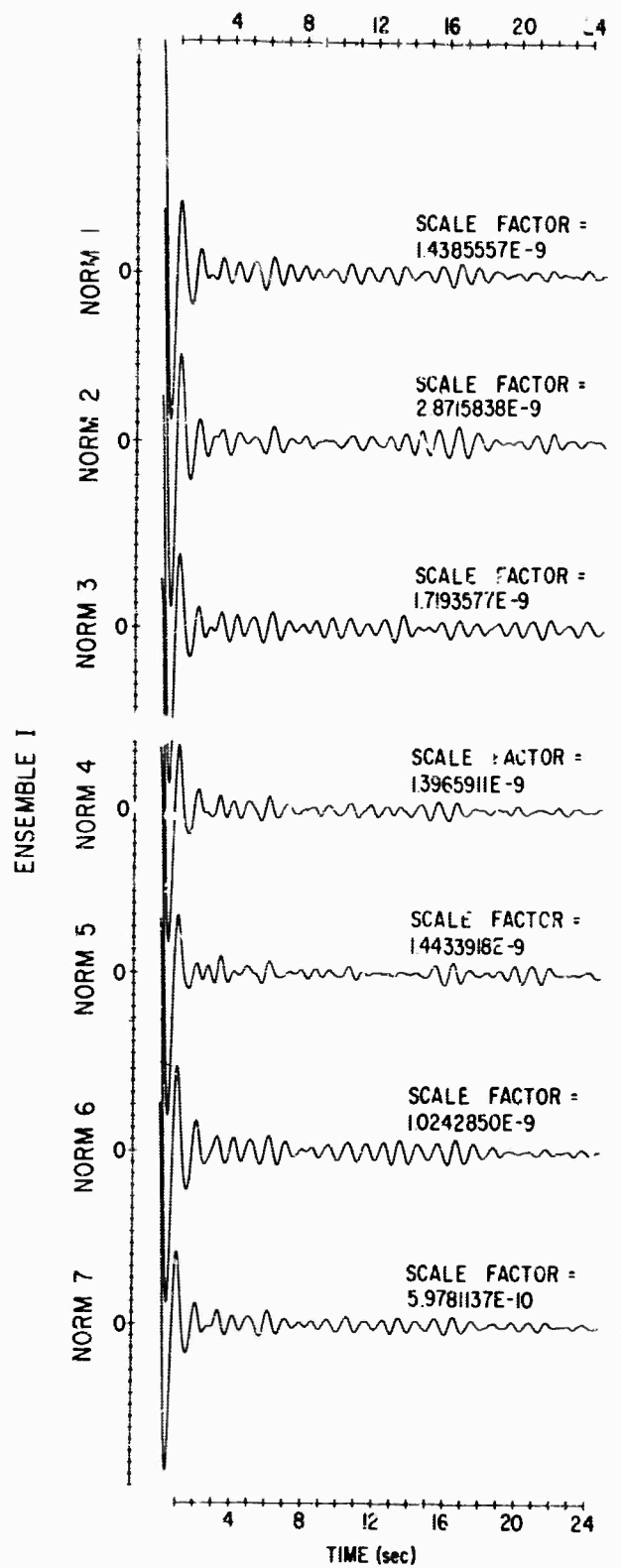


Figure II-10. Normalized Average Autocorrelations of Subgroups of Events from Ensemble I

It is difficult to find any meaningful difference either between the normalized and unnormalized autocorrelations or among the autocorrelations of the various subgroups. For this reason, it was concluded that probably no advantage would be gained by computing additional deconvolution operators.

There is clearly not enough resolution in the autocorrelations to permit conclusions about near-surface layering at CPO. There is a suggestion of persistent features in the autocorrelations at times of approximately 6, 10 and 13.3 sec. These may be associated with primary and multiple reflections from the Conrad and Mohorovicic discontinuities under the receiving station. Additional statistical significance will be provided by the results for Ensembles II and III to test this hypothesis.

C. INDIVIDUAL-EVENT DECONVOLUTION OF ENSEMBLES II AND III

From Ensembles II and III, a selection was made of 60 and 119 events with record quality sufficiently high to permit useful analysis. Figures II-11 and II-12 contain playbacks of the selected events with no differential magnifications applied. In order that the signal waveforms may be easier to observe, Figures II-13 and II-14 present the same events with magnifications applied to make all P-wave amplitudes approximately the same. For each event, a 55-point (5.5-sec) deconvolution filter was designed to whiten the spectrum. The results of filtering the records with their associated deconvolution operators are shown in Figures II-15 and II-16.

Source information for each event is presented in Figures II-11 and II-12. To permit a longer interval to be shown, this information is omitted from Figures II-13 through II-16 which display the events in the same sequence as Figures II-11 and II-12.

Playbacks of the raw data (Figures II-11 and II-12) provide valuable information regarding the nature of the ambient noise at CPO and the relative merits of the two multichannel filter systems. Ensemble III contains records output by processor IP-8, a system designed from a theoretical model of ambient noise assumed to be in the speed range of 2.5 to 3.5 km/sec. Subsequently, the theoretical model was found to be seriously in error; noise velocities as high as 4.5 km/sec were measured. Multichannel filter systems, such as MIF-4 which produced the Ensemble II data, were designed from measured noise statistics. Also, low-cut filters were added to attack the 6-sec microseism peak. Since no differential magnifications were applied in preparing Figures II-11 and II-12, the only trace-to-trace inconsistencies in amplitude should be due to adjustments made to the recording and processing system at CPO, and it is understood that these effects are of a minor nature.

(11a)

Event No.	Δ (°)	Asimuth	Focal Depth	Mag.	
2-1	12.19	26.3	14	3.8	
2-2	20.49	284.2	33	4.5	
2-3	21.85	210.1	41	4.5	
2-4	21.98	196.8	33	4.4	
2-5	22.0	197.1	33	4.1	
2-6	22.15	196.4	86	4.5	
2-7	22.46	220.9	88	4.0	
2-8	22.81	188.6	65	3.7	
2-9	23.01	258.5	33	4.2	
2-10	23.12	226.7	50	4.8	
2-11	23.53	259.4	33	4.0	
2-12	23.79	178.8	159	3.8	

(11b)

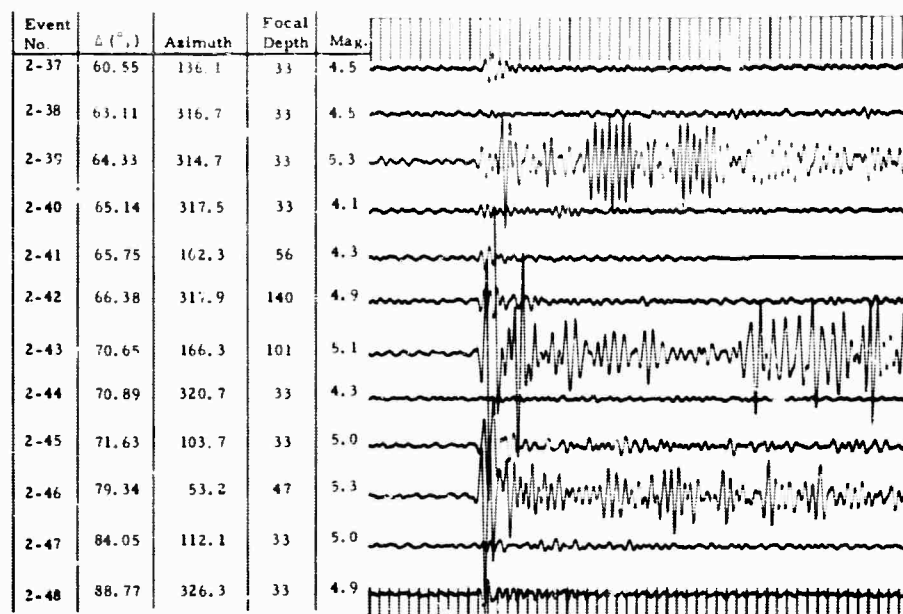
Event No.	Δ (°)	Asimuth	Focal Depth	Mag.	
2-13	23.92	183.2	50	4.5	
2-14	24.73	231.0	33	4.2	
2-15	24.95	230.5	33	4.6	
2-16	25.28	180.9	33	4.1	
2-17	25.71	176.6	63	4.4	
2-18	26.01	239.0	33	4.7	
2-19	29.26	162.1	33	4.6	
2-20	30.8	155.0	157	4.0	
2-21	30.32	155.9	116	3.9	
2-22	32.55	133.5	104	4.6	
2-23	34.72	299.1	33	3.7	
2-24	36.67	6.6	33	4.1	

(11c)

Event No.	Δ (°)	Asimuth	Focal Depth	Mag.	
2-25	38.84	260.9	33	4.0	
2-26	40.54	321.6	33	4.3	
2-27	42.78	52.2	33	4.5	
2-28	43.66	209.0	33	4.1	
2-29	45.87	325.6	51	4.2	
2-30	48.94	108.6	69	5.4	
2-31	49.25	317.3	33	4.8	
2-32	50.48	321.5	33	4.4	
2-33	52.84	160.9	230	3.7	
2-34	54.48	161.0	170	3.8	
2-35	59.22	315.0	33	4.1	
2-36	59.39	316.6	250	4.3	

Timing Lines = 1.0 Sec

(11d)



(11e)

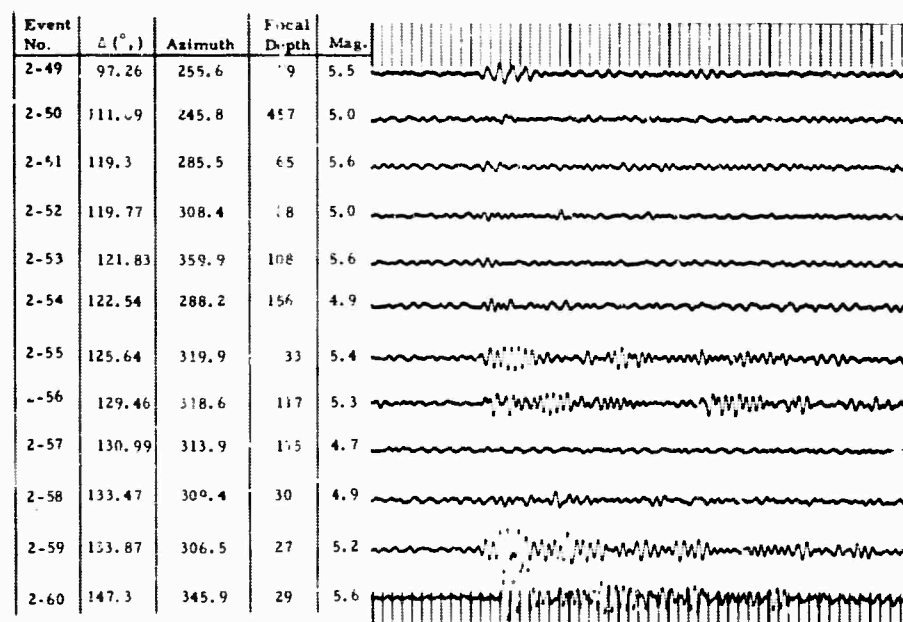


Figure II-11. MIP-4 Output Records of Ensemble II Teleseisms
(II-11a through 11e)

(12a)

Event No.	Δ (°)	Asimuth	Focal Depth	Mag.	
3-1	20.20	204.2	130	4.6	
3-2	20.37	197.1	150	4.3	
3-3	21.02	200.6	33	4.3	
3-4	21.08	302.0	33	4.2	
3-5	21.19	303.0	33	4.1	
3-6	21.4	154.3	33	4.1	
3-7	21.35	197.8	33	4.6	
3-8	21.54	140.3	50	5.5	
3-9	21.59	190.4	33	4.3	
3-10	22.05	202.1	33	4.1	
3-11	22.4	196.0	33	4.5	
3-12	22.46	220.9	33	4.8	

(12b)

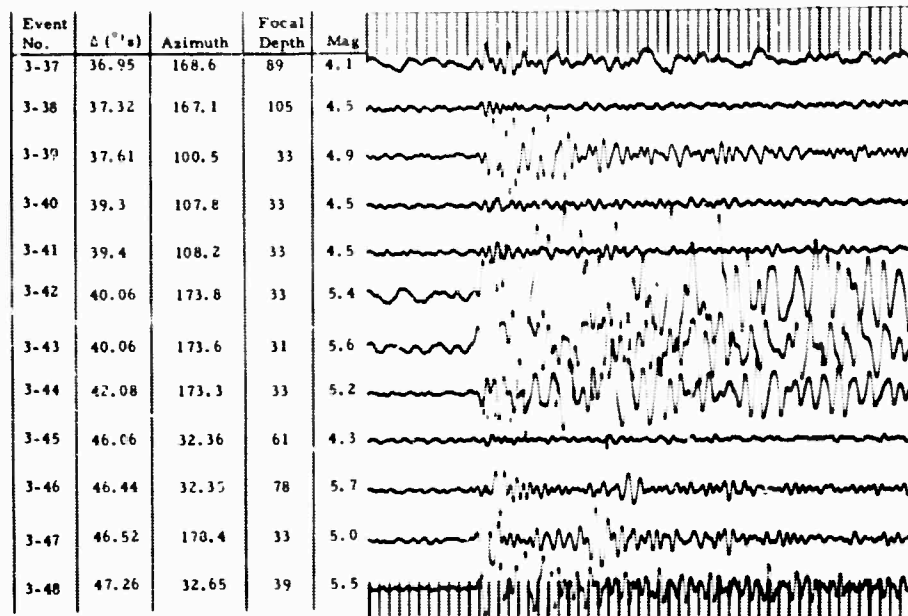
Event No.	Δ (°)	Asimuth	Focal Depth	Mag.	
3-13	22.63	193.8	33	4.3	
3-14	22.88	219.3	33	4.5	
3-15	23.07	129.8	39	4.3	
3-16	23.15	184.5	34	4.2	
3-17	23.15	184.5	33	3.7	
3-18	23.41	186.4	32	4.2	
3-19	23.76	279.6	17	4.3	
3-20	23.87	185.4	33	4.4	
3-21	25.94	174.5	33	4.6	
3-22	26.02	239.6	44	4.3	
3-23	27.15	274.2	16	4.0	
3-24	28.53	172.9	53	4.6	

(12c)

Event No.	Δ (°)	Asimuth	Focal Depth	Mag.	
3-25	30.0	155.1	173	4.1	
3-26	30.39	155.5	127	4.2	
3-27	30.73	155.4	144	4.7	
3-28	30.9	155.1	176	4.6	
3-29	31.01	155.6	140	4.5	
3-30	31.33	155.6	147	5.0	
3-31	31.5	162.3	95	4.3	
3-32	33.3	134.1	53	4.1	
3-33	33.73	159.8	31	4.2	
3-34	35.8	90.9	31	5.0	
3-35	36.16	91.0	31	4.6	
3-36	36.5	85.0	33	4.3	

Timing Lines = 1.0 Sec

(12d)



(12e)

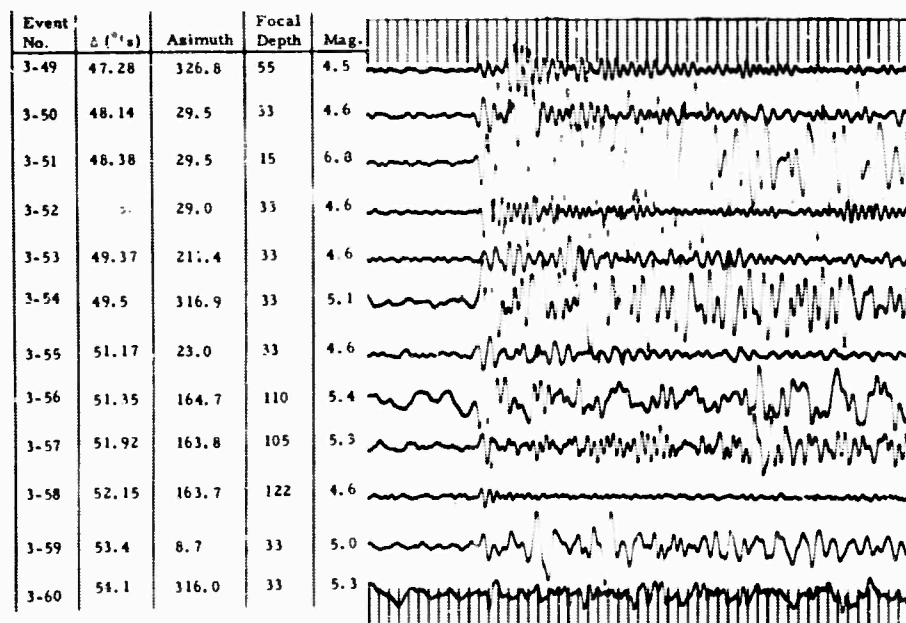
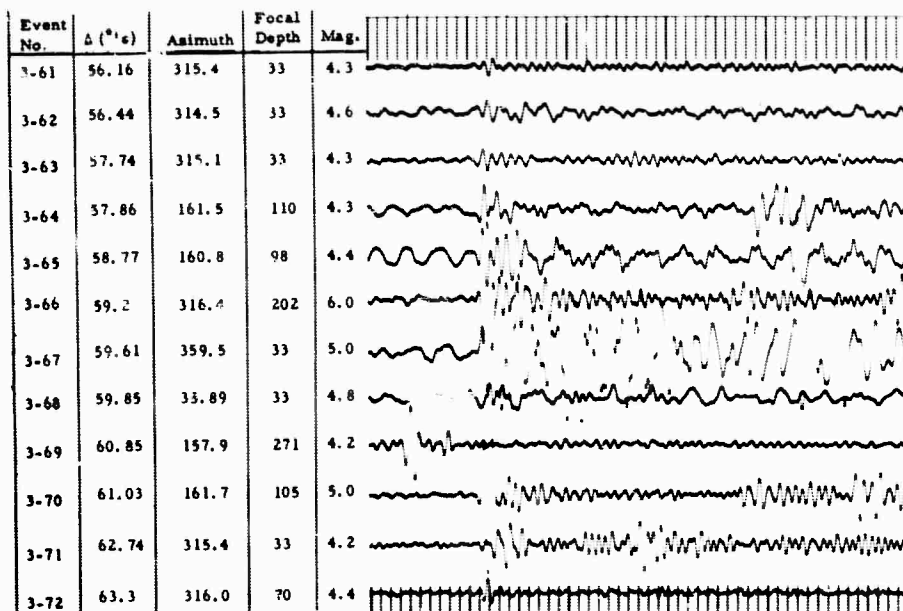
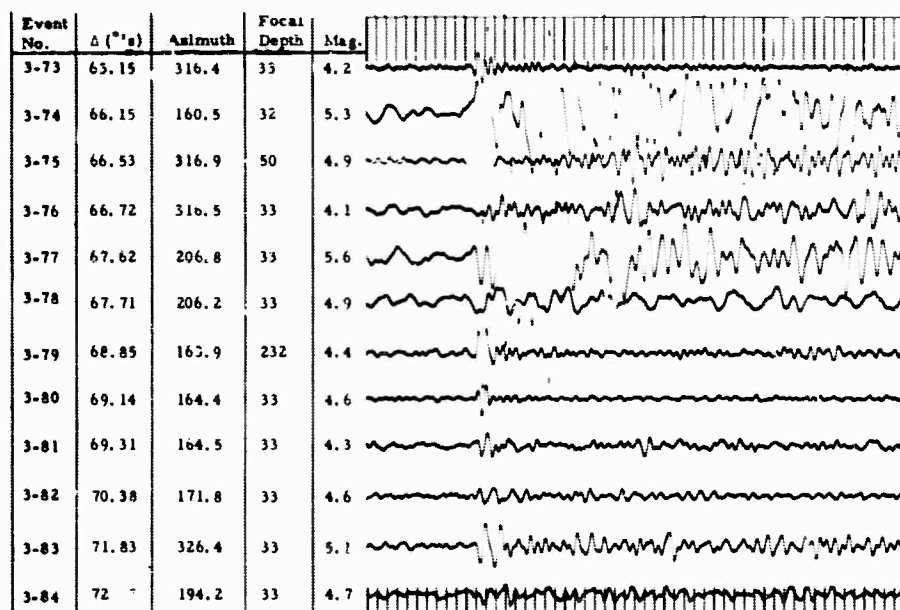


Figure II-12. IP-8 Output Records of Ensemble III Teleseisms
(II-12a through 12e)

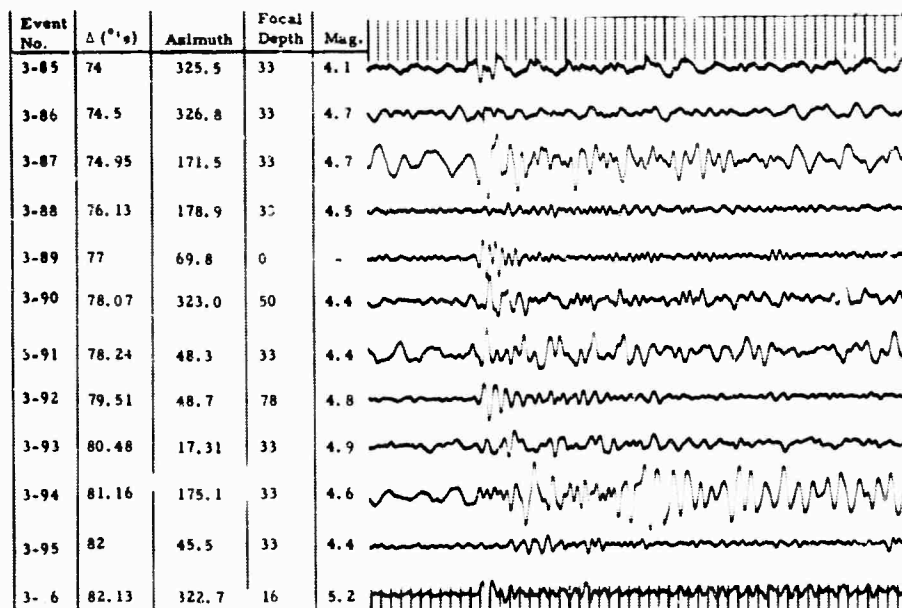
(12f)



(12g)

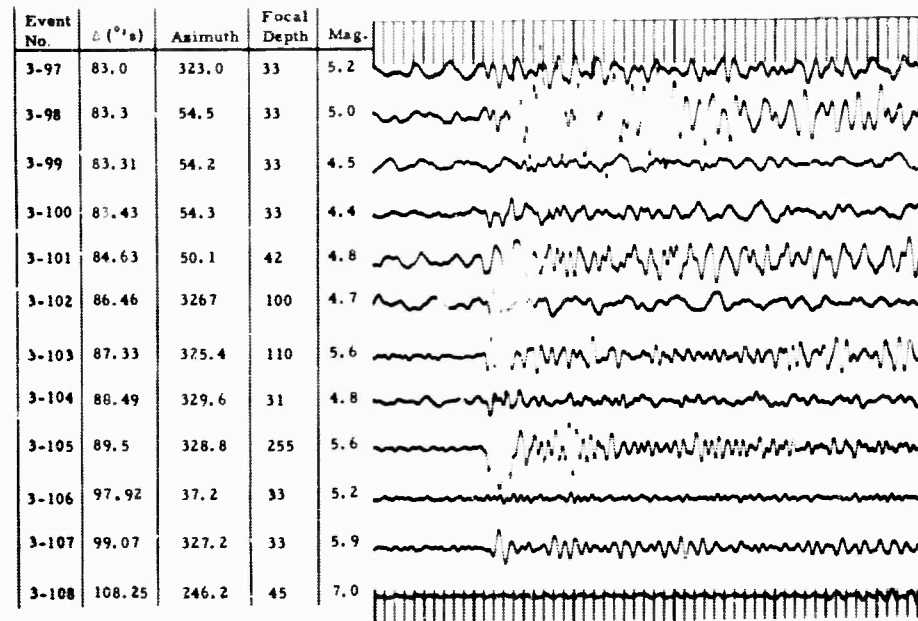


(12h)



Timing Lines = 1.0 Sec

(12i)



(12j)

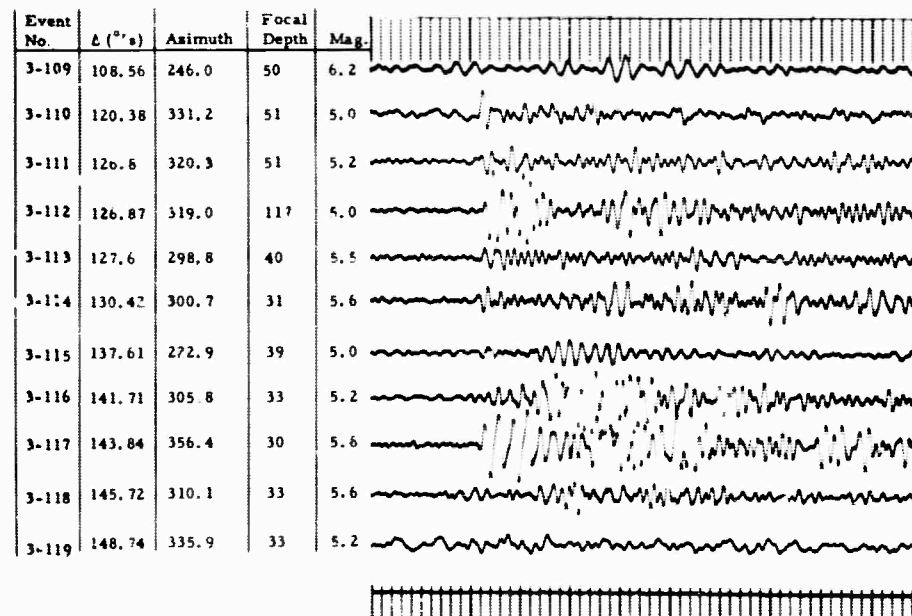
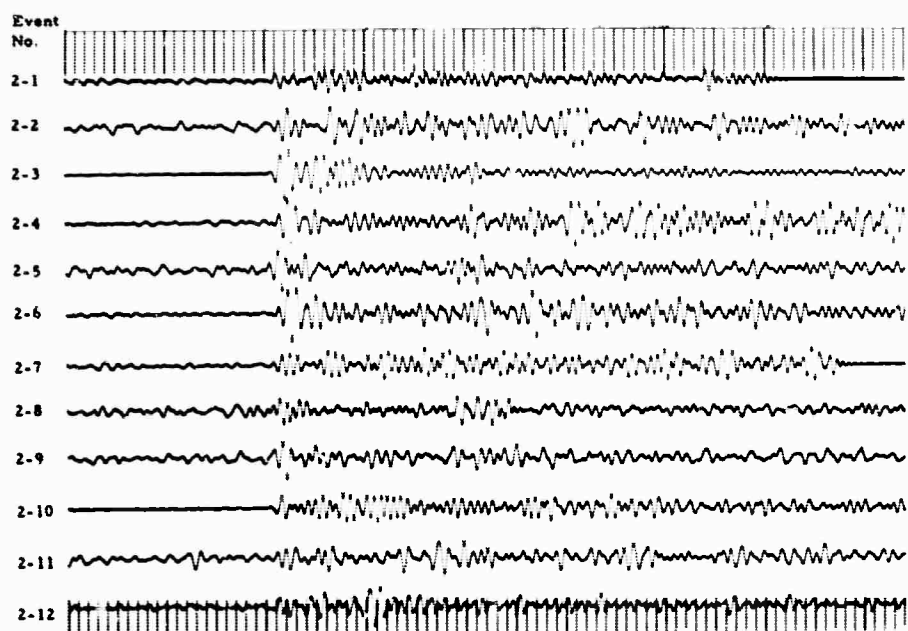
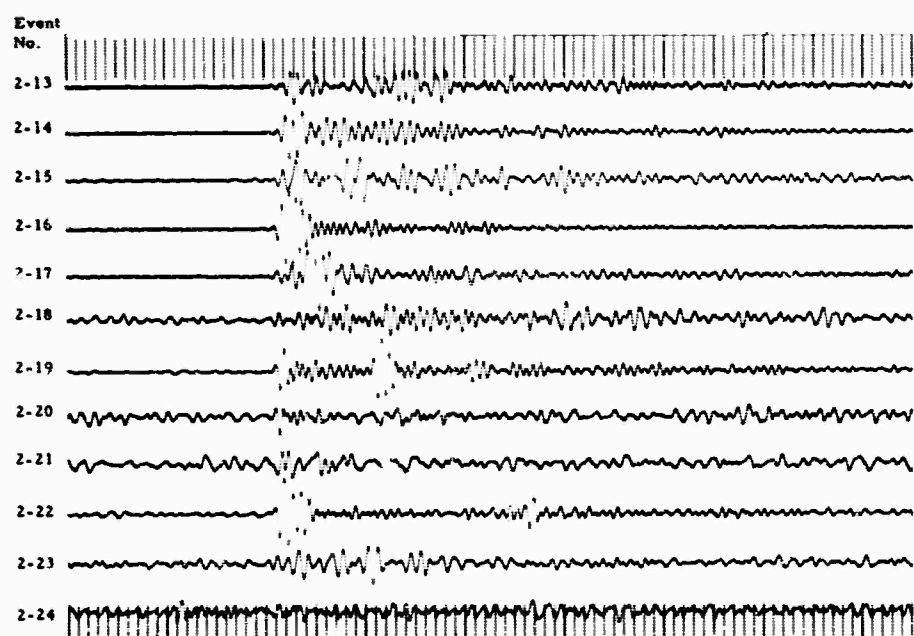


Figure II-12. IP-8 Output Records of Ensemble III Teleseisms
(II-12f through 12j)

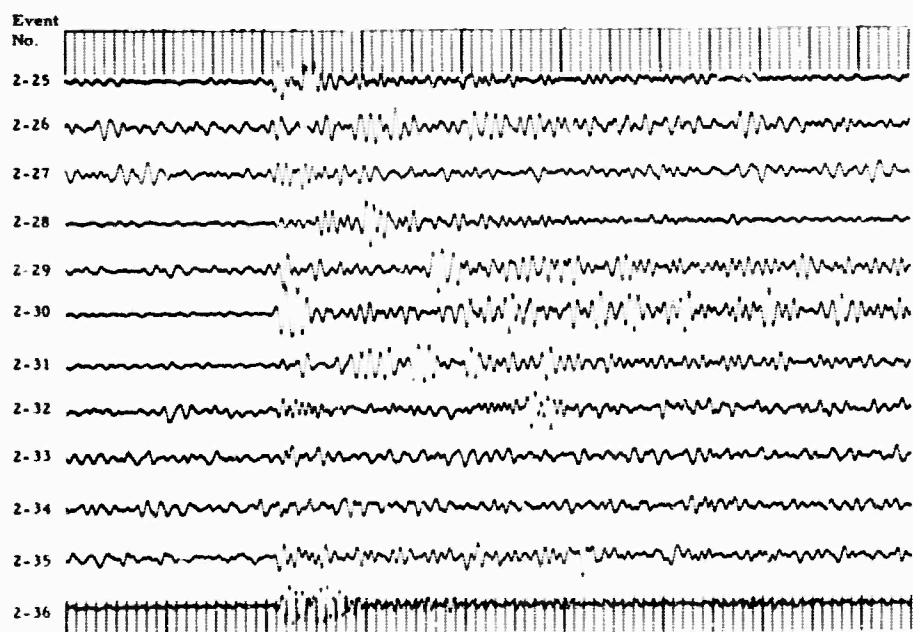
(13a)



(13b)



(13c)



Timing Lines = 1.0 Sec

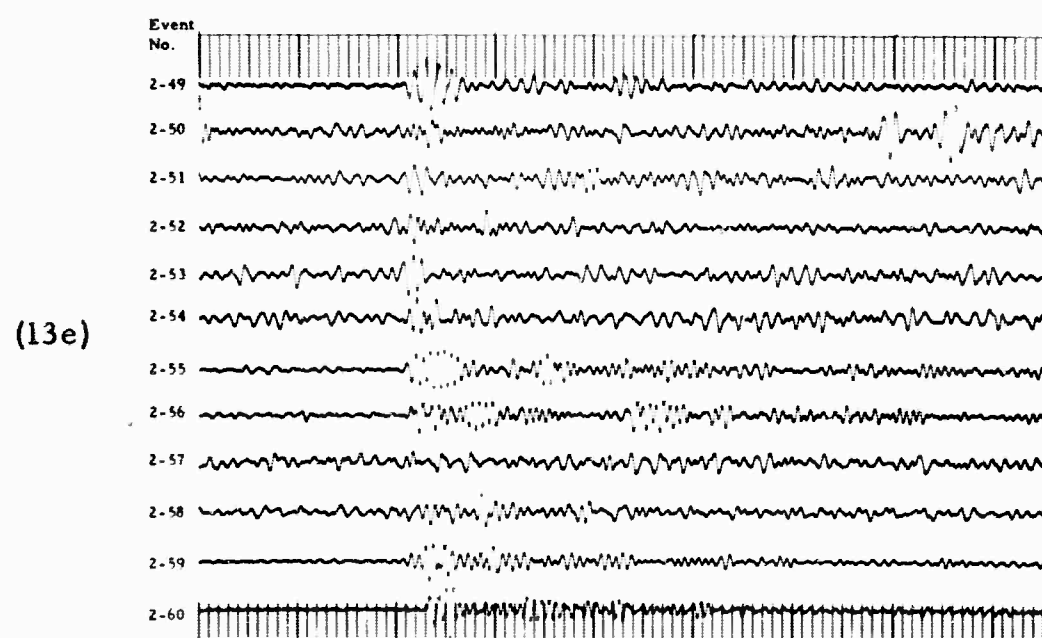
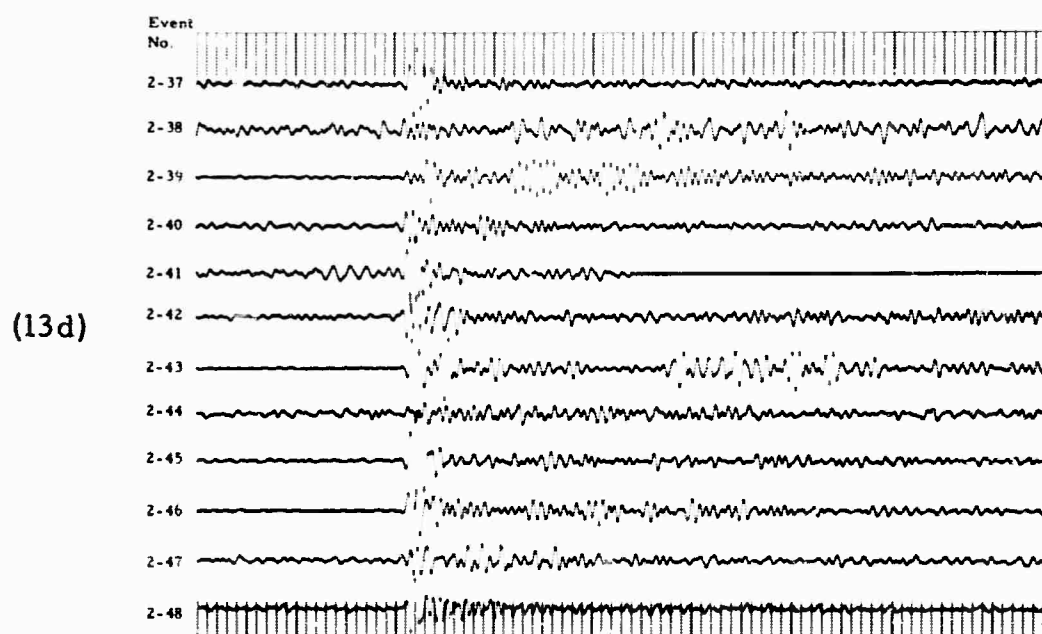
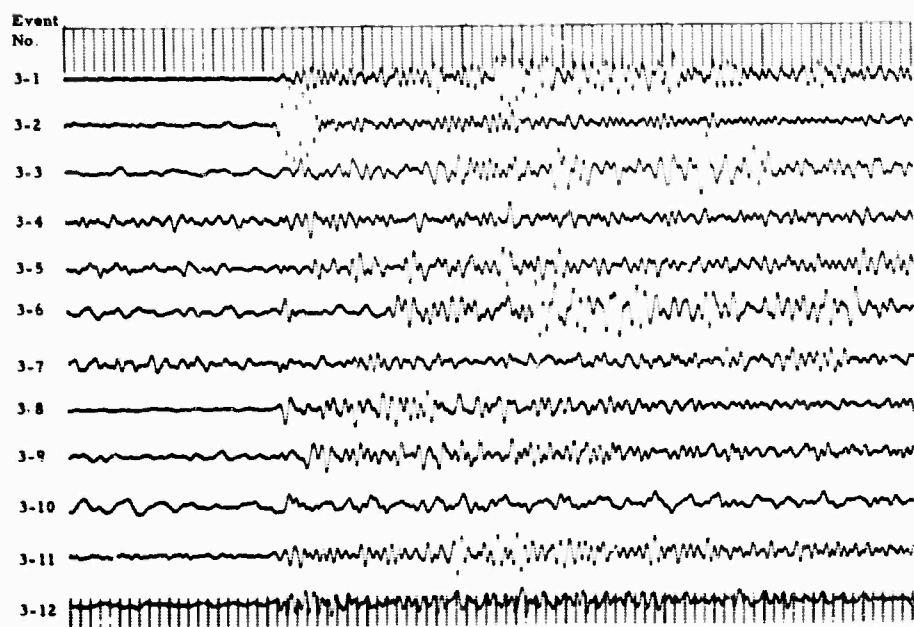
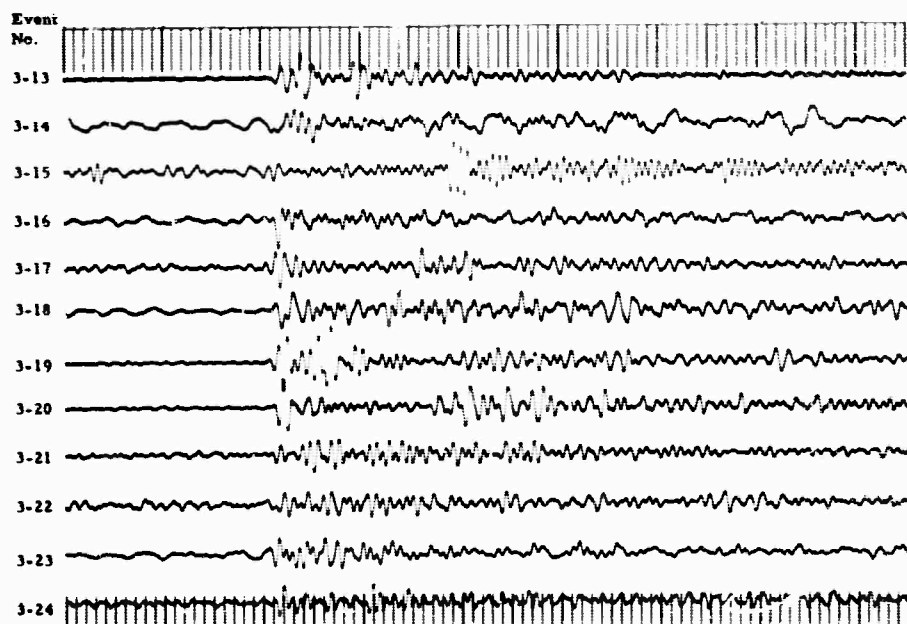


Figure II-13. Ensemble II Teleseism Records with Differential Magnifications Applied (II-13a through 13e)

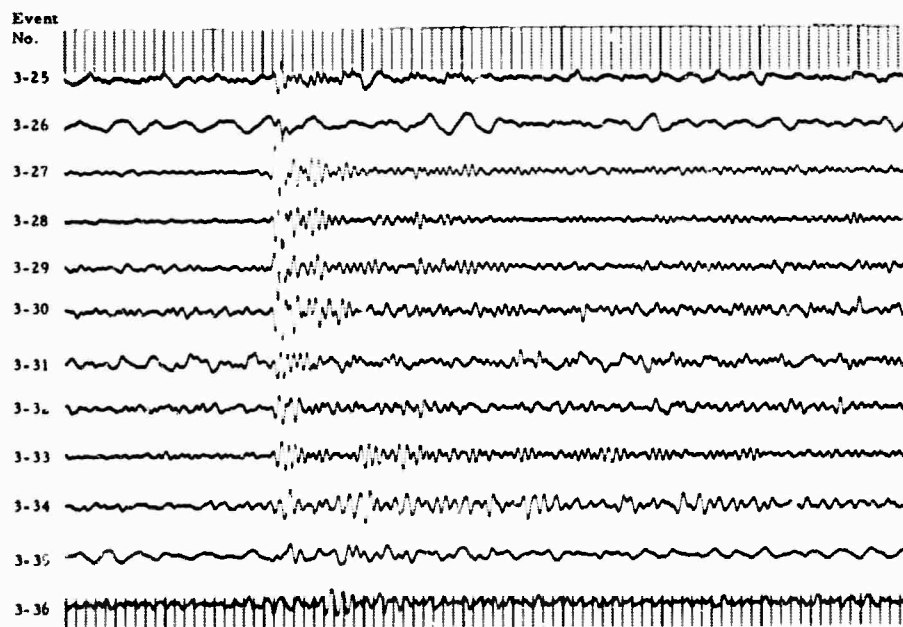
(14a)



(14b)



(14c)



Timing Lines = 1.0 Sec

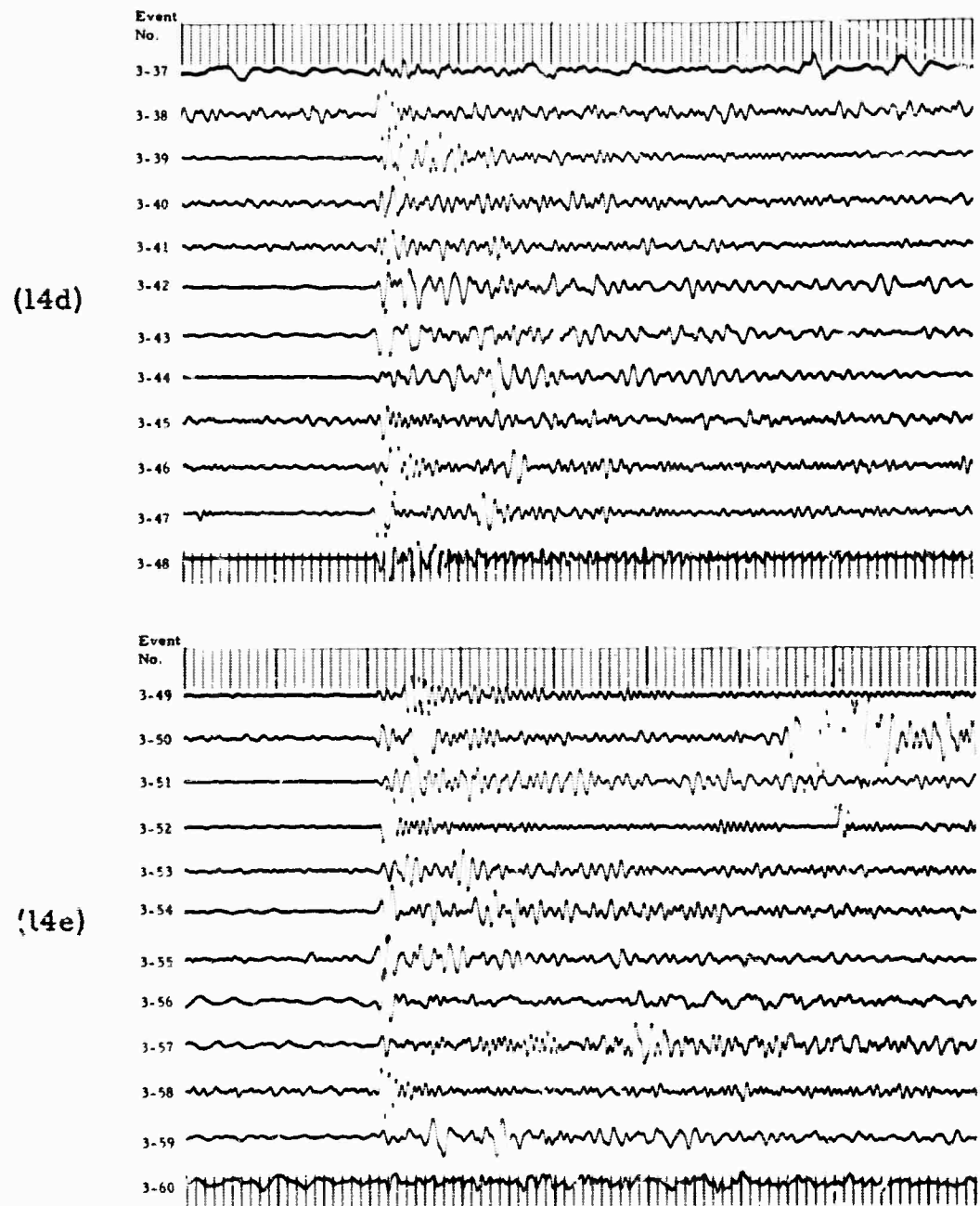
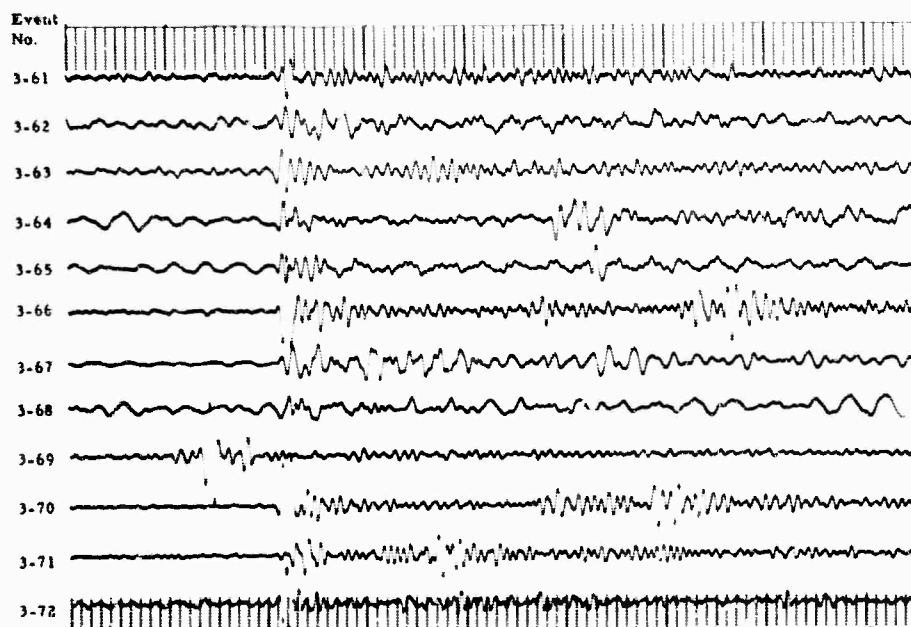
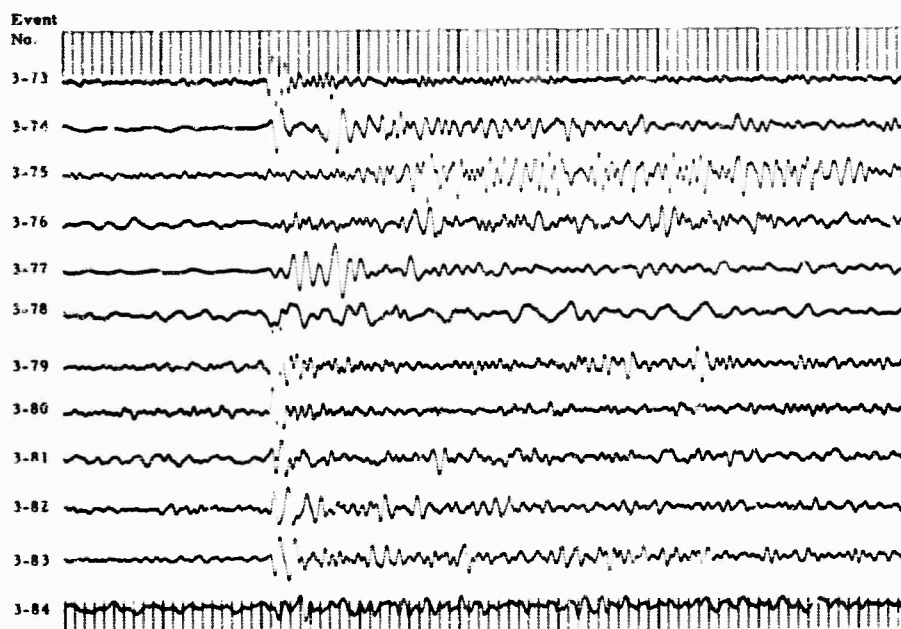


Figure II-14. Ensemble III Teleseism Records with Differential Magnifications Applied (II-14a through II-14e)

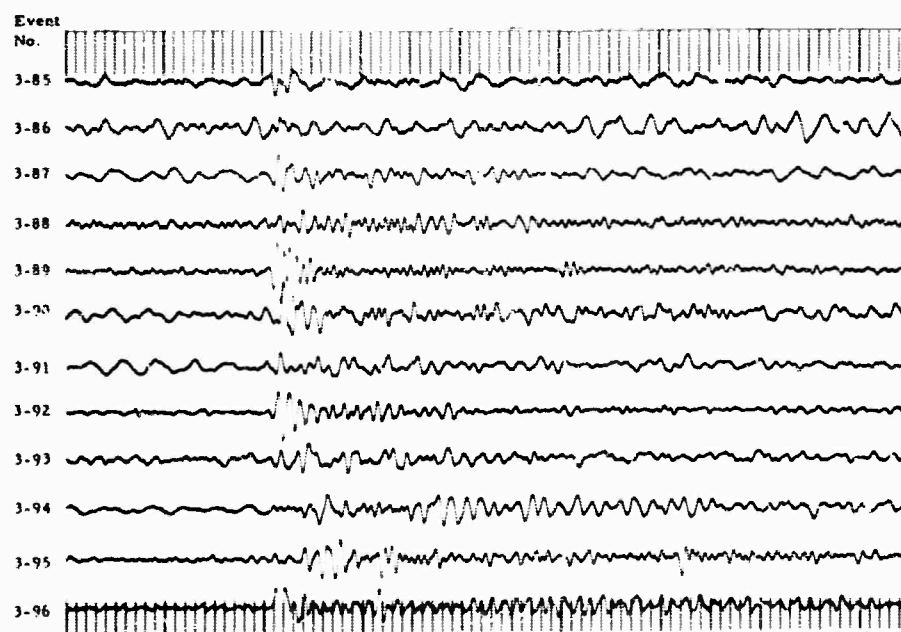
(14f)



(14g)



(14h)



Timing Lines = 1.0 Sec

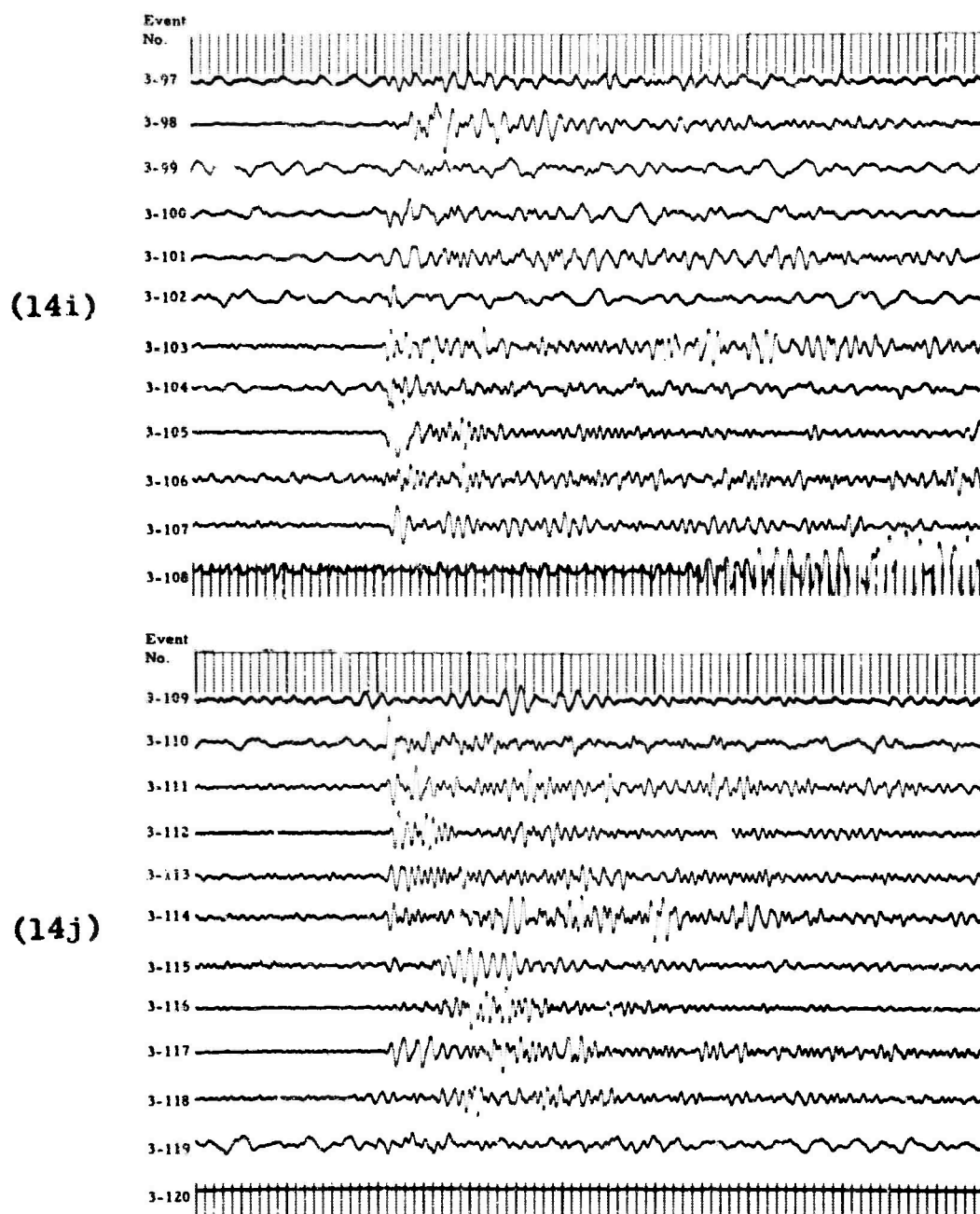
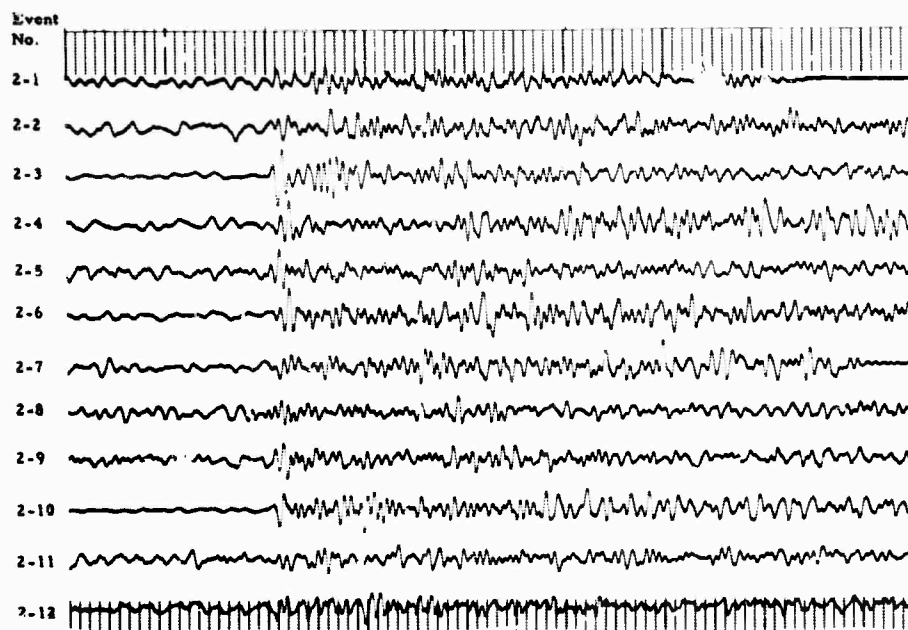
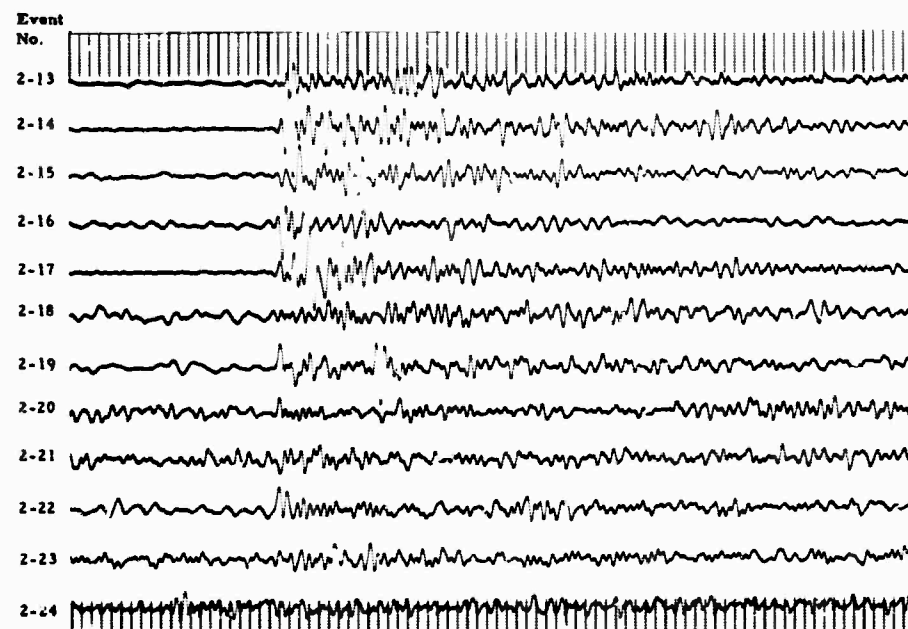


Figure II-14. Ensemble III Teleseism Records with Differential Magnifications Applied (II-14f through II-14j)

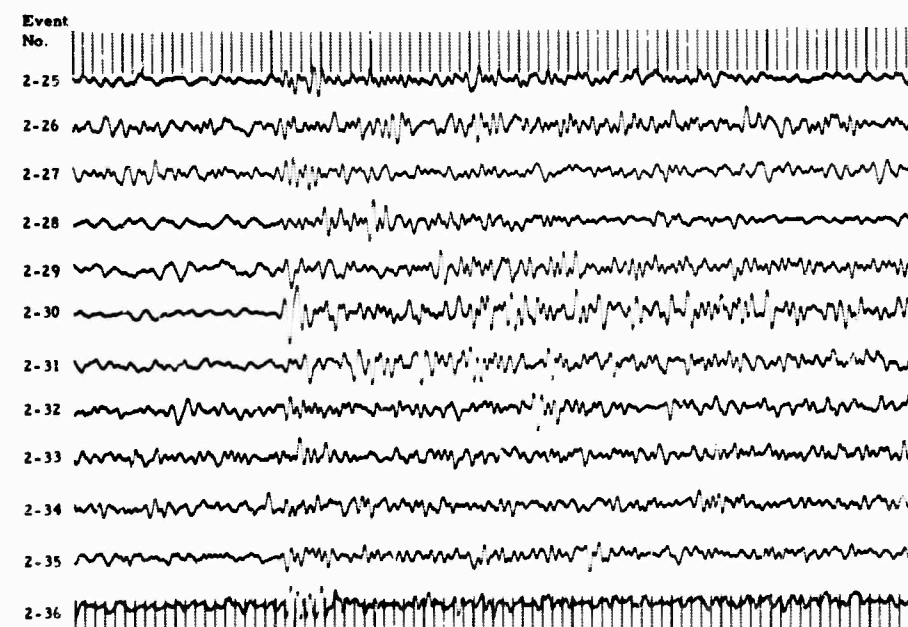
(15a)



(15b)



(15c)



Timing Lines = 1.0 Sec

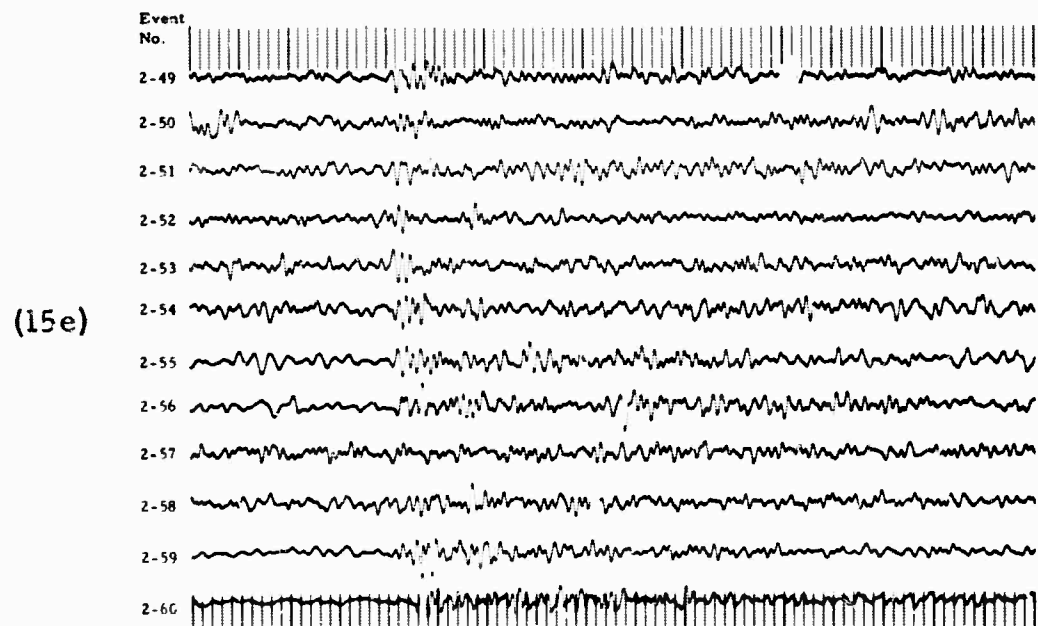
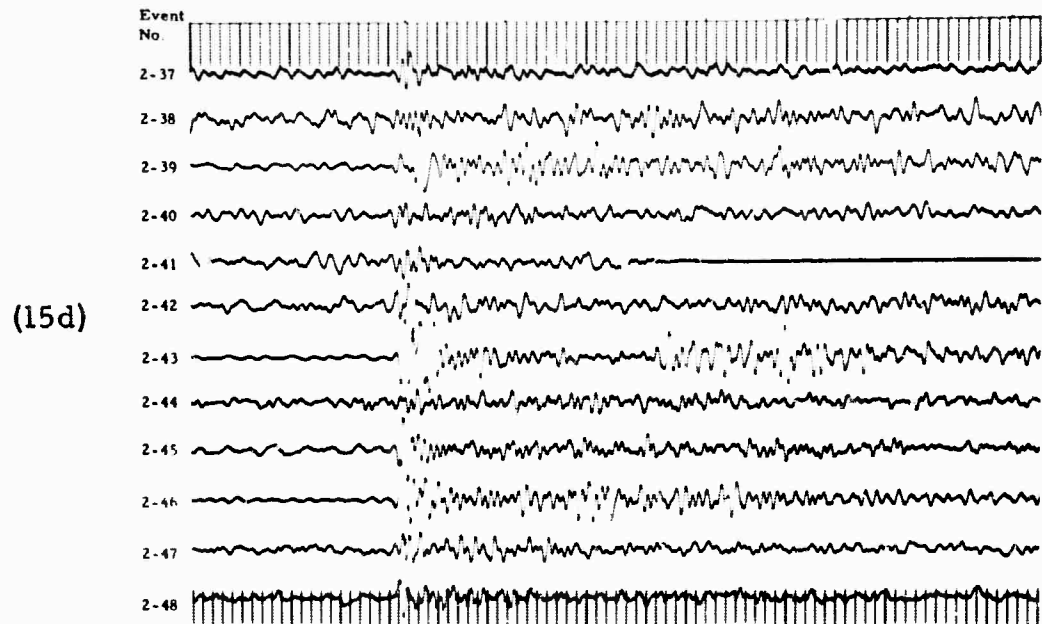
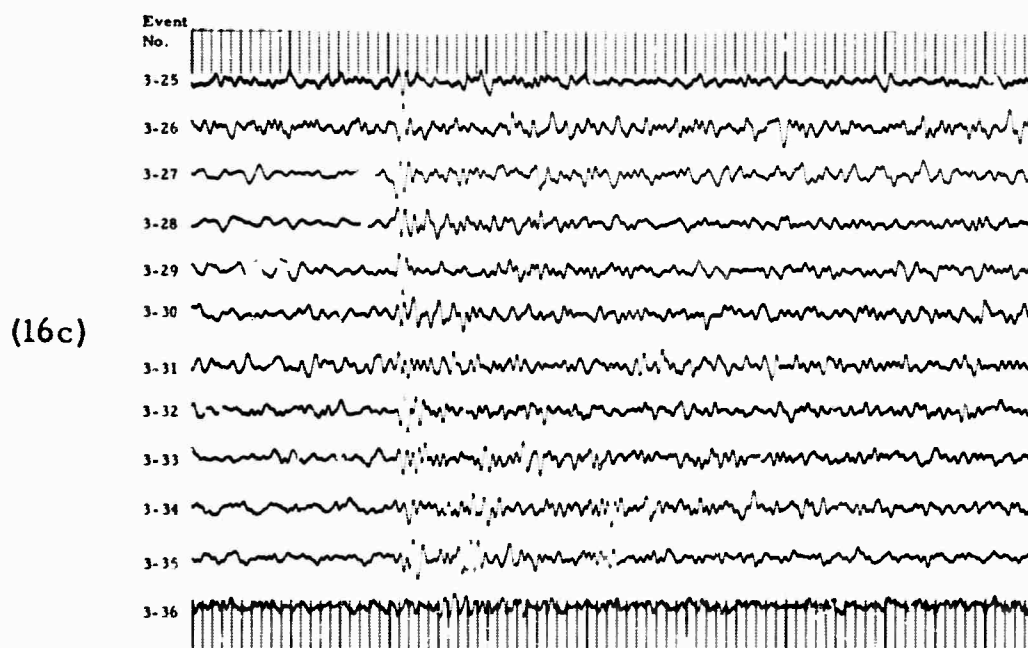
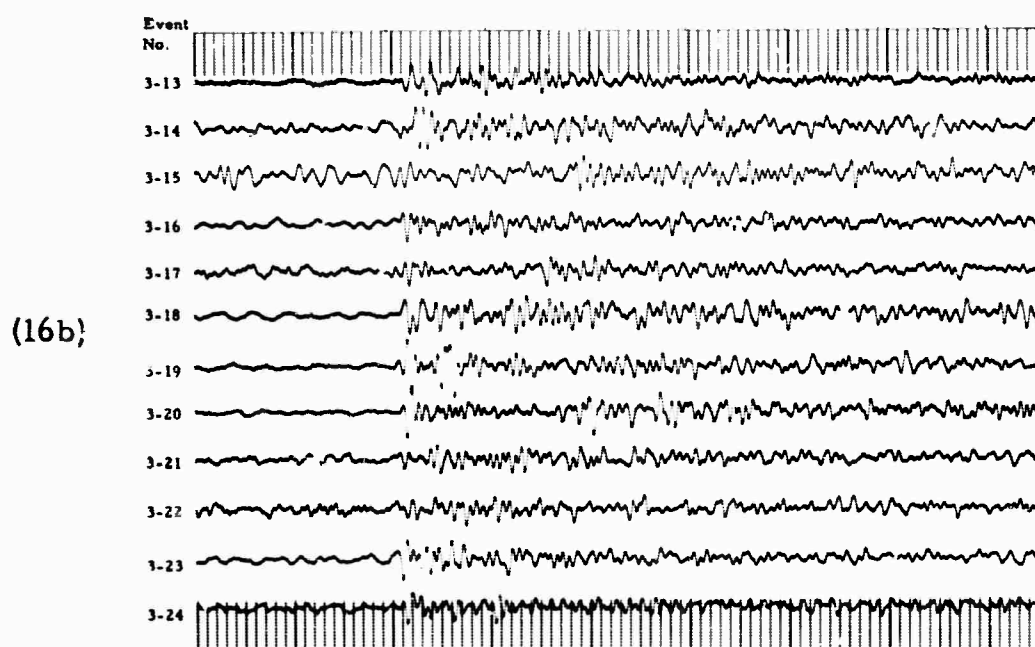
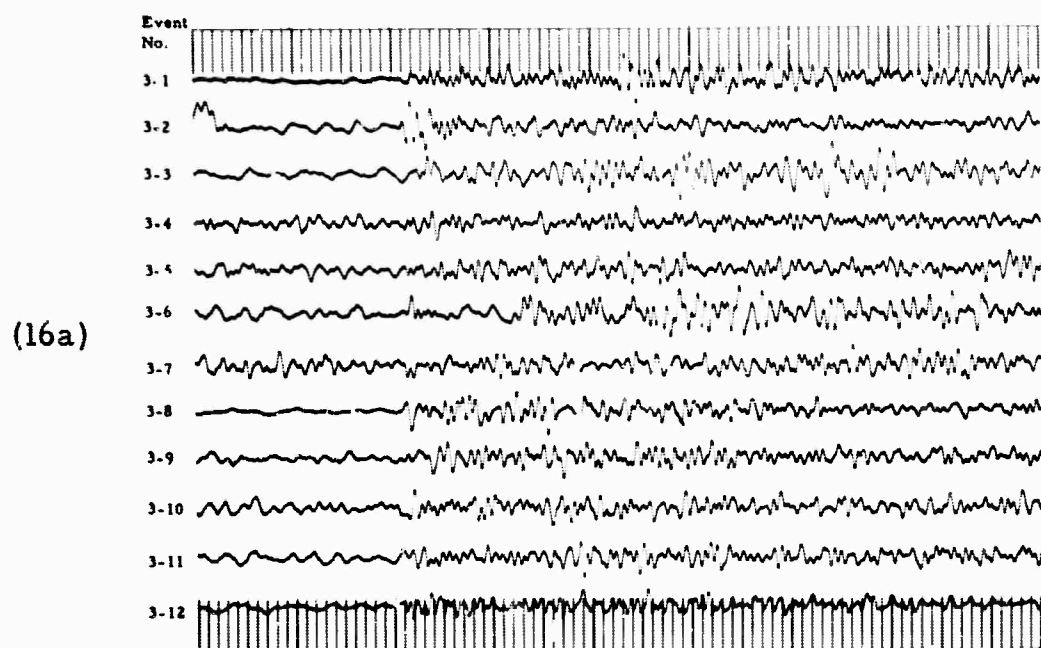


Figure II-15. Ensemble II Individually Deconvolved Events
(II-15a through 15e)



Timing Lines = 1.0 Sec

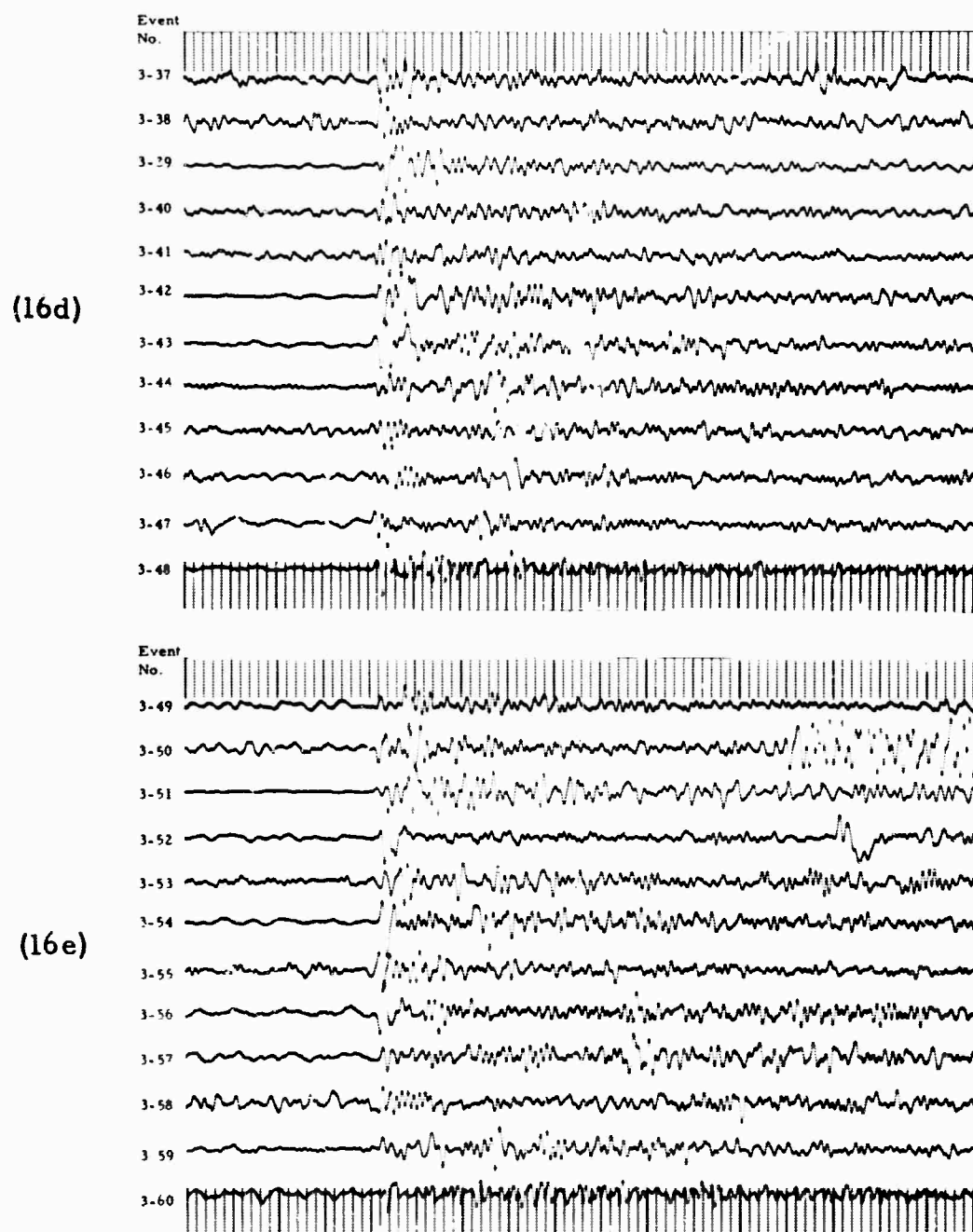
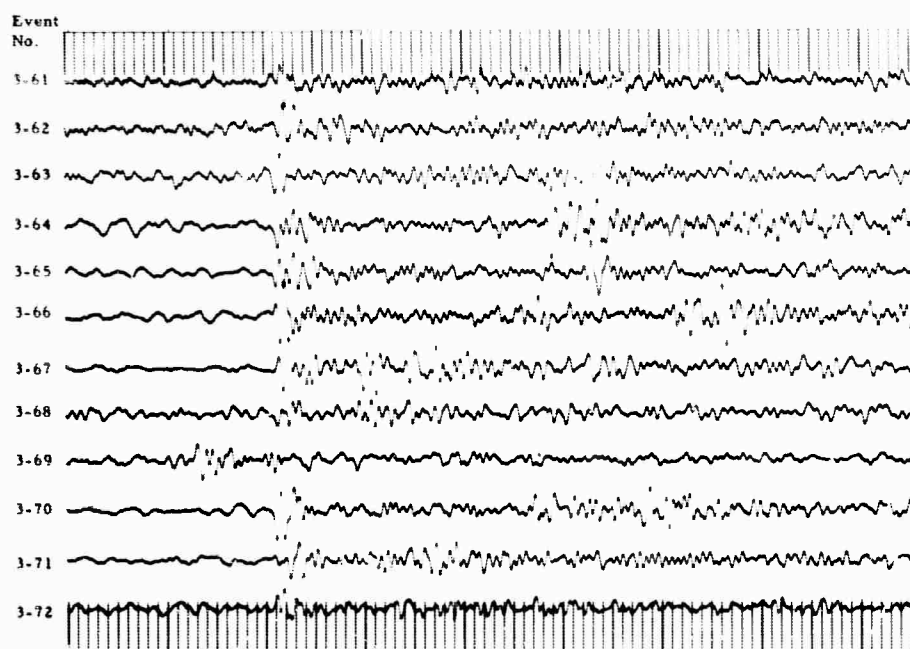


Figure II-16. Ensemble III Individually Deconvolved Events
(II-16a through 16e)

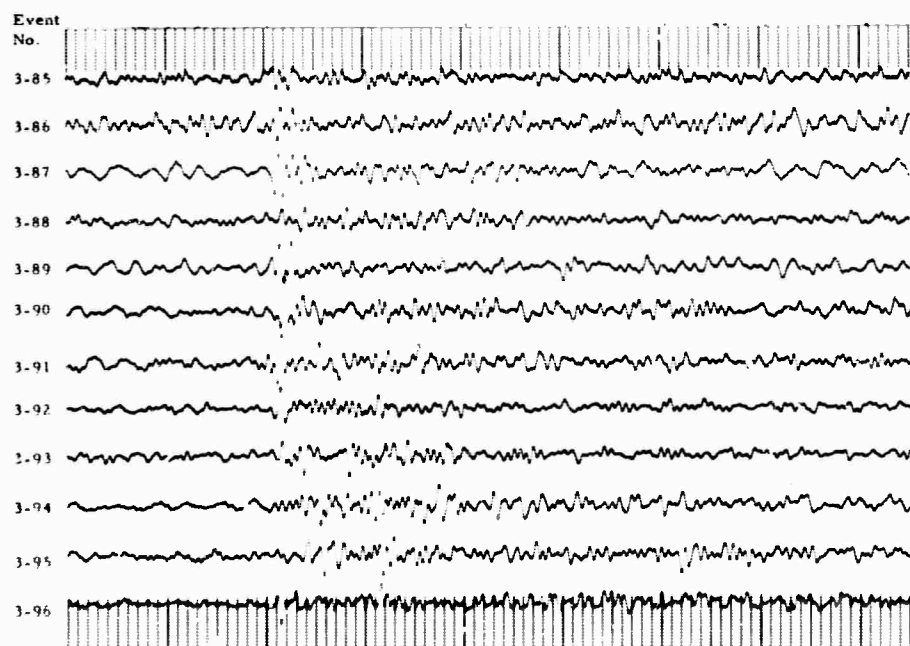
(16f)



(16g)



(16h)



Timing Lines = 1.0 Sec

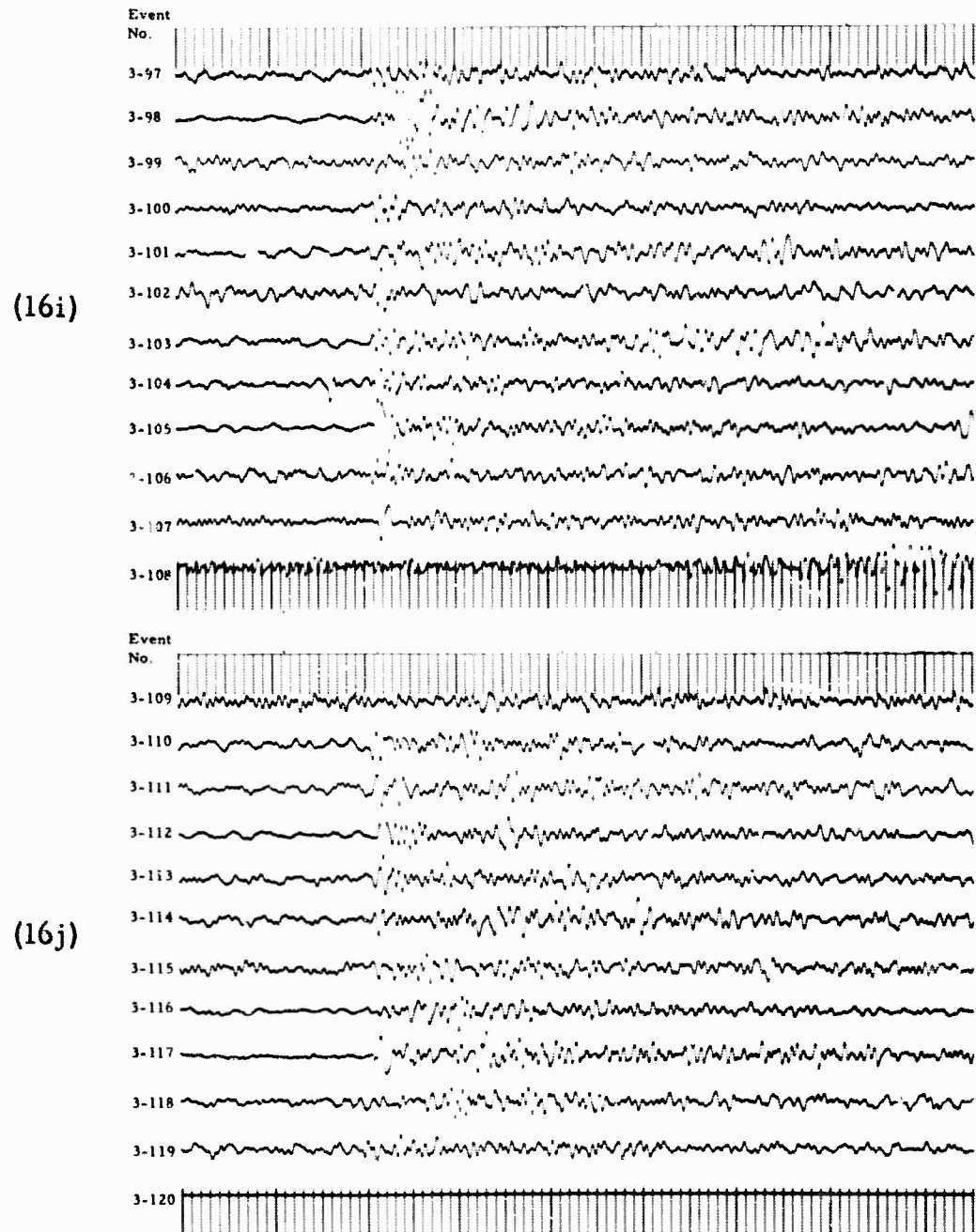


Figure II-16. Ensemble III Individually Deconvolved Events
(II-16f through II-16j)

It is clear that processor IP-8 permitted a large fraction of the surface-wave noise to pass into the output. The level of the noise is found to vary over a range of more than 10 db from trace to trace. The high noise power observed on some records suggests microseismic storms of intermittent occurrence. By contrast, the noise observed on the Ensemble II records is remarkably time-stationary. It is hypothesized that, because MIP-4 and the low-cut filters were so much more efficient at rejecting surface-wave noise, the noise which was passed was composed mainly of P-waves and the intensity of this background of P-wave noise did not fluctuate much. These results imply that a detector employing decision-making equipment should be able to operate effectively on the output of an array processor such as MIP-4 which is capable of rejecting surface-wave noise efficiently.

In Figures II-15 and II-16, it can be seen that individual-event deconvolution has succeeded somewhat in contracting the waveforms of the P-events. In many cases, the direction of first motion is easier to determine since more energy has been concentrated in the first half-cycle. However, many signal waveforms remain extremely complex. It would be expected that deconvolution should also contract the waveforms of the later arrivals, but these are no more apparent on the deconvolved records than the raw data. Presumably, this failure is caused by differences between the waveforms of P and the later-arriving phases.

It is planned to compute autocorrelations for each of the events in Ensembles II and III and obtain average correlations for various subgroups. The effect of source location on the autocorrelations will be examined with the intention of gaining information about propagation mechanisms. Ensemble average and, if it is deemed worthwhile, subgroup average autocorrelations will be used to design deconvolution filters for a detailed analysis of Ensembles II and III. The major data processing steps are summarized in the block diagram in Figure II-17.

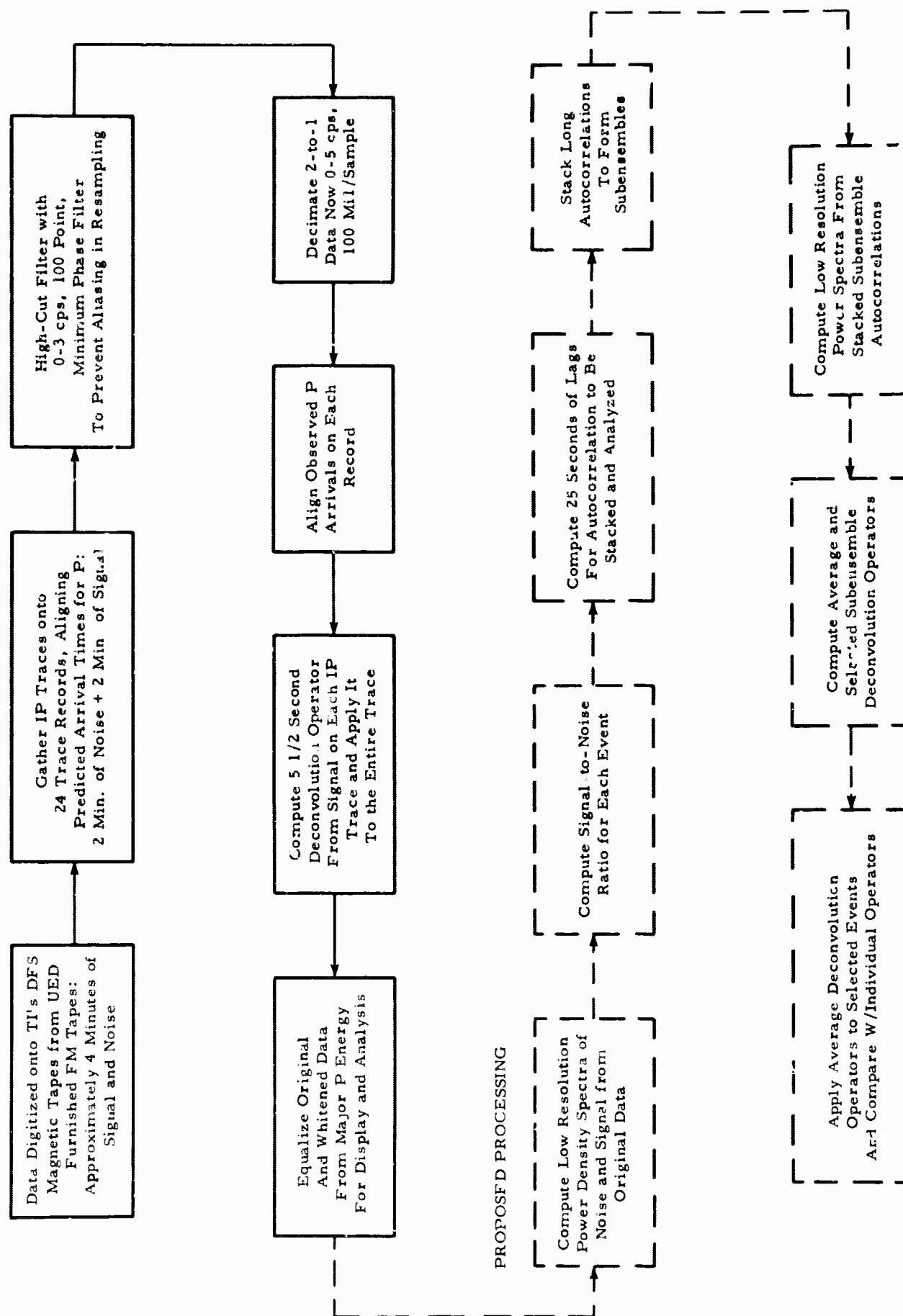


Figure II-17. Processing Sequence of Ensembles II and III Data

BLANK PAGE

SECTION III

PROBABILISTIC PROCESSING

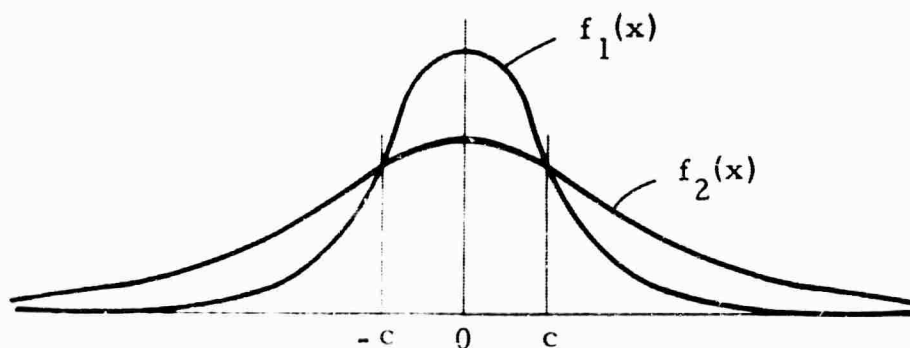
A. INTRODUCTION

Probabilistic processing is a method of processing the output data of an array of seismometers with the aim of detecting earthquake or underground nuclear blast signals in the presence of ambient seismic noise. This method is based on the assumption that the array output is Gaussian with mean zero and known covariance matrix Ω_1 or Ω_2 , depending on the absence or presence of signal.

The decision regarding presence or absence of the signal is therefore made equivalent to testing the hypothesis that the observed data are from a Gaussian population with covariance matrix Ω_1 with the simple alternative hypothesis that the covariance matrix is Ω_2 .

The univariate situation is: a single value x is observed from a Gaussian population with mean zero; it must be decided whether x is more representative of a Gaussian population with variance σ_1^2 or σ_2^2 . The two density functions are

$$\begin{aligned} f_1(x) &= \frac{1}{\sqrt{2\pi} \sigma_1} \exp(-x^2/2\sigma_1^2) \\ f_2(x) &= \frac{1}{\sqrt{2\pi} \sigma_2} \exp(-x^2/2\sigma_2^2) \end{aligned} \tag{1}$$



where $\sigma_2^2 > \sigma_1^2$. If the original likelihood of the two alternatives were equal, it is more likely that x is from $f_1(x)$ if $|x| < c$ and more likely that x is from $f_2(x)$ if $|x| > c$. So the method of processing in this case reduces to squaring the observation x and comparing the result with a fixed constant.

If a vector x of dimension k is observed, the two density functions become

$$\begin{aligned} f_1(x) &= (2\pi)^{-k/2} |\Omega_1|^{-1/2} \exp(-x^T \Omega_1^{-1} x/2) \\ f_2(x) &= (2\pi)^{-k/2} |\Omega_2|^{-1/2} \exp(-x^T \Omega_2^{-1} x/2). \end{aligned} \quad (2)$$

These equations can be compared to find the set of vectors x for which $f_1(x) > f_2(x)$. Thus if

$$x^T(\Omega_1^{-1} - \Omega_2^{-1})x \geq c = \ln(|\Omega_2|/|\Omega_1|) \quad (3)$$

then $f_2(x) \geq f_1(x)$.

Therefore, the test statistic $x^T(\Omega_1^{-1} - \Omega_2^{-1})x$ must be computed from the data. The detailed calculation of the test statistic in terms of array data is given in the following section.

A more rigorous development of the test statistic based on Bayes theorem has been presented in a preceding special report.¹⁰

B. CALCULATION OF THE TEST STATISTIC

1. Notation

The data from an array of seismometers can be represented by the matrix X where the rows correspond to the seismometers and the columns to the time sampled data

$$X = \begin{bmatrix} x_{11} & x_{12} & \cdot & \cdot & \cdot & x_{1N} \\ x_{21} & x_{22} & \cdot & \cdot & \cdot & x_{2N} \\ \cdot & & & & & \\ \cdot & & & & & \\ \cdot & & & & & \\ x_{M1} & x_{M2} & \cdot & \cdot & \cdot & x_{MN} \end{bmatrix}$$

Thus, x_{ij} is the observation from seismometer i at time j .

The elements of matrix X can be "strung out" into a single vector y in the following manner:

$$y^T = (x_1^T, x_2^T, \dots, x_N^T)$$

where $x_j^T = (x_{1j}, x_{2j}, \dots, x_{Mj})$. This vector y is now the vector of observations from which the test statistic (Equation 3) must be computed. Since the mean of y is assumed to be 0, the covariance matrix of y is just

$$\Omega_y = \overline{yy^T}$$

and the dimension of Ω_y is MN by MN since there are MN elements in the vector y . Assuming time stationarity, we can let

$$r_{|i-j|+1} = \overline{x_i x_j^T} \text{ and write}$$

$$\overline{yy^T} = \begin{bmatrix} x_1^T x_1 & x_1^T x_2 & x_1^T x_3 & \dots & x_1^T x_N \\ x_2^T x_1 & x_2^T x_2 & x_2^T x_3 & \dots & x_2^T x_N \\ \vdots & \vdots & \vdots & \ddots & \vdots \\ x_N^T x_1 & \dots & \dots & \dots & x_N^T x_N \end{bmatrix} \quad (4)$$

so that

$$\Omega_y = \begin{bmatrix} r_1 & r_2 & \dots & r_N \\ r_2^T & r_1 & \dots & r_{N-1} \\ \vdots & \vdots & \ddots & \vdots \\ r_N^T & \dots & \dots & r_1 \end{bmatrix} = R^N$$

where each submatrix r_i is an M by M matrix.

2. Inverse of R^N

The inverse of R^N can be obtained from the solutions of the two systems of equations

$$R^N \begin{pmatrix} I \\ \Gamma_N^N \\ \vdots \\ \Gamma_2^N \\ \vdots \\ \Gamma_N^N \end{pmatrix} = \begin{pmatrix} P_N \\ 0 \\ \vdots \\ 0 \end{pmatrix} \quad \text{and} \quad R^N \begin{pmatrix} \Gamma_N^{N'} \\ \vdots \\ \Gamma_2^{N'} \\ \vdots \\ I \end{pmatrix} = \begin{pmatrix} 0 \\ \vdots \\ 0 \\ P_N' \end{pmatrix} \quad (5)$$

Partition R^N in the fashion

$$R^N = \left[\begin{array}{c|c} R^{N-1} & B \\ \hline B^T & D \end{array} \right]$$

then

$$(R^N)^{-1} = \left[\begin{array}{c|c} A & \cdot \\ \hline \cdot & \cdot \end{array} \right] + \left[\begin{array}{c|c} AB\delta_1^{-1}B^TA & -AB\delta_1^{-1} \\ \hline -\delta_1^{-1}B^TA & \delta_1^{-1} \end{array} \right]$$

where the dot indicates a matrix of zeros and

$$A = (R^{N-1})^{-1}$$

$$\delta_1 = D - B^TAB$$

From Equation (5), the last M columns of $(R^N)^{-1}$ are

$$\begin{bmatrix} \Gamma_N^{N'}(P_N')^{-1} \\ \Gamma_{N-1}^{N'}(P_N')^{-1} \\ \vdots \\ \Gamma_2^{N'}(P_N')^{-1} \\ (P_N')^{-1} \end{bmatrix}$$

so that

$$\begin{bmatrix} \Gamma_N^{N'} (P_N')^{-1} \\ \vdots \\ \Gamma_2^{N'} (P_N')^{-1} \\ (P_N')^{-1} \end{bmatrix} = \begin{bmatrix} -AB\delta_1^{-1} \\ \delta_1^{-1} \end{bmatrix}$$

Since $(P_N')^{-1} = \delta_1^{-1}$ and $\begin{Bmatrix} \Gamma_N^{N'} \\ \vdots \\ \Gamma_2^{N'} \end{Bmatrix} = -AB$, it follows that

$$AB\delta_1^{-1}B^T A = \begin{bmatrix} \Gamma_N^{N'} \\ \vdots \\ \Gamma_2^{N'} \end{bmatrix} (P_N')^{-1} \begin{bmatrix} \Gamma_N^{N'} \\ \vdots \\ \Gamma_2^{N'} \end{bmatrix}^T \quad (6)$$

Now, partition

$$R^N = \begin{bmatrix} D_1 & -C^T \\ C & R^{N-1} \end{bmatrix}$$

to get

$$(R^N)^{-1} = \begin{bmatrix} \cdot & \cdot \\ \cdot & A \end{bmatrix} + \begin{bmatrix} \delta_2^{-1} & -\delta_2^{-1}C^T A \\ -AC\delta_2^{-1} & AC\delta_2^{-1}C^T A \end{bmatrix}$$

where $\delta_2^{-1} = D - C^T A C$. As before, it follows that

$$AC\delta_2^{-1}C^T A = \begin{bmatrix} \Gamma_2^N \\ \vdots \\ \Gamma_N^N \end{bmatrix} (P_N)^{-1} \begin{bmatrix} \Gamma_2^N \\ \vdots \\ \Gamma_N^N \end{bmatrix}^T \quad (7)$$

Denote by s_{ij}^N the ij^{th} M by M submatrix of the inverse of R^N . From Equations (6) and (7), the following equations can be written:

$$s_{ij}^N = s_{ij}^{N-1} + \Gamma_{N-i+1}^{N'} (P_N')^{-1} \Gamma_{N-j+1}^{N'} \quad (8)$$

$$i, j = 1, \dots, N-1$$

$$s_{i+1, j+1}^N = s_{ij}^{N-1} + \Gamma_{i+1}^N (P_N)^{-1} \Gamma_{j+1}^N \quad (9)$$

$$i, j = 1, \dots, N-1$$

Now, by subtracting Equations (8) from (9), the basic iterative formula of Equation (10) is obtained

$$s_{i+1, j+1}^N = s_{ij}^N + \Gamma_{i+1}^N (P_N)^{-1} \Gamma_{j+1}^N - \Gamma_{N-i+1}^{N'} (P_N')^{-1} \Gamma_{N-j+1}^{N'} \quad (10)$$

and the entire inverse matrix can be generated starting with the first M columns of the inverse which is the first column of the s_{ij}^N 's available from Equation (5).

3. The Quadratic Processor

Suppose the matrix $X = (x_1, \dots, x_T)$ is observed.

Then the test statistic

$$P(y_i) = y_i C y_i^T$$

can be evaluated for $i = 1, \dots, T-N+1$ where

$$y_i^T = (x_i^T, \dots, x_{N+i-1}^T)$$

$$C = \Omega_1^{-1} - \Omega_2^{-1}$$

A program to perform this calculation is being written. In addition, an integrated, squared multichannel Wiener filter output will be available as an option in the quadratic processor program to give a comparison between the two detection methods.

4. Multichannel Time Series Data Generation

It is desired to generate multichannel data $x_i^T = (x_{1i}, x_{2i}, \dots, x_{Ni})$ with the covariance matrix R^N . Let Γ_i^N $i = 2, \dots, N$ and P_N satisfy the system of Equations (5). Suppose y_i^T is a supply of vectors satisfying

$$\bar{y}_i = 0$$

$$\overline{y_i y_i^T} = I$$

Then, x_i will be generated by the following system of equations:

$$\begin{aligned} x_1 &= \epsilon_1 \\ x_2 &= \Gamma_2^N x_1 + \epsilon_2 \\ x_3 &= \Gamma_2^N x_2 + \Gamma_3^N x_1 + \epsilon_3 \\ &\vdots \\ x_N &= \Gamma_2^N x_{N-1} + \dots + \Gamma_N^N x_1 + \epsilon_N \\ &\vdots \\ x_i &= \Gamma_2^N x_{i-1} + \dots + \Gamma_N^N x_{i-N+1} + \epsilon_i \end{aligned} \tag{11}$$

The method of determining the ϵ_i is

$$\epsilon_i = Hy_i$$

where $HH^T = P_N$. The reason for this is that ϵ_i must satisfy

$$\overline{\epsilon_i \epsilon_i^T} = P_N$$

Determination of an H satisfying the above is accomplished by requiring that H be lower triangular.

5. Eigenvalues (Single Channel)

In the case of a single channel, the test statistic is

$$P(x) = x^T (\Omega_1^{-1} - \Omega_2^{-1}) x \quad (12)$$

where Ω_1 and Ω_2 are Toeplitz matrices. Let the observation vector x be transformed to z by the N by N nonsingular transformation $x = Sz$ such that

$$P(x) = P(z) = z^T S^T (\Omega_1^{-1} - \Omega_2^{-1}) Sz = z^T Dz \quad (13)$$

where D is diagonal. Then, the computation of the quadratic form is reduced to filtering operations followed by a summation of the squared outputs. An especially important transformation, diagonalizing both Ω_1^{-1} , Ω_2^{-1}

simultaneously, exists since $A = \Omega_1^{-1}$ and $B = \Omega_2^{-1}$ are positive definite.² This transformation is found by solving the following generalized eigenvalue problem.

The solution for λ 's satisfying

$$|A - \lambda B| = 0 \quad (14)$$

is called the generalized eigenvalue problem. The corresponding set of vectors x such that

$$Ax = \lambda Bx \quad (15)$$

are the generalized eigenvectors. The matrix M whose columns consist of these eigenvectors normalized so that $x^T Bx = 1$ then can be shown to satisfy

$$\begin{aligned} M^T A M &= \Lambda \\ M^T B M &= I \end{aligned} \quad (16)$$

where Λ is a diagonal matrix with elements λ .

Thus, if the S of Equation (13) is taken to be M , the diagonal matrix D satisfies

$$D = I - \Lambda$$

An iterative procedure for λ and M now will be given. Let

$$f(\lambda) = |A - \lambda B| \quad (17)$$

The first approximation to λ_1 , the smallest eigenvalue, is

$$\lambda_{11} = -f(0)/f'(0) \quad (18)$$

and the succeeding iterative values are found by the chord method. Thus,

$$\lambda_{1n} = \frac{f(\lambda_{1, n-1}) \lambda_{1, n-2} - f(\lambda_{1, n-2}) \lambda_{1, n-1}}{f(\lambda_{1, n-1}) - f(\lambda_{1, n-2})} \quad (19)$$

until

$$\lambda_{1, n} - \lambda_{1, n-1} < \lambda_{1, n} \epsilon ; \epsilon \sim 10^{-6} \quad (20)$$

is satisfied. The eigenvector corresponding to λ_1 is computed.

It is desired to calculate

$$f(\lambda)/(\lambda - \lambda_1)|_{\lambda=\lambda_1} \quad (21)$$

in order to continue the iterative process. Since $f(\lambda)$ is assumed to have a single root at $\lambda = \lambda_1$, it suffices to compute

$$f'(\lambda)|_{\lambda=\lambda_1} = \sum_{ij} B_{ij} C_{ij} \quad (22)$$

where C_{ij} is the matrix of cofactors of the elements of $A - \lambda_1 B$. The relation (Equation 22) is shown at the end of this section.

Now,

$$(A_{ij} - \lambda_1 B_{ij}) (C_{ij}) = 0 \quad (23)$$

since λ_1 is a root of $f(\lambda)$, and it follows that each column (row) of

(C_{ij}) is proportional to the unique eigenvector corresponding to λ_1 .

Thus, the rank of (C_{ij}) is one, and it follows that the matrix (C_{ij}) can be written in the form

$$(C_{ij}) = \beta x x^T \quad (24)$$

where x is the eigenvector corresponding to λ_1 . Thus,

$$f'(\lambda)|_{\lambda=\lambda_1} = -\sum B_{ij} C_{ij} = -\beta x^T B x = -\beta \quad (25)$$

If the eigenvector x has already been computed, β can be determined from

$$r_{11} = \beta x_1^2 \quad (26)$$

unless $C_{11} = 0$. At least one element, say j , of $C_{1j} \neq 0$, for, otherwise, $x \equiv 0$, so that

$$C_{1j} = \beta x_1 x_j \quad (27)$$

would determine β in general.

The chord method again is used to find the smallest θ of $f(\lambda)/(\lambda - \lambda_1)$, the first approximation of λ_2 being $\lambda_1 + k-2$ and the second approximation being λ_1 . The entire set of solutions λ and eigenvectors x are solved in this same iterative manner.

The relation (Equation 22) will now be shown. Write out $f(\lambda)$ in the form

$$f(\lambda) = \begin{vmatrix} A_{11} - \lambda B_{11} & A_{12} - \lambda B_{12} & \dots & A_{1N} - \lambda B_{1N} \\ A_{21} - \lambda B_{21} & \dots & \dots & A_{2N} - \lambda B_{2N} \\ \vdots & & & \\ \vdots & & & \\ A_{N1} - \lambda B_{N1} & \dots & \dots & A_{NN} - \lambda B_{NN} \end{vmatrix}$$

If the λ in the ij^{th} term is replaced by λ_{ij} where $\lambda_{ij} = \lambda$, then

$$f'(\lambda) = \sum_{ij} \frac{\partial f(\lambda_{11}, \dots, \lambda_{NN})}{\partial \lambda_{ij}}$$

Now,

$$\frac{\partial f(\lambda_{11}, \dots, \lambda_{NN})}{\partial \lambda_{ij}} = \frac{\partial}{\partial \lambda_{ij}} \sum_{k=1}^N (A_{ik} - \lambda_{ik} B_{ik}) r_{ik} = -B_{ij} C_{ij}$$

and Equation (22) follows.

C. PROGRESS AND FUTURE GOALS

Digital programs have been written and checked for computing the Γ and Γ' matrices and the quadratic test statistic. The program for the inverse matrix R^N has been written but not checked out. The data generation program has not been written.

It is expected that all the above programs will be completed by 30 May 1965 and then applied to real and generated data. The results will be presented in a preliminary report by 15 July 1965.

If these results indicate that the method of probabilistic processing will be useful in the problem of signal detection, a program to evaluate the eigenvalues and eigenvectors of the relevant covariance matrices will be written and the data used to reduce the evaluation of the test statistic to filtering and squaring over a gate. This more efficient method then would be applied to a set of real data and the results presented in the December 1965 report.

BLANK PAGE

SECTION IV

STUDY OF PARTIAL ARRAYS AT CPO

A. INTRODUCTION

Four multichannel filter systems for CPO were designed using the full array and three partial arrays. These systems were synthesized using measured noise correlations and an infinite velocity signal model. The MCF systems were evaluated on the computer to compare the ability of the partial arrays to suppress noise while preserving high-velocity signals.

Results show that the partial arrays are almost as effective as the full array near 1 cps. Below approximately 0.7 cps, seismometer gain inequality appears to be effecting the output of the systems. At higher frequencies, the K-space aliasing of some of the partial arrays prevents effective noise suppression.

To help evaluate the effects of seismometer gain inequalities, MCF systems will be designed using a signal model incorporating statistical gain fluctuation. This will be the subject of a separate report.

B. MULTICHANNEL FILTER SYSTEMS DESIGN

The filter systems were synthesized in the time domain by using measured noise correlations and an infinite-velocity signal model. In all cases, desired output was the noise-free signal at the center seismometer. All filters were 63 points long.

Noise data used to synthesize the systems consisted of the averaged sum of five noise samples (A, B, E, F, I) recorded at CPO in 1963. These noise samples had been prewhitened, processed through antialiasing filters and resampled to a sampling interval of 0.072 sec. This resulted in a Nyquist foldback frequency of slightly under 7 cps. In this report, all spectral analysis has been performed on the range of 0-7 cps. A detailed discussion of the preparation and evaluation of these noise samples has been published.⁸

Signal correlations used in the time-domain program for designing the filters were generated from the noise power spectrum of the center seismometer. The power spectrum of the noise used in the filter design program was scaled up by 4 to give the signal power spectrum. Since an infinite-velocity signal model was used, all signal auto- and crosscorrelations were the same.

No statistical gain fluctuation was included in the signal autocorrelations. Results indicate, however, that seismometer gain inequalities are affecting the MCF systems. This will be discussed in subsection D.

1. CPO IP 23

This system consists of five channels: the center seismometer; the sum of three seismometers on R2; the sum of three seismometers on R3; the sum of six seismometers on R4; and the sum of six seismometers on R5 (a total of 19 seismometers). See Figure IV-1. The channels which are sums of seismometer outputs are not averaged. Thus, the filter designed for a particular ring is the same as the individual filter to be applied to each seismometer in that ring.

2. CPO IP 24

In this system, the center seismometer, the sum of ring 3, the sum of ring 4, and the sum of ring 5 were used to simulate a 4-channel system (16 seismometers).

3. CPO IP 25

For this system, the center seismometer, the sum of ring 4 and the sum of ring 5 were used to simulate a 3-channel system (13 seismometers).

4. CPO IP 26

For this system, the center seismometer and the sum of ring 5 were used to simulate a 2-channel system (7 seismometers).

C. EVALUATION OF THE MULTICHANNEL FILTER SYSTEMS

To evaluate and compare the systems, two noise samples and an artificial infinite-velocity signal were computer-processed. The systems were analyzed for noise suppression, signal preservation, signal/noise improvement and wavenumber response.

The noise samples used in the evaluation were CPO noise samples A and I. They were recorded over a month apart and at different times of the day, but their frequency spectra, shown in Figure IV-2, are reasonably similar. These spectra and all other power spectra were obtained using a TI-developed spectral program. In all cases, the spectral plots were obtained using autocorrelations with time lags out to 49.

The scales of all power spectra in this report are related to $(\text{mm})^2/\text{cps}$ at 1 cps. In this report, these scales are correct at 1 cps. The prewhitening filter response at 1 cps has been taken into account. This has not been the case with previously published power spectra.

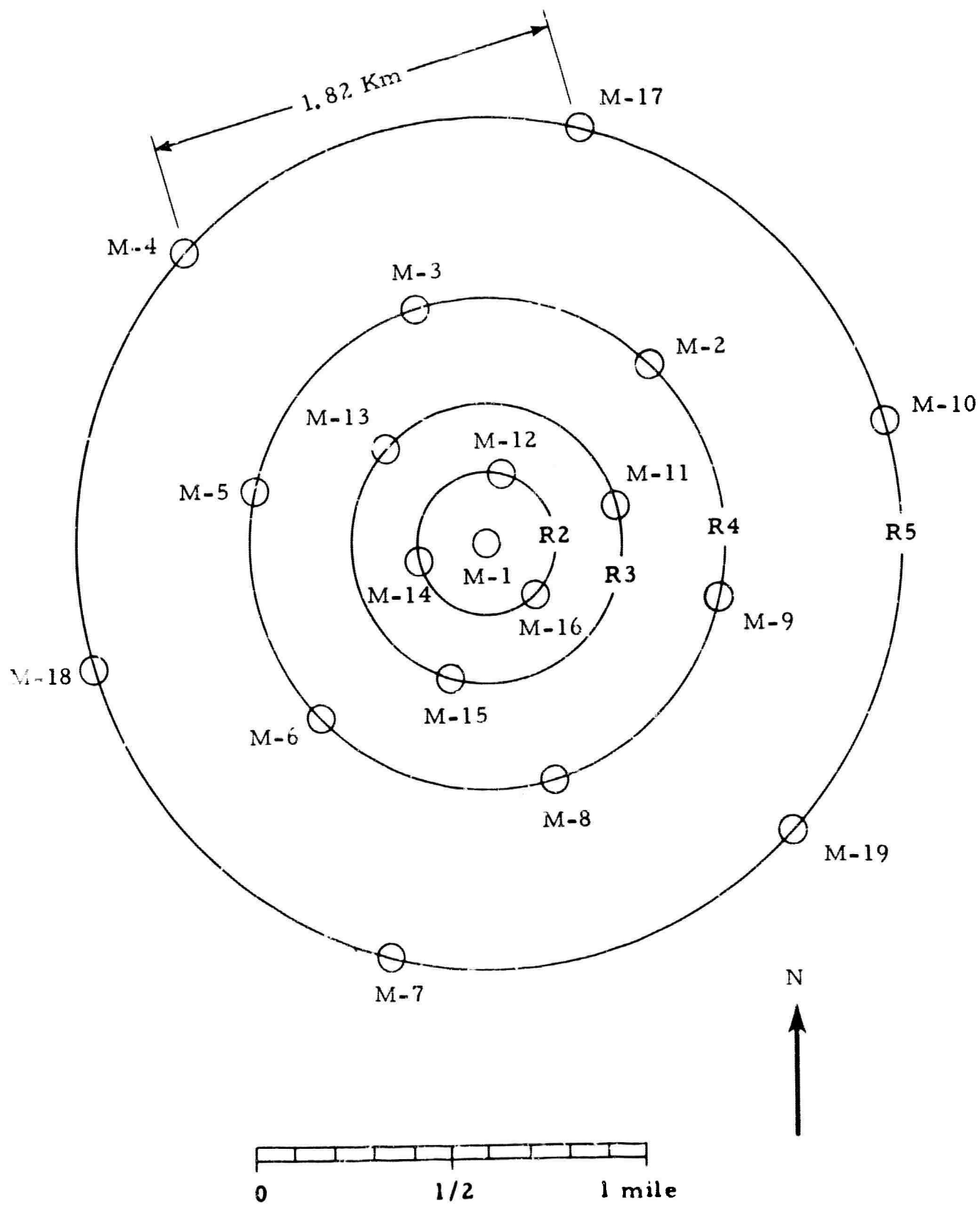


Figure IV-1. Layout of CPO Array

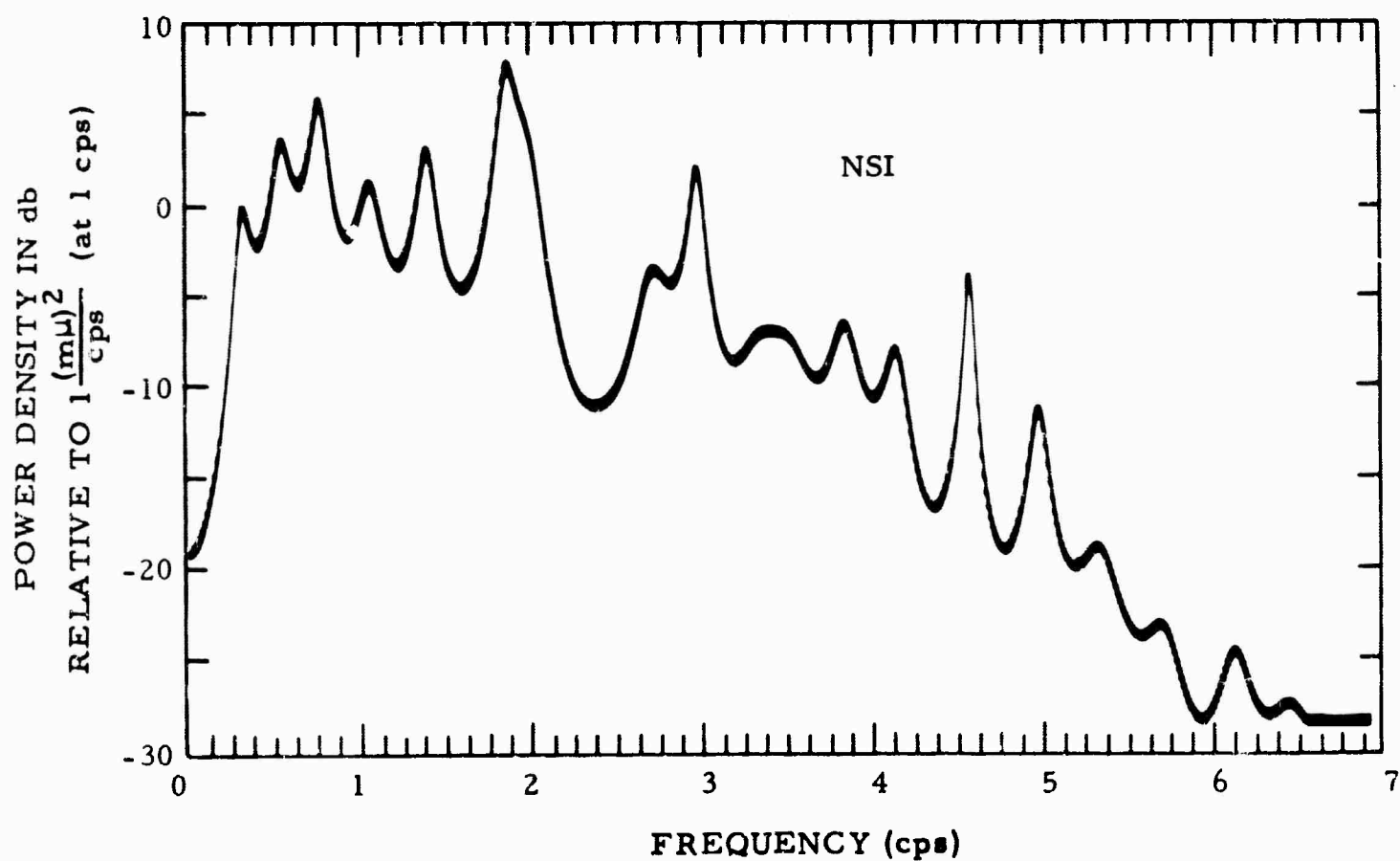
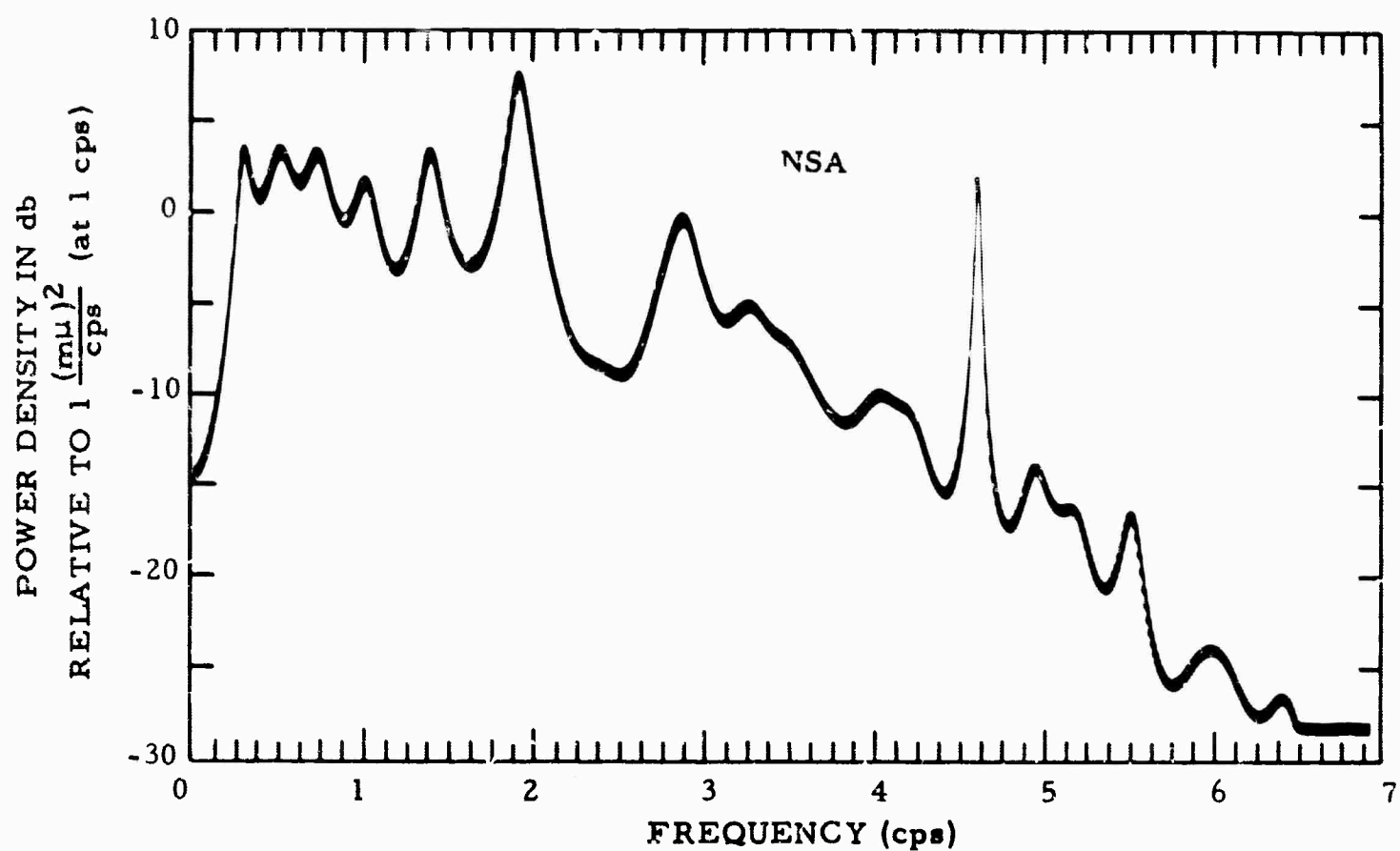


Figure IV-2. Power Density Spectra at Center Seismometer — Noise Samples A and I

Previous spectra were intended to be related to ground motion at any frequency with the aid of a curve incorporating seismometer PTA response and prewhitening filter response (Figure 4-17, Array Research Semannual Technical Report No. 1). Thus, power spectra appearing in this report will be shifted up 3 db from those previously published.

From the above cited TI report,⁸ CPO noise is shown to have the following characteristics:

- The great bulk of the noise power is concentrated below 4 cps
- The noise is generally quite predictable below 2 cps, indicating that CPO noise below 2 cps is quite coherent
- Noise power is fairly well concentrated in K-space. Wavenumber power spectra of CPO noise at frequencies of 0.5, 1, 2, and 3 cps are shown in Figures IV-17, IV-18, IV-19, IV-20 which will be discussed under subsection F

D. MCF SYSTEM'S RESPONSES TO INFINITE-VELOCITY SIGNAL

The amplitude and phase response of IP 23, IP 24, IP 25, and IP 26 to an infinite-velocity signal are shown in Figure IV-3. All systems preserve the amplitude of an infinite-velocity signal rather well and exhibit near-zero phase response which is necessary for signal preservation.

The phase and amplitude response of each channel of the four MCF systems are shown in Figures IV-4 through IV-9. The phase response of some of these individual channels shows significant deviations from 0 or 180°. This should be considered in detail as it relates to the hypotheses of space-stationarity and seismometer gain equalization.

Consider a MCF system designed using an array whose geometry is symmetrical about its center. The wavenumber response of such a multichannel filter system can be written as

$$H(f, k_x, k_y) = \sum_i H_i(f) \exp \left[-2\pi i \vec{k} \cdot \vec{r}_i \right]$$

where

$H_i(f)$ = response of the filter applied to the i^{th} seismometer

\vec{k} = vector wavenumber of any plane wave

\vec{r}_i = vector location of the i^{th} seismometer with respect to the center of symmetry

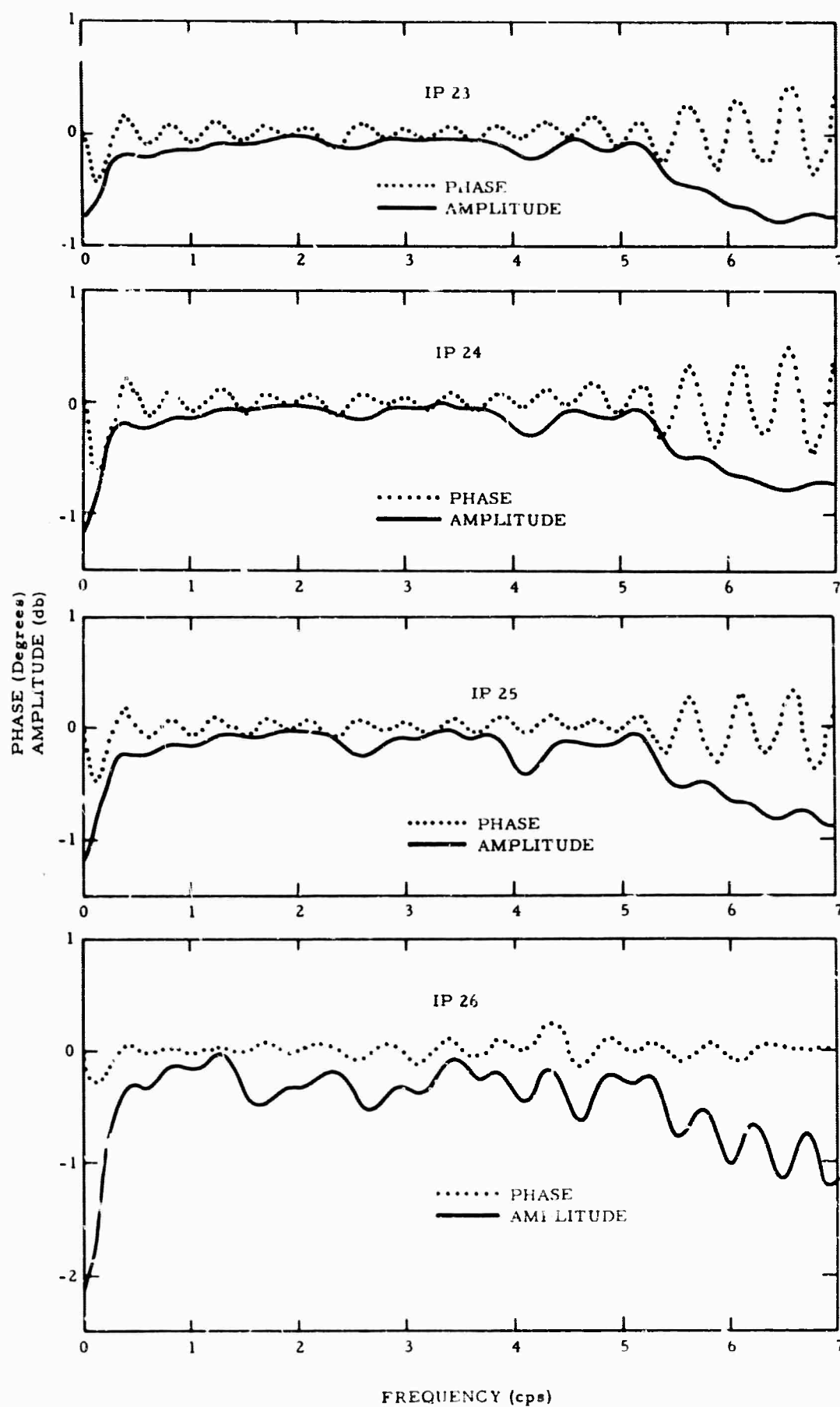


Figure IV-3. Signal Responses of the Multichannel Filter Systems — Infinite Velocity Signal

Fixing f and taking the sum over pairs of symmetrically placed seismometers (call these locations \vec{r}_{j1} and \vec{r}_{j2} where $\vec{r}_j = \vec{r}_{j1} = -\vec{r}_{j2}$), the system response can be written as

$$\sum_{j=1}^J \left| H_{j1} e^{-i2\pi |\vec{k}| |\vec{r}_j| \cos \theta} + H_{j2} e^{i2\pi |\vec{k}| |\vec{r}_j| \cos \theta} \right| + H_0$$

where

$\sum_{j=1}^J$ means summation by symmetrically placed pairs

H_0 is the filter applied to the seismometer placed at the center of symmetry--if any

θ is the angle between \vec{k} and \vec{r}_{j1} (it is a function of \vec{r}_{j1} and \vec{k})

Thus, if the filters applied to symmetrically spaced seismometers are the same, the system response becomes $\sum_{j=1}^J 2 H_j \cos (2\pi |\vec{k}| |\vec{r}_j| \cos \theta) + H_0$. This can be considered in the more useful form

$$\sum_{j=0}^J a_j(\vec{k}) \left[R(H_j) + I(H_j) \right]$$

where

a_j is real and not a function of frequency

$R(H_j)$ means the real part of the j^{th} filter

$I(H_j)$ means the imaginary part of the j^{th} filter

The MSE of the MCF system at any fixed frequency is given by

$$\text{MSE} = \iint \left\{ \left[1 - \sum_j a_j(\vec{k}) R(H_j) \right]^2 + \left[\sum_j a_j(\vec{k}) I(H_j) \right]^2 \right\} S(\vec{k}) d\vec{k}_x d\vec{k}_y + \iint \left\{ \left[\sum_j a_j(\vec{k}) R(H_j) \right]^2 + \left[\sum_j a_j(\vec{k}) I(H_j) \right]^2 \right\} N(\vec{k}) d\vec{k}_x d\vec{k}_y$$

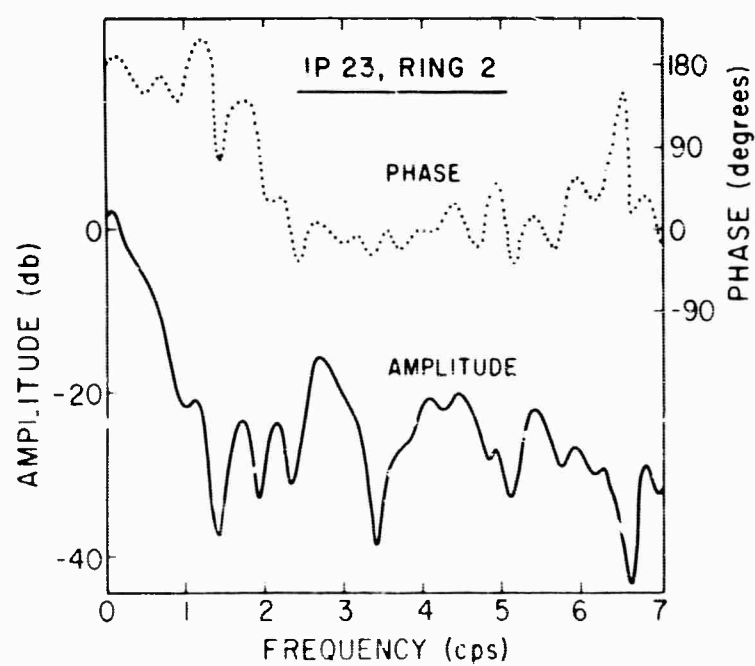
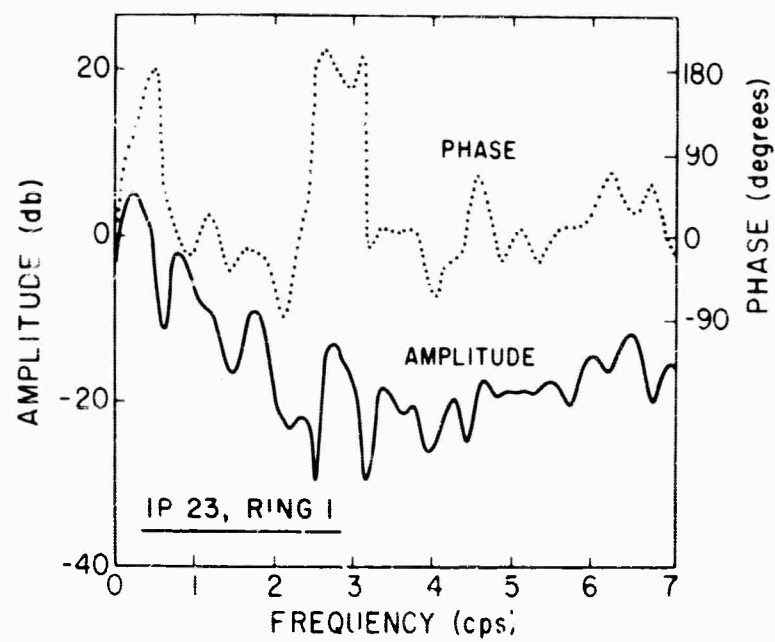


Figure IV-4. Amplitude and Phase Responses of the Filters for IP 23 Channels 1 and 2

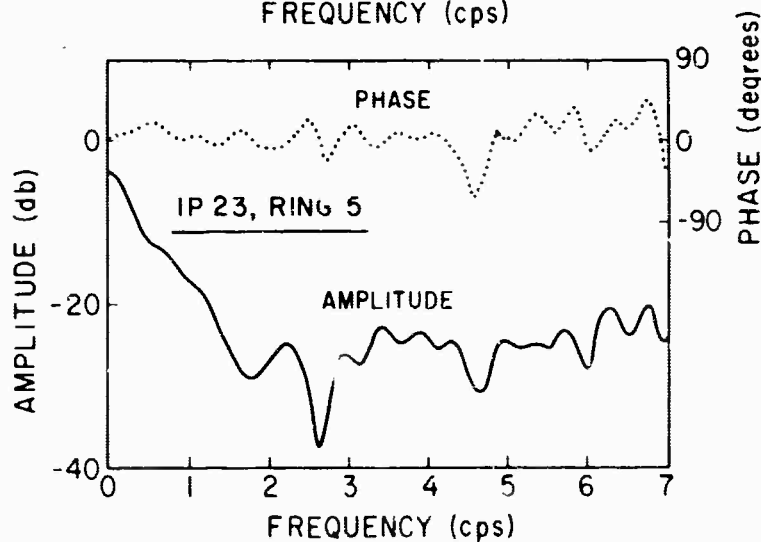
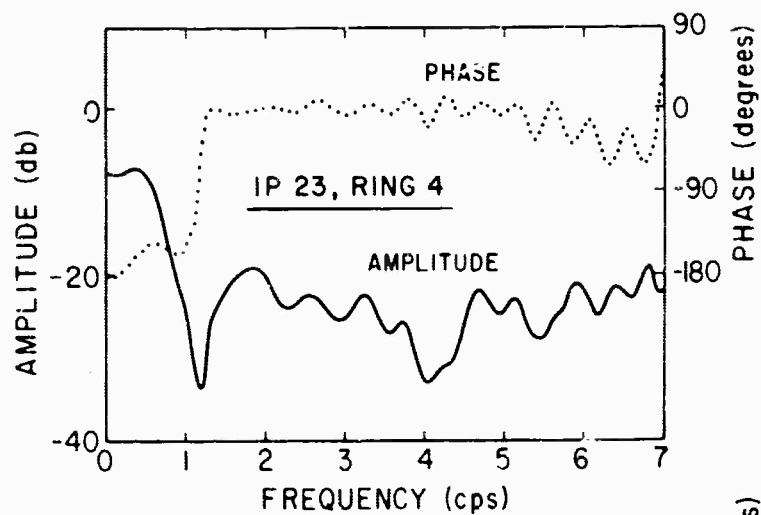
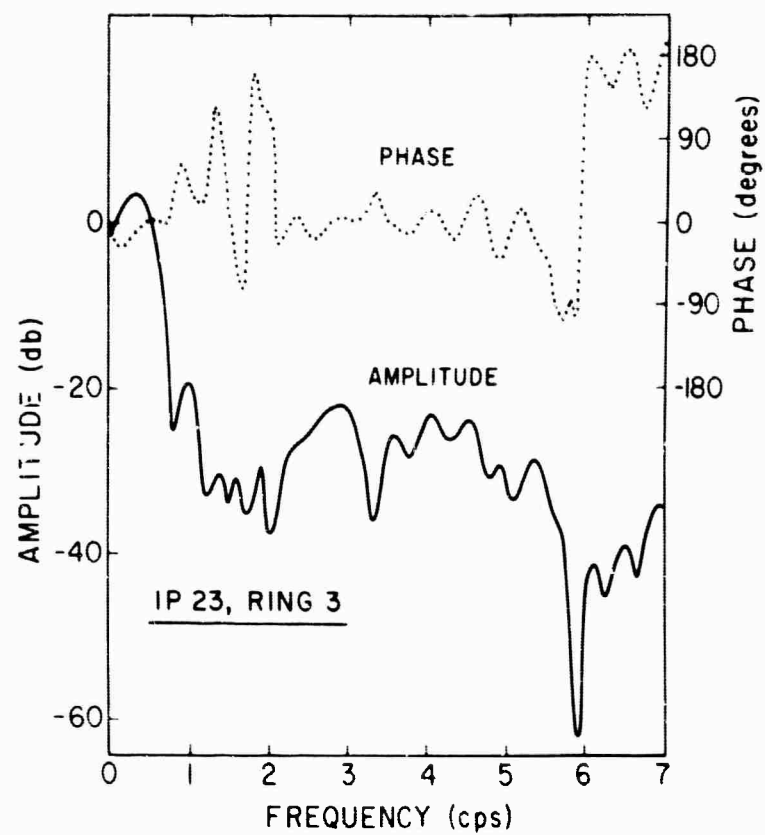


Figure IV-5. Amplitude and Phase Responses of the Filters for IP 23 Channels 3, 4 and 5

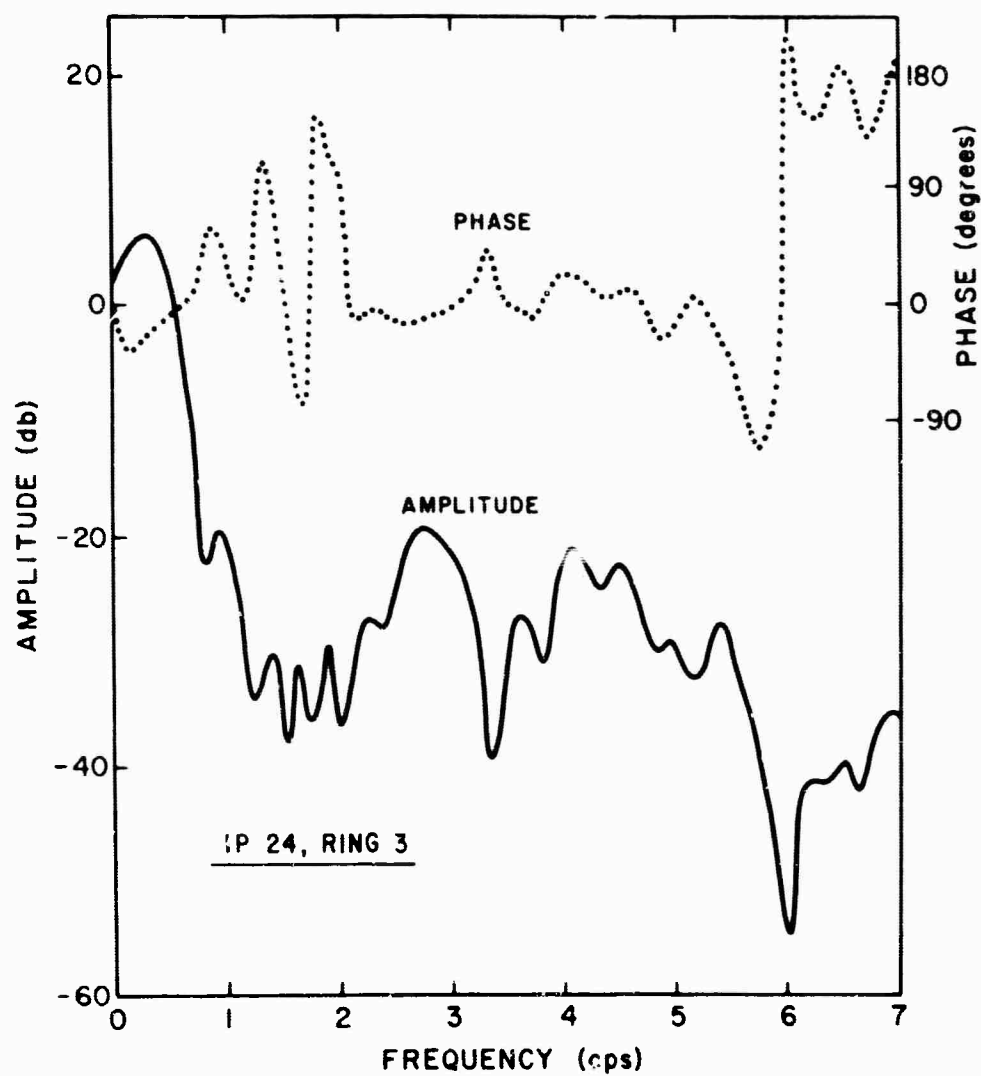
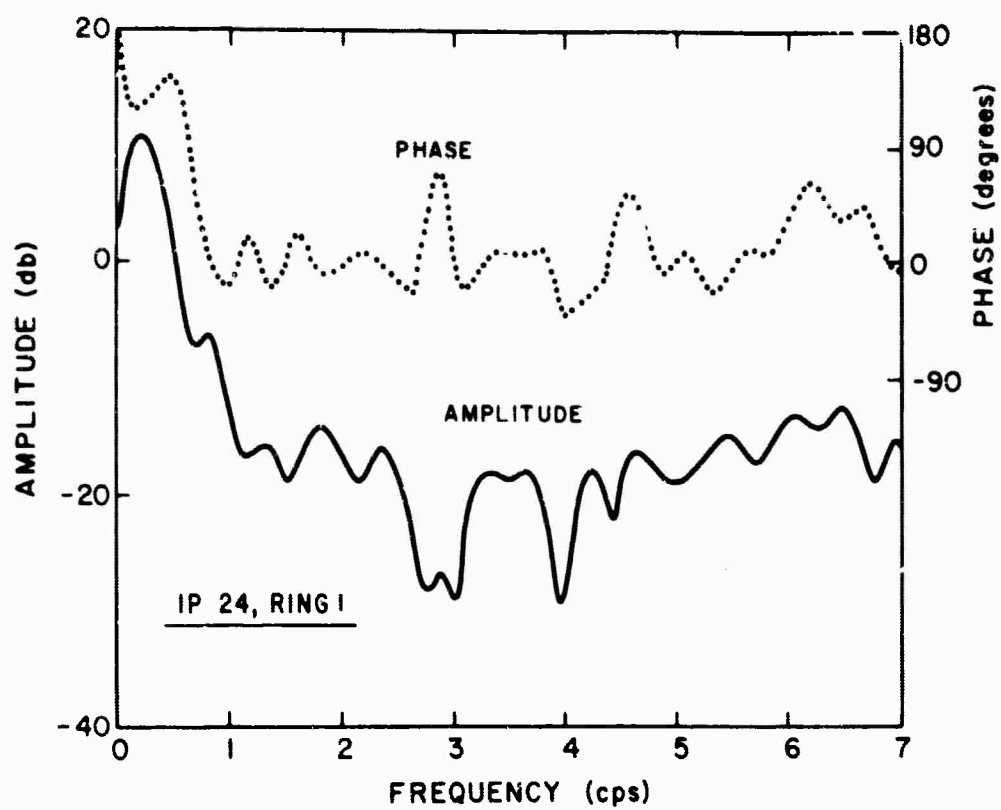


Figure IV-6. Amplitude and Phase Responses of the Filters for IP 24 Channels 1 and 2

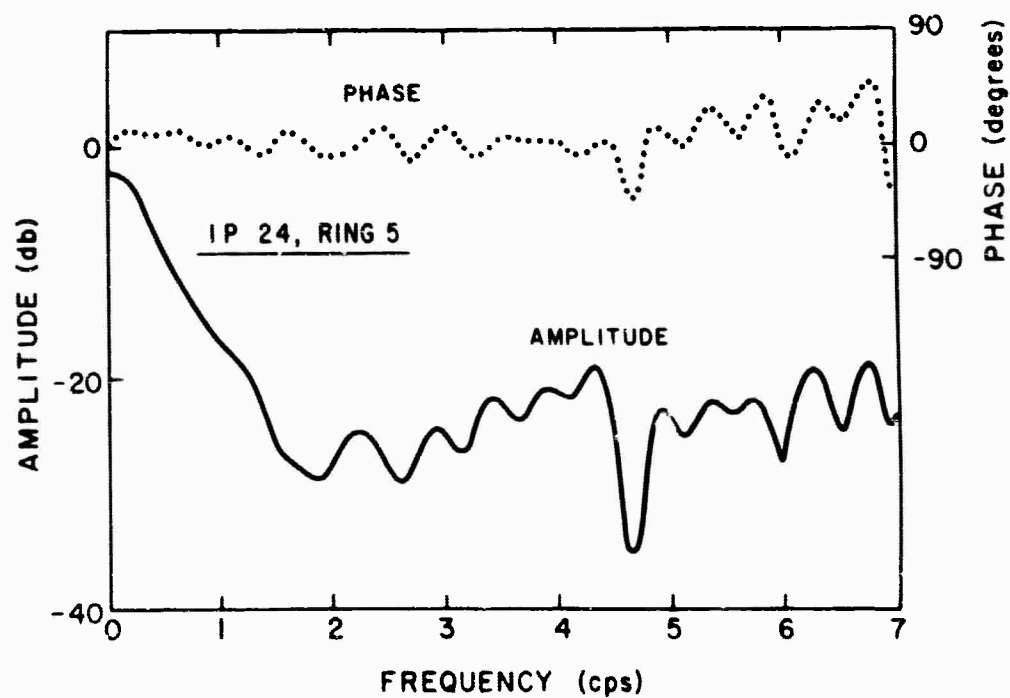
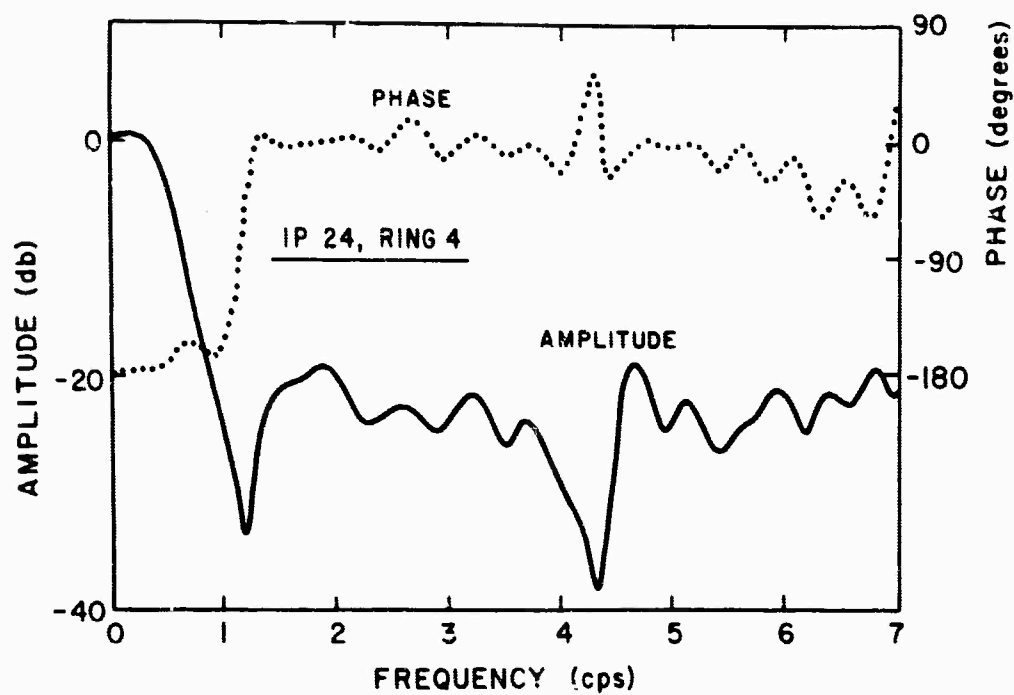


Figure IV-7. Amplitude and Phase Responses of the Filters for IP 24 Channels 3 and 4

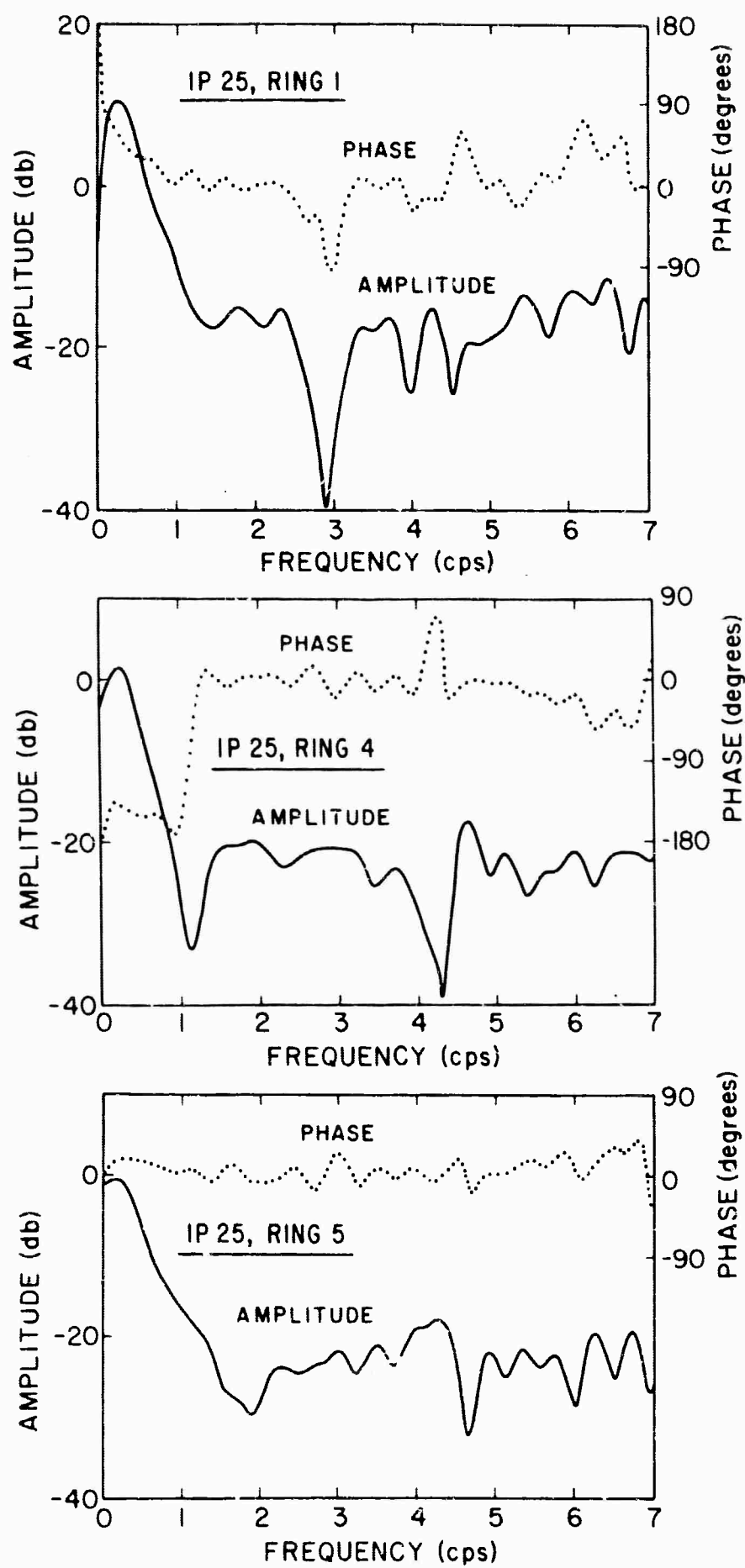


Figure IV-8. Amplitude and Phase Responses of the Filters for IP 25 Channels 1, 2 and 3

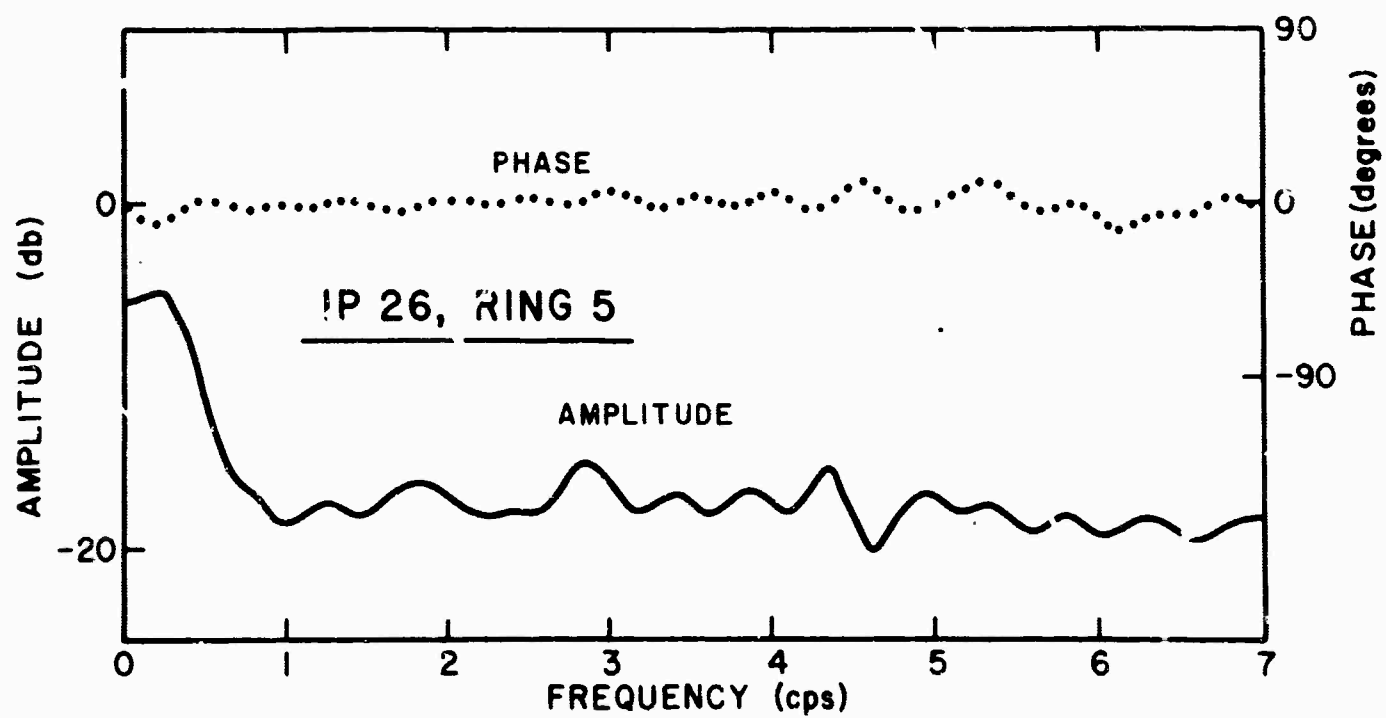
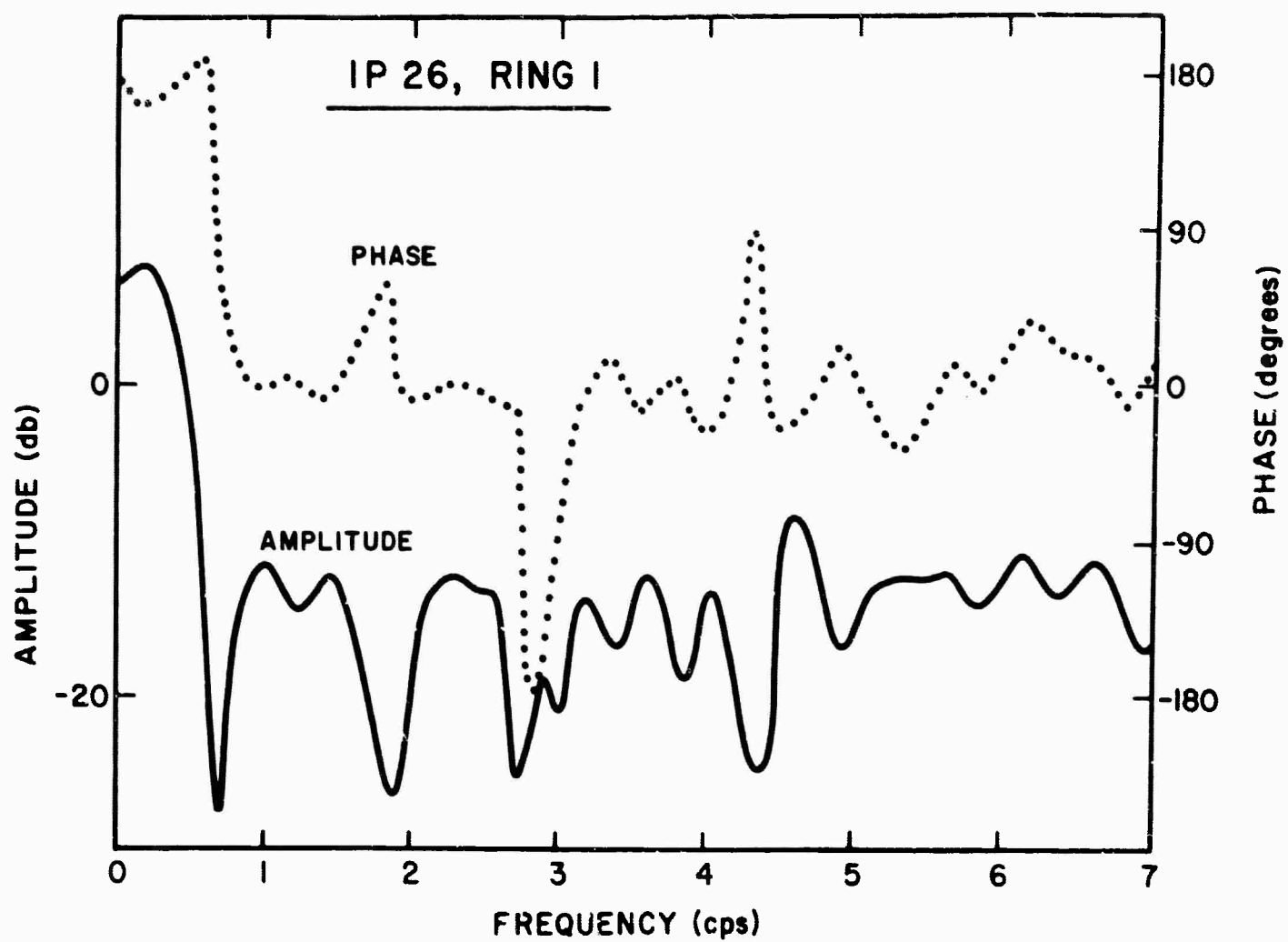


Figure IV-9. Amplitude and Phase Responses of the Filters for IP 26 Channels 1 and 2

The first integral gives the signal distortion part of the MSE, with $S(\vec{k})$ being the signal power distribution, and the second integral gives the output noise power, $N(\vec{k})$ being the noise power distribution. The expression containing the imaginary parts of the filters $\left[\sum_j a_j(\vec{k}) I(H_j) \right]^2$ is non-negative as are $S(\vec{k})$ and $N(\vec{k})$. Thus, the MSE is minimized with respect to $I(H_j)$ when

$$\sum_j a_j(\vec{k}) I(H_j) = 0$$

Since the $a_j(\vec{k})$'s are linearly independent functions of \vec{k} , i. e.,

$$a_j(\vec{k}) = 2 \cos(2\pi|\vec{k}| |\vec{r}_j| \cos \theta)$$

the above can be true over a \vec{k} region only if $I(H_j) = 0$ for all j . Therefore, given an MCF system whose channels were obtained from sums of symmetrically placed seismometers, it would be expected that the response of each filter would be real at every frequency.

For any such system whose filters are not purely real, the hypothesis that the signal and noise are plane waves is not satisfied. This might be the result of any combination of the following factors:

- (1) Signal is not space-stationary.
- (2) Noise is not space-stationary.
- (3) Statistical discrepancies caused by finite data analysis make the signal or noise appear nonstationary.
- (4) Seismometer gains (or, more generally, the frequency responses) of symmetrically placed pairs are unequal.

CPO systems IP 25 and IP 26 have individual channels which are the sum of symmetrically placed seismometers with the same filter applied to each seismometer. (In effect, the seismometer outputs on any ring are actually summed before filtering.) If the noise and signal were plane waves, the above would insist that the filter response of each channel be real. This is not the observed response, however. (See Figures IV-8, IV-9.) The CPO systems in this report were designed using artificial plane wave signals. Also, previous experience indicates

that the effects of changes due to statistical variation of the data should be small. Thus, the probable causes are reduced to combinations of (2) and (4).

R5 of IP 26 (Figure IV-9) shows noticeable deviation from 0 or 180° phase below 1/2 cps and in the range 3-7 cps. At the higher frequencies, local crustal changes probably tend to somewhat destroy space stationarity. Seismometer gain inequalities probably contribute to the nonreal response also. Below 1 cps, however, it is more reasonable to infer that seismometer gain inequalities are the dominant factor. Indeed, ambient noise generally has been found to be quite space-stationary at low frequencies.¹²

IP 25, R4 and R5 (Figure IV-8), exhibit even more deviation from 0 or 180° phase. The inference is the same as for IP 26. This system has an additional ring of six seismometers as compared to IP 26. Seismometer gain inequalities among these other seismometers could tend to make the individual channels of this MCF system more phase-deviant. The channels might have to become more phase-deviant to compensate for each other. In this system also, nonreal frequency responses of the channels are marked below 1 cps.

CPO MCF systems IP 23 and IP 24 were designed on arrays which are not entirely symmetric. Thus, a directional noise field could result in nonreal frequency response. Frequency responses of individual channels of these systems (Figures IV-4 through IV-7) exhibit such general deviation of 0° or 180° phase response that seismometer gain inequality again must be implied. This is particularly true at low frequencies where differences in seismometer responses on a given ring due to directional effects would be minimized.

Study of the phase responses of the individual channels from the various systems strongly indicates seismometer gain inequalities, particularly below 1 cps. K-space responses also indicate the same thing. This will be discussed under subsection F. To evaluate the effect of seismometer gain inequalities on the partial arrays further, MCF systems incorporating statistical gain fluctuation in the signal model will be synthesized and evaluated. This will be the subject of a special report which will be forthcoming shortly.

The ability of the four systems to preserve signals of less than infinite velocity will be discussed under subsection F.

E. NOISE SUPPRESSION AND SIGNAL-TO-NOISE IMPROVEMENT

Figure IV-10 shows time functions of the two input noise samples and the filtered output of each MCF system for each noise sample. These MCF systems' output traces then were used for the spectral and spectral-ratio analysis presented in this report. The 5-ring summed traces of each noise sample show the noise as it was input into the MCF systems. The traces are explained in detail in the figure.

IP 23, 24 and 25 appear to reject the noise almost equally well, while IP 26, which was designed using only the center seismometer and the outside ring of six does a noticeably poorer job.

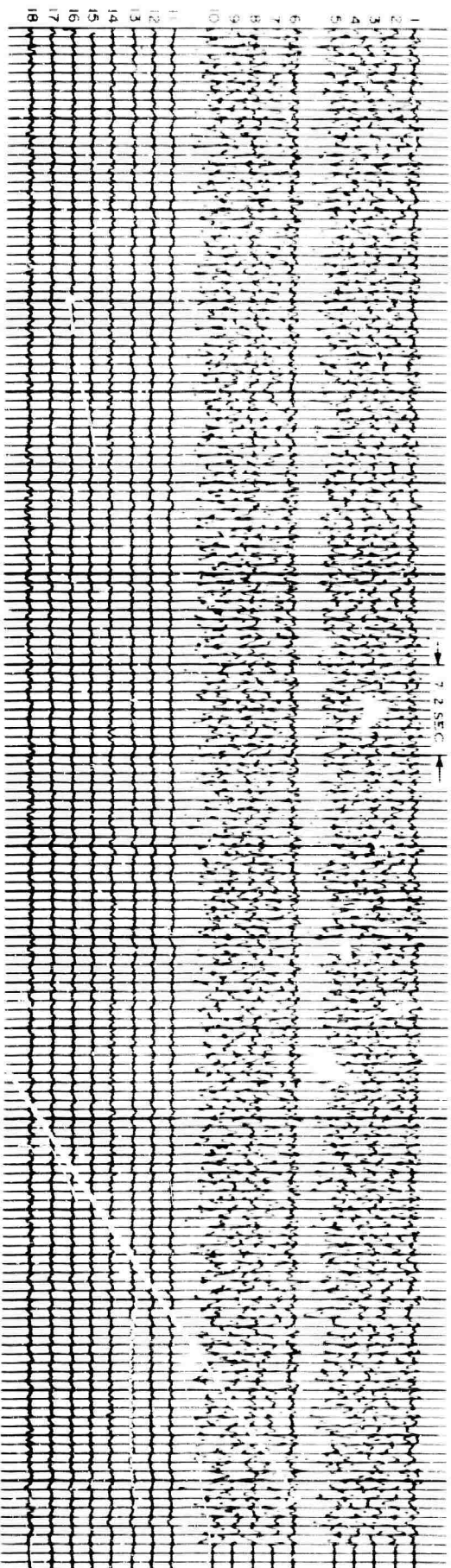
Figures IV-11 and IV-12 show the power spectra of NSA processed by IP 23, 24, 25, and 26. Figure IV-13 shows the signal-to-noise improvement (signal power out/noise power out divided by signal in/noise power in) obtained for NSA from these same MCF systems. Since the signal responses of all the systems are so nearly uniform (Figure IV-3), S/N improvement ratios are essentially a measure of noise suppression.

For NSA, the S/N improvements obtained from IP 23, 24, and 25 show only moderate differences and are nearly identical up to 2-1/2 cps. IP 26 shows significantly less S/N improvement between 1.5 and 5 cps but, below 1.5 cps, gives results comparable with the other systems.

Figures IV-14 and IV-15 show the power spectra of NSI processed by IP 23, 24, 25, and 26. Figure IV-16 shows the S/N improvement obtained for NSI from these same systems.

Between about 3/4 and 1-1/2 cps, all systems give similar S/N improvement. Below 3/4 cps, S/N improvement increases as the number of seismometers increases. Below 3/4 cps, improvement obtained from IP 26 for NSI is down 3-4 db as compared with IP 23. This was not observed for NSA (Figure IV-13). Indeed, below 3/4 cps, S/N improvement is generally better for NSI than for NSA in these low frequencies. S/N improvements for NSA from all systems are comparable to those obtained by IP 26 for NSI. Any combination of the following could account for this discrepancy:

- Seismometer frequency responses may have changed between the time NSA was recorded and NSI was recorded. They were taken over a month apart.
- The seismic sources and thus the K-space distribution of the low-frequency noise are different for NSA and NSI. These two noise samples show a somewhat different power spectra below 3/4 cps.



- | | |
|--|----------------------------|
| 1) NSA CENTER SEISMOMETER | 11) NSA PROCESSED BY IP 23 |
| 2) NSA RING 2 (Sum of 3 Seis Outputs-not Averaged) | 12) NSA PROCESSED BY IP 24 |
| 3) NSA RING 3 (Sum of 3 Seis Outputs-not Averaged) | 13) NSA PROCESSED BY IP 25 |
| 4) NSA RING 4 (Sum of 6 Seis Outputs-not Averaged) | 14) NSA PROCESSED BY IP 26 |
| 5) NSA RING 5 (Sum of 6 Seis Outputs-not Averaged) | 15) NSI PROCESSED BY IP 23 |
| 6) NSI CENTER SEIS | 16) NSI PROCESSED BY IP 24 |
| 7) NSI RING 2 (Sum of 3 Seis Outputs-not Averaged) | 17) NSI PROCESSED BY IP 25 |
| 8) NSI RING 3 (Sum of 3 Seis Outputs-not Averaged) | 18) NSI PROCESSED BY IP 26 |
| 9) NSI RING 4 (Sum of 6 Seis Outputs-not Averaged) | |
| 10) NSI RING 5 (Sum of 6 Seis Outputs-not Averaged) | |

Figure IV-10. Time Traces of NSA and NSI — Unfiltered and Filtered

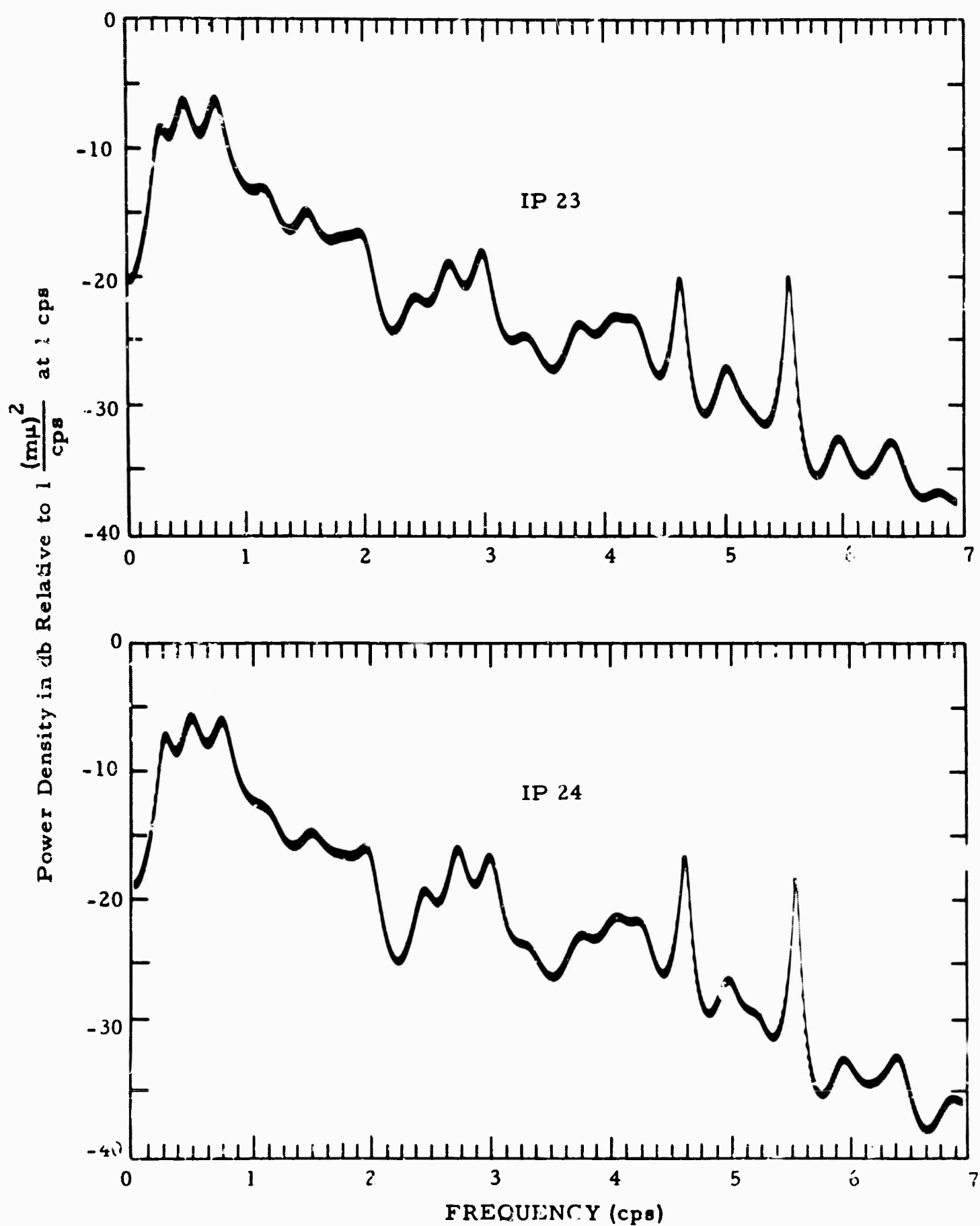


Figure IV-11. Power Spectra of NSA Processed by IP 23 and IP 24

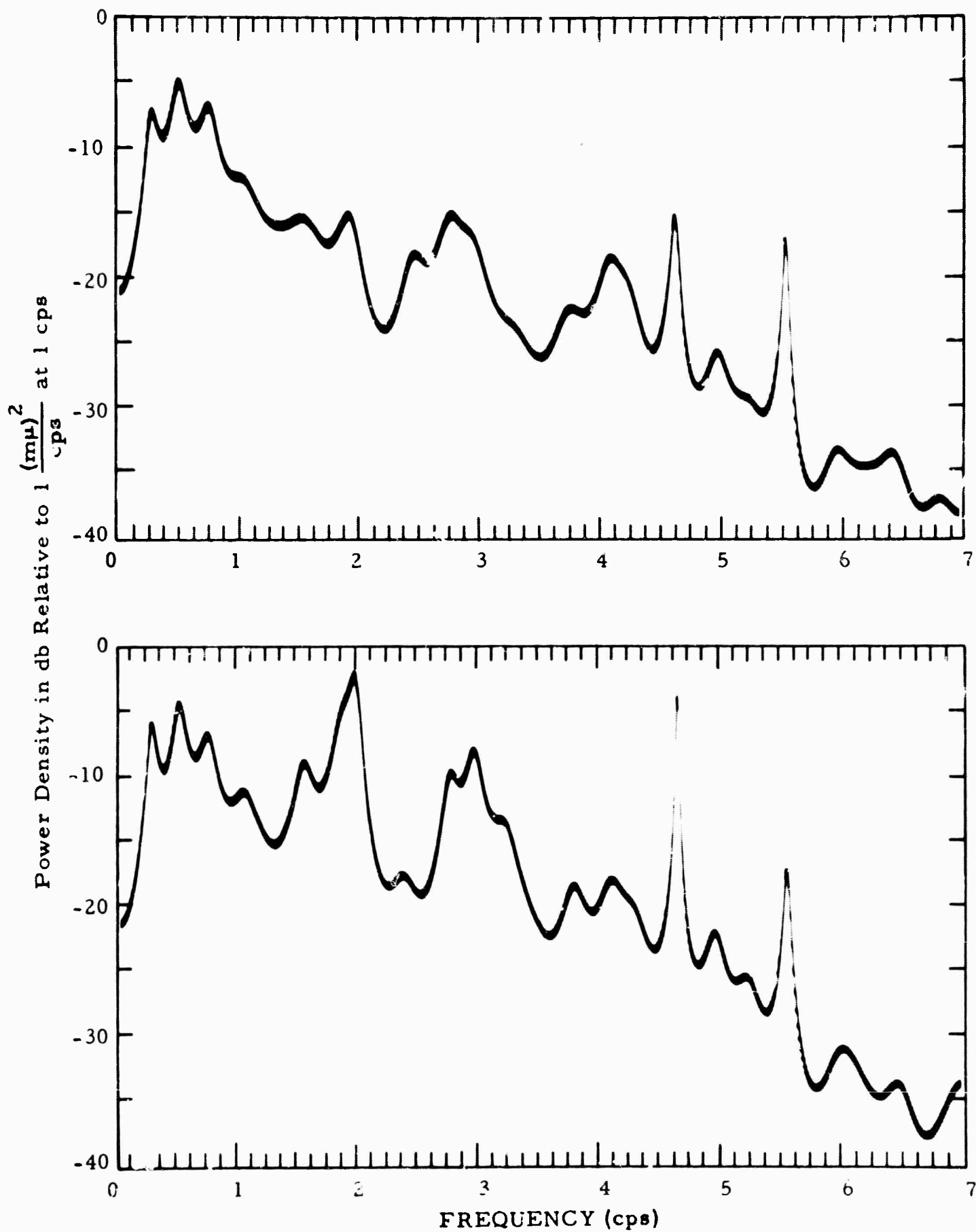


Figure IV-12. Power Spectra of NSA Processed by IP 25 and IP 26

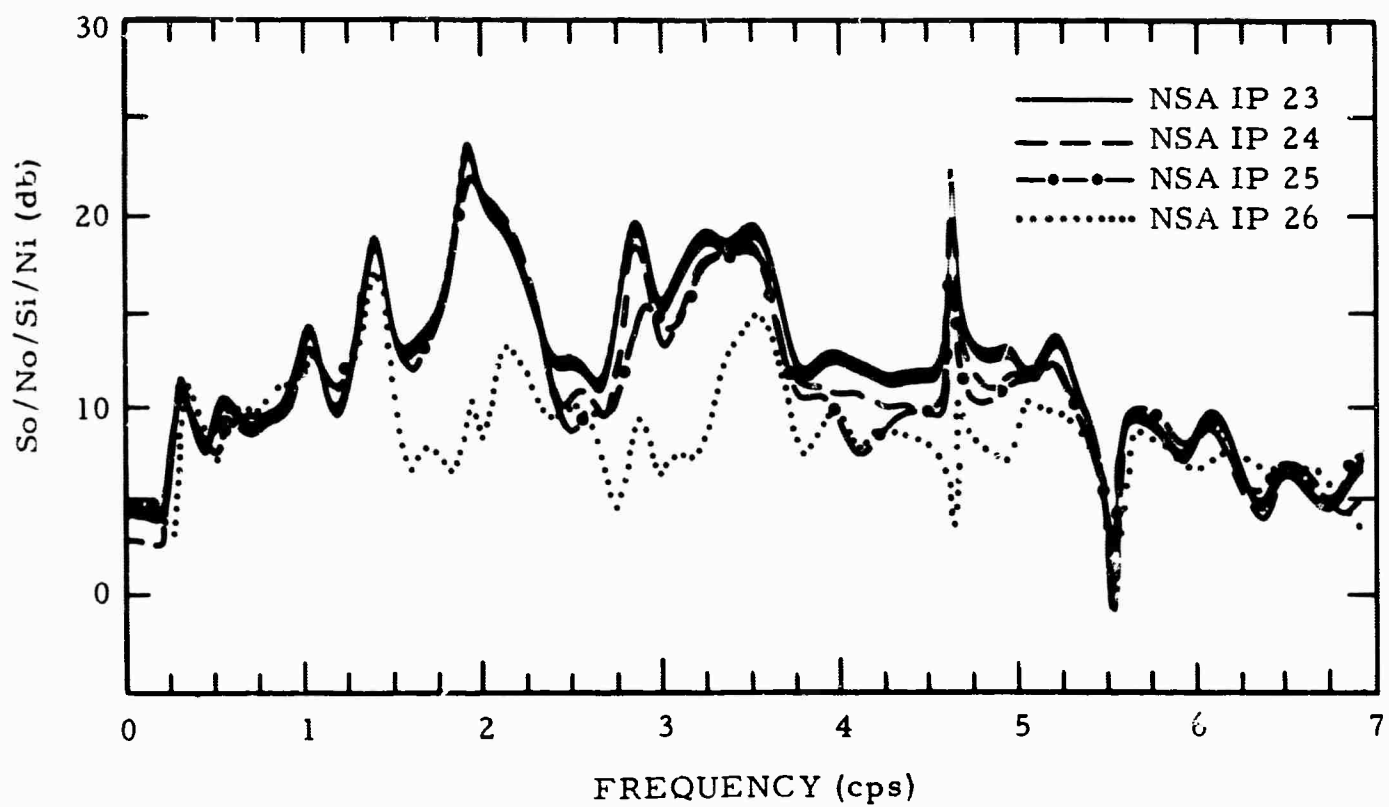


Figure IV-13. Signal-To-Noise Ratio Improvements Obtained Processing NSA and an Infinite Velocity Signal

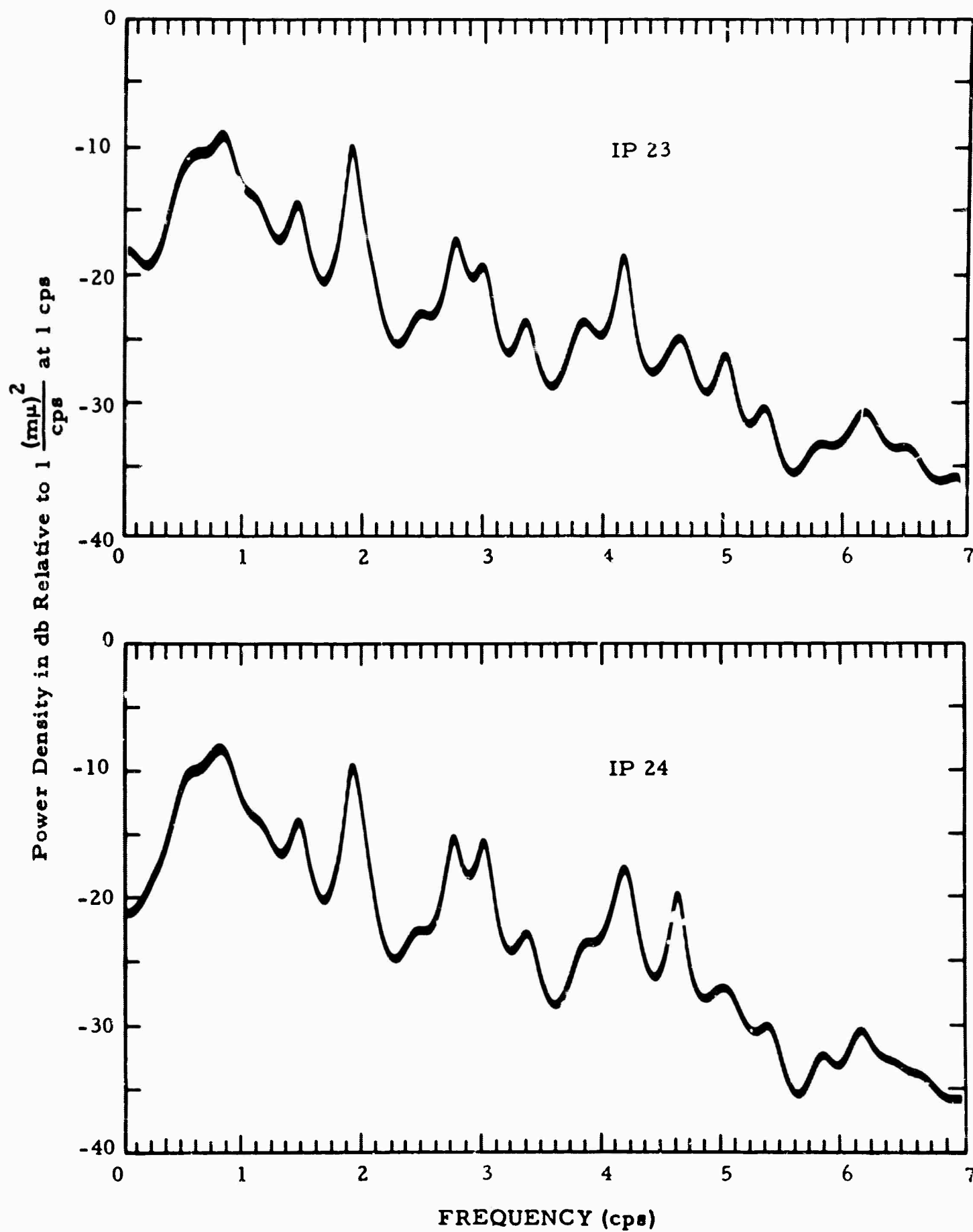


Figure IV-14. Power Spectra of NSI Processed by IP 23 and IP 24

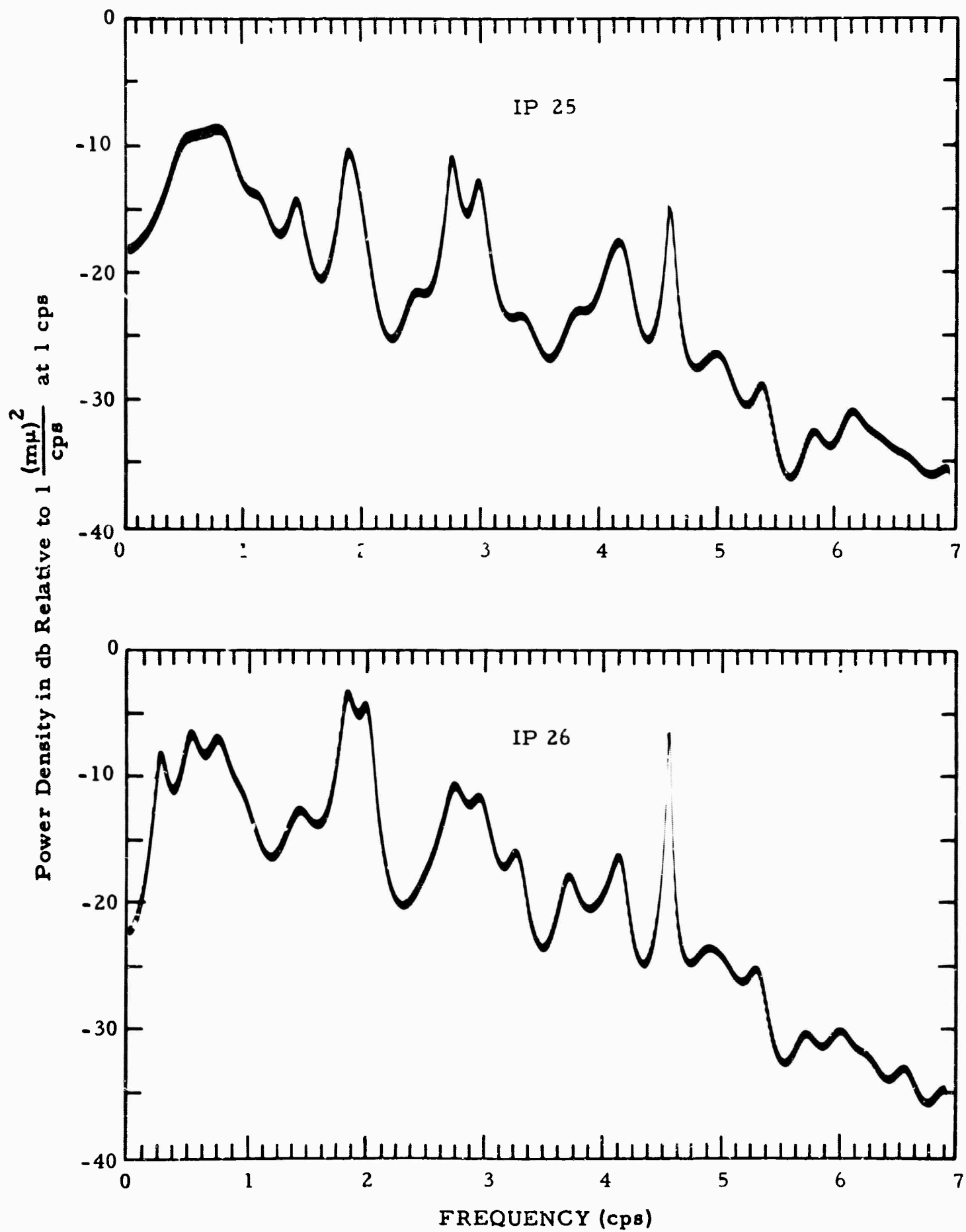


Figure IV-15. Power Spectra of NSI Processed by IP 25 and IP 26

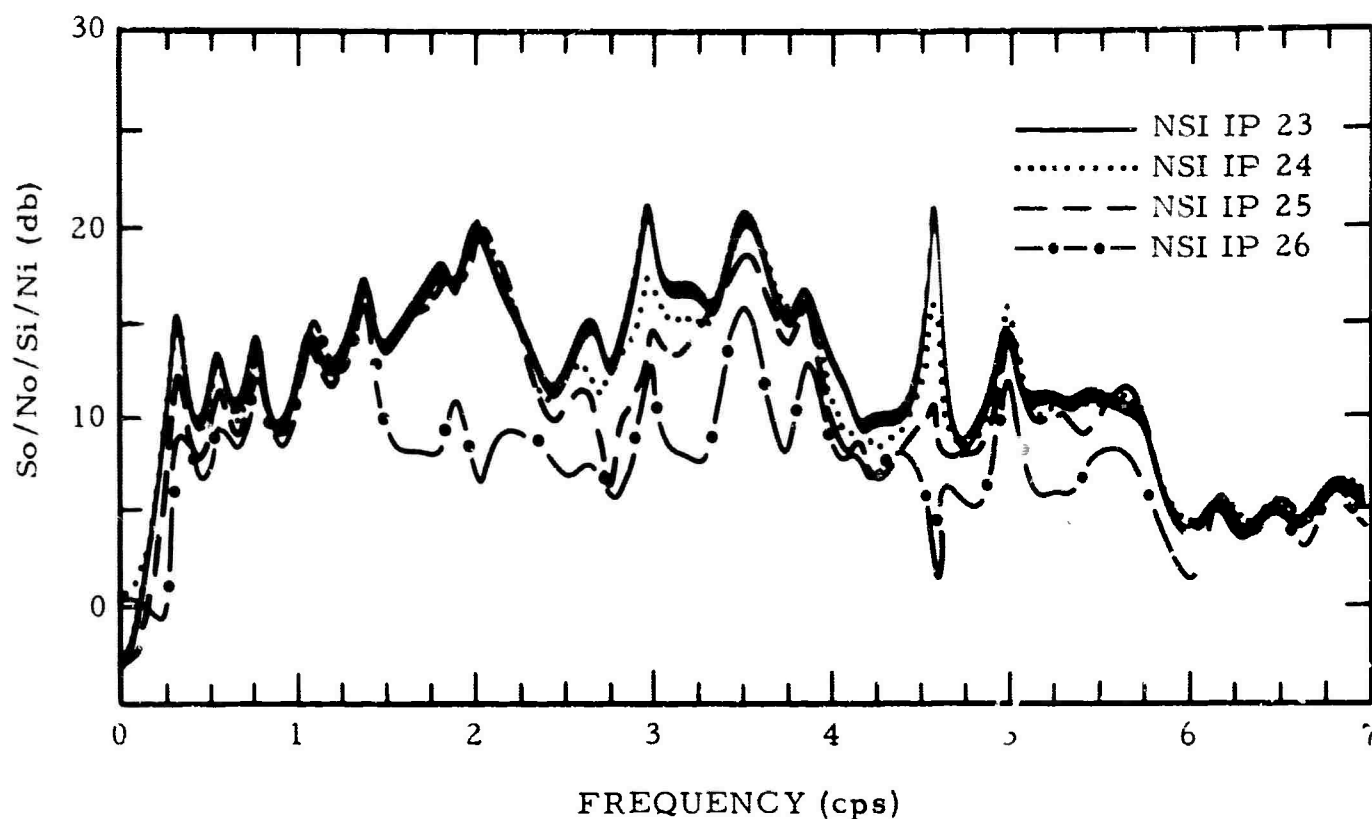


Figure IV-16. Signal-To-Noise Ratio Improvements Obtained Processing NSI and an Infinite Velocity Signal

Above 1-1/2 cps, the MCF systems appear to operate on NSI in a manner generally similar to NSA. IP 23, 24 and 25 give similar S/N improvement to 2-1/2 cps. Above 2-1/2 cps, the differences among these three systems are generally 2-4 db but range to over 10 db. Above 1-1/2 cps, S/N improvement obtained from IP 26 is generally down 5-10 db as compared with IP 23.

From a comparison of S/N improvements obtained from the four MCF systems, the following conclusions can be reached:

- IP 25 (13 seismometers) generally has noise rejection capability nearly equal to that of IP 23 (19 seismometers) below 2-1/2 cps.
- Below 1-1/2 cps, IP 26 (seven seismometers) shows noise rejection which is generally only moderately less than IP 23

- Seismometer gain inequalities may be giving a false picture for NSI below 3/4 cps. Greater S/N improvement shown by the system employing more seismometers may be false S/N improvement obtained by using the seismometer gain inequalities to suppress noise. The artificial signal used in obtaining the S/N improvements would not be affected by seismometer gain inequalities. Thus, such a system would give better S/N improvement for the synthesized situation than for an actual signal. Below 1 cps, seismometer gain inequalities are indicated by the wavenumber responses of the systems (subsection F).

Thus, for noise suppression in the frequency range where distant mantle P-wave power is concentrated,

- Both IP 25 and 26 are generally satisfactory.
- IP 23 is not a significantly better system than IP 25.
- IP 23 is only moderately superior to IP 26.

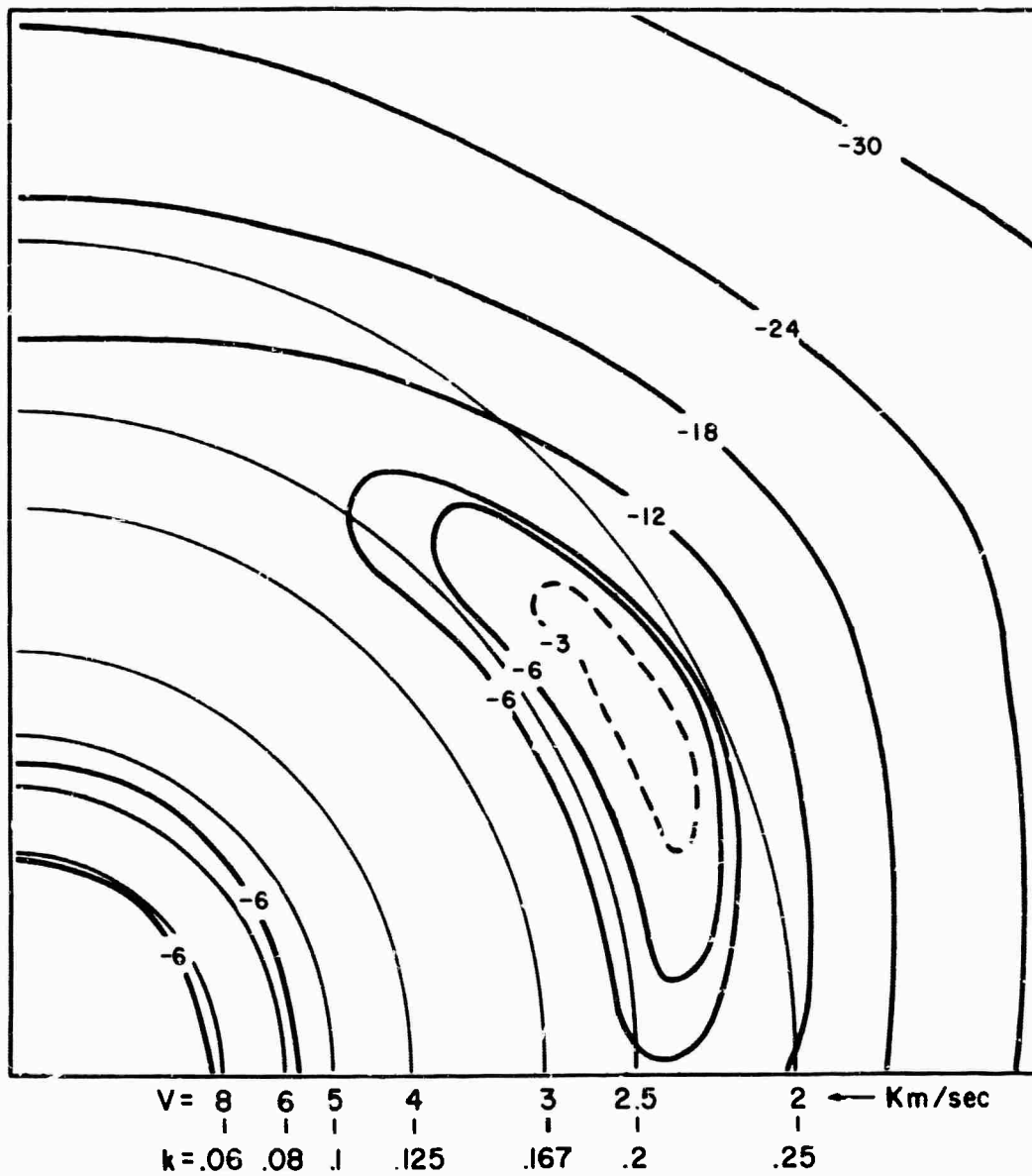
F. K-SPACE RESPONSE OF SYSTEMS

Wavenumber responses of the four systems were computed at 0.5, 1.0, 2.0, and 3.0 cps. A mathematical development of this technique can be found in John Burg's "Three-Dimensional Filtering with an Array of Seismometers," Geophysics, October 1964, p. 699-700. Results are presented as contour maps in wavenumber space (Figures IV-17, IV-18, IV-19, and IV-20). Contours below approximately -24 db were removed to make a more presentable map.

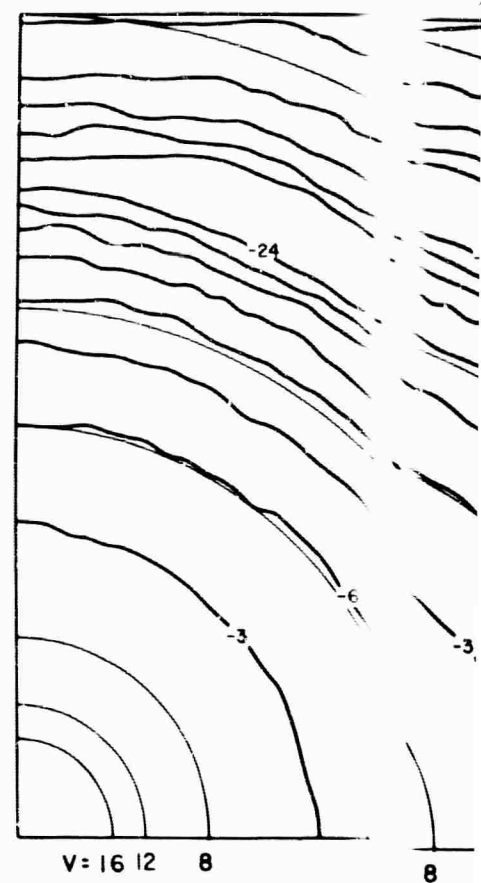
K-space responses of the four systems at a particular frequency have been combined into one figure with the wavenumber power spectra of the noise at that frequency. K-space power spectra of the noise are reproductions of those previously published.⁸

Figure IV-17 shows the wavenumber responses of IP 23, 24, 25, and 26 and the noise power spectra at 0.5 cps. Comparison of wavenumber responses and noise power spectra indicates seismometer gain inequalities at this frequency. The noise power is concentrated in an annulus representing velocities around 2.5 km/sec. IP 23 attenuates most strongly plane waves with a velocity of about 2.5 km/sec. IP 24 attenuates most strongly plane waves with velocity approximately 2.6 km/sec.

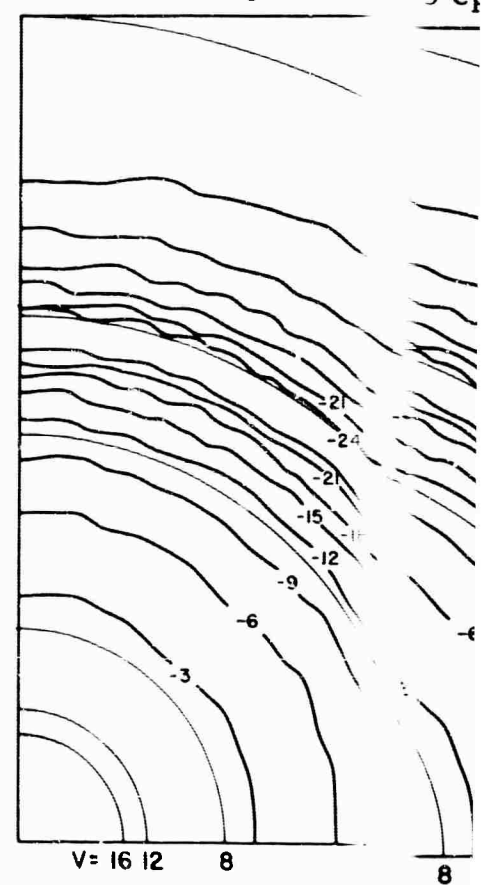
NOISE POWER at 0.5 cps



IP 23 at 0.5 cps

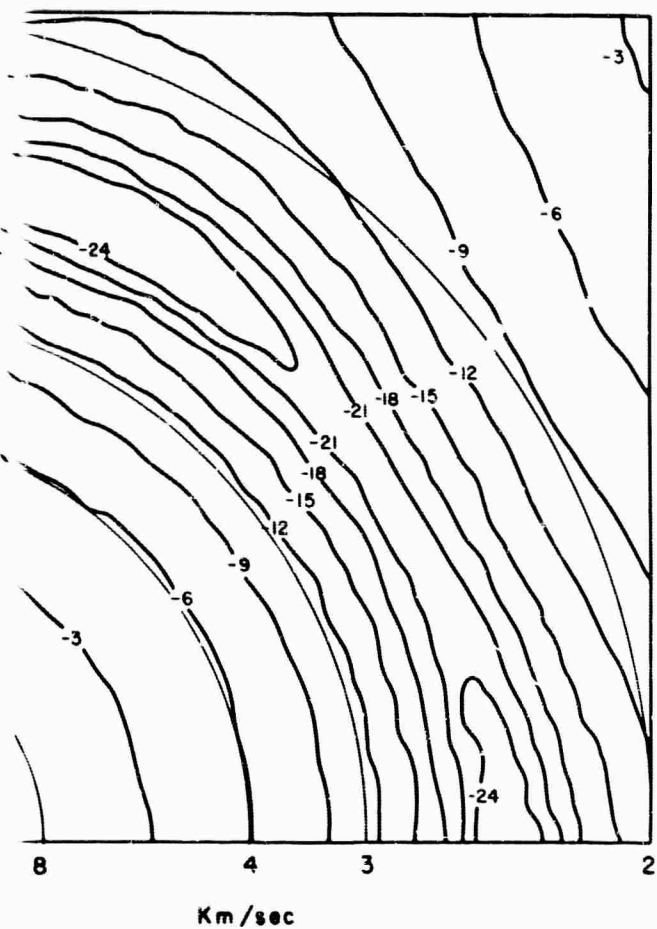


IP 25 at 0.5 cps

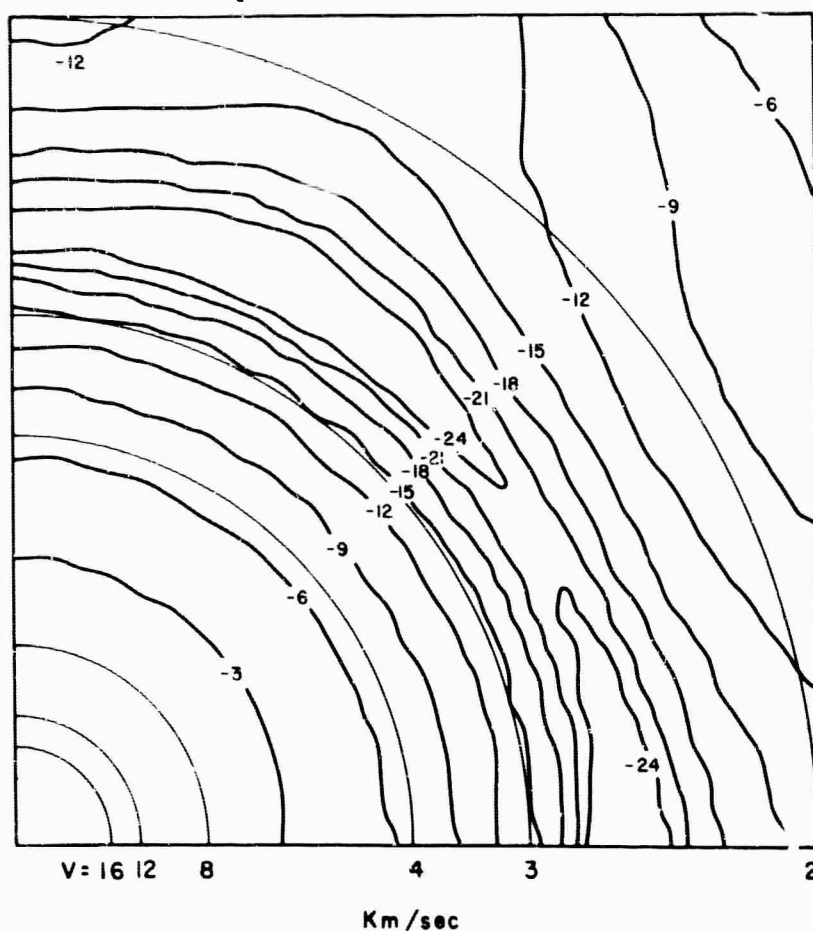


A

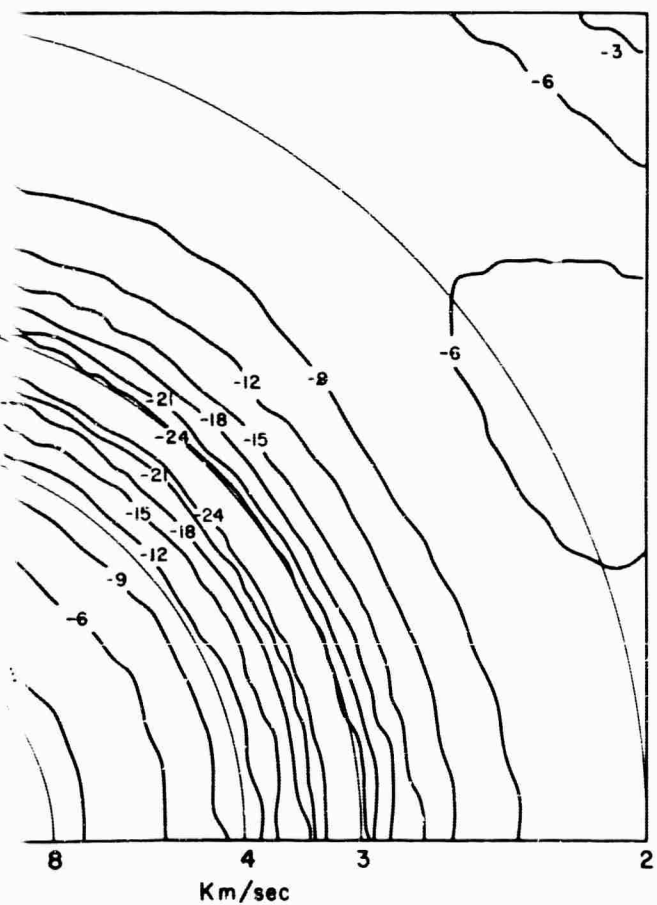
5 cps



IP 24 at 0.5 cps



5 cps



IP 26 at 0.5 cps

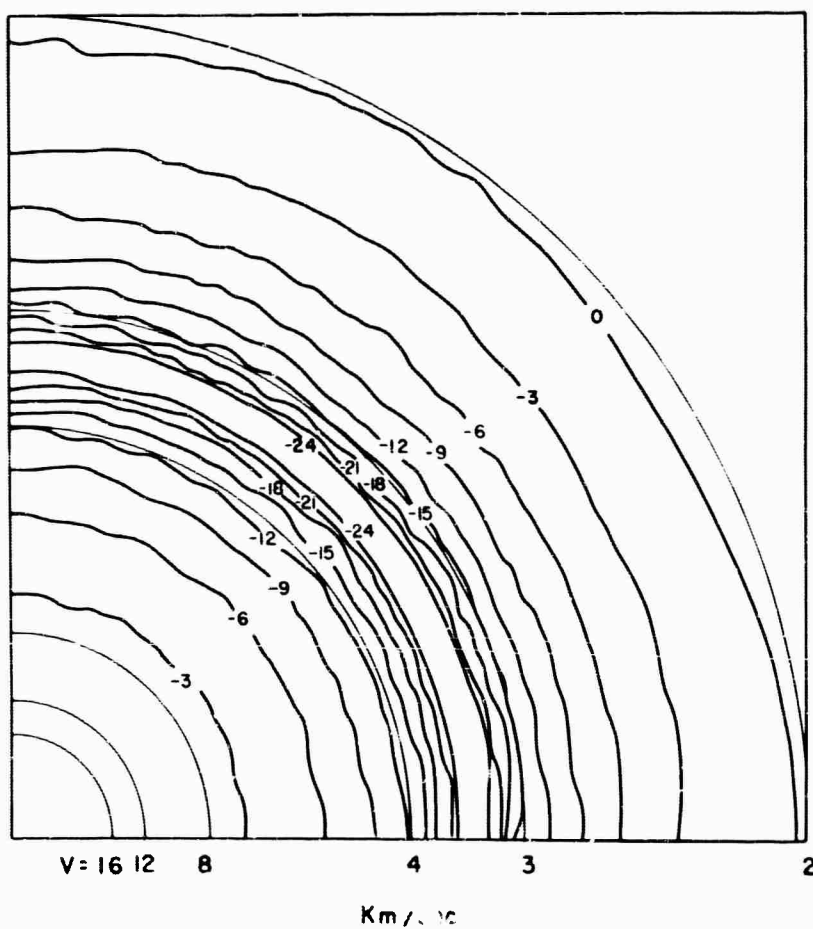
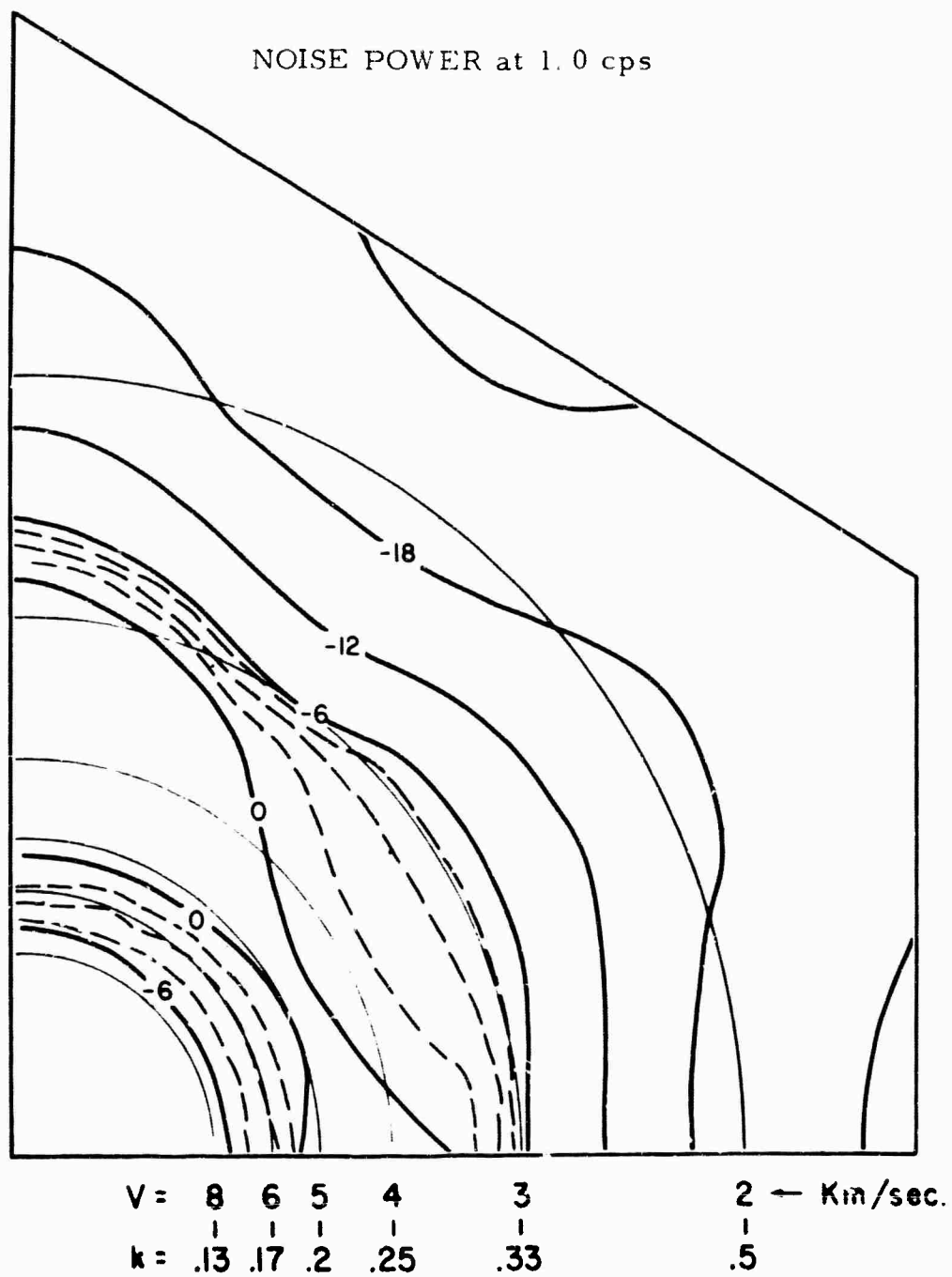
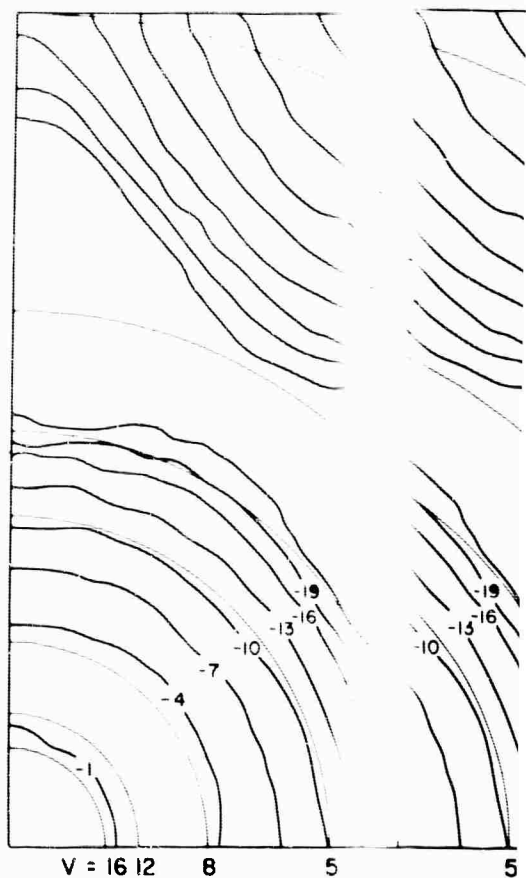


Figure IV-17. Wavenumber Responses of the Multichannel Filter Systems and Wavenumber Distribution of the Noise Power at 0.5 Cps

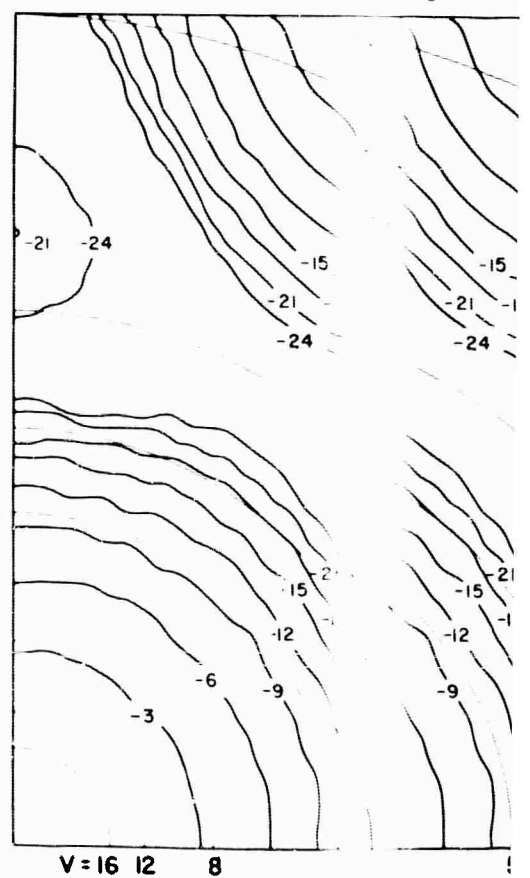
B



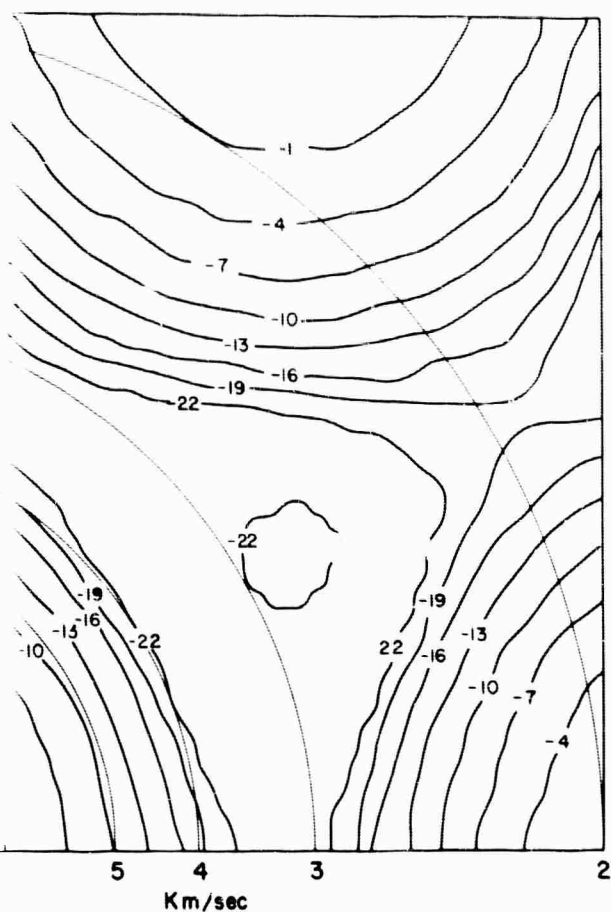
IP 23 at 1.0 cps



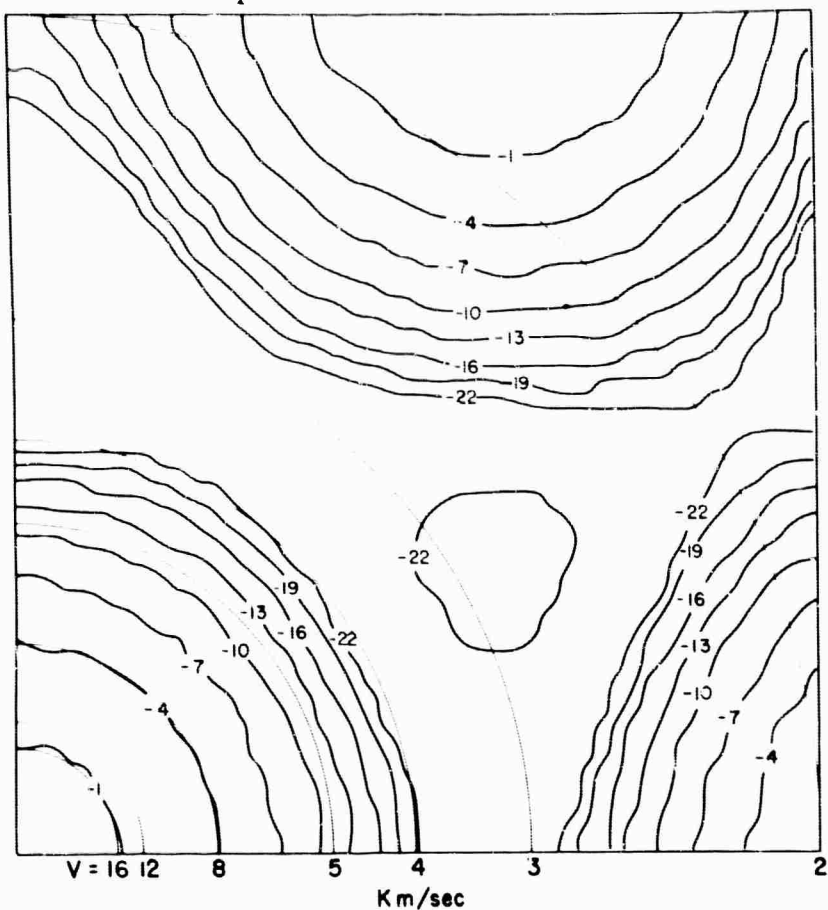
IP 26 at 1.0 cps



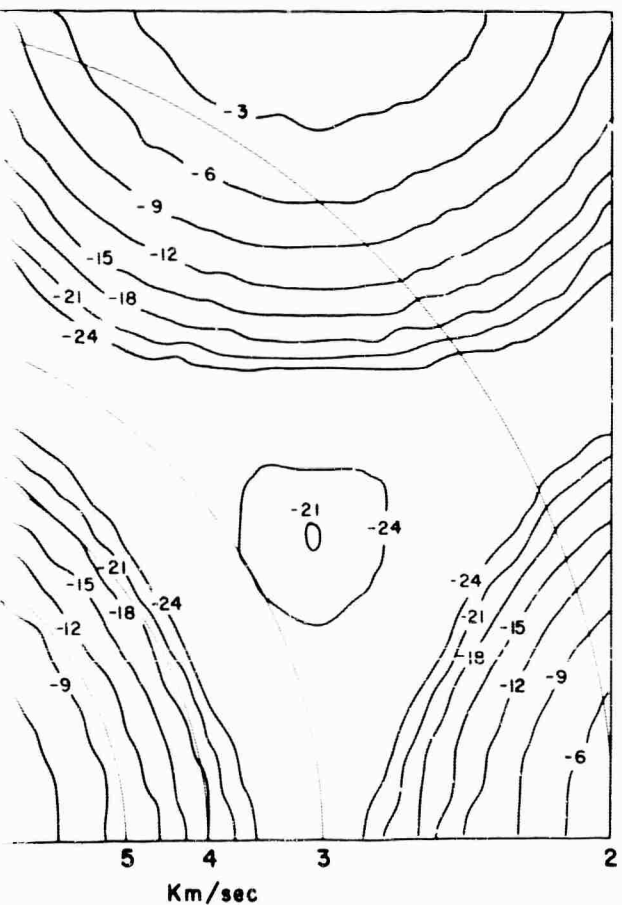
ps



IP 24 at 1.0 cps



cps



IP 25 at 1.0 cps

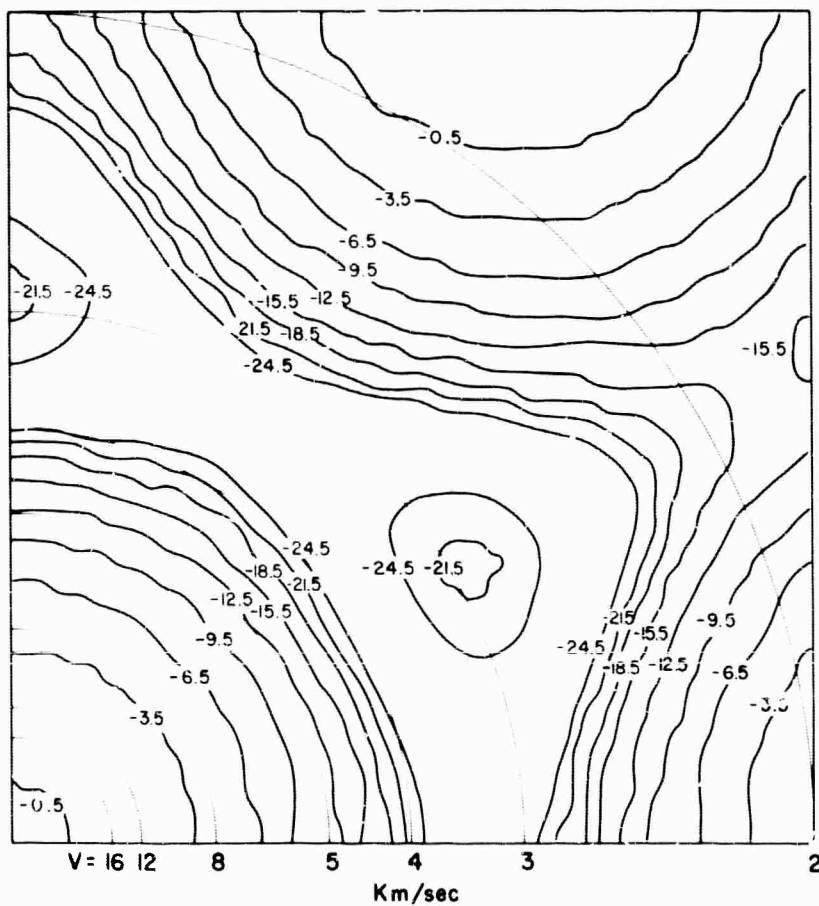
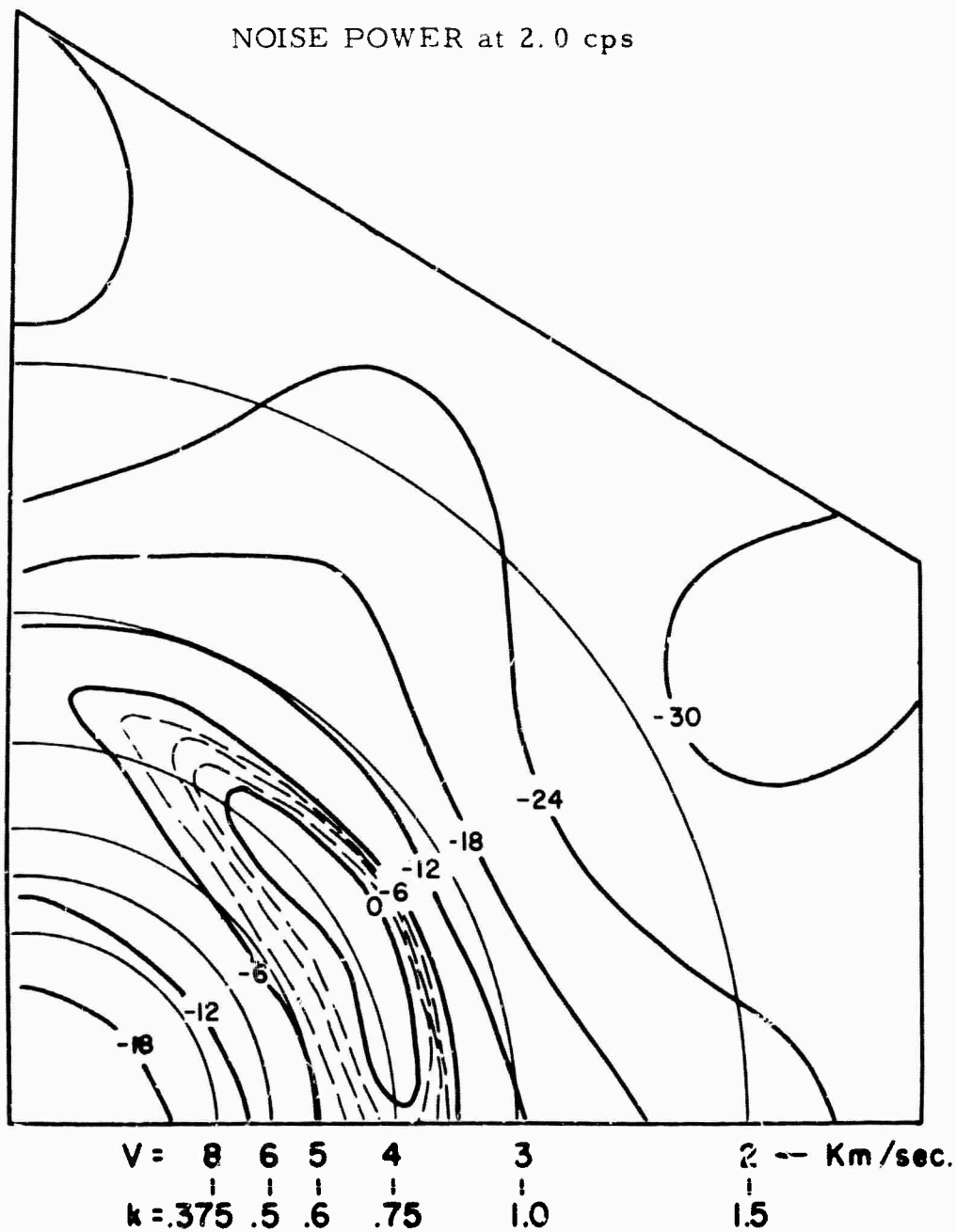
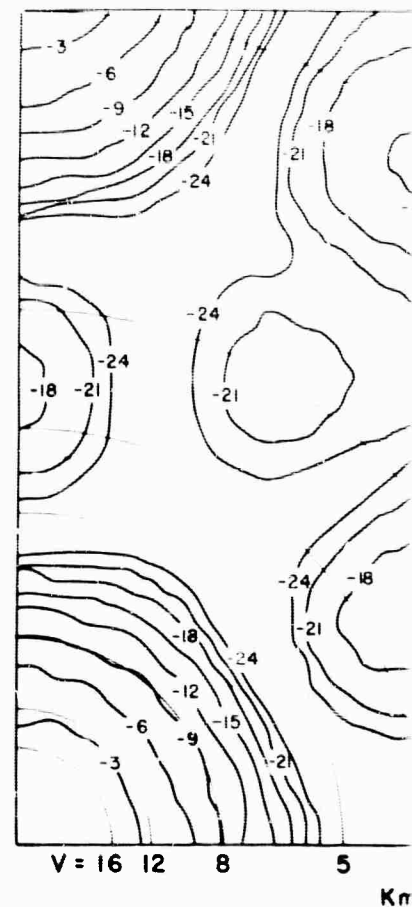


Figure IV-18. Wavenumber Responses of the Multichannel Filter Systems and Wavenumber Distribution of the Noise Power at 1.0 Cps

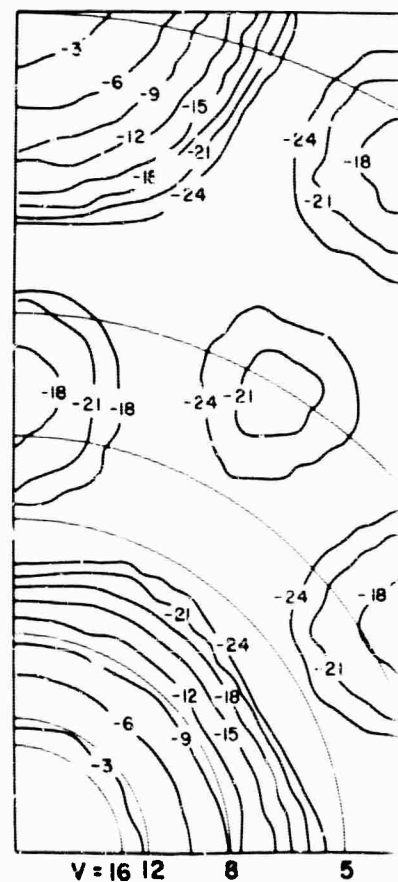
B



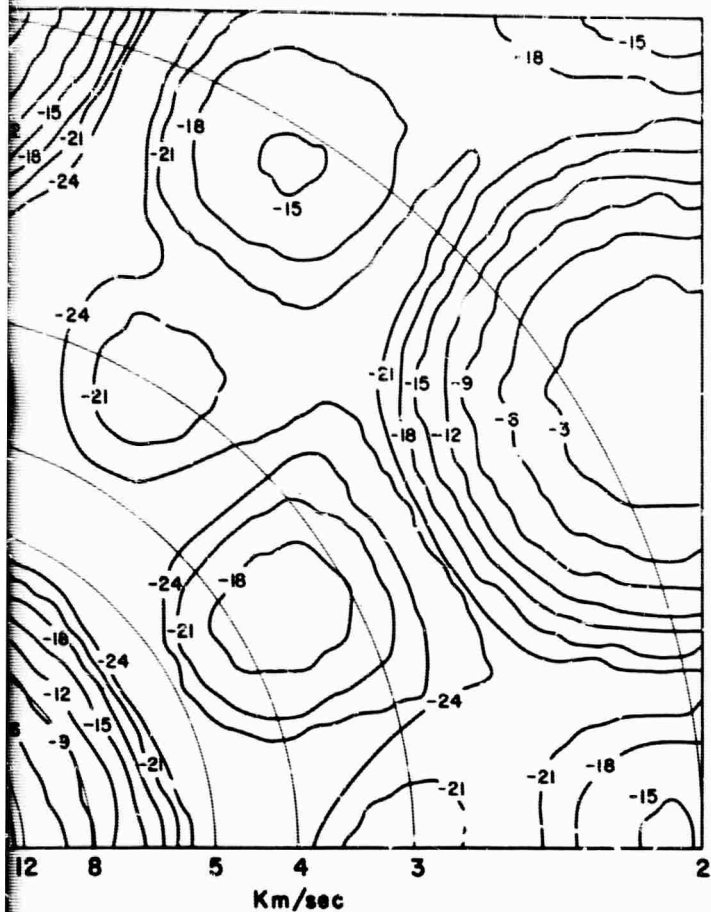
IP 23 at 2.0 cps



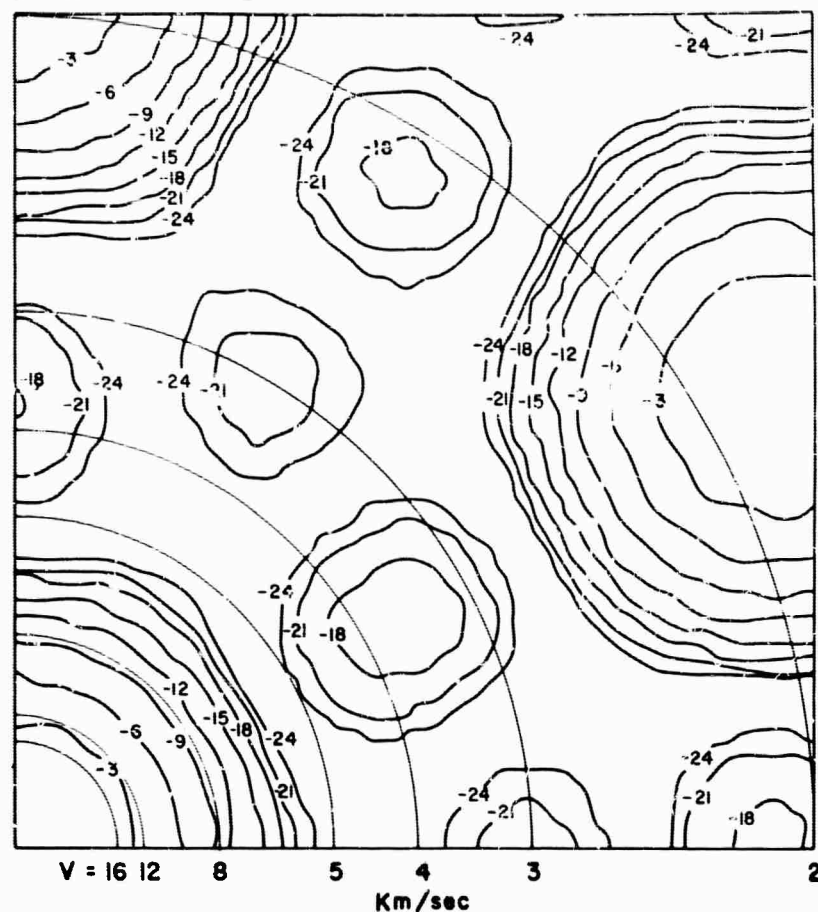
IP 25 at 2.0 cps



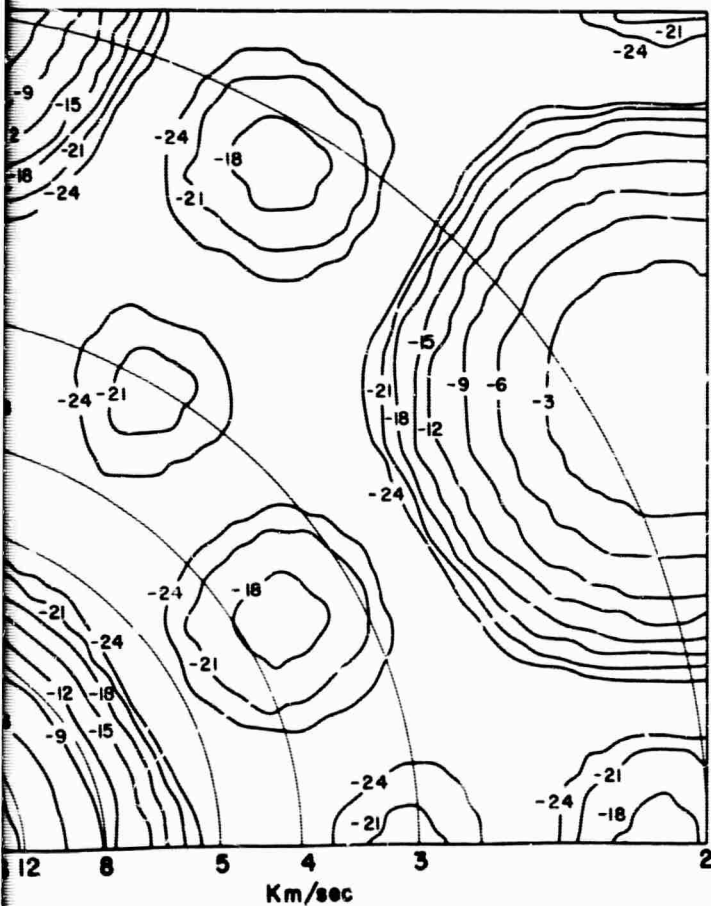
2.0 cps



IP 24 at 2.0 cps



2.0 cps



IP 26 at 2.0 cps

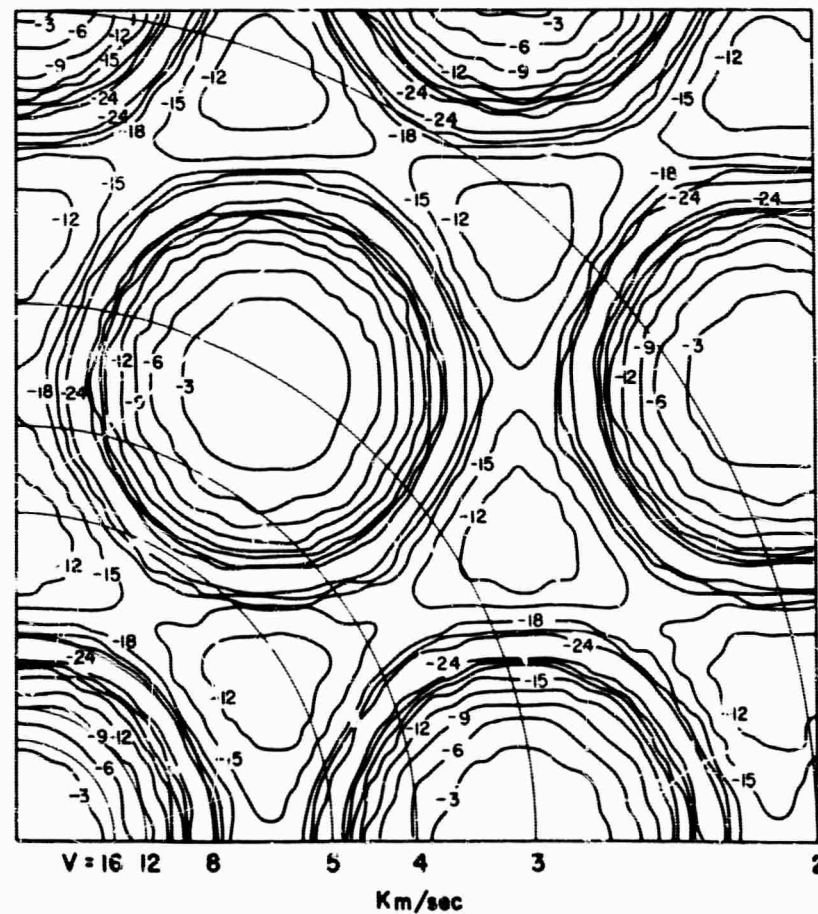
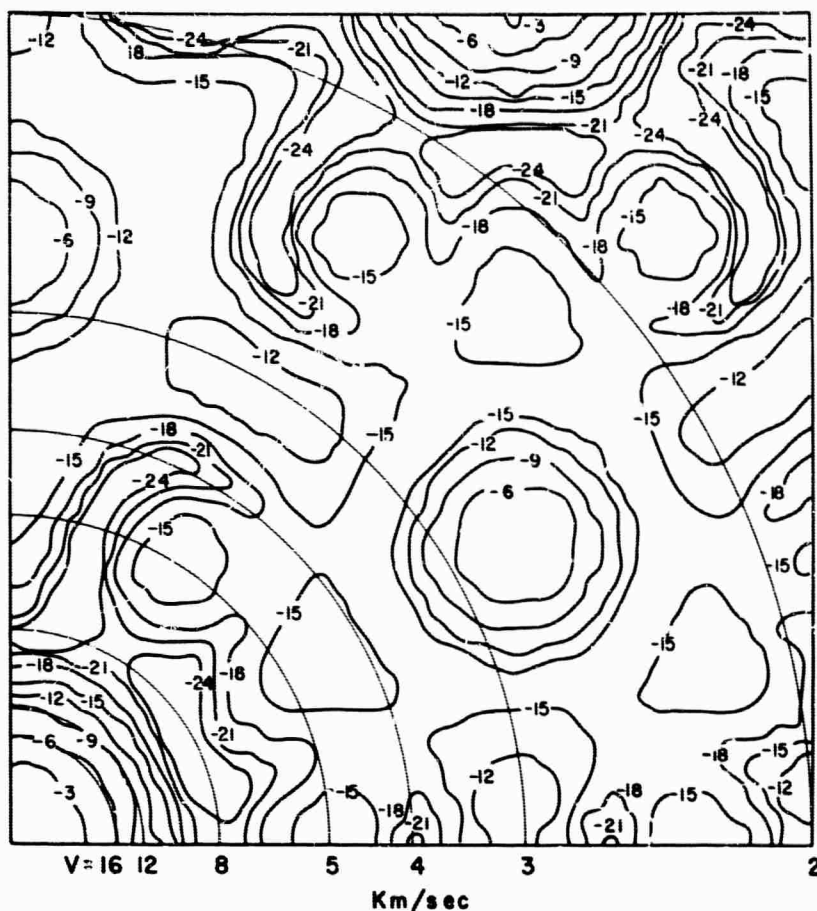
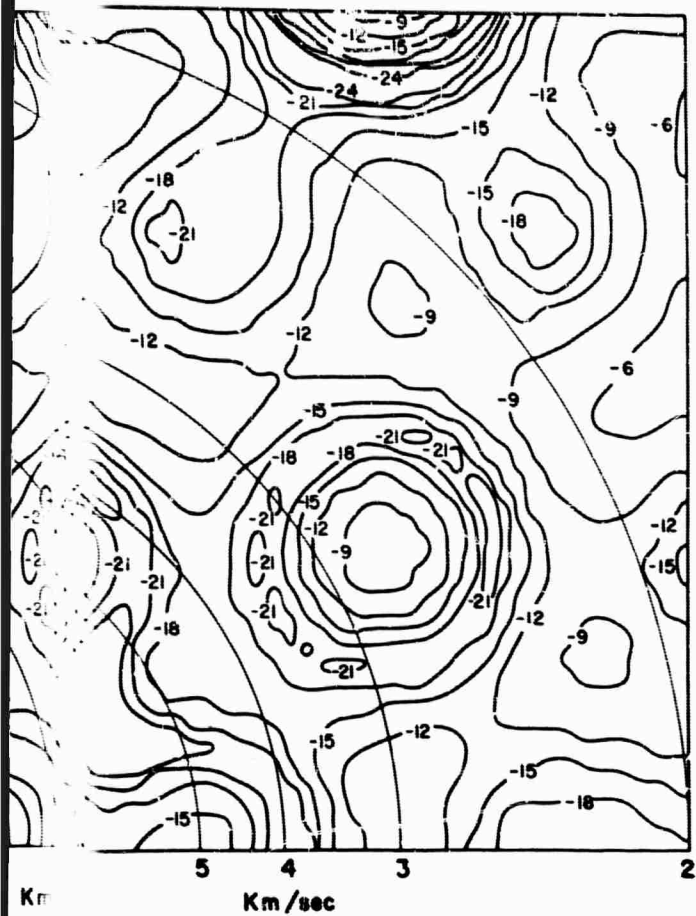


Figure IV-19. Wavenumber Responses of the Multichannel Filter Systems and Wavenumber Distribution of the Noise Power at 2.0 Cps

B

cps

IP 24 at 3.0 cps



cps

IP 26 at 3.0 cps

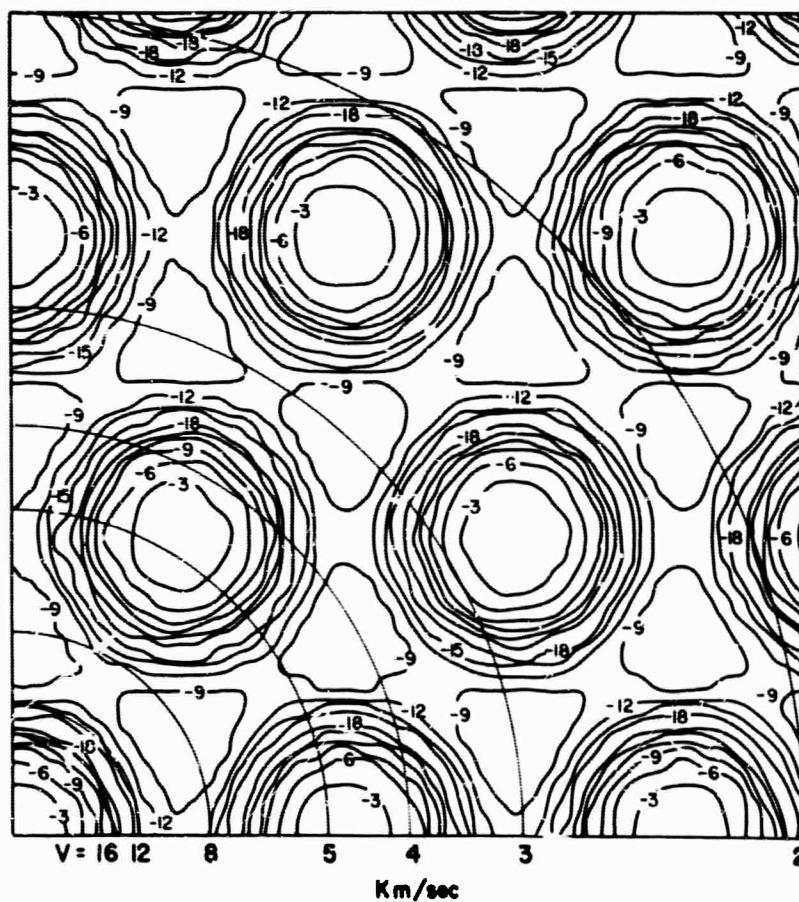
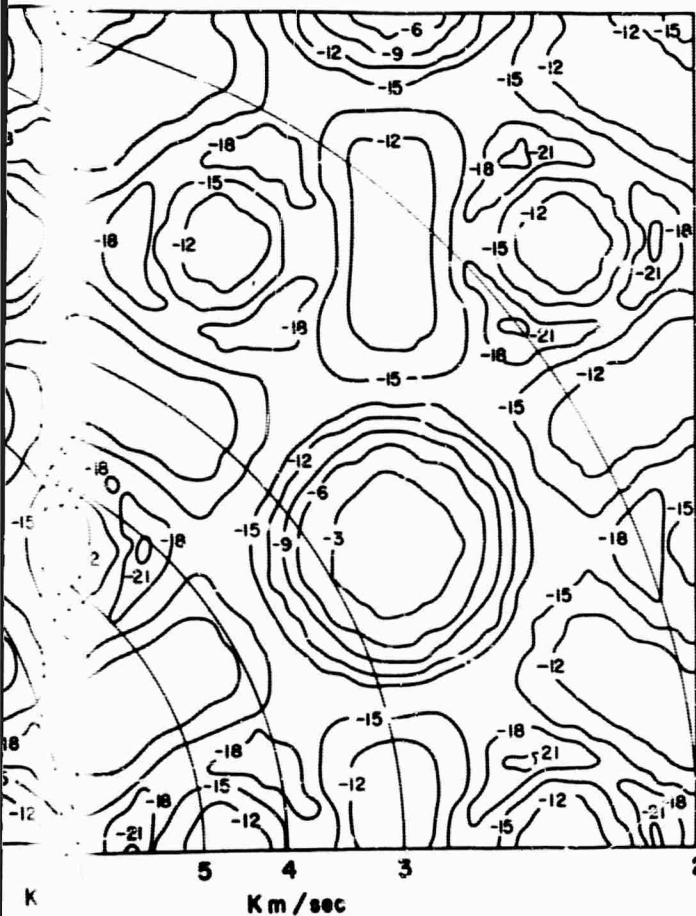


Figure IV-20. Wavenumber Responses of the Multichannel Filter Systems and Wavenumber Distribution of the Noise Power at 3.0 Cps

B

IP 25 attenuates most strongly plane waves with a velocity of about 3 km/sec, and IP 26 attenuates most strongly plane waves with a velocity of about 3.5 km/sec. The systems show markedly different K-space responses. This is characteristic of MCF systems which have seismometer gain inequalities. The K-space plots show the MCF systems responses as they would appear if all seismometers were gained equally. The actual MCF systems, which incorporate seismometer gain inequalities, probably have similar wavenumber responses at 0.5 cps. A detailed study of seismometer gain inequality effects has been published.¹³

The noise power at 0.5 cps falls off rapidly on the annulus representing horizontal velocities of less than 2 km/sec. This strongly affects the responses of the systems. Indeed, IP 26, which suppresses noise almost as well as the other systems at this frequency, actually gains up the power of plane wave with these velocities.

At 0.5 cps, all systems preserve power in plane waves with velocities greater than 12 km/sec. In no case is such a wave attenuated by as much as 3 db.

Figure IV-18 shows wavenumber responses of IP 23, 24, 25, and 26 and the noise power spectra in the K-plane at 1 cps. Comparison of noise spectra with the various system responses gives good general agreement with the S/N improvement of the multichannel filter systems at 1 cps.

On the disk representing velocity greater than 3 km/sec, all the MCF systems have similar responses. This corresponds to velocities where the noise power is generally concentrated. As would be expected, all systems give about the same S/N improvement (10 db) at 1 cps with a difference of only about 1 db.

Aliasing and pseudo-aliasing show up in the MCF response maps, but their effect is outside the range of appreciable noise power concentration. The only true alias shows on the map of IP 26.

All MCF systems preserve plane wave energy with horizontal velocities greater than 12 km/sec. On the circle representing these velocities, power is down less than 3 db for all systems.

Figure IV-19 shows wavenumber responses of IP 23, 24, 25, and 26 and the noise power spectrum in K-space at 2 cps. Comparison of system responses to noise distribution gives generally good agreement with the observed S/N improvement of the MCF systems at 2 cps.

The noise power at 2 cps is strongly concentrated in an annulus representing velocities between 3.5 and 5 km/sec. In this same annulus, IP 23, 24 and 25 exhibit attenuation of 18 db or more. In general, K-space response of each of these systems is very similar. At 2 cps,

channels 2 and 3 of IP 23 and channel 3 of IP 24 are contributing relatively little to the output of the MCF systems. At 2 cps, all these systems show equal S/N improvement within 1 db.

IP 26 shows space-aliasing which results in passing much of the noise energy at 2 cps. As this would indicate, S/N improvement at 2 cps is about 12 db less for IP 26 than for the other systems.

IP 23, 24 and 25 preserve plane wave power for velocities above 12 km/sec. These systems show attenuation of 4 db or less on this range of velocities. IP 26, however, attenuates plane waves with a velocity of 12 km/sec approximately 10 db.

Figure IV-20 shows wavenumber responses of IP 23, 24, 25, and 26 and the spectrum of the noise power at 3 cps. Comparison of system responses with noise power spectra again gives generally good agreement with the observed S/N improvement ratios at 3 cps.

The noise power is generally concentrated in an annulus representing velocities around 4 km/sec. Total noise power at 3 cps is down 5-10 db from the frequencies previously considered.

In the stronger noise band, the responses of IP 23, 24 and 25 are quite variable. IP 23 attenuates the noise somewhat better than IP 24 which, in turn, is a better system than IP 25. True aliasing occurs in IP 25 just on the edge of the band of noise power concentration. At 3 cps, the S/N improvement differences among these three systems are about 5 db, with IP 23 being best and IP 25 poorest on both processed noise samples.

Close-spaced aliasing dominates the IP 26 wavenumber response at 3 cps. This system would have relatively poor ability to attenuate noise in any reasonable velocity band. As this would indicate, the S/N improvement of IP 26 is down about 10 db from that of IP 23 at 3 cps.

At 3 cps, none of the MCF systems satisfactorily preserves the energy of 12-km/sec plane waves. All systems show attenuation of more than 6 db in this velocity range. This bad tendency becomes more marked as the number of seismometers is reduced. IP 26 attenuates high-velocity plane waves ($V > 12$ km/sec) as much as 18 db.

Analysis of wavenumber responses of the various systems taken with S/N improvement indicates that

- Seismometer gain inequalities appear to be affecting MCF systems significantly below 1 cps
- Below about 1-1/2 cps, IP 26 (seven seismometers) is almost as good a system as IP 23 (19 seismometers); i.e., below 1.5 cps, IP 26 preserves signals with apparent horizontal velocities > 12 km/sec and suppresses noise almost as well as IP 23.
- Below 2-1/2 cps, IP 25 (13 seismometers) is very nearly the equal of IP 23 (19 seismometers). Again, the desirable system preserves signal with propagation velocities > 12 km/sec and suppresses noise.

Thus, for evaluation of distant P-wave signals, IP 25 is essentially as good as IP 23, and IP 26 is nearly as good as IP 23. It is apparent that R2 and R3 contribute little to the ability of the CPO array to enhance distant mantle P-wave signals. R4 is of questionable value. Seis gain inequalities may be affecting the comparisons below 3/4 cps, so the value of R4 has not been definitely determined. MCF systems which will be designed incorporating statistical gain fluctuations should help evaluate the usefulness of R4.

BLANK PAGE

SECTION V

INITIAL PROCESSING AND ANALYSIS OF THE LONG TFO NOISE SAMPLE

This section contains information concerning the recording and preliminary processing and analysis of a 20-min ambient seismic noise sample from the ring array, the large cross array and a 3-component seismometer at Tonto Forest Seismological Observatory. Also presented is an analysis of calibration data for the large cross array recorded on the same day as the long noise sample. Section VI contains a more detailed analysis of this noise sample.

A. RECORDING AND PRELIMINARY PROCESSING AND ANALYSIS

A long sample of ambient seismic noise, slightly less than 20 min long, was edited from a DFS recording taken at Tonto Forest Seismological Observatory on December 20, 1963. During this time period, average wind velocity was 1 to 5 mph, and the temperature was 20° F. This noise sample was free of recording errors and appeared to be free of non-seismic noise such as spiking. The sampling period of the field recording was 24 msec, which gives 50,000 points in 20 min. Because of limitations on input computer capacity, this long noise sample was divided into 10 samples labeled C, D, E, F, G, H, I, J, K, and L, respectively, which were 2 min each in duration with a 2 sec overlap in time for every two adjacent noise samples. Thus, each of the 10 noise samples contained 5000 points with an average overlap of 83-1/3 points in the adjacent noise samples. The GCT start time for noise sample C was 05:55:00, and the GCT stop time for noise sample L was 06:14:42.

Figure V-1 shows the geometry of Tonto Forest Seismological Observatory. Table V-1 shows the trace position of seismometers and rings on the field reel. The first five traces contain the ring-averaged summations. Ring 1 is seismometer Z16, and the remaining four rings are the averaged sums of the seismometers in their respective rings. Thus, ring 2 consists of seismometer Z10, Z11, Z17, Z22, Z21, and Z15; ring 3 of seismometers Z5, Z12, Z23, Z27, Z20, and Z9; ring 4 of seismometers Z4, Z6, Z18, Z28, Z26, and Z14; and ring 5 of seismometers Z1, Z2, Z7, Z13, Z24, Z29, Z31, Z30, Z25, Z19, Z8, and Z3. Traces 6 through 16 are the 11 seismometers in the NS arm of the cross array, with the seismometers going in order from south to north. Traces 17 through 26 are the seismometers in the EW arm, proceeding east to west except that the center seismometer is not repeated and that seismometers 70 and 25 are interchanged. Trace 27 contains vertical seismometer Z1. Traces 28 and 29 contain the

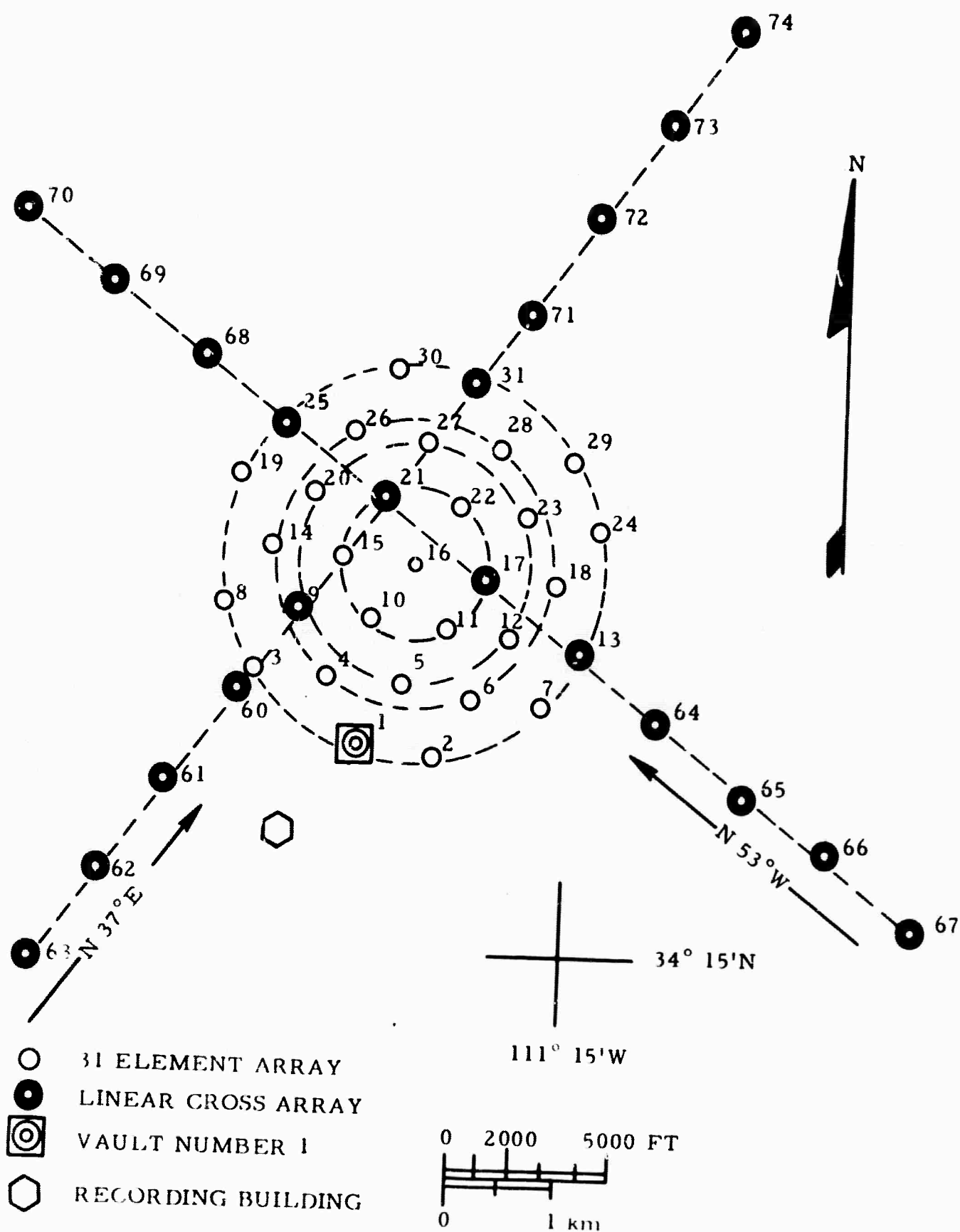


Figure V-1. Arrays at Tonto Forest Seismological Observatory (TFO)

Table V-1

TRACE IDENTIFICATION, MOTOR CONSTANTS
AND GROUND DISPLACEMENTS

<u>Trace No.</u>	<u>Seismometer Identification</u>	<u>G (newtons/amp)</u>	<u>Ground Displacement (mm 0-P)</u>
1	Z16		
2	R2		
3	R3		
4	R4		
5	R5		
6	Z63	0.425	17.92
7	Z62	0.410	17.29
8	Z61	0.430	18.13
9	Z60	0.420	17.71
10	Z9	0.415	17.50
11	Z21	0.405	17.08
12	Z31	0.435	18.35
13	Z71	0.415	17.50
14	Z72	0.445	18.77
15	Z73	0.425	17.92
16	Z74	0.420	17.21
17	Z67	0.415	17.50
18	Z66	0.415	17.50
19	Z65	0.395	16.66
20	Z64	0.350	14.76
21	Z13	0.415	17.50
22	Z17	0.445	18.77
23	Z70	0.410	17.29
24	Z68	0.420	17.71
25	Z69	0.405	17.08
26	Z25	0.425	17.92
27	Z1		
28	Z36 E-W		
29	Z37 N-S		
30	Cal. T.B.		
31	GCT		

east-west and north-south horizontal seismometers, respectively. These two seismometers are located in the vault with seismometer Z1. Trace 30 which is used for recording the calibration signal during station calibration was blank during this recording, and trace 31 contained the GCT timing pulses.

The first 27 traces, i.e. the five rings, the linear cross array and seismometer Z1, of each of the 10 noise samples were filtered with a symmetric 43-point prewhitening and antialiasing filter and then decimated by 3 to yield filtered 72-msec data. Traces 28 and 29 which contain the output of the east-west and north-south horizontal seismometers, respectively, were not filtered but were decimated. The square wave function, which was placed in trace 30 during the running of the Edit II program and may be used to generate timing lines for playback purposes, also was decimated by 3. The Edit II information on these 10 noise samples has been presented in a previous report.² The frequency response of the prewhiten-filter is in Figure V-2. In applying this 43-point filter to the 10 noise samples, only the completely filtered outputs were desired. Thus, the outputs were 21 points shorter on each end. This was the reason for having overlap in the 10 noise samples. To join the 10 noise samples back into one long

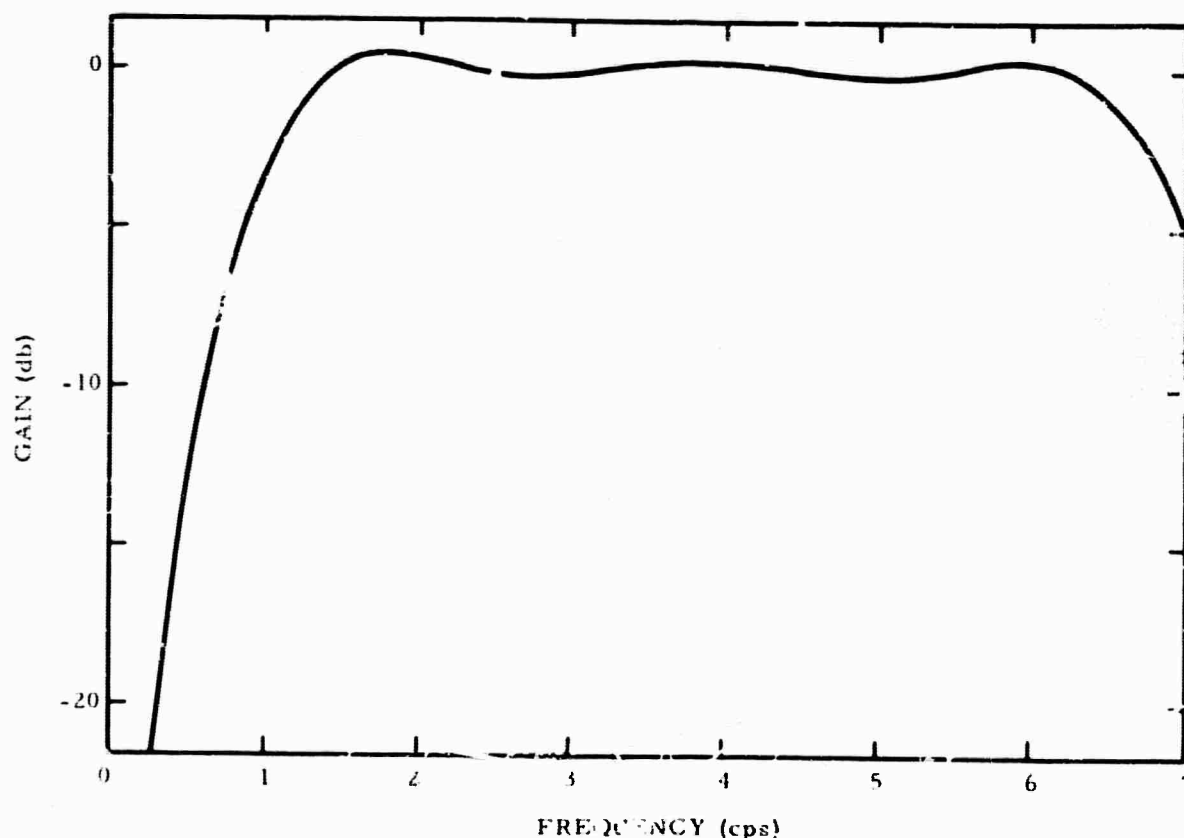


Figure V-2. Frequency Response of Prewhitening and Antialiasing Filter

sample after decimation by 3, special care had to be taken in where to start the decimation of each noise sample to insure that the long noise sample did contain every third point in time after joining the decimated samples. When the 10 filtered and decimated noise samples were appended, there were 16,407 points with a frequency range from 0 to $6-17/18$ cps.

Power density spectra were computed from the long noise sample for each of the 21 seismometers in the linear cross array. Figures V-3 through V-6 show these spectra which were obtained from autocorrelations with lags out to $\tau = \pm 61$. Also, the spectral ratios relative to the center seismometer, seismometer Z21, were computed for each of the other 20 seismometers. These results are pictured in Figures V-7 through V-10.

Two channel coherence estimates also were computed at this time for seismometers Z63 and Z64, Z65 and Z66, and Z68 and Z69. These coherences, shown in Figures V-11 and V-12, were found from correlation functions with lags out to $\tau = \pm 124$. In this set of illustrations, the notation 63 x 64 refers to the coherence between seismometers Z63 and Z64.

The prewhitened long noise sample was bandpass-filtered and again resampled by 3 to yield 216-msec data with a frequency range of 0 to $2-17/54$ cps. At this point, the data also were scaled by a factor of 4. Figure V-13 shows the frequency response of this long decimation-by-3 filter over the range of 0 to $6-17/18$ cps and also of 0 to $2-17/54$ cps.

A 6-point deconvolution filter designed from seismometer Z21 with 10 percent white noise was applied to the 216-msec data. The frequency response of this filter is shown in Figure V-14, and the combined response of the three filters which have been applied to the long noise sample are shown in Figure V-15. For completeness, Figure V-16 shows the response of the J-M PTA system used at TFO.

Power density spectra with maximum lag of $\tau = \pm 61$ for seismometers Z62, Z21, Z73, Z65, and Z70 are shown in Figure V-17. These spectra were taken after the 216-msec data were deconvolved.

B. CALIBRATION ANALYSIS OF THE LARGE CROSS ARRAY

A calibration run at 1 cps on the linear cross array was recorded on the same date as the preceding noise recording. The GCT start time for the calibration was 04:15:32, and the GCT stop time was 04:16:00 for all 21 seismometers. Taking into account the motor constants of the seismometers, these calibration data were analyzed to give absolute scales for the power density spectra of the earth motion at 1 cps.

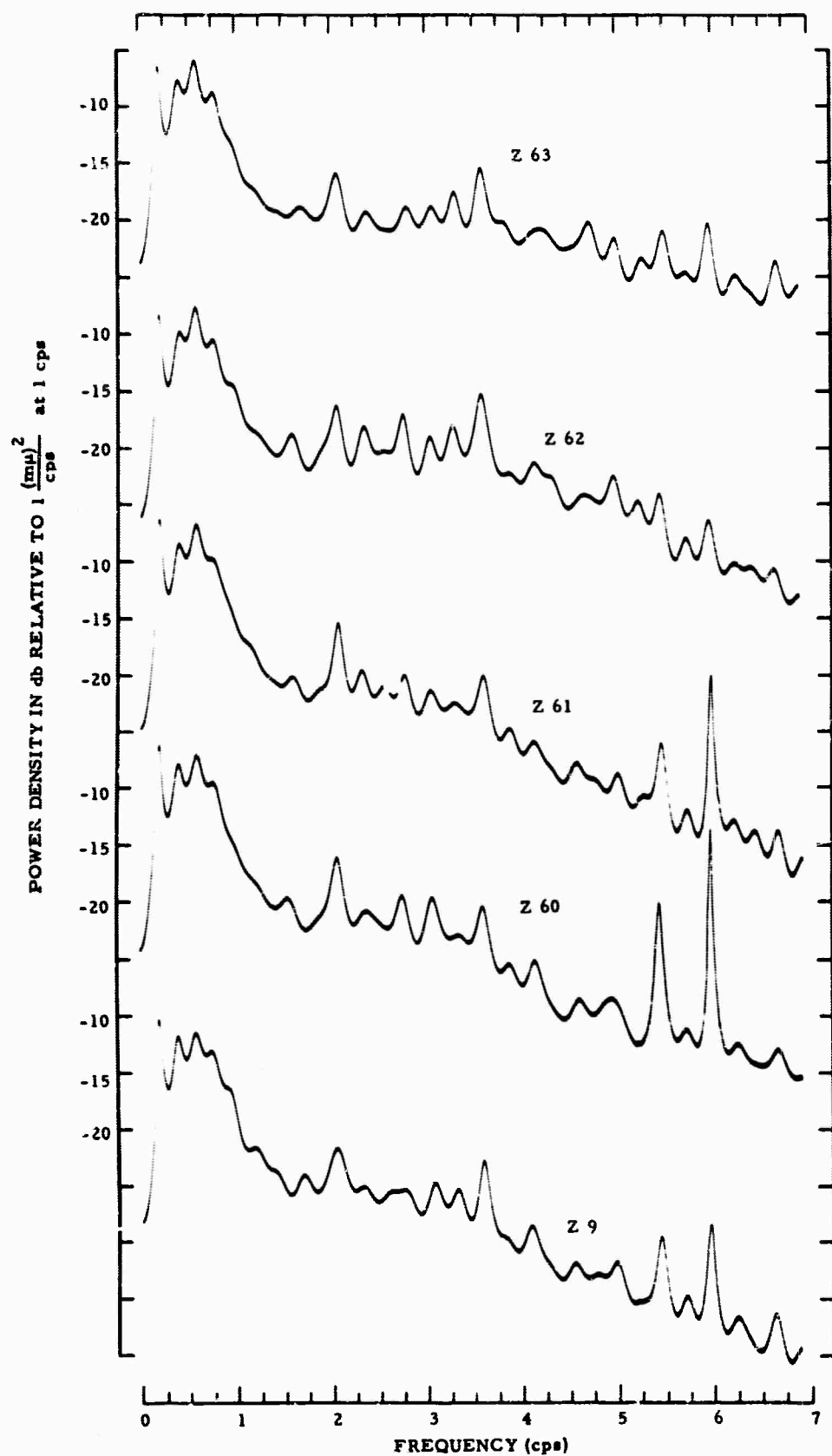


Figure V-3. Power Spectra of Seismometers Z63, Z62, Z61, Z60, and Z9

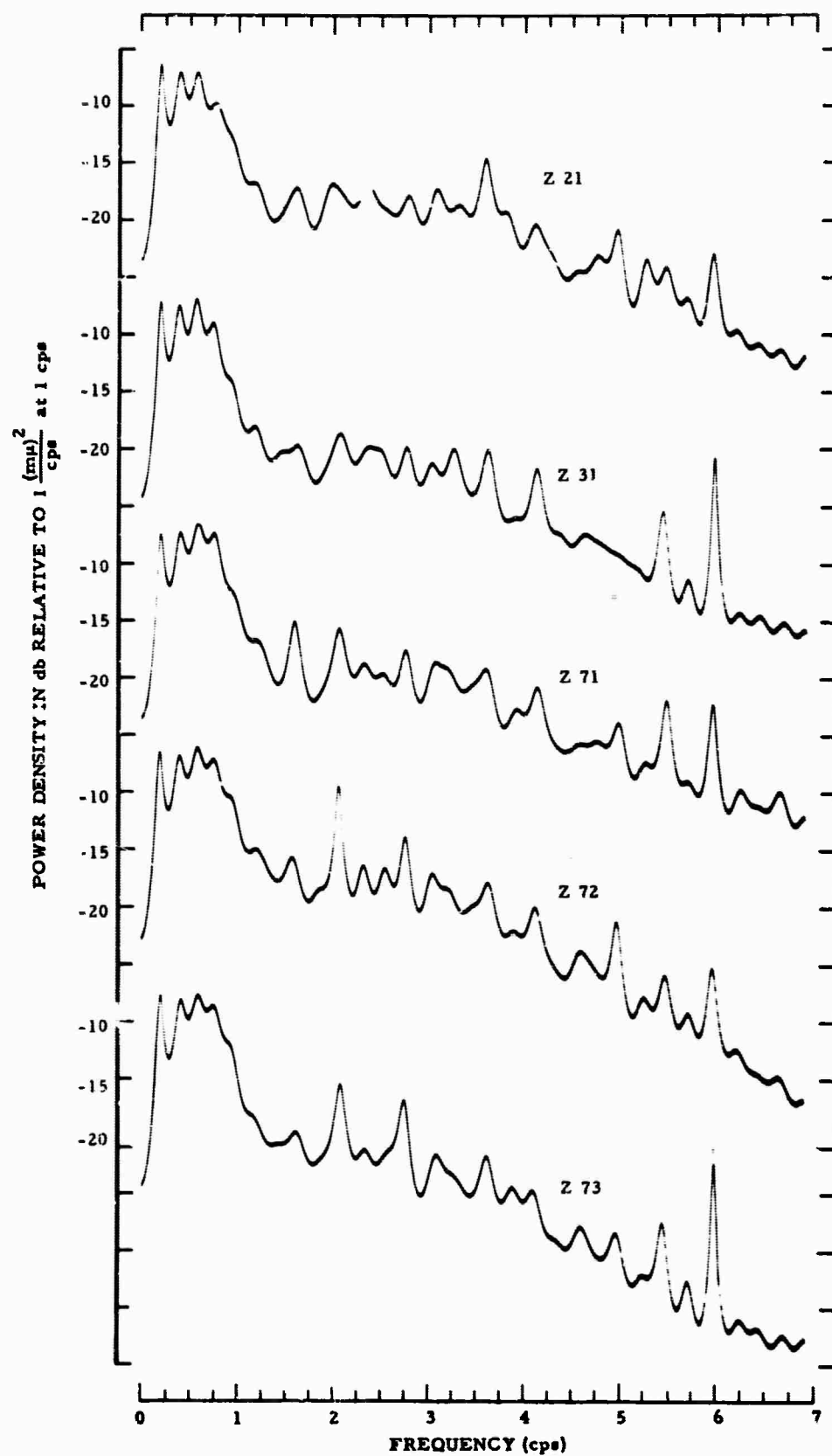


Figure V-4. Power Spectra of Seismometers Z21, Z31, Z71, Z72, and Z73

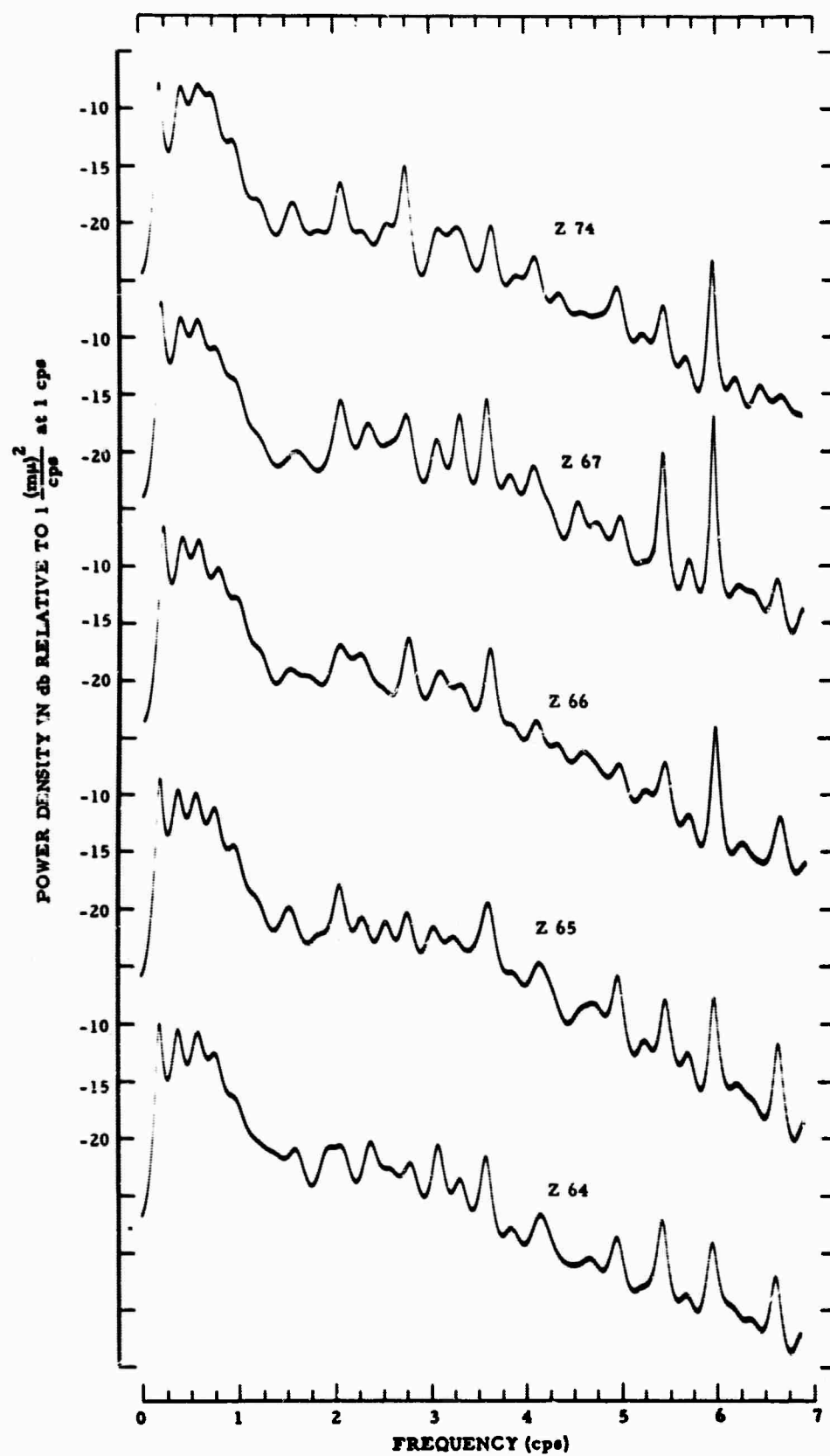


Figure V-5. Power Spectra of Seismometers Z74, Z67, Z66, Z65, and Z64

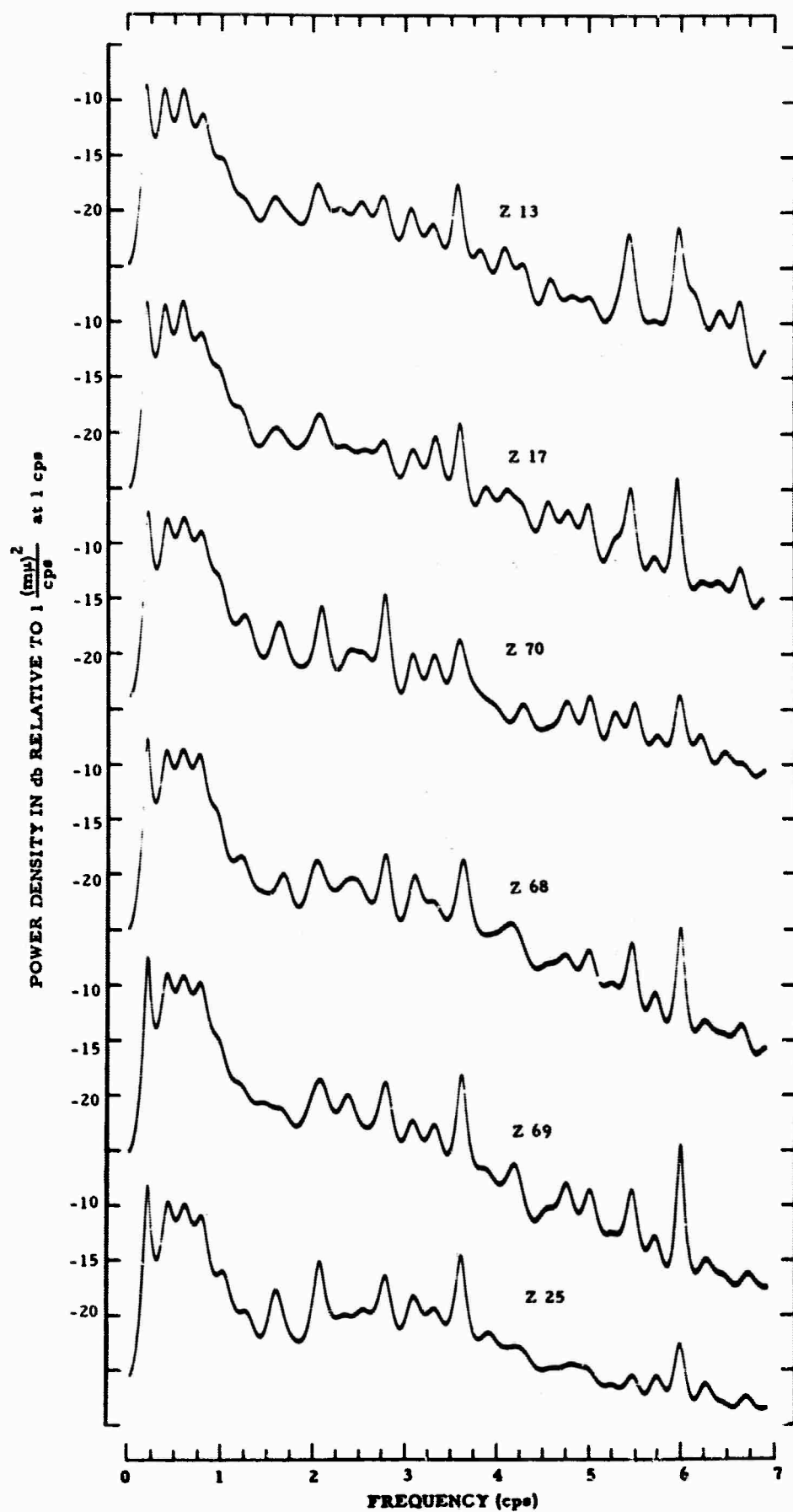


Figure V-6. Power Spectra of Seismometers Z13, Z17, Z70, Z68, Z69, and Z25

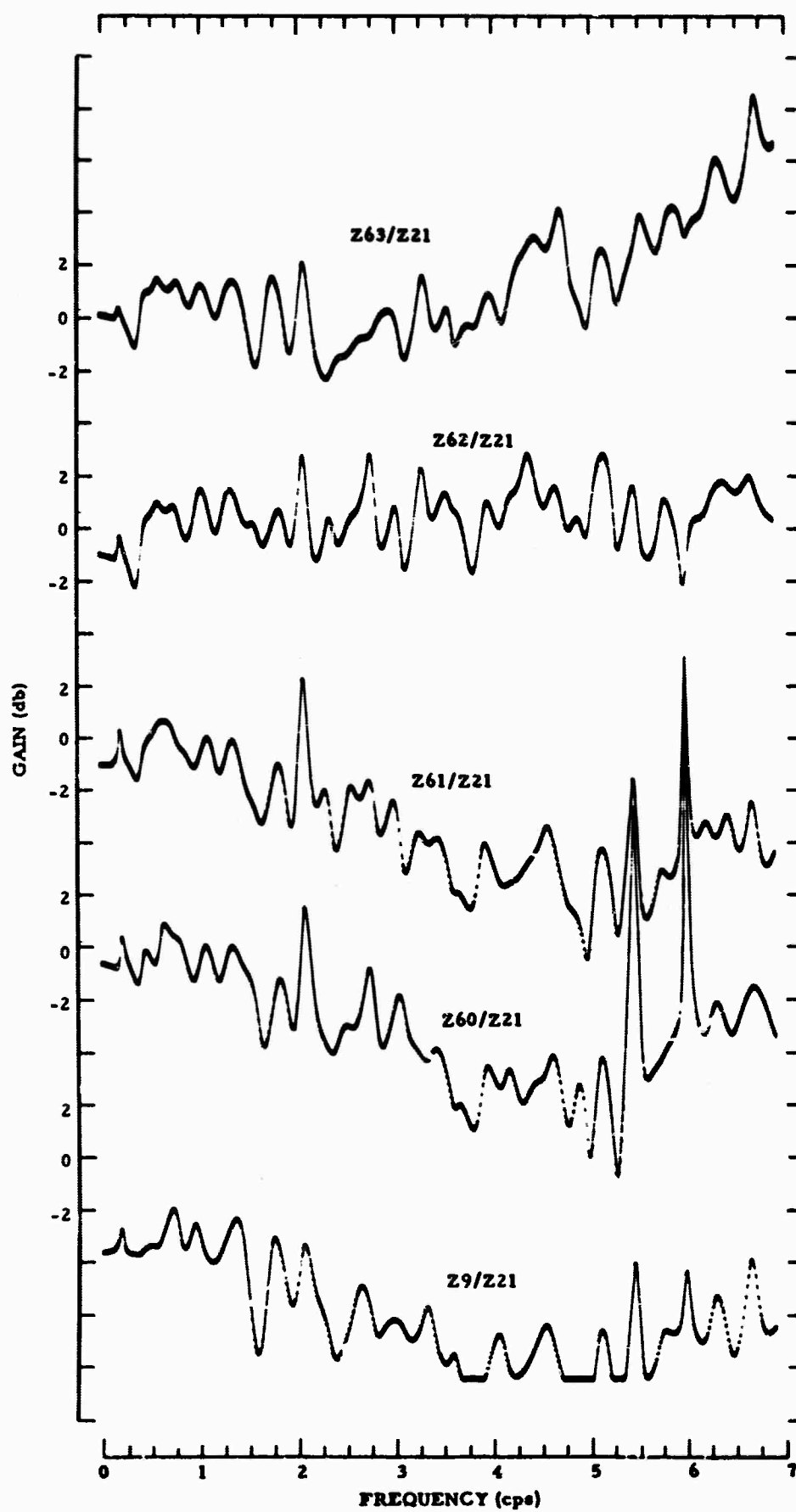


Figure V-7. Power Spectra Ratios of Z63, Z62, Z61, Z60, and Z9 Relative to Seismometer Z21

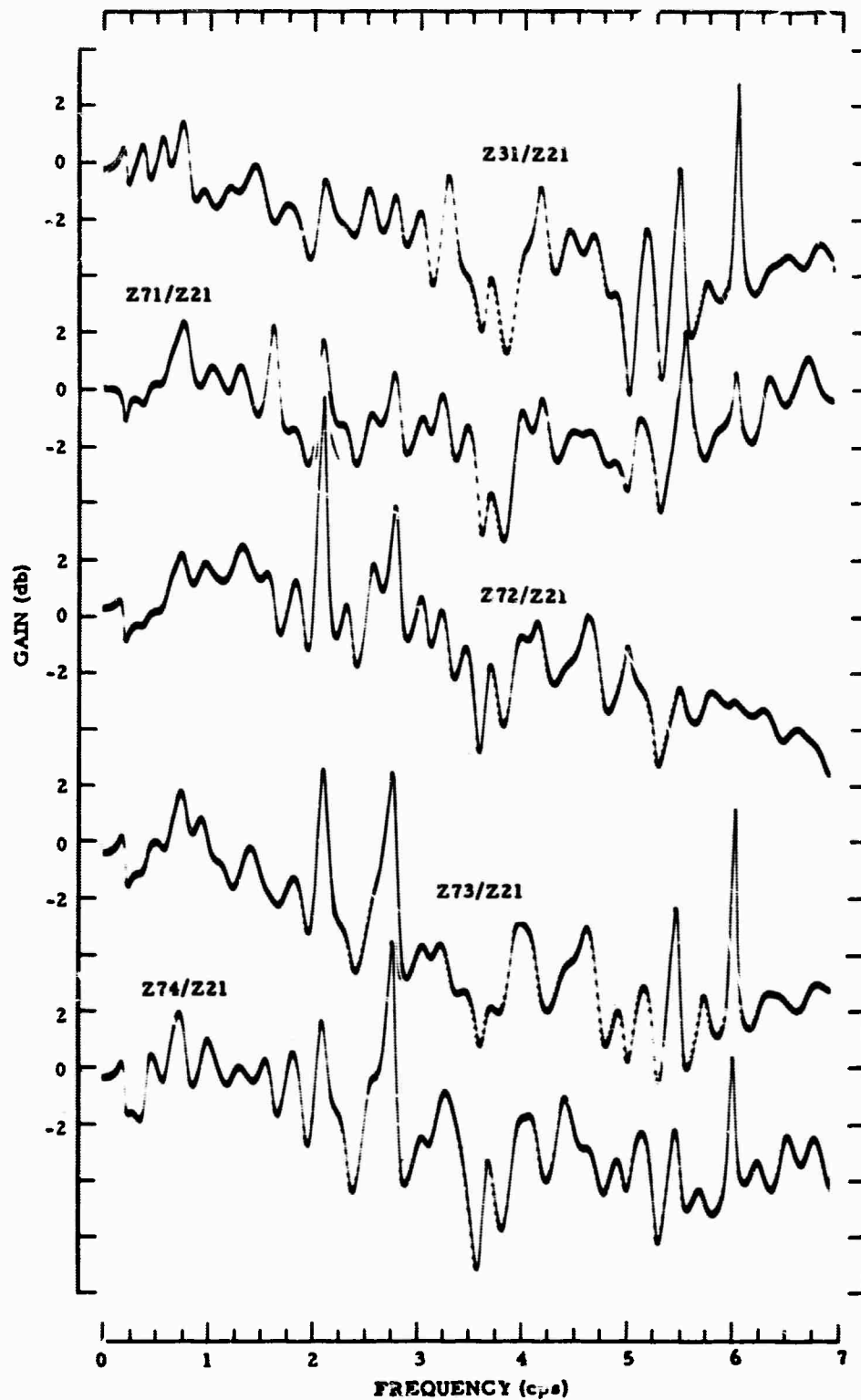


Figure V-8. Power Spectra Ratios of Z31, Z71, Z72, Z73, and Z74 Relative to Seismometer Z21

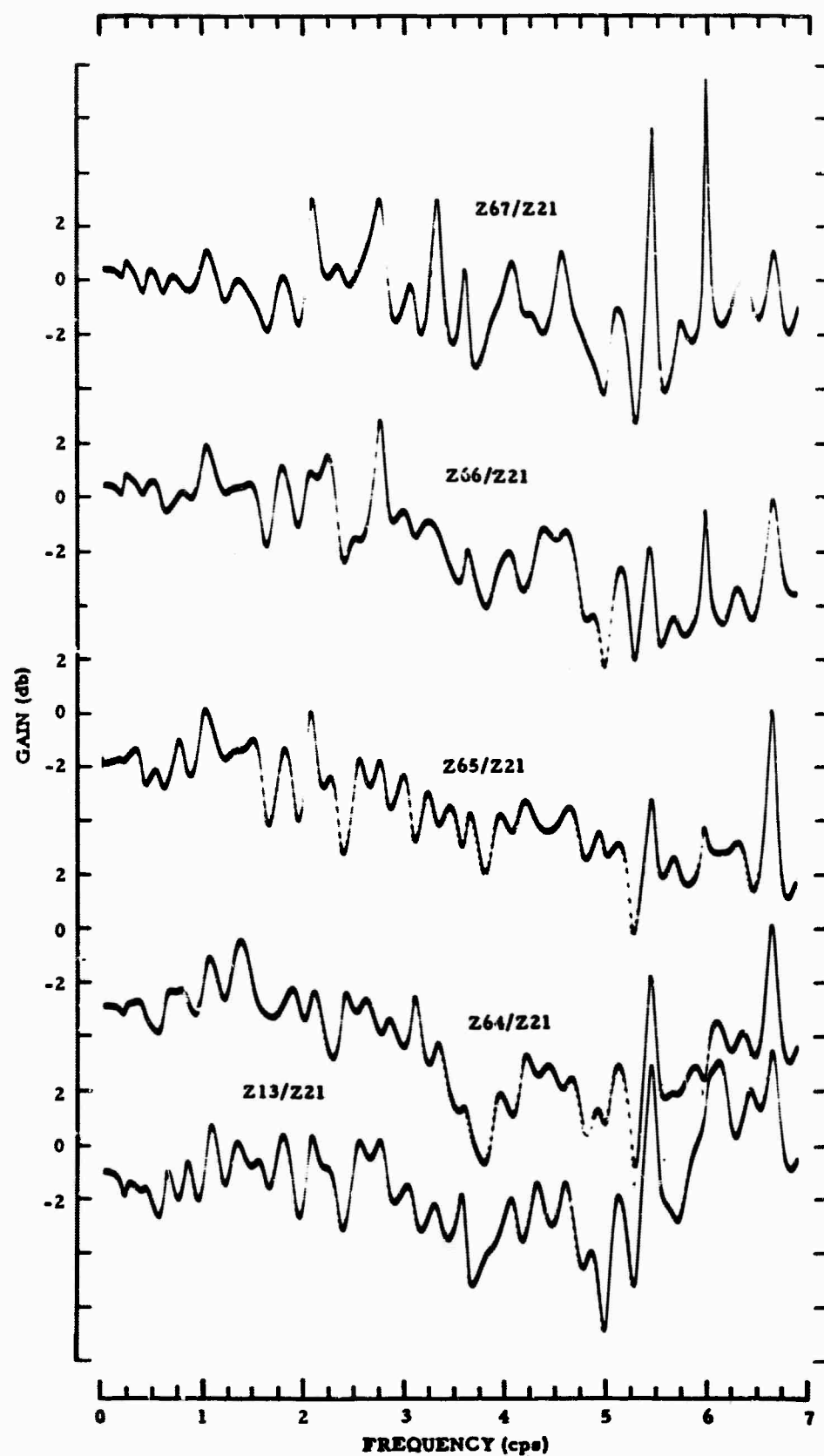


Figure V-9. Power Spectra Ratios of Z67, Z66, Z65, Z64, and Z13 Relative to Seismometer Z21

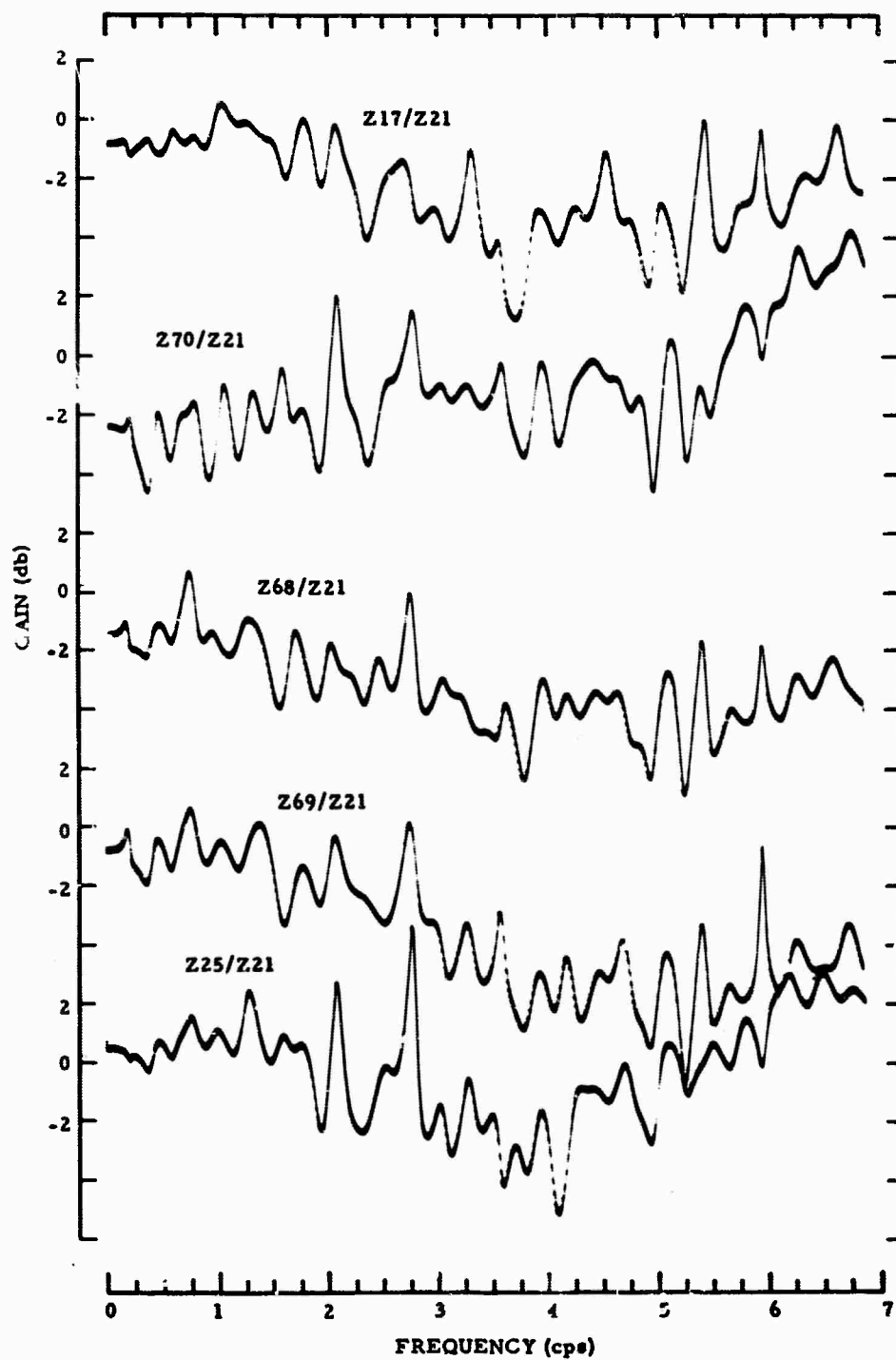


Figure V-10. Power Spectra Ratios of Z17, Z70, Z68, Z69, and Z25 Relative to Seismometer Z21

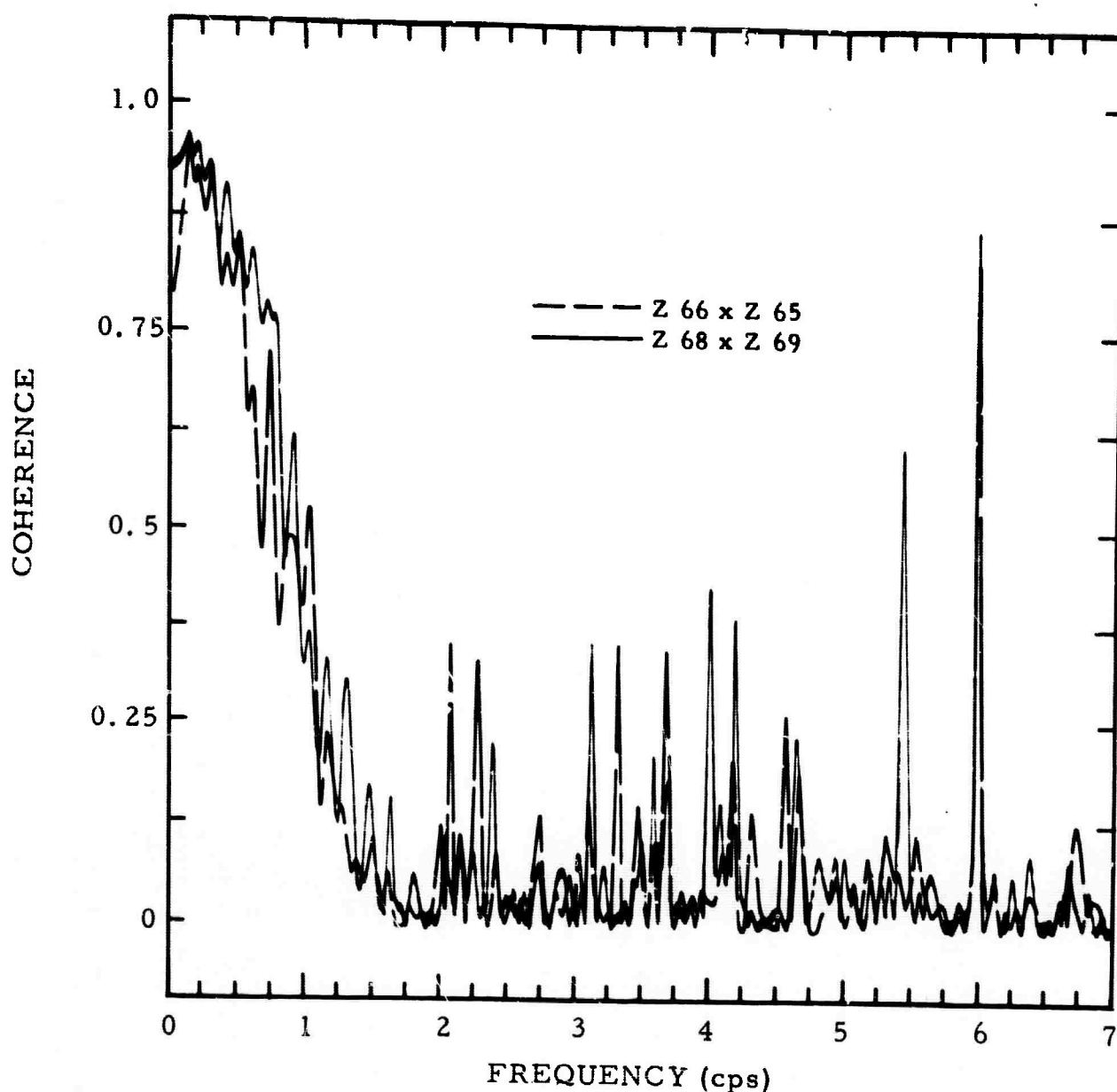


Figure V-11. Coherences Between Seismometers Z66 and Z65 and Between Seismometers Z68 and Z69

On occasion, the motor constant of calibration coil G in the J-M seismometers at TFO is checked. The motor constant is determined in the following manner. Several weight lifts are taken with a weight whose mass is W_t grams, and the trace deflection X_w is recorded in millimeters for each trial. Then d-c pulses I in amperes are applied to the calibration coil and the current adjusted until the trace deflection due to current X_i is within 10 percent of X_w in amplitude. The corresponding X_i and I then are used in the following formula to calculate G:

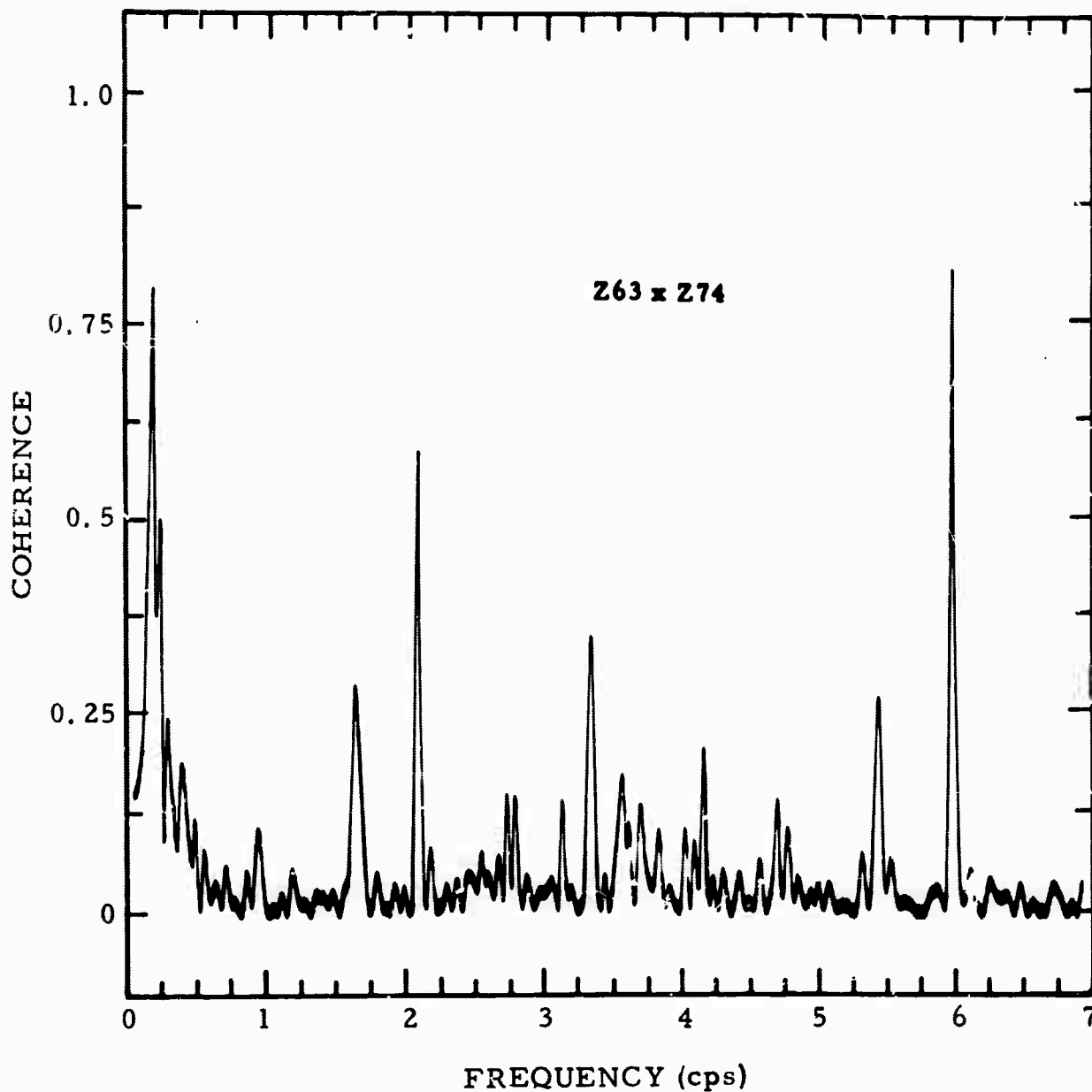


Figure V-12. Coherence Between Seismometers Z63 and Z74

$$G = \frac{980 \times 10^{-5} w_t \left(\frac{x_i}{x_w} \right)}{I} \text{ newtons/ampere}$$

Table V-1 also shows the motor constants of the seismometers in the linear cross array. These motor constants were taken from a data sheet dated December 16, 1963.

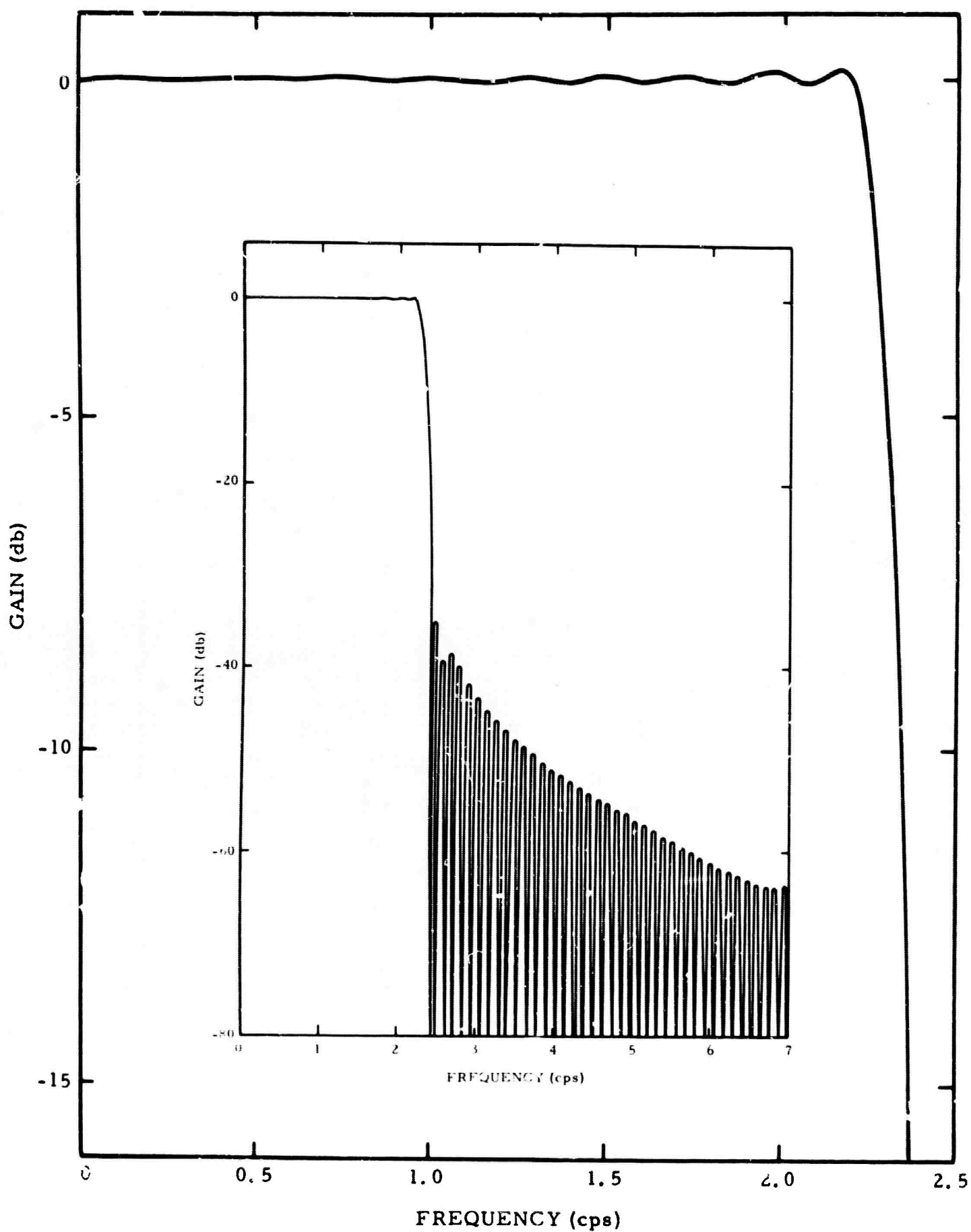


Figure V-13. Frequency Response of Bandpass Filter, 0 to 2-17/54 cps

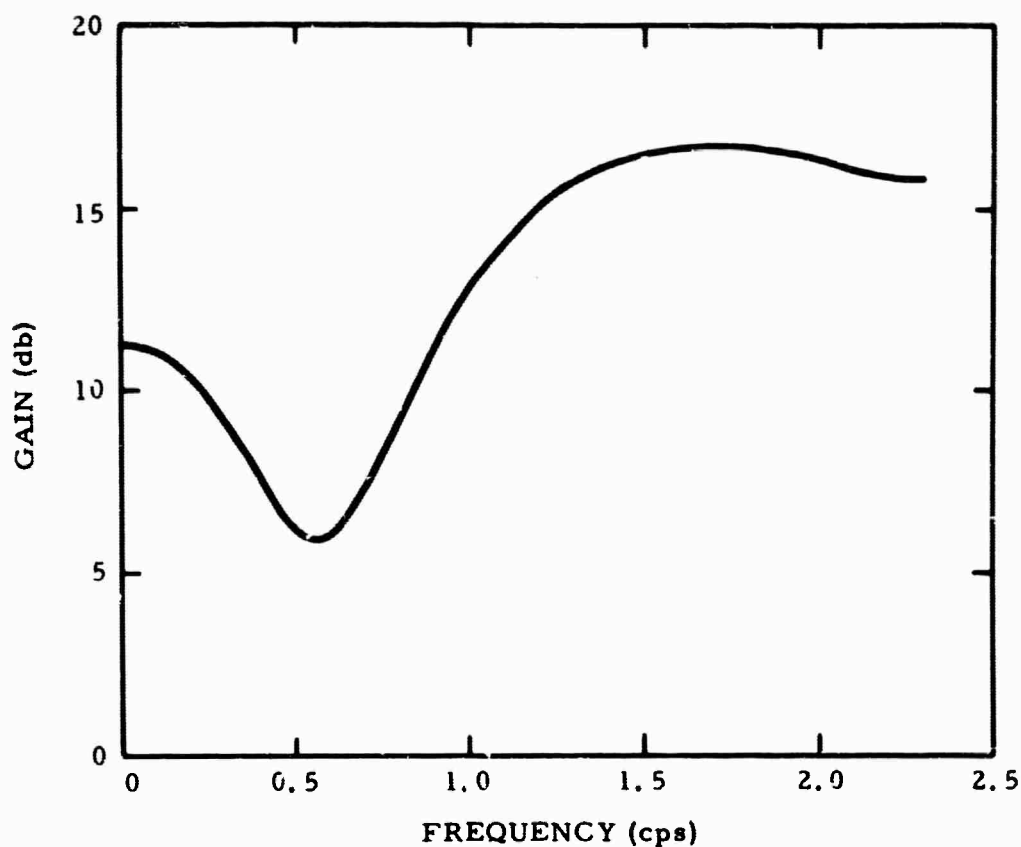


Figure V-14. Frequency Response of the Deconvolution Filter

The formula used for computing earth motion in millimicrons zero-to-peak is

$$\text{Earth Motion in } \mu\text{m 0-P} = \frac{G \times I \times 10^6}{4\pi^2 f^2 M}$$

where G is the motor constant in newtons/ampere, I is the input current in milliamps 0-P, f is the frequency in cps, and M is the mass of the seismometer in kilograms. The mass of the Johnson-Matheson seismometer was 18.02 kg, frequency was 1 cps and input current was 0.03 ma 0-P. The computed equivalent earth motions also are listed in Table V-1.

Ground displacement for seismometer Z63 was 17.92 μm zero-to-peak. At the time of the calibration, the DFS contained a -12 db attenuator card but, during the noise recording, no attenuation was used. Therefore, effective displacement can be considered to be 4.48 μm zero-to-peak.

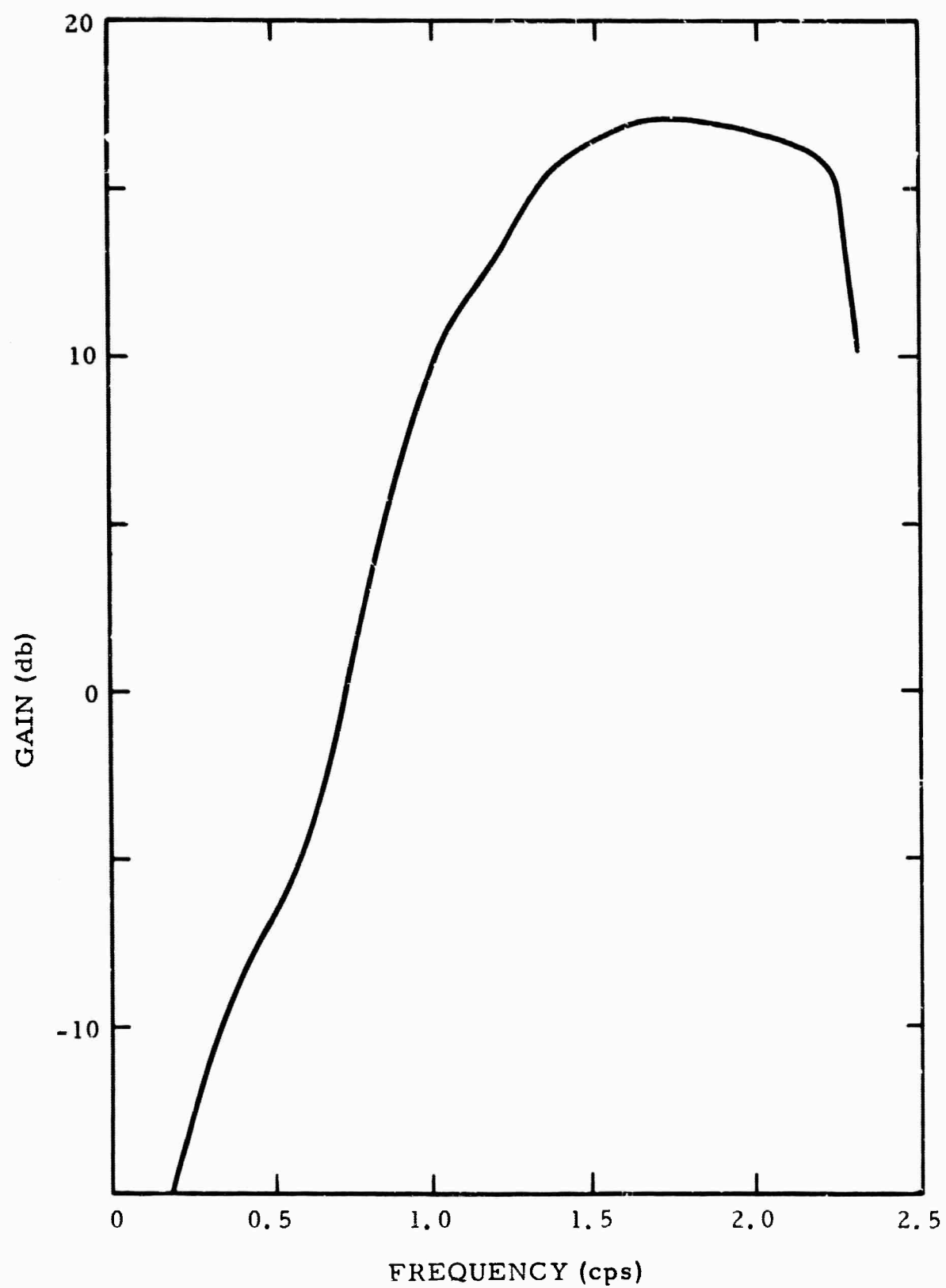


Figure V-15. Combined Frequency Response of the Prewhitening Filter, the Bandpass Filter and the Deconvolution Filter

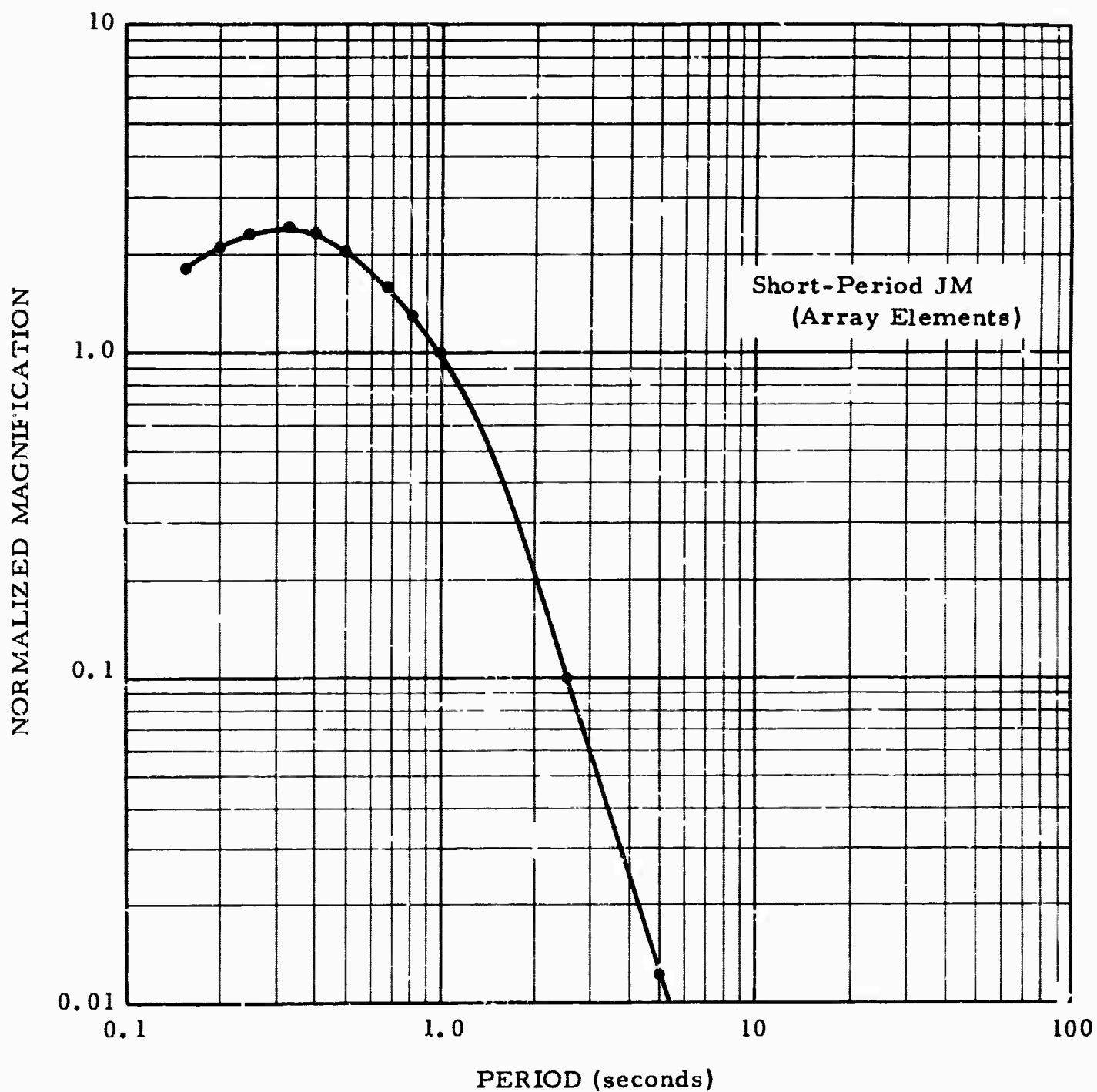


Figure V-16. Response of the J-M Data PTA Seismometer System
Used at TFO

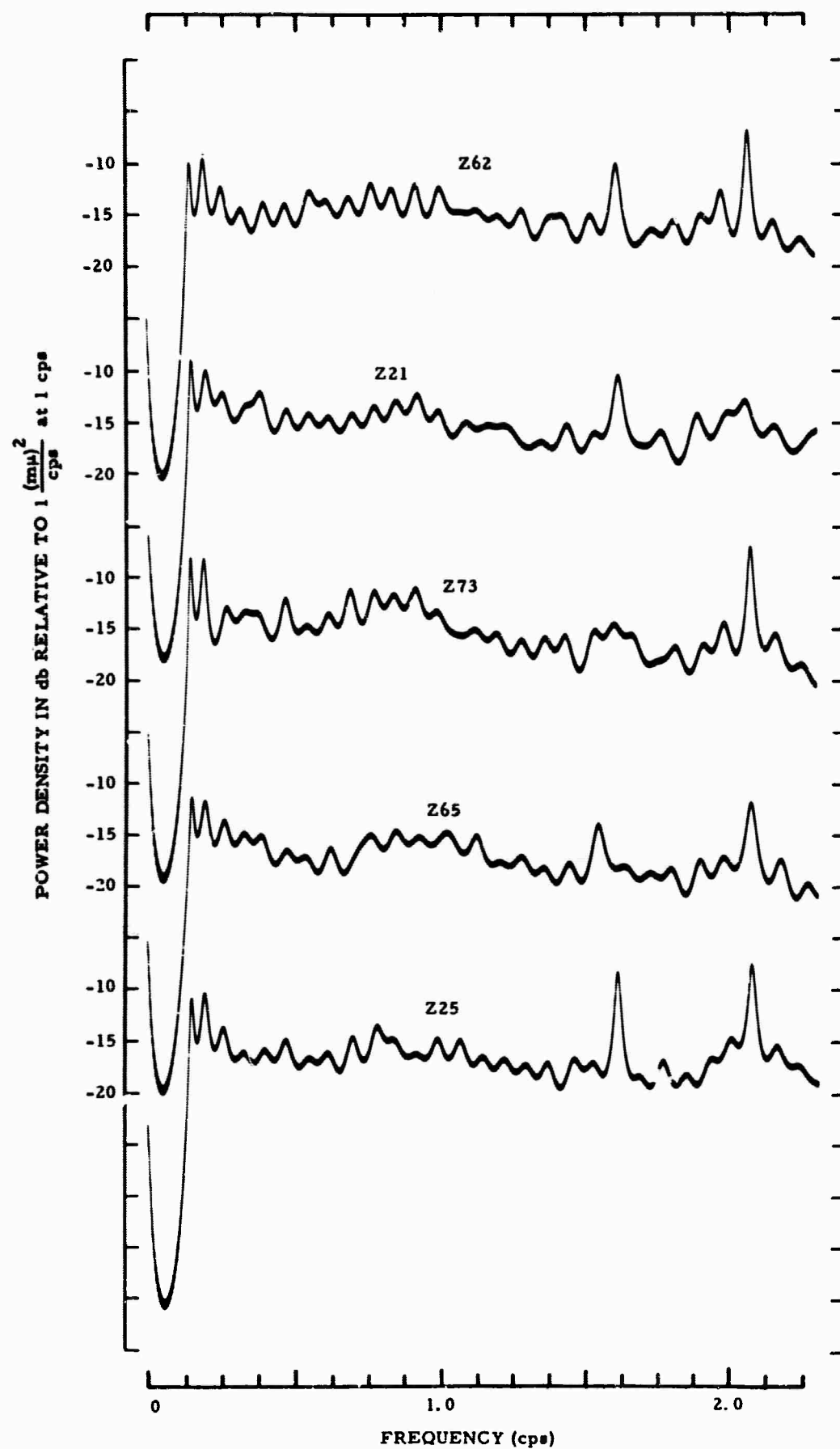


Figure V-17. Power Spectra of Z62, Z13, Z73, Z65, and Z70 after Deconvolution

The transfer function of the seismometer to magnetic tape system at 1 cps is given by $K = \frac{B}{A}$ where A is the zero-to-peak equivalent earth motion in millimicrons at 1 cps and B is the zero-to-peak amplitude of the recorded numerical cosine function on the tape.

The number B is found from a computer program which

- Determines frequency f of the calibration signal (recorded on trace 30) by counting the zero-crossing of the sine wave
- Calculates the Fourier transform of the seismometer traces $g_n(t)$ at that frequency, i.e.,

$$C_n(f) = \Delta t \sum_{j=0}^{N-1} g_n(j\Delta t) (\cos 2\pi f j \Delta t - i \sin 2\pi f j \Delta t)$$

B then is given by $\frac{2|C(f)|}{N\Delta t}$ where Δt is the sampling period.

This program also calculates the d-c level of the traces and the amplitude and phase of $C_n(f)$ relative to trace 11 which is the center seismometer in the cross array. The output of this program is shown in Table V-2 and explained in Table V-3.

The 0 db relative to 1 $\frac{(\text{mm})^2}{\text{cps}}$ at 1 cps is equal to $10 \log_{10} K^2$
 $= 20 \log_{10} K$. Hence, for seismometer Z63, $B = \frac{2(36554)}{(1138)(0.024)}$ and, thus,

$$20 \log_{10} \frac{2(36554)}{(1138)(0.024)} = 55.5$$

All the 0-db values for the 21 seismometers were computed according to the preceding process.

Table V-4 gives the 0-db ground motion value for the center seismometer in the cross array and the relative 0-db values for the other seismometers. Also listed is 10 times the logarithm of the average square value of the tape numbers for the center seismometer during various processing stages and the relative db values for the other traces. Variations in the relative db value for a trace after the various processing stages are

Table V-2

CALIBRATION ANALYSIS OUTPUT FOR TFO CROSS ARRAY

(a) Calibration on Linear Cross Array at TFO
 (b) 001747
 001016
 (c) 000001
 (d) 001138
 (e) 000024
 (f) 000027
 (g) 000030
 (h) .98828E+0
 (i) .20667E+3

(j)	(k)	(l)	(m)	(n)
000006	000032	.36554E+5	.10153E+1	-.22031E+1
000007	000032	.34223E+5	.95071E+0	.05245E+0
000008	000028	.36263E+5	.10073E+1	-.24094E+1
000009	000024	.36392E+5	.10109E+1	-.37767E+0
000010	000024	.34517E+5	.95886E+0	-.34411E+1
000011	000016	.35997E+5	.10000E+1	-.00000E+0
000012	000008	.36834E+5	.10231E+1	-.36230E+1
000013	000003	.35809E+5	.99477E+0	-.13254E+1
000014	-000004	.36161E+5	.10046E+1	-.30773E+1
000015	-000004	.37787E+5	.10498E+1	-.26682E+1
000016	-000009	.37855E+5	.10515E+1	-.27556E+1
000017	000007	.38848E+5	.10791E+1	-.65394E+0
000018	000091	.38261E+5	.10629E+1	-.20666E+1
000019	000012	.36289E+5	.10080E+1	-.21401E+1
000020	000014	.35863E+5	.99626E+0	.26157E+1
000021	000010	.35962E+5	.99902E+0	.18254E+1
000022	000015	.37569E+5	.10437E+1	.34235E+1
000023	000027	.37588E+5	.10441E+1	.10162E+2
000024	000021	.36351E+5	.10097E+1	.19582E+1
000025	000031	.38456E+5	.10683E+1	.35180E+1
000026	000020	.36766E+5	.10212E+1	.34516E+1

Table V-3

EXPLANATION OF TABLE V-2

- (a) Title, assigned on input
- (b) Input event number
Output event number
- (c) Block number of first zero crossing of calibration trace
- (d) Number of blocks chosen as Fourier transform gate
- (e) Sample rate
- (f) Number of cycles in gate
- (g) Trace on which calibration appears
- (h) Computed frequency of the calibration signal
- (i) Phase angle of reference trace in degrees
- (j) Trace number
- (k) D-C level
- (l) Absolute value of Fourier transform
- (m) Relative amplitude
- (n) Relative phase angle in degrees

due to differences in its power spectrum relative to the spectrum of the center seismometer (trace 11). These variations are small. However, in comparing the relative total powers and the relative 0-db levels, there are appreciable differences on some traces. In particular, the calibration on seismometer Z9 (trace 10) says that its noise power is more than 3 db less than Z21 (trace 11). These results show at least that the calibration measurements are a poor way of normalizing ambient seismic noise.

Table V-4

0-DB GROUND MOTION VALUES AND TOTAL POWER OF TRACES
AFTER VARIOUS PROCESSING STAGES FOR TFO CROSS ARRAY

Trace	0-db Ground Motion	Trace Power in db after Prewhitening and Decimation by 3	Trace Power in db before Prewhitening and Decimation by 3	Trace Power in db after Repeat Decimation by 3, Gain by 4 and Deconvolution
6	-0.3	-0.4	0.2	0.1
7	-0.6	-1.3	-0.4	-0.4
8	-0.5	-0.8	-1.4	-1.2
9	-0.2	-0.5	-1.0	-1.0
10	-0.6	-3.8	-4.5	-4.3
11	55.8	61.3	43.7	65.5
12	-0.4	-0.4	-1.0	-1.2
13	-0.3	-0.6	-0.2	0.0
14	-0.8	-0.7	-0.2	0.6
15	0.0	-0.3	-0.6	-0.4
16	+0.1	-0.1	-0.3	-0.1
17	+0.4	0.2	0.5	0.6
18	+0.3	0.3	0.3	0.6
19	+0.3	-1.7	-1.8	-1.3
20	+1.2	-2.0	-1.9	-1.4
21	-0.2	-1.9	-1.8	-1.3
22	-0.5	-1.5	-1.6	-1.2
23	+0.3	-2.0	-1.8	-1.7
24	-0.2	-1.6	-2.0	-2.0
25	+0.6	0.1	-0.6	-0.4
26	-0.2	0.2	0.2	0.4

BLANK PAGE

SECTION VI

FURTHER ANALYSIS OF TFO AMBIENT NOISE

A. SUMMARY

This section presents the complete set of all auto- and cross-correlation functions from the 21 seismometers in the large cross array at TFO as found from the long noise sample discussed in Section V. Also presented is the complete set of 10 coherences between the two horizontal seismometers and three vertical seismometers. The analysis of this data shows that the 4 to 6 sec energy is coming from N60° E with a velocity of about 3.4 km/sec. The other energy below 1.2 cps is mantle P-wave noise, which is definitely non-isotropic. Above 1.2 cps, the energy is random, seismometer to seismometer, except for some highly coherent lines in the spectra. The horizontal seismometer in line with the 4 to 6 sec energy shows a high coherence with the vertical seismometers in that frequency range, but the transverse seismometer has very small coherence with all other seismometers. This is further proof that this energy is Rayleigh motion. The presence of Love wave energy on the transverse seismometer can be inferred from its lack of coherence with the other seismometers.

B. PROCESSING OF THE AUTO- AND CROSSCORRELATION FUNCTIONS

All possible auto- and crosscorrelation functions between the 21 seismometers in the large cross array at TFO were computed from the long ambient noise sample discussed in Section V. The correlations were computed from the noise traces after they had been resampled down to 216 msec data and had been deconvolved. Thus the Nyquist fold-over frequency, W , was 2.315 cps and the power spectra were almost white except for the lack of energy below 0.1 cps and the presence of line spectra. The correlations were all computed out to ± 61 lags or 13.176 sec. In addition, the auto- and crosscorrelations were appropriately scaled to make the zero lags on all autocorrelations equal. (Some noise traces were low in power; see Section V.)

Four symmetrical, 41-point, digital bandpass filters were computed by Fourier transformation of the frequency bands, 0 to $\frac{W}{6}$, $\frac{W}{6}$ to $\frac{W}{3}$, $\frac{W}{3}$ to $\frac{W}{2}$, and $\frac{W}{2}$ to W (0 to 0.386 cps, 0.386 to 0.772 cps, 0.772 to 1.157 cps, and 1.157 to 2.315 cps). The frequency responses of these 4 bandpass filters are shown in Figure VI-1. Each of the 231 correlation functions were filtered by each bandpass filter. Only fully filtered outputs were calculated and thus the resulting correlation functions were 20 points shorter on each end; i. e., $\tau = \pm 41$ lags or ± 8.856 sec. The filtered correlation functions were not normalized among themselves, but the results from the first three filters were scaled up by 6 and the results from the last filter were scaled up by 2 so that the resulting autocorrelations would be comparable in magnitude to the unfiltered autocorrelations.

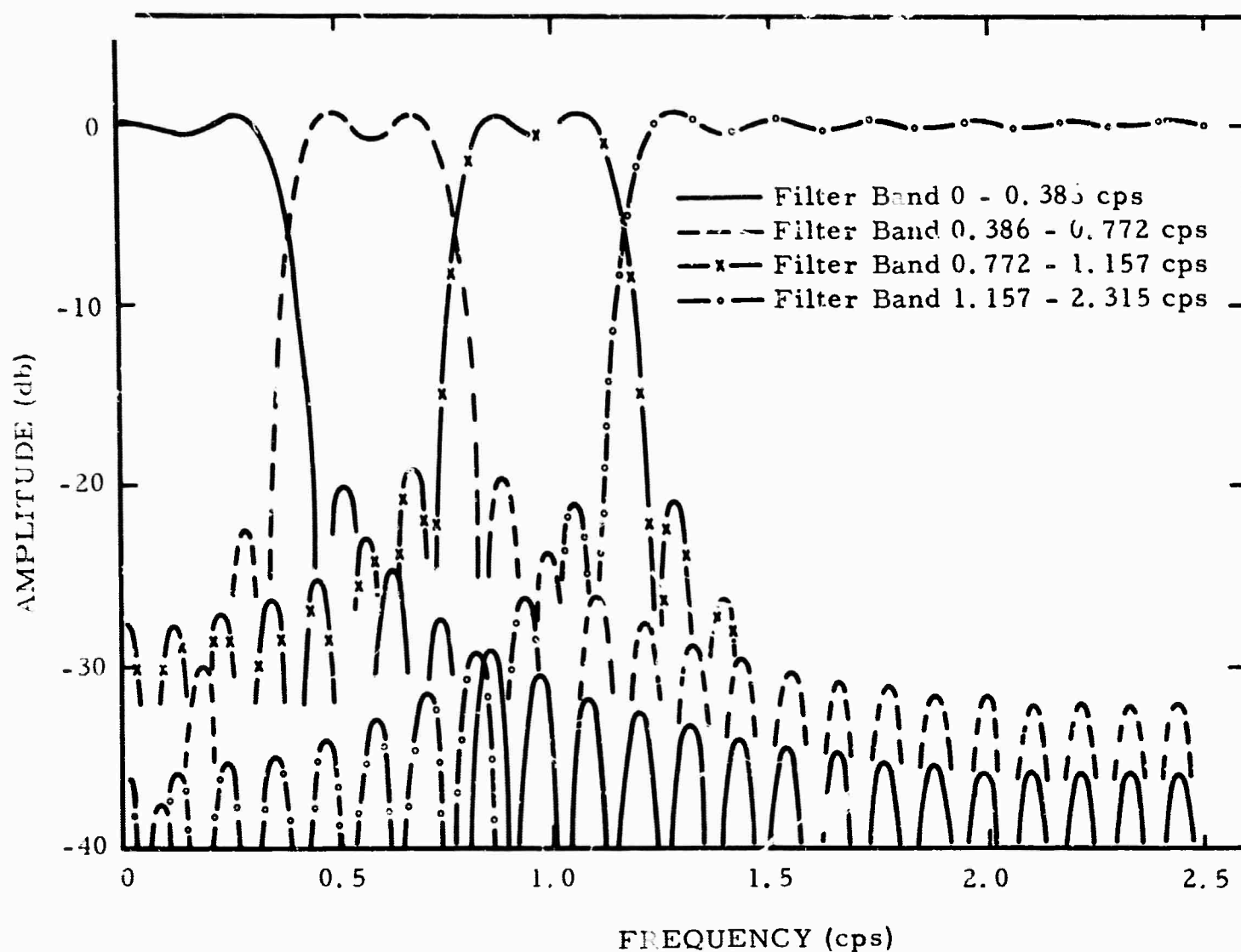


Figure VI-1. Frequency Responses of the Band Pass Filters Applied to the Correlation Functions

Figures VI-2 through VI-6 show all auto- and crosscorrelations from just the north-south line in the cross array. The autocorrelations lie along the main diagonal of the figures and go in order from left to right, south to north as can be seen from the inset of the TFO geometry. Figure VI-2 shows the unfiltered correlations; Figure VI-3, the 0 to 0.386 cps correlations; Figure VI-4, the 0.386 to 0.772 cps correlations; Figure VI-5, the 0.772 to 1.157 cps correlations; Figure VI-6, the 1.157 cps to 2.315 cps correlations.

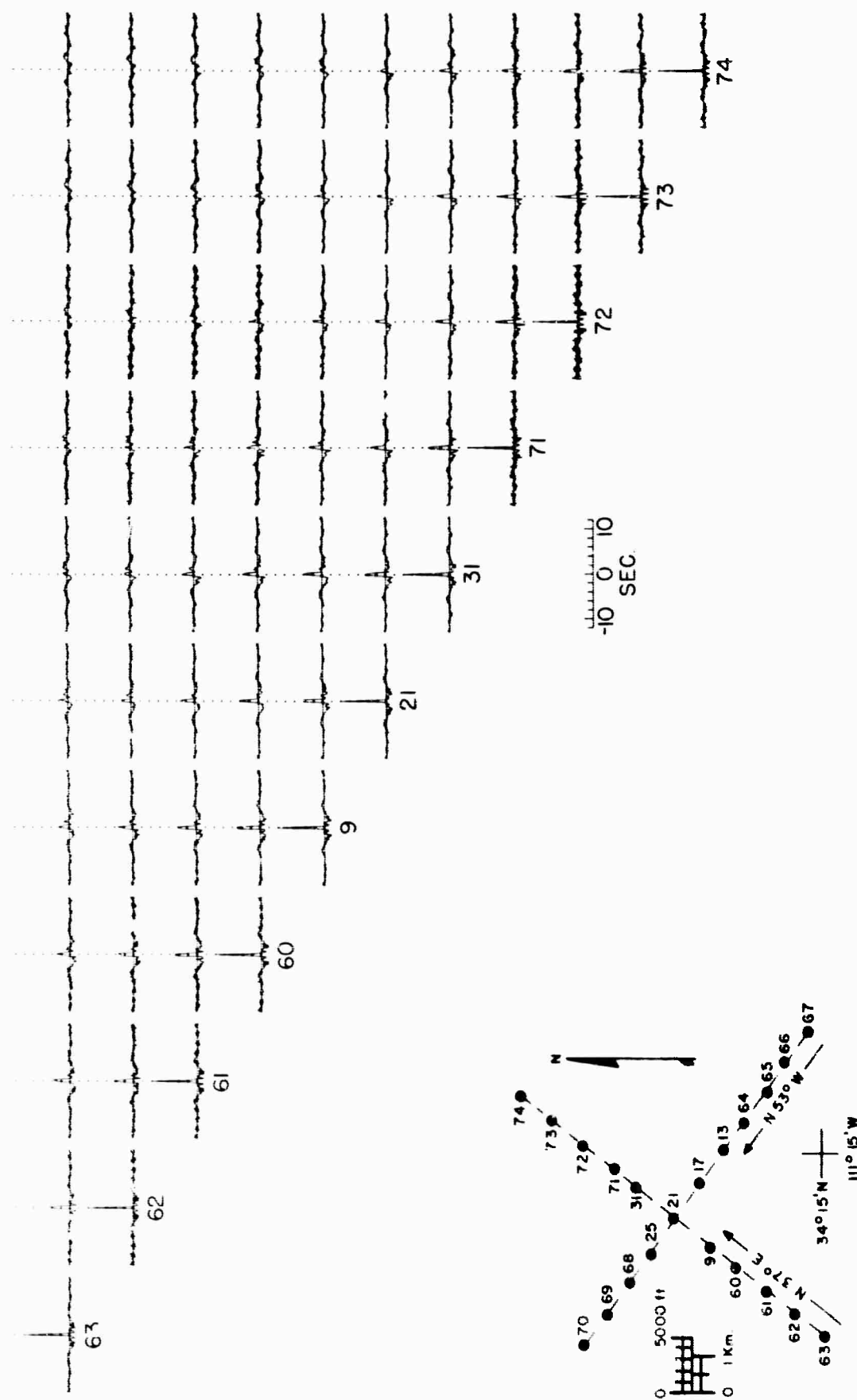


Figure VI-2. Correlation Functions for the NS Line Full Frequency Band of 0 to 2.315 Cps

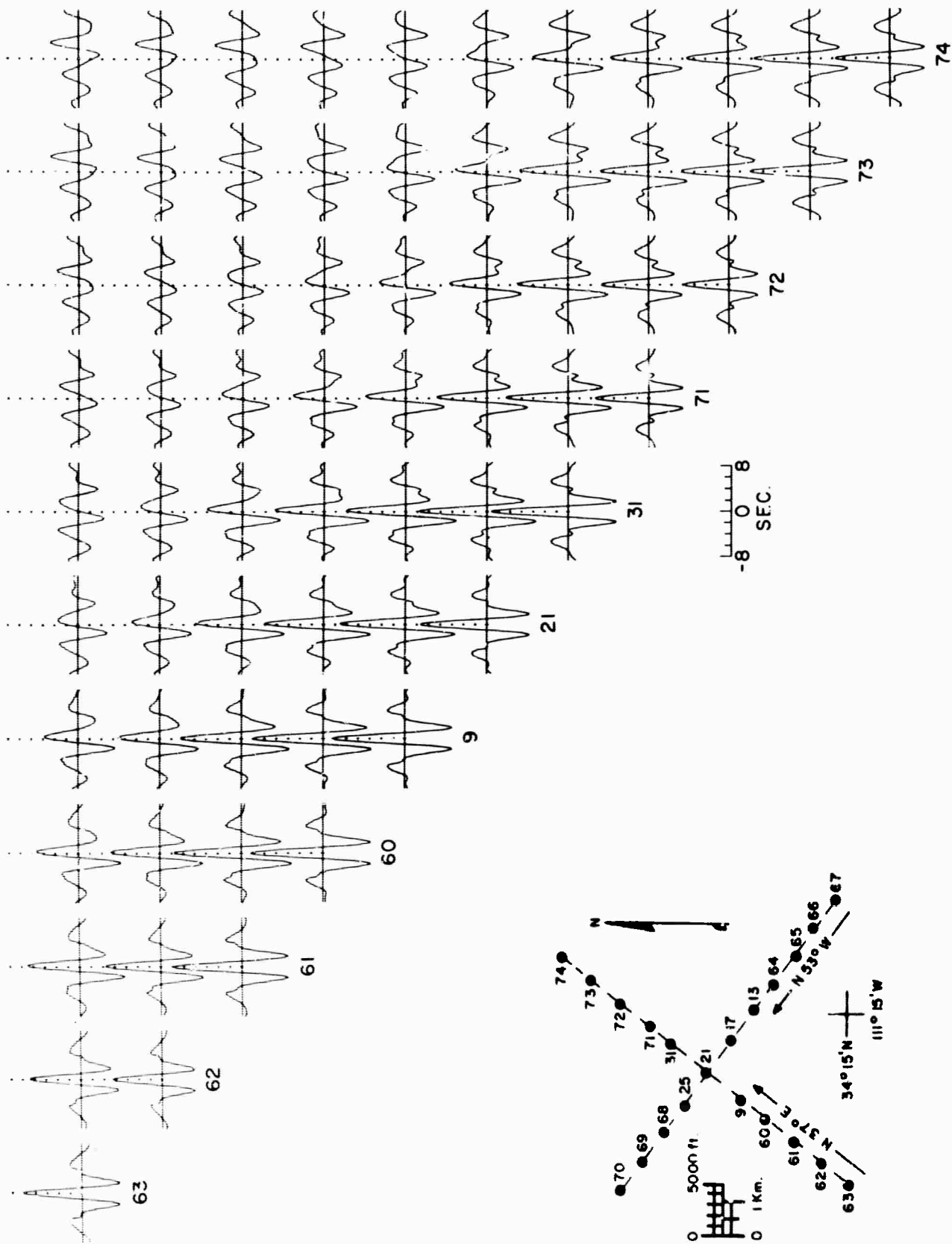


Figure VI-3. Correlation Functions (X6) for the NS Line Frequency Band of 0 to 0.386 Cps.

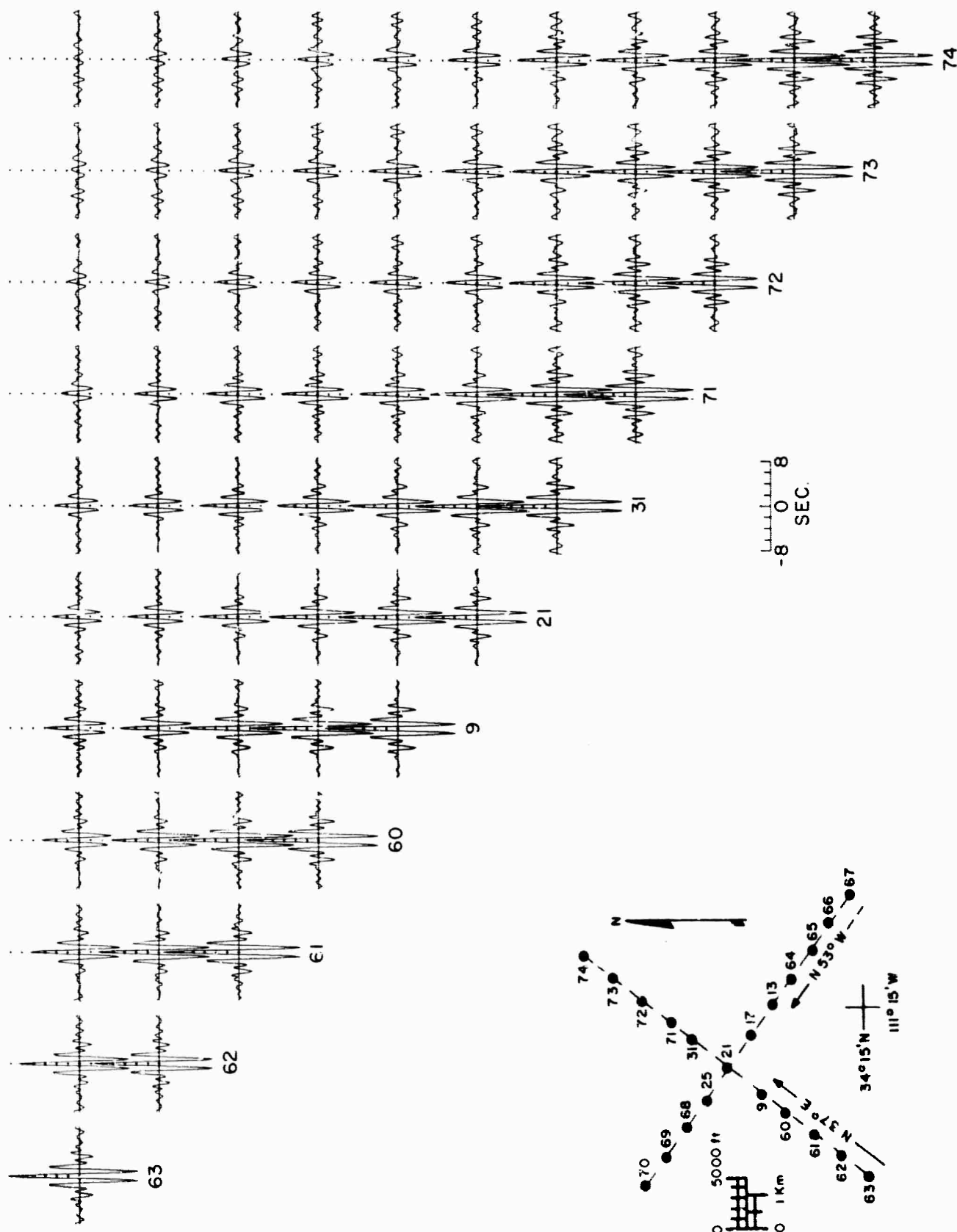


Figure VI-4. Correlation Functions (X6) for the NS Line Frequency Band of 0.386 to 0.772 Cps

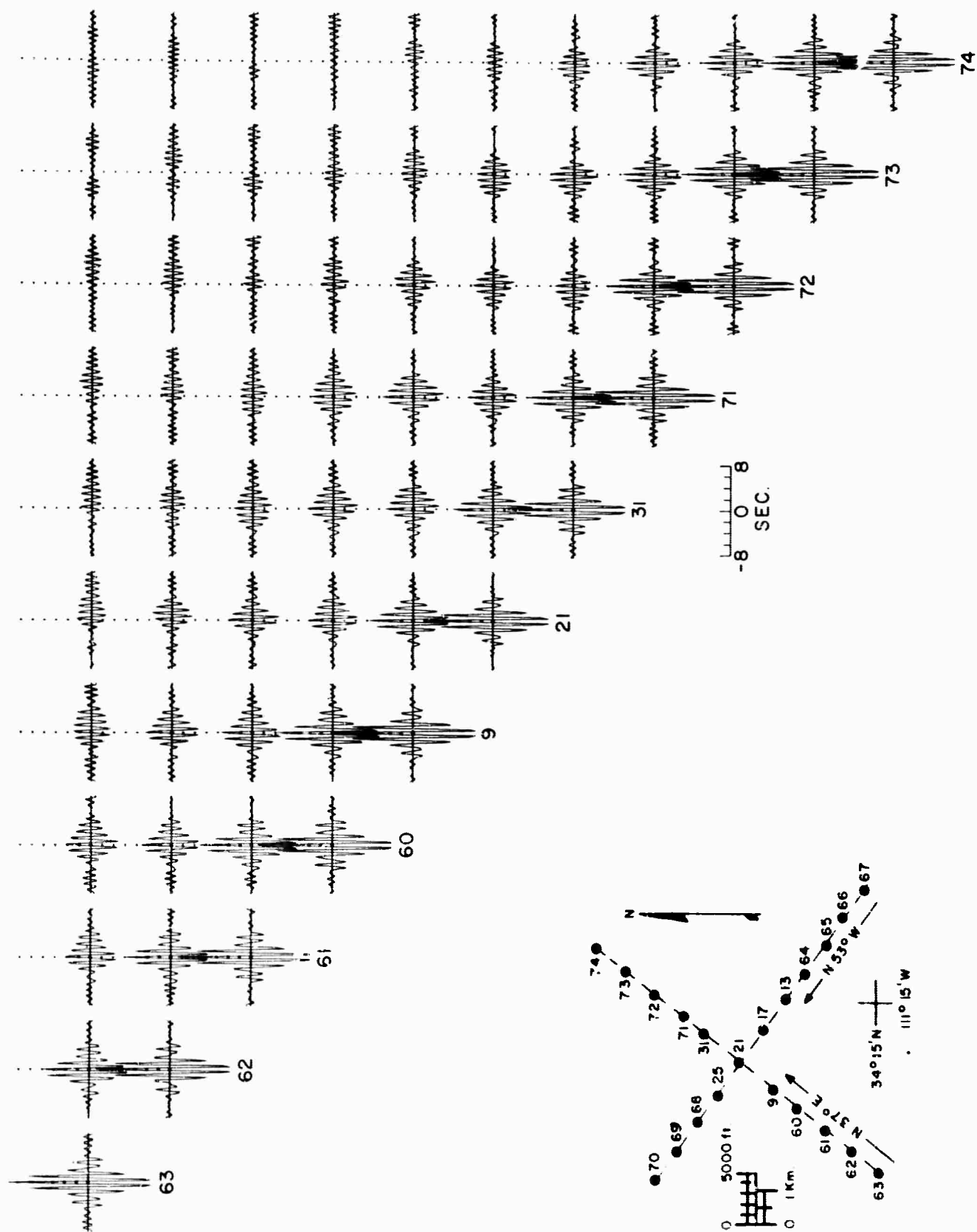


Figure VI-5. Correlation Functions (X6) for the NS Line Frequency Band of 0.772 Cps to 1.157 Cps

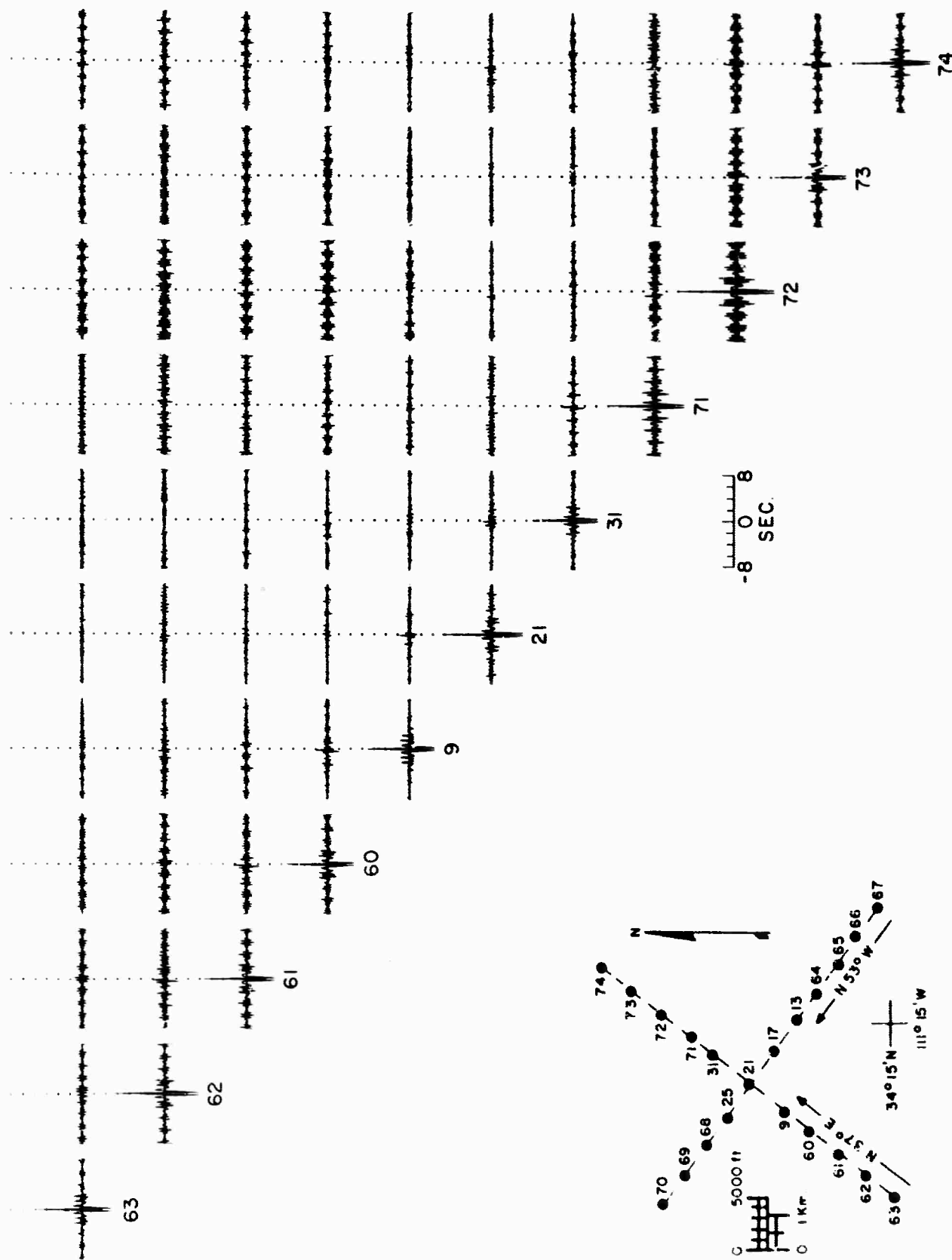


Figure VI-6. Correlation Functions (X2) for the NS Line Frequency Band of 1.157 Cps to 2.315 Cps

The crosscorrelations in these figures and in the other correlation displays lie at the appropriate grid locations. For example, in Figure VI-2 the upper right hand correlation is Z63XZ74. The definition of Z63XZ74

$$Z63XZ74(\tau) = \frac{1}{N} \sum_{i=1}^N g_{63}(n \Delta t) g_{74}(n \Delta t - \tau)$$

is used for the crosscorrelation functions.

Figures VI-7 through VI-11 are a similar set for the east-west line of the cross array, where left to right along the diagonal is east to west along the line. Note that the center seismometer, Z21, is repeated in the figures. Figures VI-12 through VI-16 are a similarly filtered set for the correlations between the two lines of seismometers. Again the center seismometer correlations are repeated in these figures for spatial consistency in the figures.

C. ANALYSIS OF THE CORRELATION DISPLAYS

An immediately noticeable property of the correlation functions is their space stationarity. All autocorrelation functions are quite similar, reflecting the similarity of their power spectra. However, more interesting is the similarity of the crosscorrelations which lie on lines parallel to the main diagonal in Figures VI-2 through VI-11. The seismometers in the two lines are approximately equal spaced (about 1 km apart) and thus, if the ambient noise field at TFO is space stationary, then the observed similarity should exist. In the case of Figures VI-12 to VI-16, space stationarity requires that the crosscorrelations symmetrically placed with respect to Z21XZ21 should be time reverses of each other, which is approximately observed. Considering the quality of the data, the following analysis of the wavenumber structure of ambient noise at TFO is on a firm foundation.

In looking at the low frequency, 0 to 0.386 cps band, it is evident that there is a strong directional 4 to 6 sec period wave going across the array. Figure VI-3 shows a moveout of about 1.6 sec across the 10 km length of the NS line with the energy hitting seismometer Z74 before Z63. Figure VI-8 shows a smaller moveout across the length of the EW line with the energy hitting the east end before the west end. The energy must be strongly directional because of the high coherence across the array. In addition to this low frequency energy, there is evidence of higher frequency energy which has little or no moveout; i.e., mantle P-wave energy. Because of the interference of these two types of energy, Figure VI-13 is most useful in determining the direction of arrival of the 4 to 6 sec energy. By looking at the correlations, say, in the last column of Figure VI-13, the Z60XZ20 crosscorrelation function is the most symmetric, indicating that the low frequency wave front arrives at these two seismometers at the same time. From this pair and other pairs with good symmetry, the wave motion is consistently found to lie along the line N60°E. Estimating the moveout between a pair of seismometers lying along this line; i.e., Z74 and Z68 or Z63 and Z13 (both have a separation of 5.8 km and about 1.7 sec moveout) a velocity of about 3.4 km/sec coming from N60E can be estimated for the 4 to 6 sec period energy. This result is in agreement with previous work; see Section II of reference 1. The velocity is very reasonable for Rayleigh wave motion.

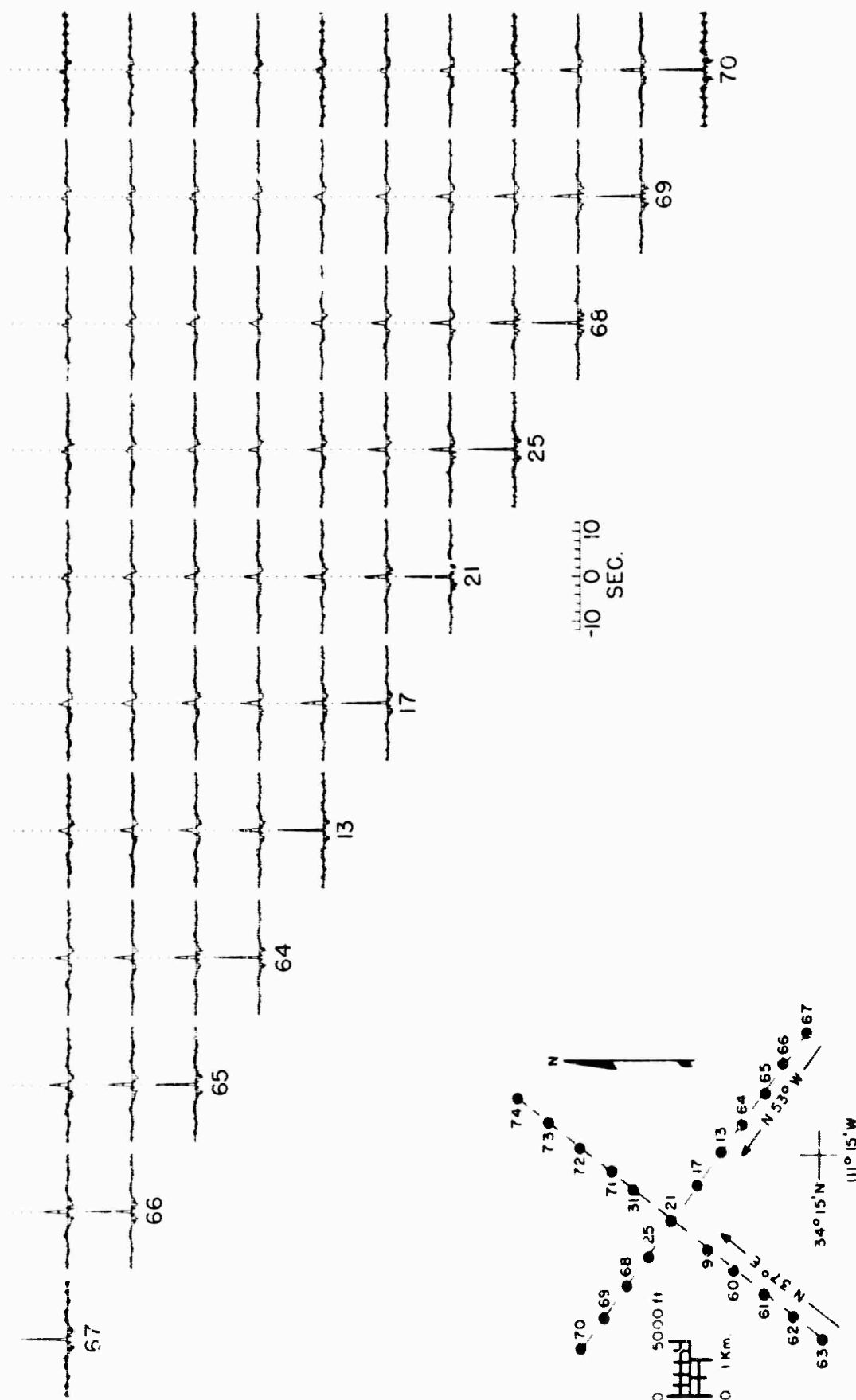


Figure VI-7. Correlation Functions for the EW Line Full Frequency Band of 0 to 2.315 Cps

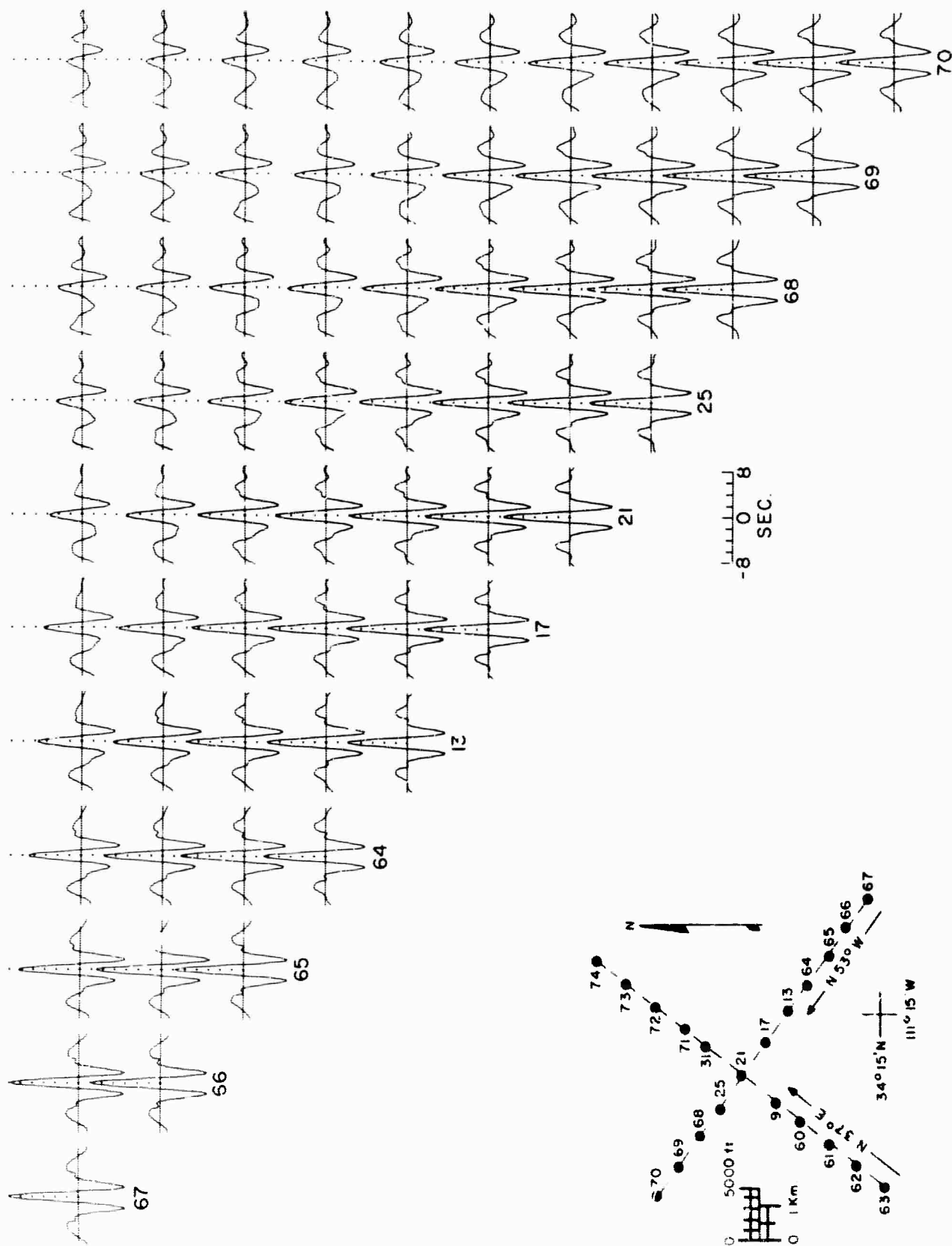


Figure VI-8. Correlation Functions (X6) for the EW Line Frequency Band of 0 to 0.386 Cps

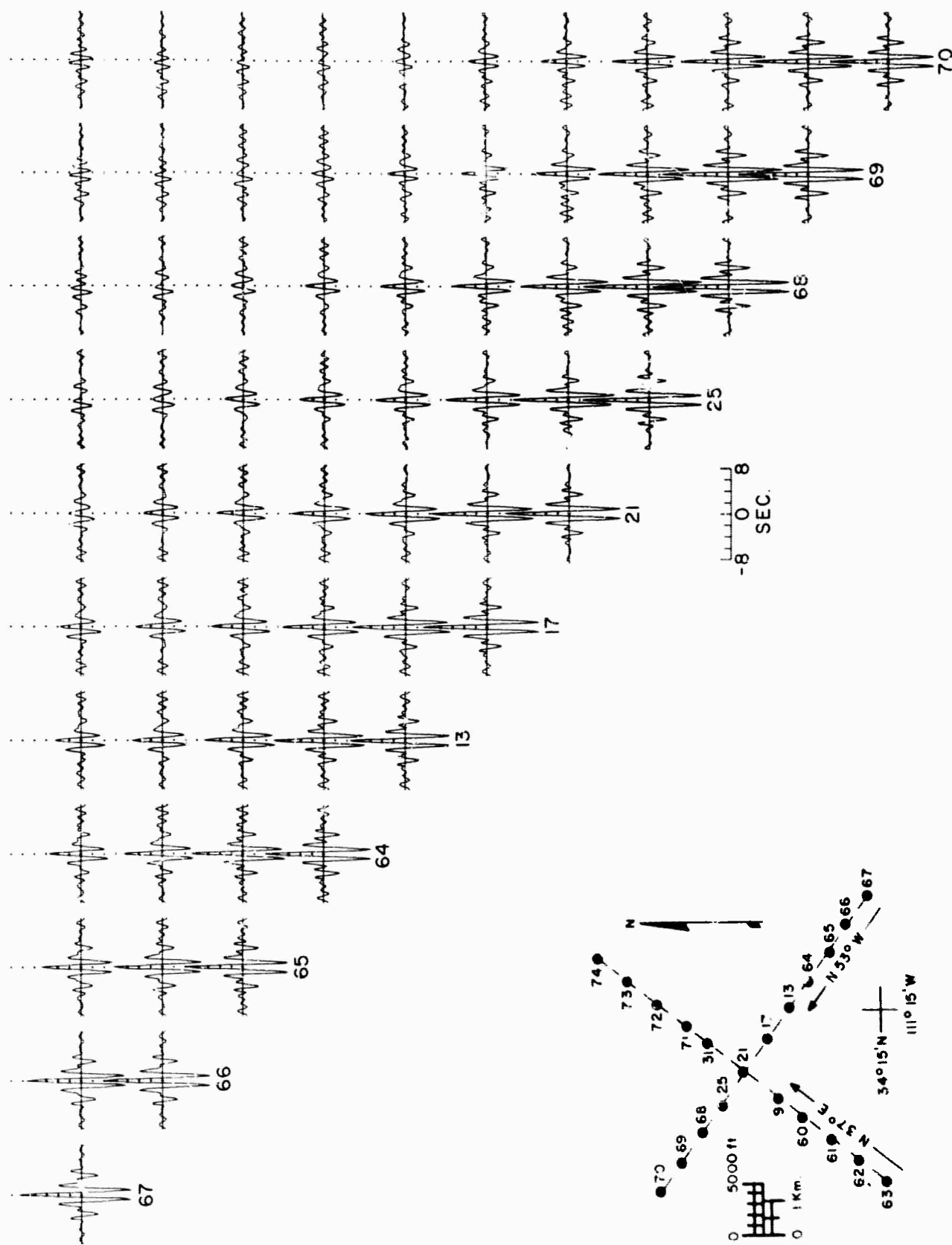


Figure VI-9. Correlation Functions (X6) for the EW Line Frequency Band of 0.386 cps to 0.772 Cps

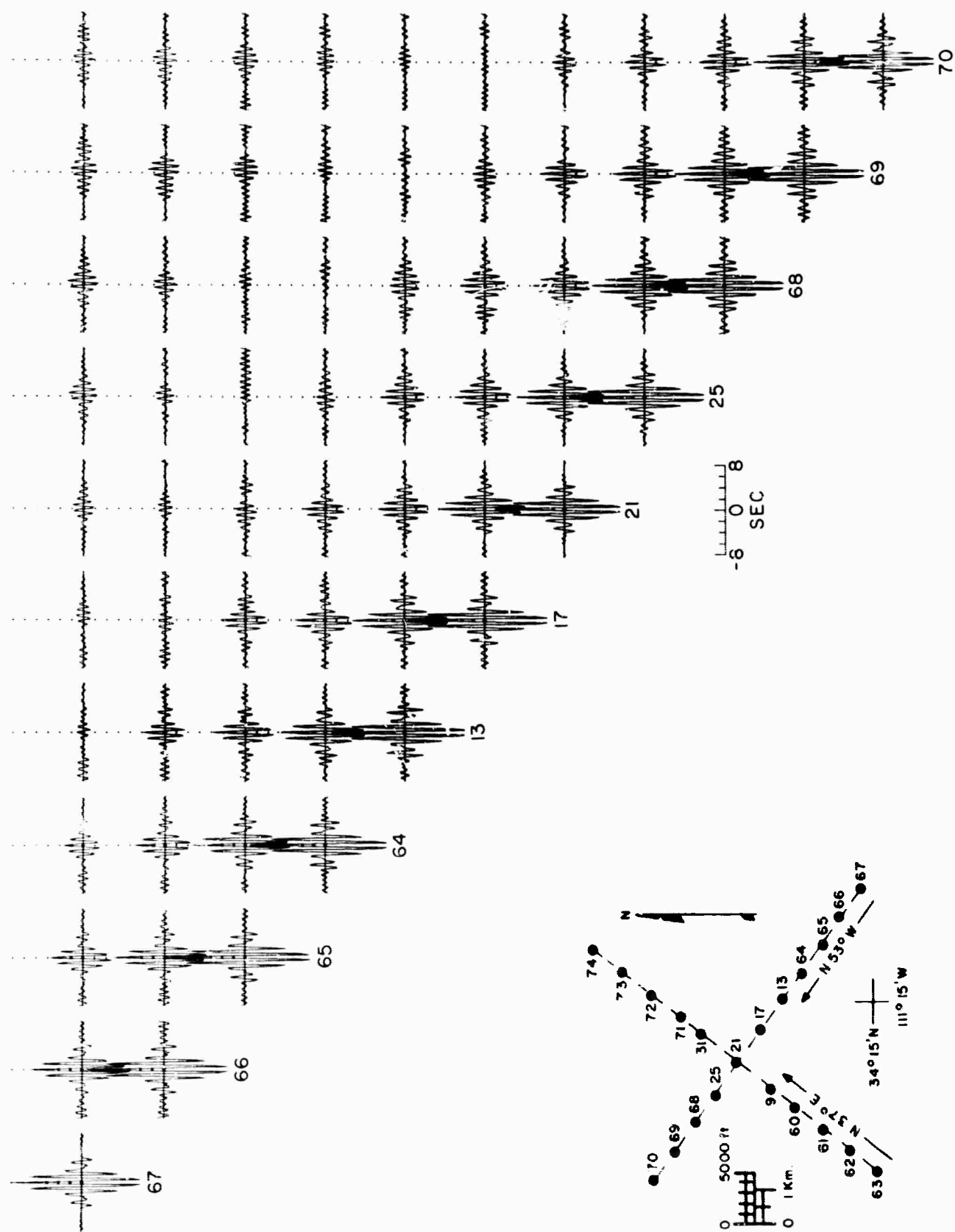


Figure VI-10. Correlation Functions (X6) for the EW Line Frequency Band of 0.772 to 1.157 Cps

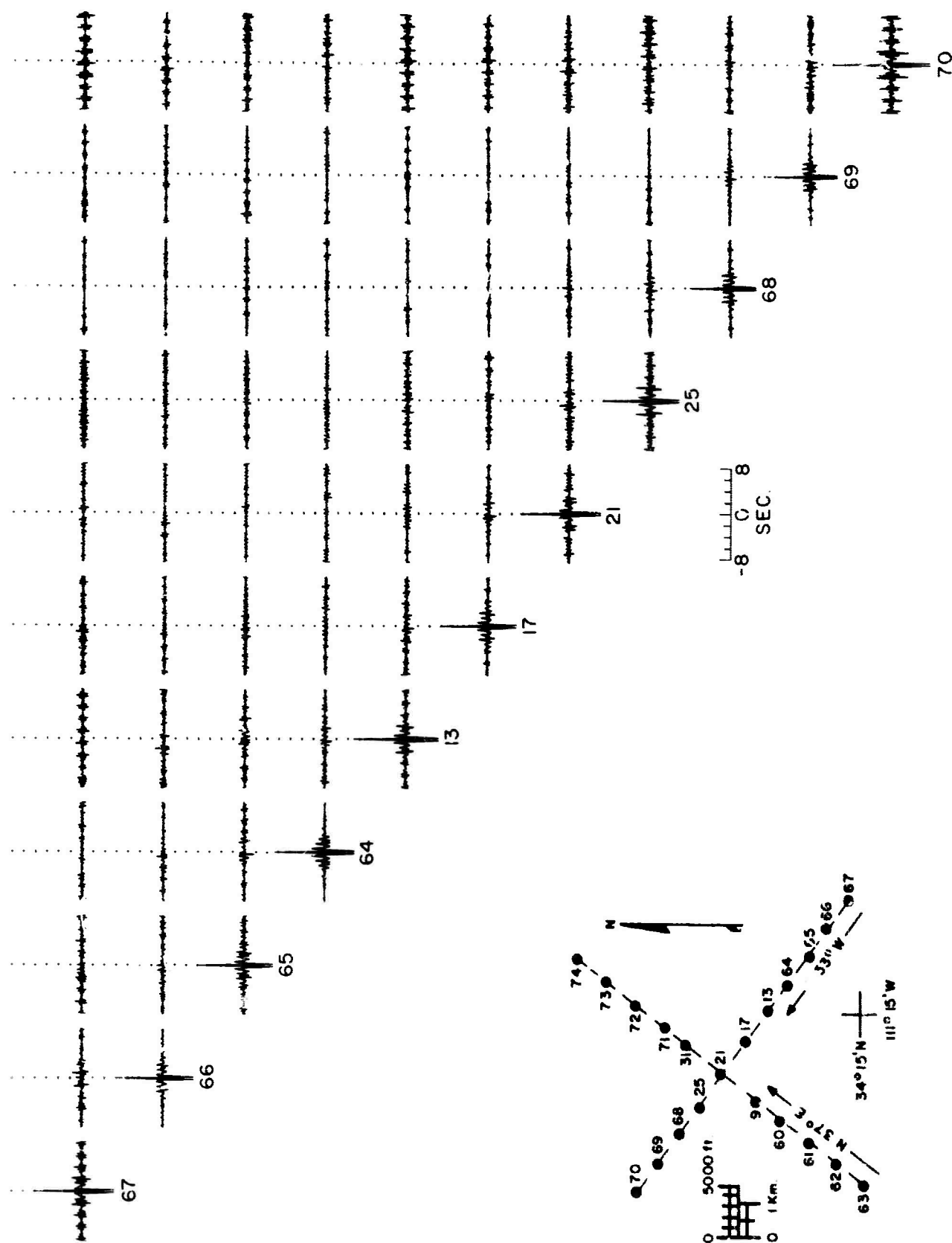


Figure VI-11. Correlation Functions (X2) for the EW Line Frequency Band of 1.157 to 2.315 Cps

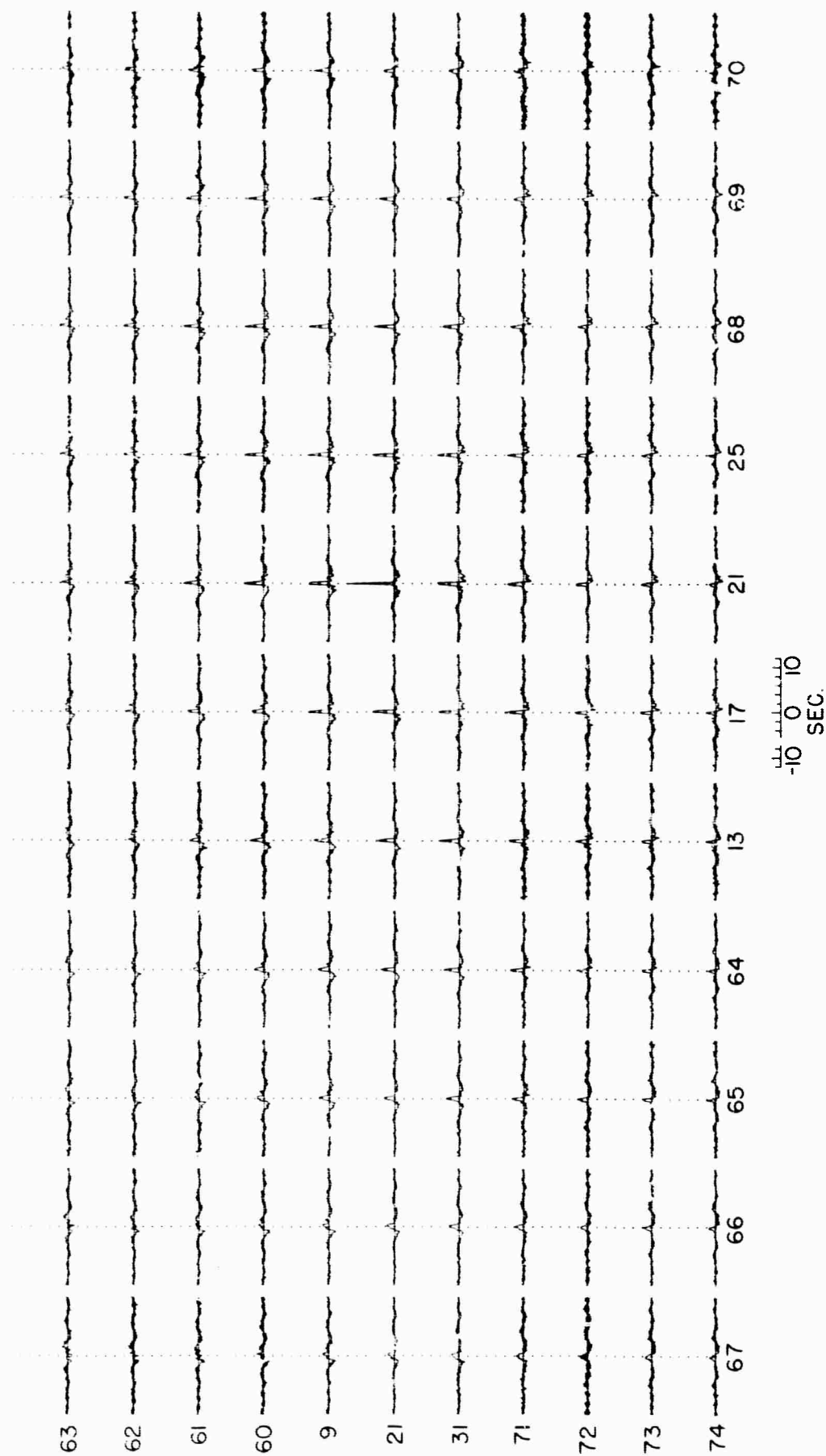


Figure VI-12. Correlation Functions Between the Two Lines Full Frequency Band of 0 to 2.315 Cps

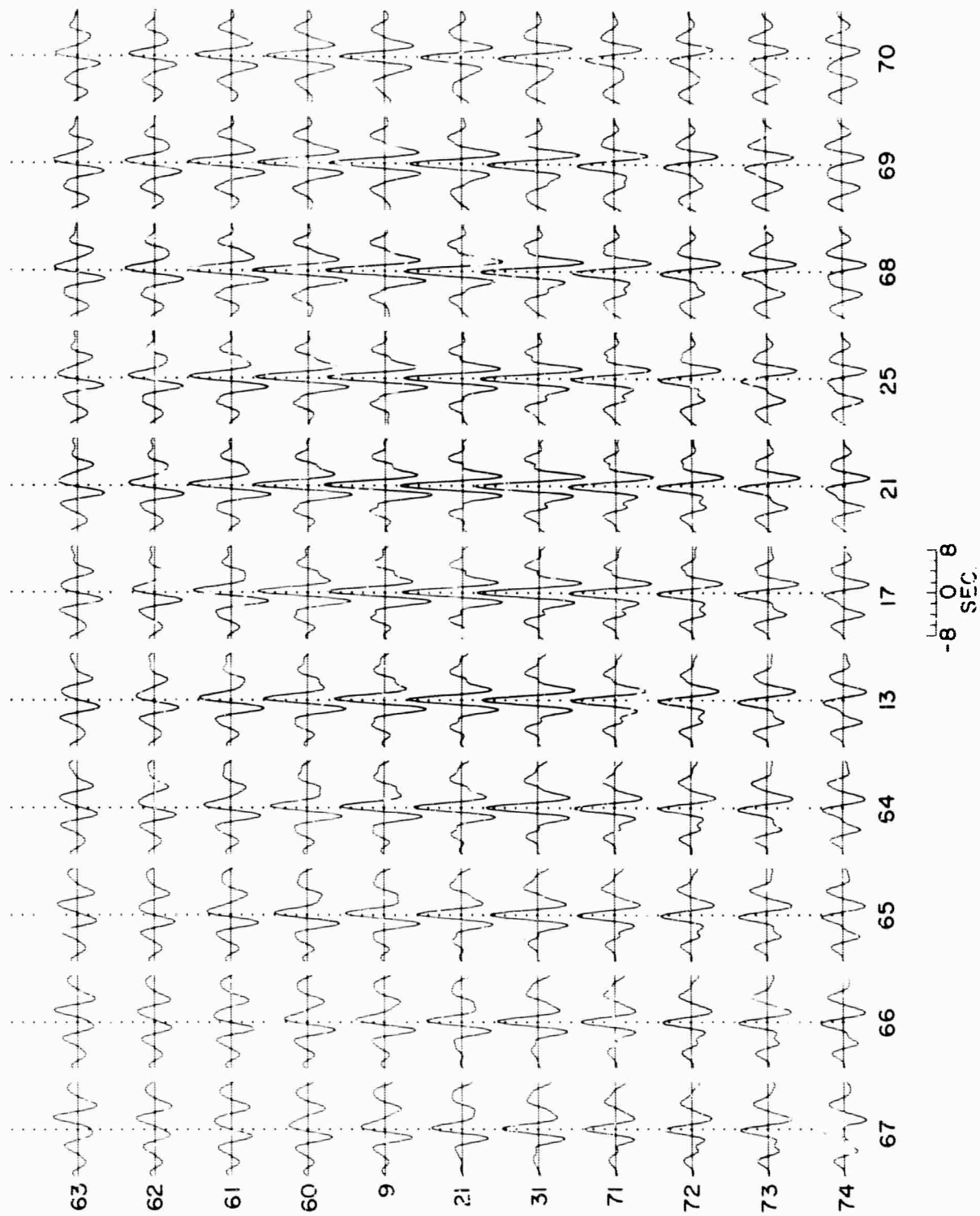


Figure VI-13. Correlation Functions (X6) Between the Two Lines Frequency Band of 0 to 0.386 $C_F.s$

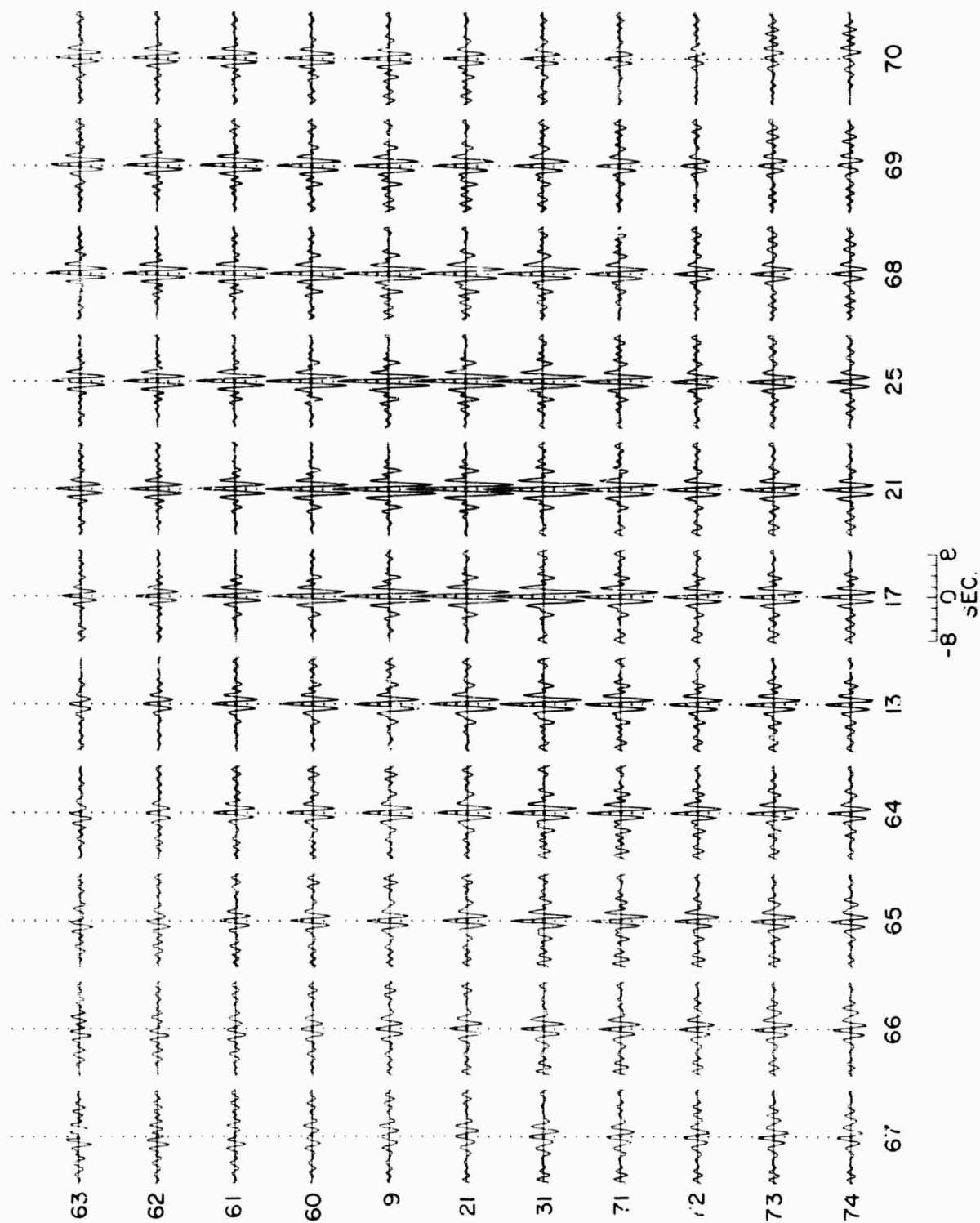


Figure VI-14. Correlation Functions (X6) Between the Two Lines Frequency Band of 0.386 to 0.772 Cps

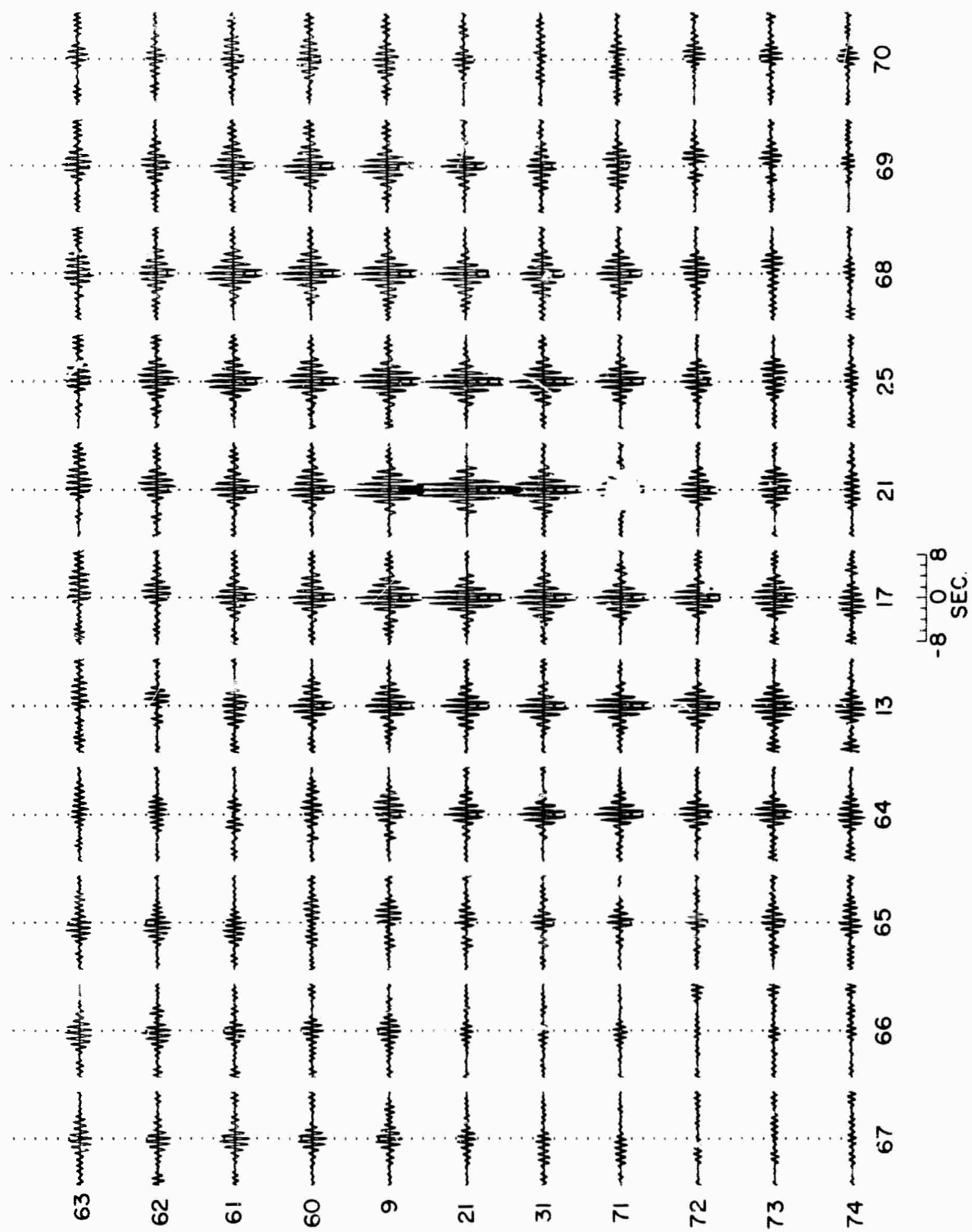


Figure VI-15. Correlation Functions (X6) Between the Two Lines Frequency Band of 0.772 to 1.157 Cps

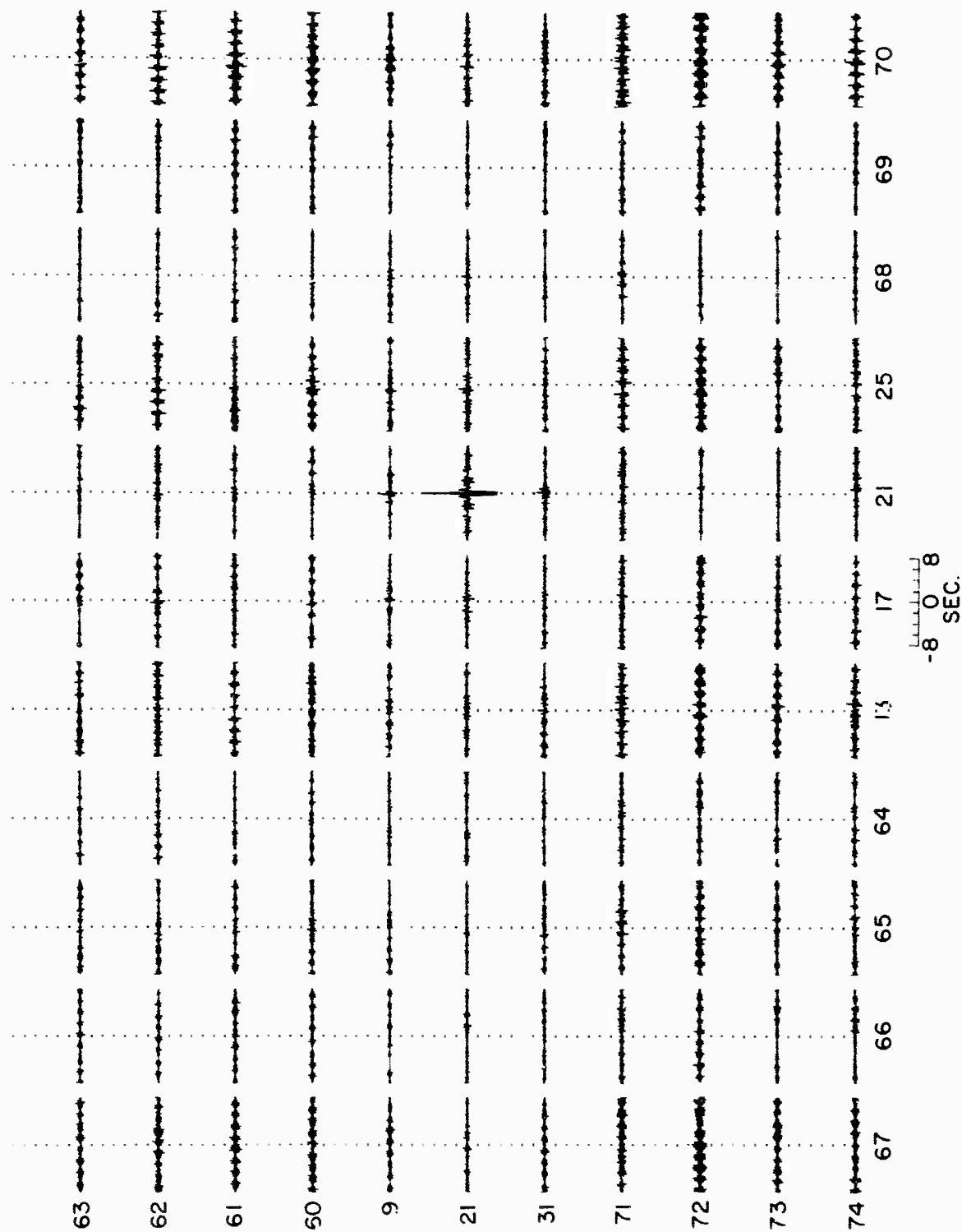


Figure VI-16. Correlation Functions (X2) Between the Two Lines Frequency Band of 1.157 to 2.315 Cps

The frequency bands of 0.386 to 0.772 cps and 0.772 to 1.157 cps appear to be mainly mantle P-wave energy since the correlations have very little moveout. A striking phenomena is the vanishing and reappearance with phase reversal of the crosscorrelations with increase in separation distance. This property indicates a range of velocities for the mantle P-wave energy. In particular, if the energy were isotropically distributed from ∞ to a lowest velocity V (like the solid disk models used for signals in designing multi-channel filter systems), the null distance, X, would occur when

$$J_1\left(2\pi X \frac{f}{V}\right) = 0 \quad ; \quad J_1(1.2197 \pi) = 0$$

or

$$V = \frac{2Xf}{1.2197} \quad (\text{See reference 12.}) \quad (1)$$

From Figure VI-9, the correlation between Z65 and Z70 is small, giving a null distance of about 8.5 km. Using a center frequency of .58 for the 0.386 to 0.772 cps band, the value of V given by Equation (1) is about 8 km/sec. Along the NS line in this band, Figure VI-4, the null distance is the full length of the line or about 10.7 km. This gives a V of about 10 km/sec. In the frequency band of 0.772 to 1.157 cps, Figure VI-10 nulls at Z17XZ70 or a distance of 5.4 km. Using a center frequency of 0.97 cps, the velocity V is given as 8.6 km/sec. Figure VI-5 nulls at Z61XZ70, giving a V of 13.6 km/sec. Thus, along the north-south arm the correlations seem to agree with a solid disk model with a minimum velocity of about 12 km/sec, but along the east-west line the minimum velocity is about 8 km/sec. These results would fit a model of a solid ellipse with the longer axis along the east-west line. Furthermore, there is a slight moveout on the correlation functions from one end to the other end on both lines of the cross array. The moveouts indicate more energy is coming from the NNW. From these observations, it is clear that the distribution of mantle P-wave noise is not isotropic.

In the frequency band above 1.157 cps, there is little coherent energy and no evidence of space stationarity. The only coherent energy seems to be due to lines in the spectra of the seismometers and this coherence is not space stationary. This indicates that there is no particular velocity structure to the ambient noise at TFO above 1 cps which is in agreement with previous results.¹

D. PREPARATION OF THE HORIZONTAL-VERTICAL COHERENCE DATA

The noise samples from the EW and NS horizontal seismometers, which are located in the vault with the vertical seismometer Z1, were not filtered by the prewhitening, antialiasing filter used on the rest of the traces before they were resampled down to 72 msec data. Refer to Section V. A digital filter was designed so that it had the same frequency response as the prewhitening filter in the range of 0 to 2-17/54 cps and applied to the 216 msec horizontal traces. Thus, the resulting horizontal traces were corrected so that the total digital filtering applied to them agreed with that applied to the vertical seismometers.

Because the 4 to 6 sec energy was coming from N60°E, the two horizontal seismometers were combined to produce (1) a rotated EW seismometer, REW, which would be in line with this microseismic noise; and (2) a rotated NS seismometer, RNS, which would be transverse to this energy. Thus, the linear combinations used were

$$\text{REW} = 0.5 \text{ NS} + 0.866 \text{ EW}$$

and

$$\text{RNS} = 0.866 \text{ NS} - 0.5 \text{ EW} \quad (2)$$

Three vertical seismometers, Z1, Z13, and Z25, were selected to be analyzed in connection with the rotated horizontals. This set of verticals gave one seismometer located at the two horizontals, one in line with the low frequency directional energy at a distance of 2.2 km and one transverse to the energy at a distance of 3 km. After all filtering had been completed, a small portion of the noise samples for Z13, Z25, Z1, EW, NS, RNS and REW is shown in Figure VI-17.

Figure VI-18 shows the auto-power spectra of the three vertical seismometers and the two rotated horizontal seismometers. Two auto-power spectra estimates for each seismometer were obtained from the two channel coherence program, one using correlations with lags of ± 61 (13.176 sec) and the other with lags out to ± 124 (26.784 sec). Calibration data for the vault seismometers was lacking, so that there is no absolute scales given for these spectra. Figures VI-19 through VI-23 show the complete set of 10 coherences between the five seismometers for the two different correlation lag values.

E. ANALYSIS OF THE HORIZONTAL-VERTICAL COHERENCES AND POWER SPECTRA

In looking at Figures VI-18 thru VI-23, the high coherence between the inline horizontal with the three vertical seismometers for the 4 to 6 sec energy is striking. The transverse horizontal has no coherence with the verticals or with the inline horizontal except for line spectra in the higher frequency regions.

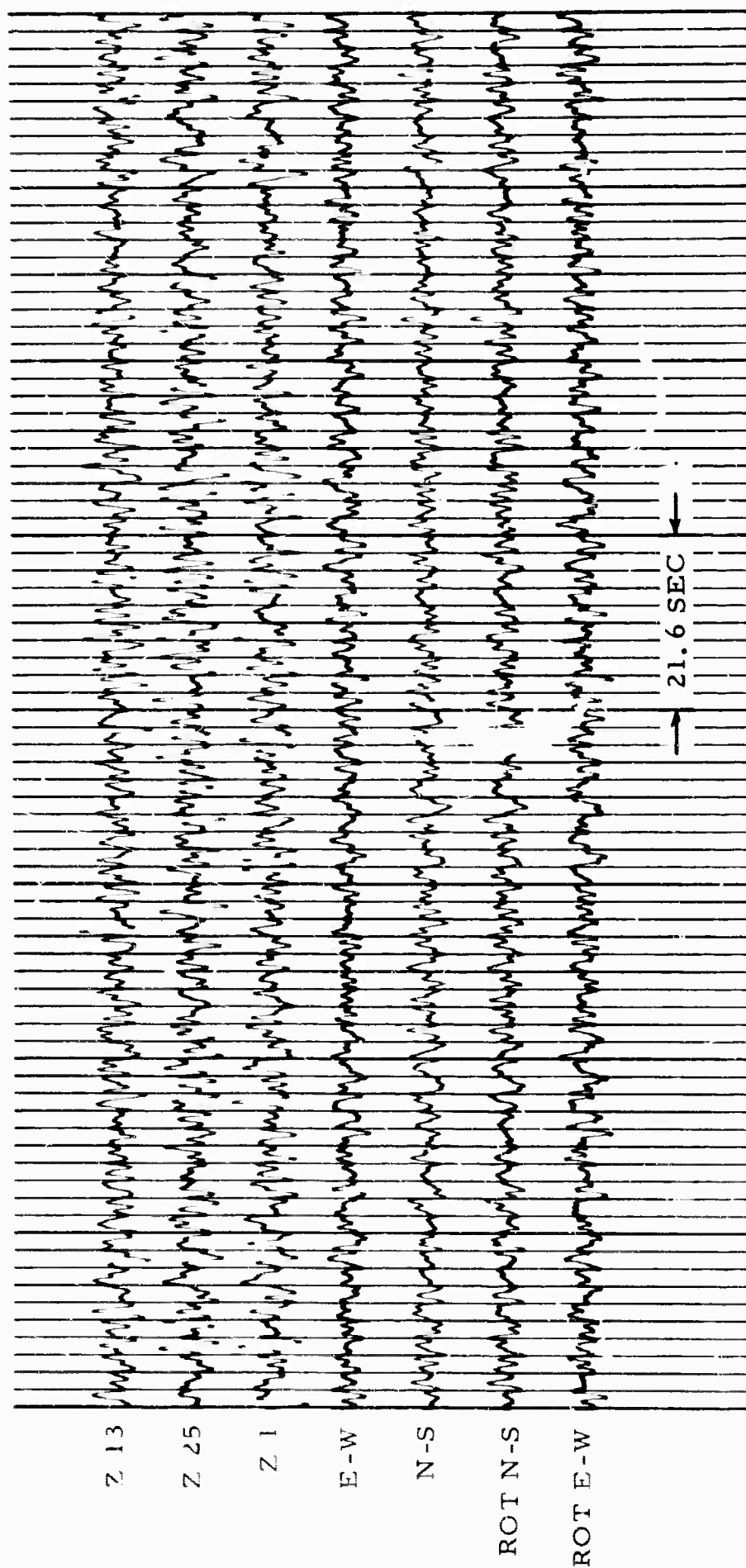


Figure VI-17. A Portion of the Noise Samples for Z13, Z25, Z1, EW, NS, RNS and REW

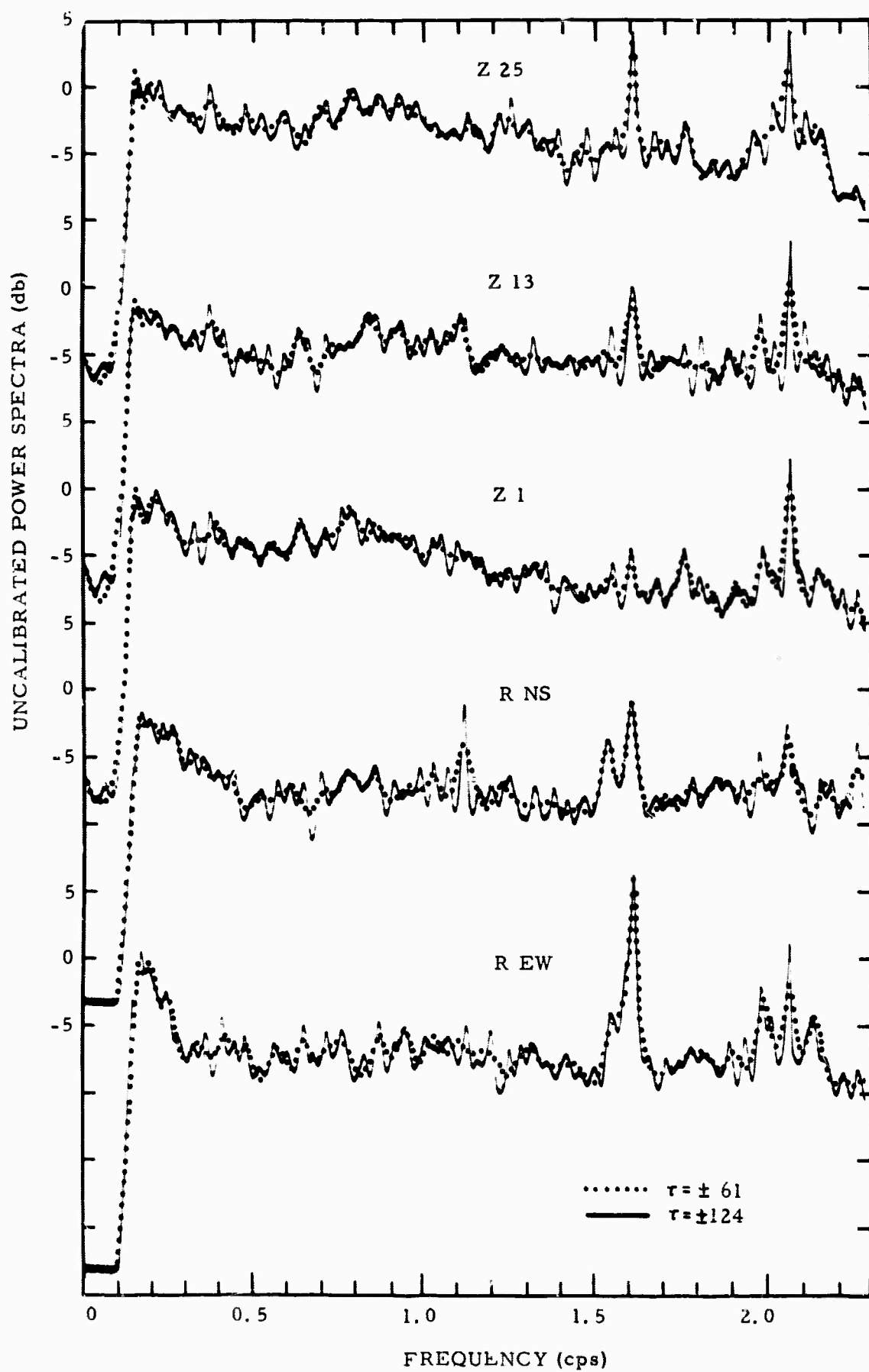


Figure IV-18. Uncalibrated Power Spectra For Z25, Z13, Z1, RNS and REW

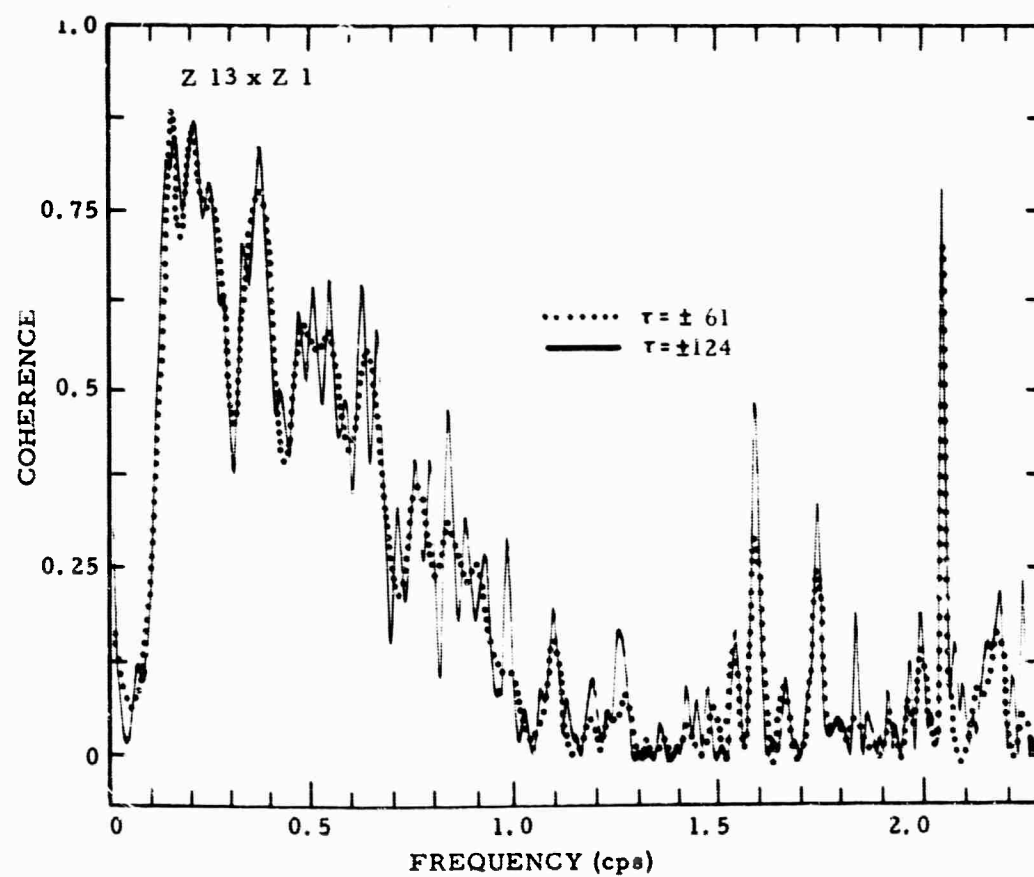
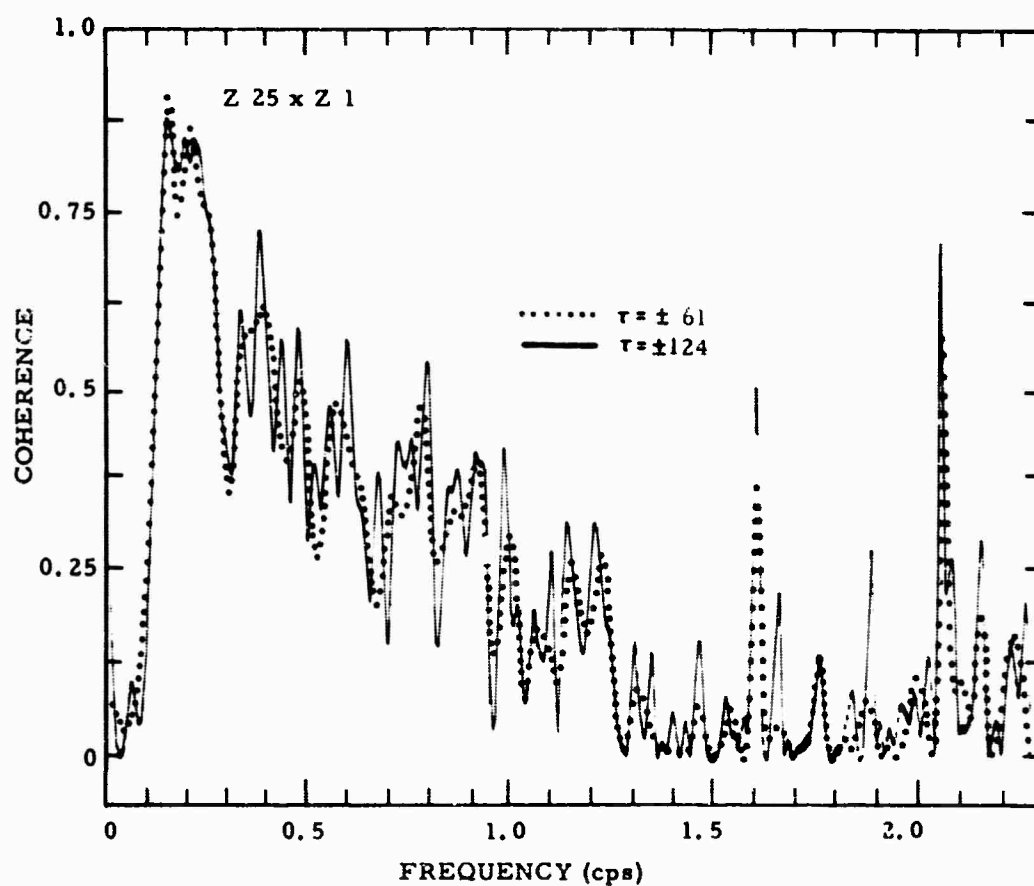


Figure VI-19. Coherences For Z13XZ1 and Z25XZ1

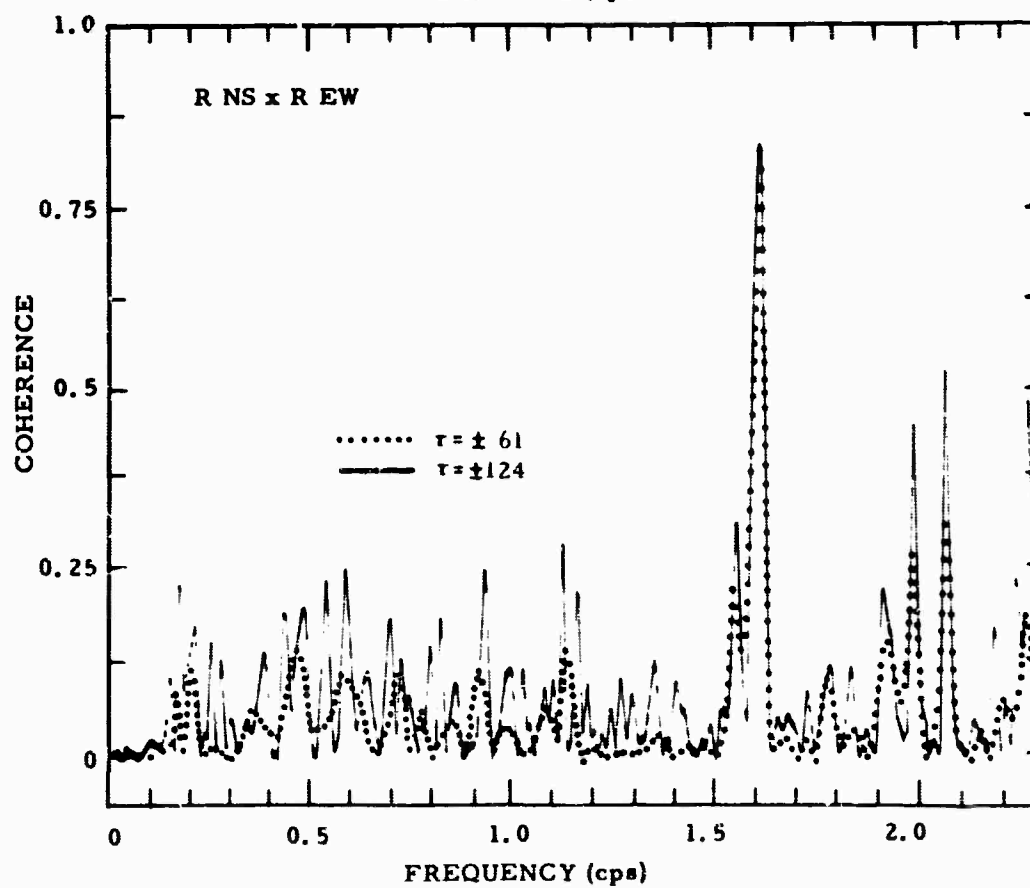
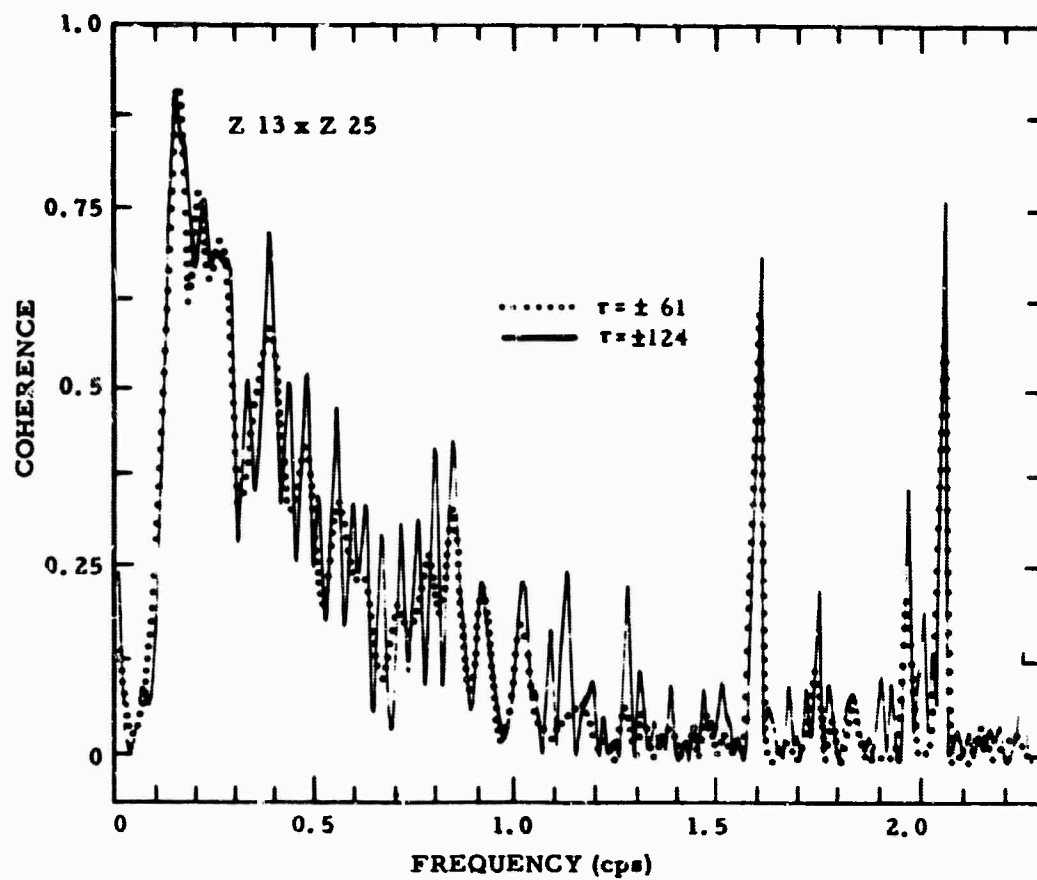


Figure VI-20. Coherences For Z13XZ25 and RNSXREW

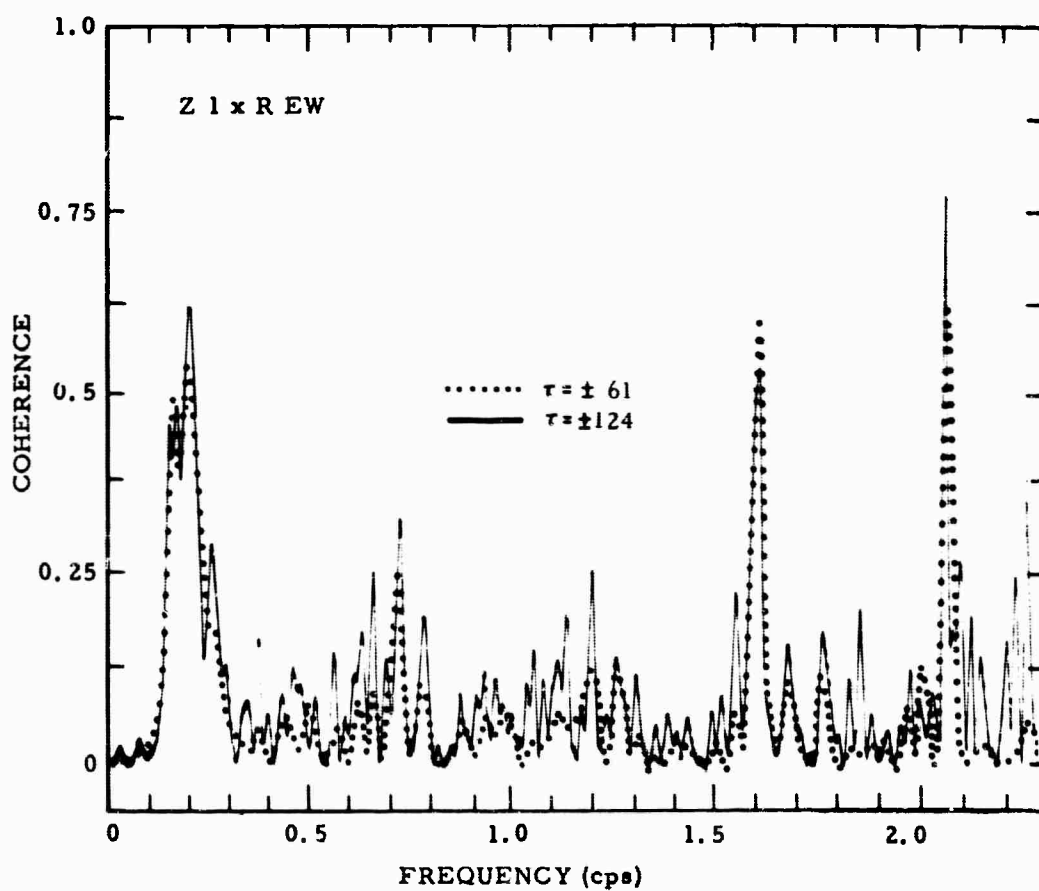
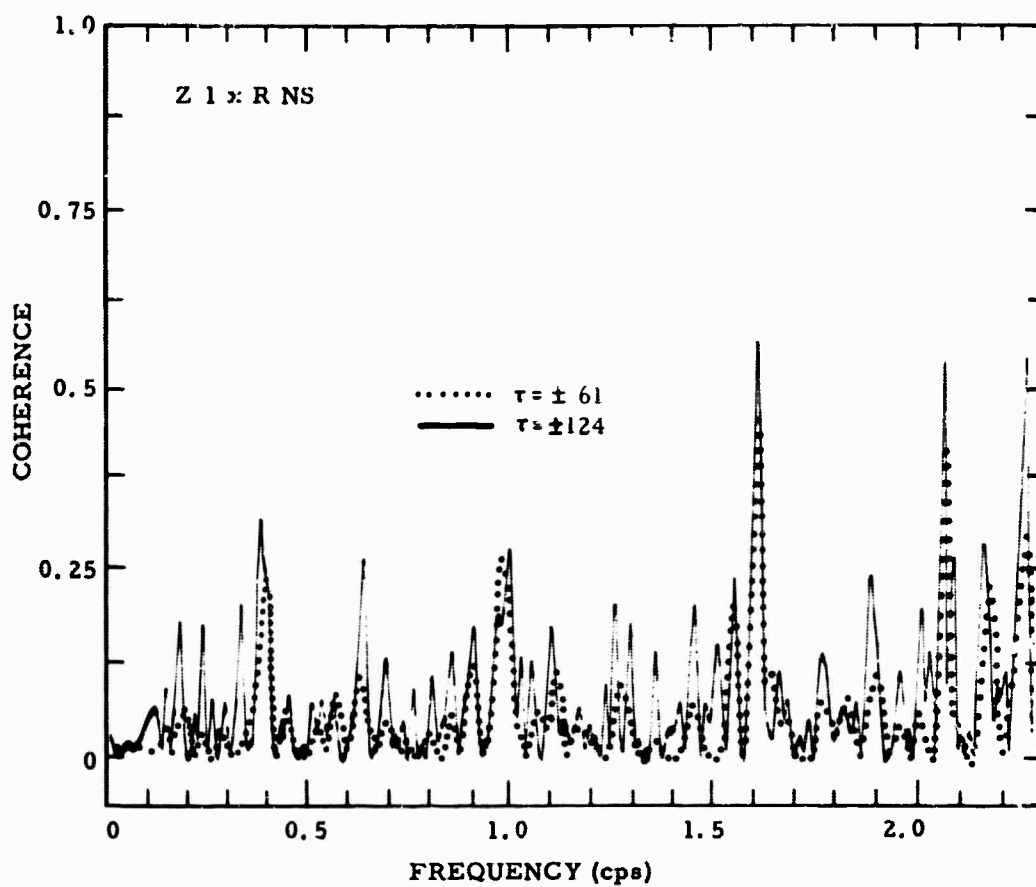


Figure VI-21. Coherences For Z1XREW and Z1XRNS

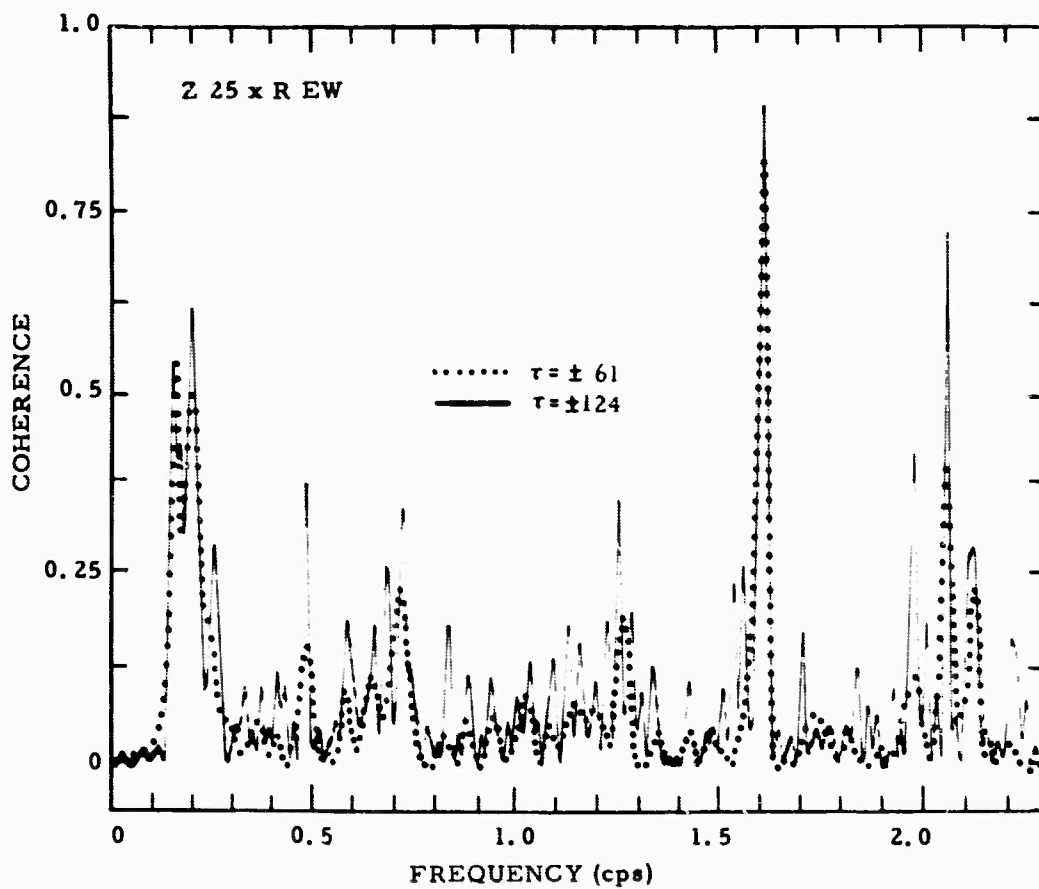
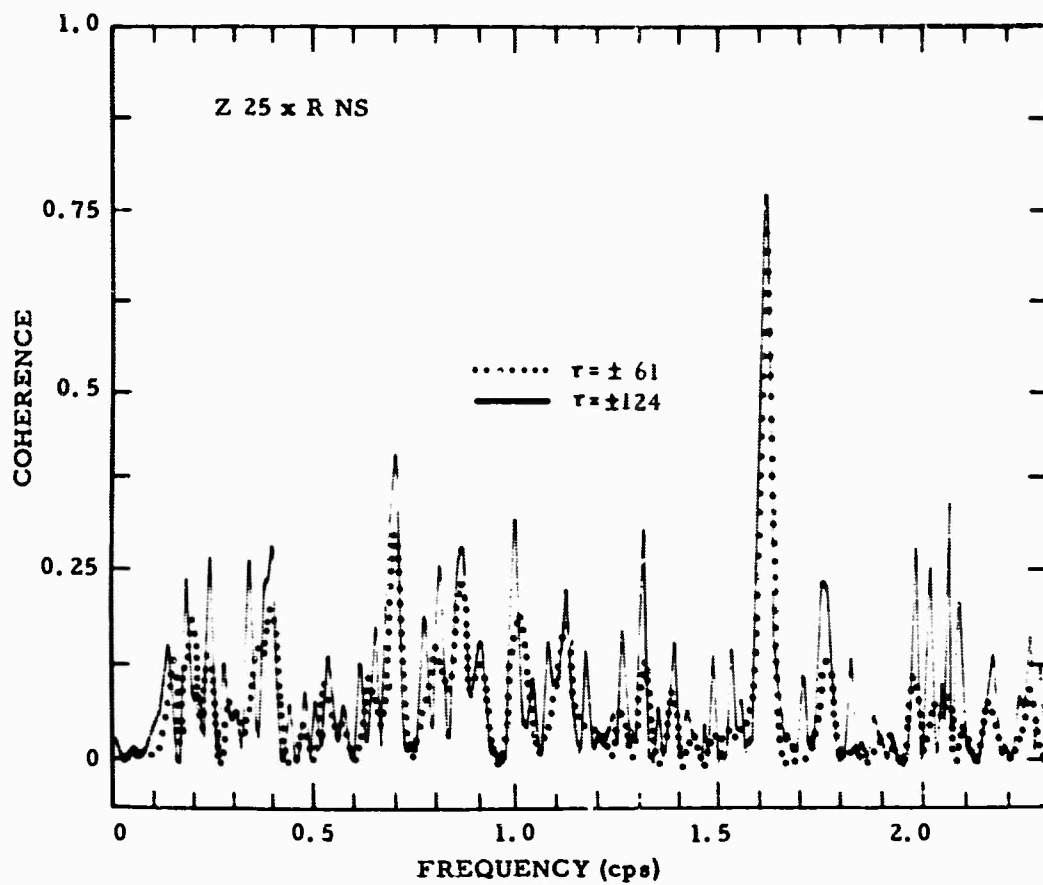


Figure VI-22. Coherences For Z25XREW and Z25XRNS

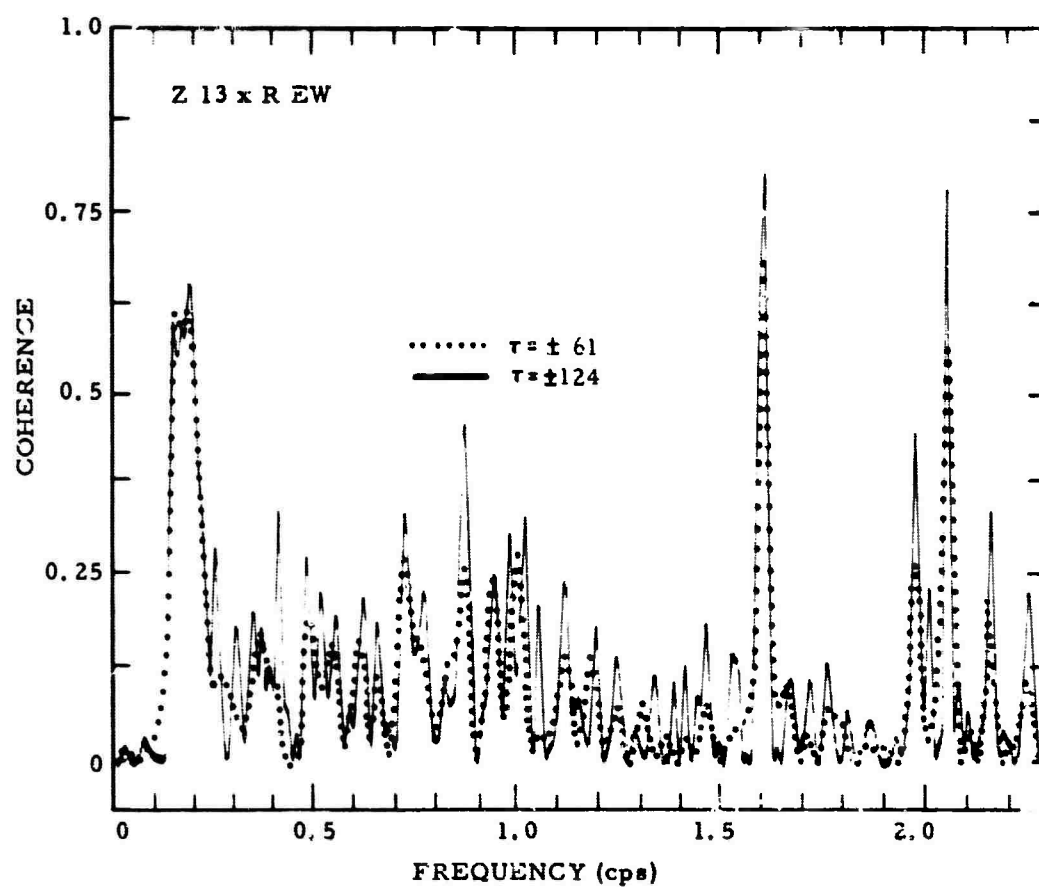
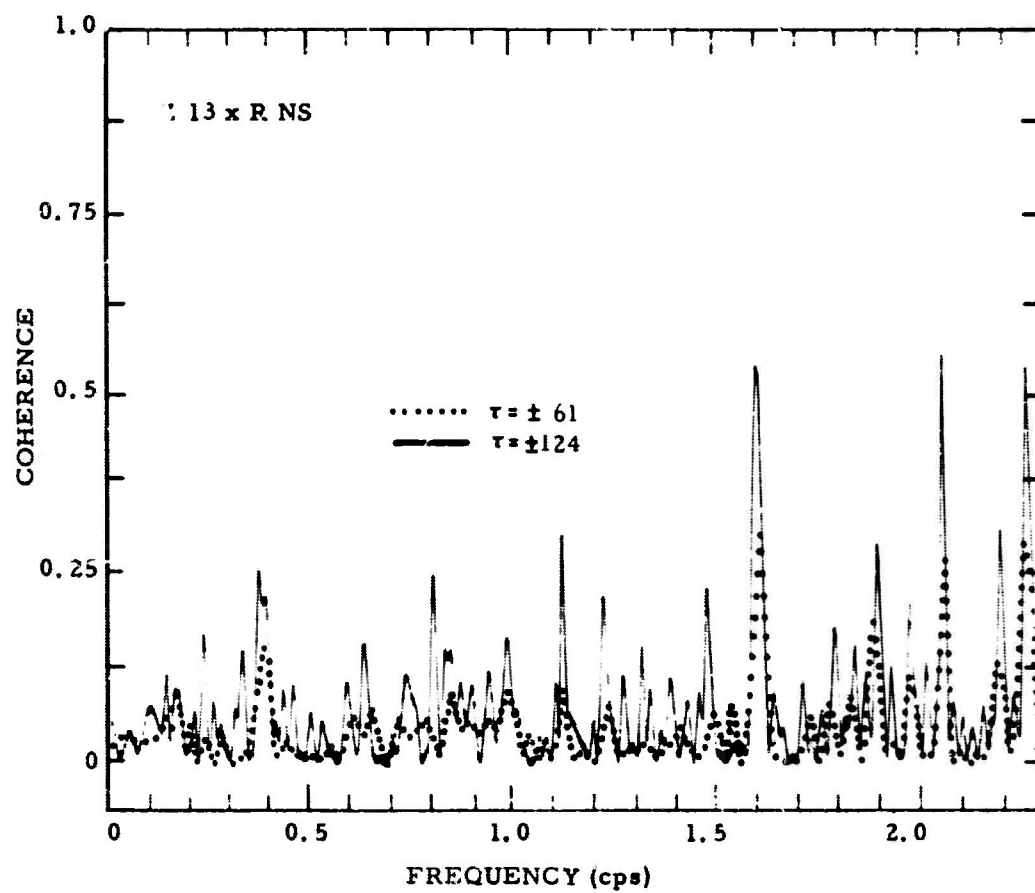


Figure VI-23. Coherences For Z13XREW and Z13XRNS

This is a clear indication that the 4 to 6 sec energy is Rayleigh wave energy and is coming from about N60°E. The difference in the spectra of the two horizontal seismometers (Figure VI-18) in the frequency range of 0.1 to 0.5 is open to discussion. However, the lack of coherence of the energy on the transverse horizontal with the other seismometers indicates that it is Love wave energy coming from the same direction as the Rayleigh wave energy.

These results indicate that an array of 3-component seismometers could be used to separate teleseismic signals from Rayleigh and Love wave ambient noise.

SECTION VII

REFERENCES

1. Texas Instruments Incorporated, 1964: Array Research Semiannual Technical Report No. 2 prepared for AFTAC, Contract AF 33(657)-12747, Nov. 15.
2. Texas Instruments Incorporated, 1964, Multichannel filter systems for Tonto Forest Observatory, part 1: Array Research Special Report No. 2 prepared for AFTAC, Contract AF 33(657)-12747, Sept. 1.
3. Texas Instruments Incorporated, 1964, Multichannel filter systems for Tonto Forest Observatory, part 2: Special Report No. 3 prepared for AFTAC, Contract AF 33(657)-12747, Sept. 21.
4. Schneider, W. A., K. L. Larner, J. P. Burg, and M. M. Backus, 1964, A new data-processing technique for the elimination of ghost arrivals on reflection seismograms: Geophysics, v. 29, p. 780-805.
5. Texas Instruments Incorporated, 1965, Horizontal and vertical arrays for teleseismic signal enhancement: UBO model theoretical results: Array Research Special Report No. 6 prepared for AFTAC, Contract AF 33(657)-12747, Feb. 15.
6. Texas Instruments Incorporated, 1964: Array Research Semiannual Technical Report No. 1 prepared for AFTAC, Contract AF 33(657)-12747, May 15.
7. Texas Instruments Incorporated, 1964, Synthesis and evaluation of a nineteen-channel filter system for extraction of teleseismic P-waves from ambient seismic noise at Cumberland Plateau Seismological Observatory: Report prepared for AFTAC Contract AF 33(657)-12331, Jan. 20.
8. Texas Instruments Incorporated, 1963, Synthesis and evaluation of six multichannel filter systems based on measured correlation statistics of ambient noise at Cumberland Plateau Observatory designed to operate on rings of seismometers: Report prepared for AFTAC, Contract AF 33(657)-12331, Dec. 31.
9. Texas Instruments Incorporated, 1965, Worldwide collection and evaluation of earthquake data: Semiannual Technical Report No. 1 prepared for U. S. Dept. of Commerce (C&GS), Contract AF 19(604)-8517, Apr. 28.

10. Texas Instruments Incorporated, 1964, Basic theory of probabilistic processing: Array Research Special Report No. 4 prepared for AFTAC, Contract AF 33(657)-12747, Dec. 3.
11. Hildebrand, F. B.: Methods of Applied Mathematics (New York, 1952) p. 46-49.
12. Texas Instruments Incorporated, 1963: Array Research Section III of Phase II Final Part 2 Wichita Mountains Seismological Observatory Special Report prepared for AFTAC, Contract AF 33(657)-12331, Mar. 26.
13. Texas Instruments Incorporated, 1964, A re-evaluation of S/N improvement for CPO using local noise: Array Research Special Report No. 5 prepared for AFTAC, Contract AF 33(657)-12747, Dec. 15.